

Turbulence and Sound Generated by a Rotor Operating Near a Wall

Henry Hall Murray IV

Thesis submitted to the faculty of the Virginia Polytechnic Institute and State University in partial fulfillment of the requirements for the degree of

Master of Science

In

Aerospace Engineering

William J. Devenport

William Nathan Alexander

K. Todd Lowe

29 April 2016

Blacksburg, Virginia

Keywords: Rotor, Acoustics, Boundary Layer, Tip Gap, Turbulence Ingestion Noise, Particle Image Velocimetry, Phase Averaged, Experimental, Wind Tunnel, Microphone, Wall Pressure, Blade Vortex Interaction, Propeller-Hull Vortex, Pirouette Vortex, Vortex Interaction Noise

Turbulence and Sound Generated by a Rotor Operating Near a Wall

Henry Murray

ACADEMIC ABSTRACT

Acoustic and aerodynamic measurements have been carried out on a rotor operating in a planar turbulent boundary layer near a wall for a variety of thrust conditions and yaw angles with respect to the inflow. At the highest thrust condition a strong flow reversal in the wall-rotor tip gap was observed. Average velocity fields filtered by the angular position of the rotor show that the flow reversal is fed by jets of fluid that tend to form below the blade as it passes by the wall. Instantaneous velocity measurements show the presence of strong vortices in the tip gap. These vortices were characterized and found to be both stronger and more numerous on the downstroke side of the tip gap. Additionally, vortices with the same handedness as the bound circulation in the blade were more numerous and only located on the downstroke side of the tip gap. Those with the opposite handedness were found to be only located on the upstroke side. Unexpectedly strong far-field acoustic response at the blade passage frequency at this highest thrust condition and is believed to be due to an interaction of the blade tip with these vortices. At moderate thrust, when the rotor was yawed toward the downstroke side the far field acoustic response at the blade passage frequency was found to increase. The opposite was true as it was yawed toward the upstroke side. At the highest thrust, however the unyawed rotor had the strongest blade passage frequency response which is believed to be due to stronger vortex-tip interaction in this case.

Turbulence and Sound Generated by a Rotor Operating Near a Wall

Henry Murray

PUBLIC ABSTRACT

This thesis details the findings from an experiment that was carried out on a fan, or rotor, operating in the air flow past a wall. The air flow forms a boundary layer near the wall that contains a lot of unsteady velocity fluctuations, or turbulence. The rotor blades then create noise as they interact with this unsteady inflow. The goals of this experiment were 1) to investigate what is happening to the air in the gap between the rotor and the wall and 2) to document the sound that the rotor makes at a large range of operating conditions. To this end the rotation rate of the rotor was varied such that a variety of thrust conditions could be studied and the angle of the rotor to the inflow was varied so that a range of off axis, or yawed, operating conditions could be studied. Measurements were taken of the sound the rotor produced, the pressure on the wall closest to the rotor, and of the velocity of the air in the tip gap, or the space between the wall and rotor. This thesis aggregates all of these measurements, at all of the operating conditions studied, together to build a coherent picture of the interaction of the rotor with the inflow turbulence and with the wall.

It was found that at the highest rotation rate the air in the tip gap was actually pulled backwards upstream and then into the rotor. This is because it is spinning so quickly and the presence of the wall on one side starves it for air there, forcing air to come back up from downstream. Further analysis of the air in the tip gap showed that the flow reversal tends to be driven by each blade passing by the wall. The air in the tip gap was found to be very unsteady and to often contain strong vortices, or small areas of circular flow. The locations and strengths of these vortices was also quantified and they were found to be both much stronger and more numerous when the rotor was unyawed, or pointing exactly upstream.

In the noise measurements, it was found that the case with the rotor spinning the fastest was much louder than would be predicted by the blades just interacting with the boundary layer turbulence. Specifically, the sound is much louder than the predictions at frequencies corresponding to the blade passage frequency, or the frequency at which blades pass by the wall, and its multiples. Relating this to the velocity measurements in the tip gap, it is hypothesized that the additional noise is the result of the rotor blades interacting with the vortices commonly found there.

At the highest rate of rotation, the fan was found to be loudest when it was unyawed. This is hypothesized to be due to increased interactions of the blade tips with the vortices in the tip gap in this case due to their increased presence compared to the yawed cases. However, at moderate and low rotation rates, the rotor was found to be louder when it was yawed toward the side where the blades were approaching the wall. This is believed to be a consequence of the change in the angle of the blades to the air when they are closest to the wall at yawed conditions.

Acknowledgements

These past two years in graduate school have been quite an adventure and I would not be where I am today without the influence of a great many people around me.

First and foremost I would like to thank my advisor Dr. William Devenport. Without his weekly suggestions, insights, and feedback this work would not have come together as it did. I had never worked on research in my undergrad career here at Virginia Tech and looking back I had little idea what I was getting myself into with graduate school. Dr. Devenport took a chance and gave me the opportunity to work on an extremely interesting project in his group and I think that, after a lot of hard work these past two years, I have really been able to contribute in a meaningful way to this project and advance our understanding of rotor-wall interaction noise.

I would also like to thank Dr. W. Nathan Alexander for his insights with everything acoustics related and for being available and happy to answer the multitude of questions that I have asked him over the past two years. I would like to thank Dr. Todd Lowe for his insights in PIV and for helping me realize the potential contained within the overabundance of data I had right in front of me.

I would also like to thank my parents and my brother for being a constant source of support and encouragement throughout all my years here at Virginia Tech and especially during these past two years in graduate school. They have always been there for me, pushing me to reach my full potential and to do what I think is best; for that I will be forever grateful.

All the graduate students and faculty in the CREATE research group on the top floor of McBryde have been instrumental in my development as a researcher and in my progress throughout this project. In particular I would like to thank Manuj Awasthi, Ian Clark, Liselle Joseph, Dan Cadel, Ken Brown, Tamy Guimarães, Nick Molinaro and everyone else I have worked with and routinely bothered with questions over the past two years. The collaborative environment of the research group as a whole made it easy to ask questions and bounce ideas off each other in addition to creating a fun work environment every day. My friends, especially the Mangi and also my roommates, made graduate school a memorable and enjoyable time. I am grateful for them dragging me away from my work when I was spending too much time on it, for the superb help received in my project, and for helping me keep things in perspective during my time in graduate school. I will miss you all very much when I move out of Blacksburg and onto the next stage of my life.

Lastly, I would like to especially thank the Office of Naval Research, and specifically Dr. Ki-Han Kim and Dr. John Muench, for their support under grants N00014-14-1-0141 and N00014-16-1-2395. I would also like to acknowledge and thank the Virginia Tech Institute for Critical Technology and Applied Science (ICTAS), and the Virginia Space Grant Consortium for their support of myself and this research effort. Without all of their support this project would not have been possible.

Table of Contents

Chapter 1: Introduction.....	1
1.1 Background and Motivation.....	1
1.2 Literature review	1
1.3 A Brief Explanation of the Fundamental Theories of Leading and Trailing Edge Noise	2
1.3.1 Leading Edge Noise	2
1.3.2 Trailing Edge Noise	3
1.4 The Thrusting Regime and the Haystacking Pattern in Turbulence Ingestion Noise	4
1.5 Rotor Testing in the Braking Regime and Wind Turbine Applications.....	7
1.6 Previous Rotor Experiments at Virginia Tech	10
1.7 Acoustic Predictions for the Rotor in a Turbulent Boundary layer.....	14
1.8 The Pirouette Effect and the Propeller Hull Vortex.....	16
1.9 Conclusion of Literature Review	19
1.10 Objectives of this Thesis.....	20
Chapter 2: Experimental Setup, Instrumentation, & Conditions	22
2.1 Virginia Tech Stability Tunnel and Semi-Anechoic configuration	22
2.2 Rotor System.....	24
2.3 Acoustic Measurements: Inflow Microphones	27
2.4 Mean Wall Pressure Measurements	30
2.5 PIV Measurement System.....	31
2.5.1 Measurement Post-Processing Details in DaVis 8.2 from LaVison	35
2.5.2 Estimate of the Particle Response Time Based on Stokes Drag	35
2.6 Definition of Experimental Coordinate System.....	36
2.7 Test Matrix and Experimental Conditions	37
2.8 Uncertainty in the Measurement Systems.....	38
Chapter 3: Experimental Results and Analysis.....	42
3.1 Verification of the Boundary Layer	42
3.1.1 Zero Pressure Gradient Boundary Layer.....	42
3.1.2 Boundary Layer Profile Comparison	43
3.2 Thrusting Regime.....	44
3.2.1 Baseline Case – Moderately Thrusting	44
3.2.2 Effects of Advance Ratio in a Near Wall Rotor.....	48
3.2.3 Vortex Identification and Quantification in Instantaneous Velocity Fields.....	57
3.3 The Effects of Yaw on a Thrusting Rotor	62

3.3.1	An Explanation of the Geometric Consequences of Rotor Yaw.....	62
3.3.2	A Discussion of Flow Measurements as a Function of Rotor Yaw	64
3.3.3	Evidence of the Stagnation Region in Mean Wall Pressure Measurements	68
3.3.4	Acoustic Effects of Yaw in Region #1: No Pressure Gradient Reversal	69
3.3.5	Acoustic Effects of Yaw on Region #2: Pressure Gradient Reversal Observed	70
3.3.6	Reynolds Stress and Phase Averaged Velocity Measurements as a Function of Yaw	72
3.3.7	Vortex Identification in the Yawed Rotor at High Thrust	75
3.4	Braking Regime	80
3.4.1	Acoustic Measurements of the Braking Rotor	80
3.4.2	Wall Pressure Measurements	84
3.4.3	Near Wall Fluid Flow Measurements	87
Chapter 4:	Conclusions.....	93
4.1	Unyawed Thrusting Conditions:	93
4.2	Thrusting Rotor at Yaw to the Mean Inflow	94
4.3	Braking advance ratios:.....	96
Chapter 5:	References.....	97
Appendix A –	Annotated List of Figures.....	101
Appendix B –	Extra Figures	104

Chapter 1: Introduction

1.1 Background and Motivation

Rotor or fan noise is the dominant noise source in a wide variety of applications in everyday life. Rotors cover an enormous range of scales and applications, from computer cooling fans to window fans to aircraft propellers and jet engines to wind turbines. The noise and noise pollution created by each of these examples is becoming an increasingly important concern in our society as noise regulations become stricter and public awareness of noise pollution rises. Despite the large range of scales and applications in which rotor noise occurs there are several common generation mechanisms.

Two sources of rotor noise are self-noise and inflow turbulence noise. Self-noise is the result of viscous interactions of the blade with the air and includes turbulent and laminar boundary layer trailing edge noise and trailing edge vortex shedding noise. Inflow turbulence noise, also referred to as leading edge noise, is the result of the rotor ingesting a time-varying non-uniform flow field. This turbulent inflow creates unsteady lift forces on the blade which in turn induce sound in the far field.

Both turbulence ingestion noise and rotor blade trailing edge noise are significant sources of acoustic radiation in both propellers and turbines. They both occur in applications like jet engine fans, rear mounted propellers in aerospace and marine applications, and also in wind turbines. The focus of this thesis is the experimental study of a rotor immersed in an equilibrium, planar, turbulent boundary layer near a flat plate. This study is designed to systematically examine the noise produced by such a rotor at a variety of positive and negative thrust conditions and yaw angles. It will also examine the fluid dynamic mechanisms that contribute to this noise generation. In addition, it provides a systematic test case with which to validate acoustic predictive codes developed by our partners at Florida Atlantic University. This is all in an effort to better understand and predict rotor noise and therefore control and reduce it in the equipment design stage.

1.2 Literature review

This thesis follows a substantial body of work studying a rotor in turbulence and documents the third in a series of experiments at Virginia Tech which address the case of a rotor in a planar boundary layer, i.e. non-axisymmetric, anisotropic turbulence ingestion. However, this is the first experimental study to the author's knowledge to address the case of non-axisymmetric turbulence ingestion by a rotor in yaw.

Due the large range of application in which rotors generate noise, testing is usually conducted solely in either the braking or thrusting regime in order to simulate the dynamics of a propulsor or a turbine, respectively. However, in this case an opportunity was recognized to test an idealized model rotor in a planar turbulent boundary layer near a wall in both regimes within the same test. The literature addresses rotor testing in the braking and thrusting cases separately and, as such, the same will be done here. First however, the fundamental theories of leading and trailing edge noise as they apply to a rotor will be explained to provide a background for the literature review.

1.3 A Brief Explanation of the Fundamental Theories of Leading and Trailing Edge Noise

1.3.1 Leading Edge Noise

The fundamental theory for the current understanding of leading edge noise from a rotor starts with understanding the generation of this noise in the non-rotating frame. For this explanation we will start with the canonical case of a single airfoil that experiences a uniform inflow that is perturbed by a single spanwise oriented turbulent eddy. A two dimensional profile of this case is shown in Figure 1 below.

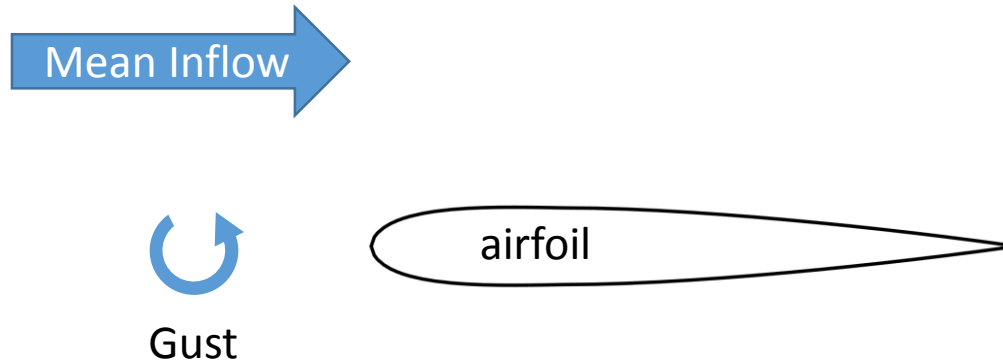


Figure 1: Diagram of a spanwise oriented gust impacting a 2D airfoil.

Amiet (1975) was the first to address the theoretical prediction of sound from this case. He realized that an airfoil in a non-uniform inflow will experience a fluctuating lift due to its non-constant angle of attack and that this should result in the generation of sound. He builds off the work of Liepmann (1955) who was inspired by the work of Sears (1941). Sears explained that as a turbulent eddy impacts an airfoil, the velocity component perpendicular to both the span and chord, also called the upwash velocity, creates a momentary change in the angle of attack of the airfoil. This unsteady change in angle of attack causes an unsteady change in lift on the spanwise section of the airfoil that this turbulent eddy impacts. A portion of the resulting pressure fluctuations are then radiated to the far field as acoustic energy (Dean (1971)). The way in which the blade responds to a turbulent interaction and radiates some of that energy to the far field as sound is characterized by the blade response function.

Since the upwash is the driving component in determining the momentary change in angle of attack of the airfoil, the upwash correlation along the span of the airfoil is the critical parameter of the inflow turbulence that dictates the level of the acoustic pressure fluctuations in the far field (Moreau *et al.* (2005)). When a spanwise section of the blade sees the same upwash change from the same turbulent eddy it will see the same angle of attack change and the entire spanwise section will respond in the same way. If this section is large it will result in a louder sound radiated to the far-field because coherent acoustic waves from the blade radiate much more effectively than incoherent noise.

Sevik (1974) applied this theory to the rotating frame and was able to successfully predict the broadband turbulence ingestion noise from a rotor. Continuing along this development it was found that the interaction of each blade with the inflow turbulence cannot be treated independently as long as the turbulent eddies are large enough such that they interact with more than one blade. Majumdar and Peake (1998) demonstrated that the inflow turbulence to a thrusting rotor distorts and stretches into long thin elements, resulting in each turbulent eddy being cut by multiple blades.

The interaction with multiple blades by the same turbulent eddy causes a similar response by each blade and results in a “haystacking” pattern in the farfield sound with spectral humps centered slightly above the Blade Passage Frequency (BPF) and its harmonics. The analytical theory behind the prediction of the haystacking noise is explained by Blake (1986), section 12.6.2. He uses the case of a 2D row of blades ingesting an idealized vortex and then derives the unsteady loading equation on an individual blade as a function of the integral lengthscale. His explanation also implies that the correlation lengthscale in the direction aligned with the axis of rotation of the rotor is the most significant parameter for the rotating frame. This correlation lengthscale dictates the number of blades that will interact with the same turbulent eddy and therefore the strength of the narrowband response seen at multiples of the BPF in the far field spectra.

1.3.2 Trailing Edge Noise

The treatment of trailing edge noise is somewhat different from leading edge noise in that there are five unique physical phenomena that cause farfield noise commonly referred to as trailing edge noise. The five sources are: turbulent boundary layer trailing edge noise (TBL-TL noise), laminar boundary layer vortex shedding noise (LBL-VS noise), separation-stall noise, trailing edge bluntness vortex shedding noise, and tip vortex formation noise. A comprehensive review of each of these types of trailing edge noise and semi-empirical prediction methods for each of them is contained in Brooks, Pope, and Marcolini (1989). A brief summary of the five different types of trailing edge noise will be presented here with special emphasis on those found relevant in this study.

In general trailing edge noise is produced by viscous interaction of an airfoil with a clean inflow. In TBL-TE noise, the laminar boundary layer undergoes transition to turbulence as the fluid flows across the surface of the airfoil. This turbulent boundary layer eddies convect with the mean flow across the trailing edge, which is extremely efficient at scattering the turbulent pressure fluctuations to the far field as sound. Ffowcs Williams and Hall (1970) developed an edge scattering model in an effort to describe this type of trailing edge noise. The sound level of TBL-TE noise has also been shown in a number of experiments to scale on the 5th power the freestream velocity. TBL-TE noise is believed to be present in the high frequency region in almost every case examined in this study.

Separation and stall noise occurs when the airfoil is at a large angle of attack and the flow over the suction side separates from the surface. It is found to be on the order of 10dB louder than trailing edge noise when it occurs. It would replace TBL-TE noise as the dominant source of noise at high angles of attack. Patterson *et al.* (1973) used surface pressure to far-field correlations to show that at deep stall the noise predominantly comes from the chord as a whole, but at mild stall the noise is radiated from the trailing edge. Current state of the art separation noise predictions are based on empirical data and are developed in Brooks, Pope, and Marcolini (1989).

LBL-TE noise occurs when a laminar boundary layer covers at least most of one side of the airfoil and is the result of vortex shedding from the trailing edge. The vortex shedding is coupled to an acoustically excited aerodynamic feedback loop that produces quasi-tones related to the rate of the vortex shedding. It is thought that the acoustic waves travel back upstream and excite instabilities which create Tollmien-Schlichting waves. These then grow and perpetuate the vortex shedding at the same frequency. This mechanism is also known to occur predominantly at low angle of attack conditions.

A general trend of the frequency dependence was found by Paterson *et al.* (1973) by scaling on the Strouhal number, defined below in Equation (1), using laminar boundary layer thickness at the trailing edge as the length scale. In this case, f is the shedding frequency, d is the relevant lengthscale, and v is the freestream velocity. LBL-TE noise is believed to be a major contributor to the sound spectrum at high

frequencies at certain thrust conditions in this study which correspond to low angle of attack conditions for the outer parts of the blade.

$$St = \frac{fd}{v} \quad (1)$$

Tip vortex formation noise is believed to be caused by the turbulence associated with the local separated flow over the tip of a finite wing. The tip vortex contains a thick turbulent core and the fluid dynamic mechanism for the noise generation is believed to be trailing edge noise due to the tip vortex core passing over the trailing edge at the wing tip.

Trailing edge bluntness vortex shedding noise is another notable form of airfoil self-noise. A blunt trailing edge has been shown to shed vortices when the trailing edge thickness is large compared to the boundary layer displacement thickness. This results in a high frequency broadband sound that is commonly observed in wind turbines.

1.4 The Thrusting Regime and the Haystacking Pattern in Turbulence Ingestion Noise

A thrusting rotor ingesting turbulence generates a broadband noise signature that is a combination of both turbulence ingestion noise and airfoil self-noise. In recent years a large body of work has been devoted to understanding and predicting this complex phenomena. To adequately understand and predict the sound generated by a rotor in turbulence a number of complex interactions must be understood. These include the characterization of the inflow turbulence, how this turbulence distorts with the mean inflow shear, the interaction of the rotor blades with the distorted turbulent field, the blade-to-blade coherent effects of turbulent structures that interact with multiple blades, and the directionality of the far field sound both in total levels and frequency distribution.

Since this is such a complex task it is understandable that the simplest case of a rotor ingesting homogeneous isotropic turbulence was considered first. Sevik (1974) was the first to address this simplified problem. His ground breaking work predicted that the power spectral density of the sound depended on the integral lengthscale of the turbulence divided by the axial velocity, essentially a characteristic timescale of the turbulence passing by the rotor blade under Taylor's frozen turbulence hypothesis.

In order to verify his predictions, Sevik compared them to measurements of the unsteady thrust spectrum of a 10 bladed rotor ingesting grid generating turbulence in the Garfield-Thomas Water Tunnel at Penn State. He found that the theory, although accurately capturing the inverse relationship between the unsteady thrust response and frequency, was unable to account for the broadband spectral humps centered at frequencies slightly above multiples of the BPF. The reason for this is that Sevik's initial predictions did not take into account haystacking, or blade-to-blade coherence effects, because he assumed that each "eddy" the propeller encounters is struck no more than once by a blade, as explained in Martinez (1996).

The discovery of haystacking noise was a significant contribution to the understanding of turbulence ingestion noise. It is very distinct in the far field acoustic spectra and is characterized by an organization of the broadband spectra into a series of spectral humps centered slightly above multiples of the BPF and its harmonics and decreases in amplitude at successively higher harmonics. The illustration in Figure 2 below shows the typical spectral shape of haystacking noise from a rotor.

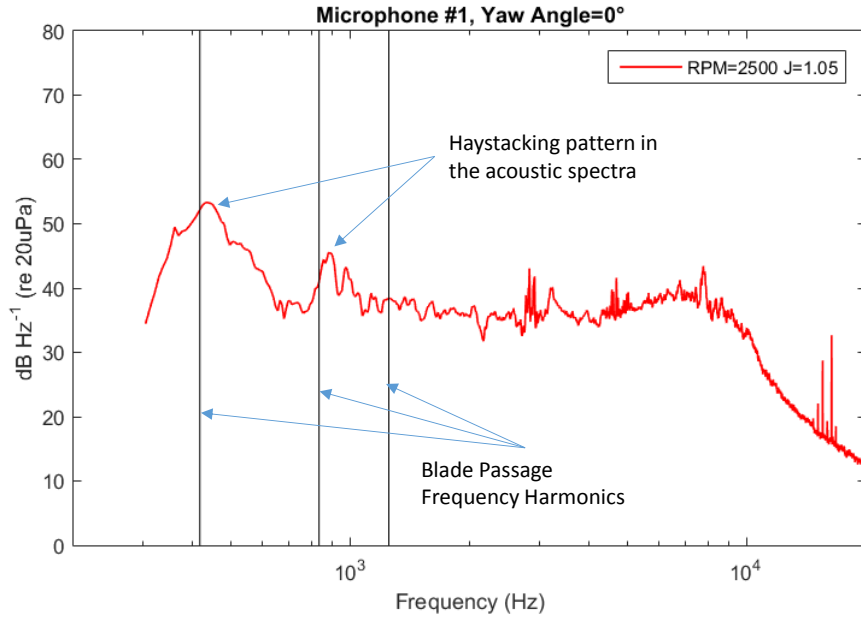


Figure 2: Illustration of the haystacking pattern in an example acoustic measurement of the rotor in this test.. Note that the spectra humps are centered slightly above the blade passage frequency harmonics. The reason for the slight red shifting of the haystacking peaks is illustrated, as shown in Wisda *et al.* (2014), below in Figure 3. Consider two eddies that are approaching the boundary layer with opposite skewness in the spanwise direction, as illustrated by the red and blue ovals below. These eddies will be cut by consecutive fan blades in a manner that varies with both time and spanwise position. The blades sweeps from bottom to top of the figure starting with the leftmost arrow and working to the right. It will interact with the blue eddy with a frequency below higher than blade passage frequency due to its skew. Conversely, the blades will then interact with eddies skewed in the opposite direction, red in the figure below, at a frequency below the blade passage frequency. The blades however interact with the blue eddies more times, due to their skew, than the red eddies. In this illustration the blue eddy is cut nine times while the red eddy is cut only six times. The haystacking pattern in turbulence ingestion noise is created as a result of a coherent interaction of consecutive blades with the same eddy. This tends to create a stronger haystacking response from the blue skewed eddies, which is also at slightly higher frequencies than the blade passage frequency, and this causes a shift in the haystacking peaks in the overall time averaged spectra.

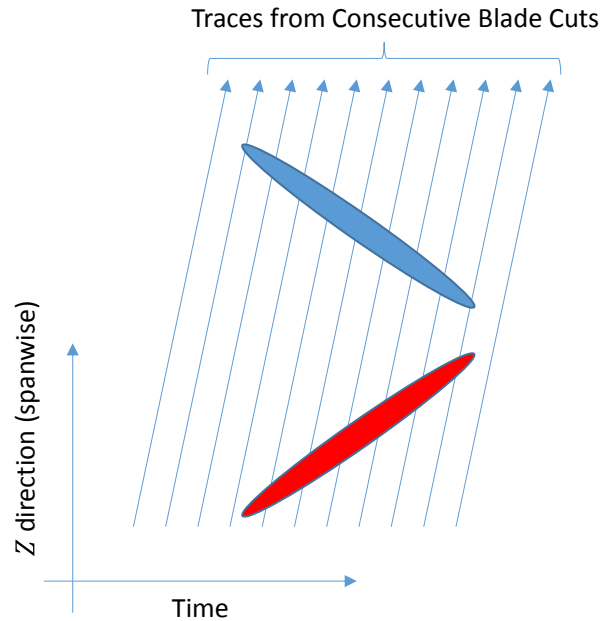


Figure 3: Example of bias in the blade interaction with skewed eddies in the boundary layer. The blue eddy is cut at a frequency slightly higher than the blade passage frequency and is also cut more times. This results in the overall shift in the haystacking peaks toward higher frequencies seen in the time averaged spectra.

Majumdar and Peake (1998) examined, from a theoretical perspective, the nature of the sound generated by a rotating fan. They investigated both a static ground test scenario as well as an inflight scenario and found that the spectral shape of the far field noise was highly dependent on the inflow conditions. The static condition results in a large inflow distortion as the rotor draws in air from all directions ahead of the blades, which causes a stretching of the natural atmospheric turbulence into long thin filaments, as shown in Figure 4 below. These long thin spaghetti-like filaments are then chopped up by consecutive fan blades resulting in a very strong coherent response at the BPF and its harmonics, or haystacking noise, in the farfield. The high inflow velocity of the inflight conditions means that there is much less inflow distortion to the fan. Consequently there is also less haystacking noise in flight. Similarly, Hanson (1974) showed that haystacking noise was enhanced when the inflow turbulent structures were large relative to the blade spacing.

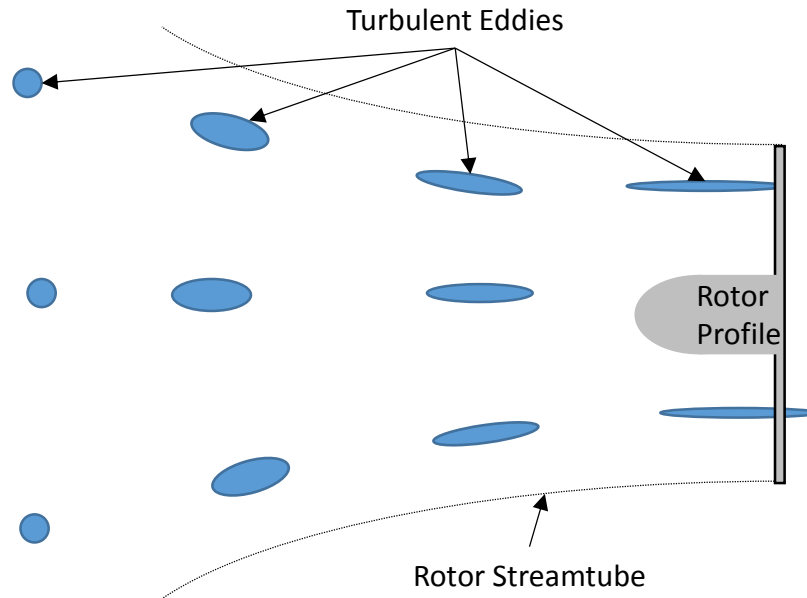


Figure 4: The distortion and axial elongation of atmospheric turbulence into a stationary thrusting rotor, one of the cases examined by Majumdar and Peake (1998) and a major contributing factor to the haystacking phenomena observed in the acoustic spectra from turbulence ingestion noise.

Haystacking noise has also been seen in a number of studies since Sevik's original experiment. These include Sharpf and Muellur (1995), Minniti *et al.* (2001) and (2001a), Wojno *et al.* (2002), and Stephens and Morris (2009). Predictions methods for haystacking leading edge noise have been explored by a number of studies, including Blake (1986) section 12.6.2, Martinez (1997), Glegg and Walker (1999), among others. A particular focus of the work of Ganz (1998), Stephens and Morris (2009) and Glegg and Walker (1999) was the axisymmetric case of a fan ingesting the boundary layer grown on an inlet duct upstream of the fan. This case is undoubtedly relevant for high bypass ratio jet engines however in the broader picture it only examines the anisotropic time invariant case of blade-turbulence interaction since the casing boundary layer is axisymmetric.

The non-axisymmetric case is of increasing interest because it relates to cases of pusher propellers that are ingesting turbulence from an upstream structure or surface. However, this case is significantly more difficult since the blades now interact with an anisotropic and time varying turbulent field. The work in this area has been sponsored by the Office of Naval Research in recent years and increasing progress has been made on this difficult problem. Catlett *et al.* (2012) pioneered this effort by examining the case of a propeller mounted to the trailing edge of a large airfoil such that it ingested the thick turbulent boundary layer grown along both sides of the airfoil.

Another highly relevant scenario in the non-axisymmetric case is one where the rotor is operated near a wall such that it is partially immersed in an anisotropic and inhomogeneous turbulent boundary layer. This scenario has been investigated in detail through a series of experiments at Virginia Tech beginning in 2009 and the results of which are summarized below. The current experiment builds on their foundation so it is important that their contributions are elaborated and explained.

1.5 Rotor Testing in the Braking Regime and Wind Turbine Applications

The study of aerodynamic noise is a topic of sustained interest for large scale wind turbines (Wagner *et al.* 1996). Due to difficulties with power transmission, offshore wind farms are not as

economically feasible as land based turbines. Public opposition to wind turbines is largely derived from the noise they produce and this can be very problematic to the expansion of the wind power industry in populated areas. At this time, it is not known with certainty whether inflow turbulence or self-noise is the principal contributor to the overall wind turbine far field noise or under what physical conditions one source dominates the other. It is difficult to quantify the inflow turbulence noise, mainly due to the difficulty in characterizing the atmospheric boundary layer turbulence directly upstream of the rotor. Therefore, the focus of this experiment in the braking regime is the examination of the conditions and frequencies for which inflow turbulence noise or self-noise become dominant.

It is well known that the inflow of a rotor is distorted as it approaches the blade disk. In the case of a wind turbine or braking rotor, the inflow is compressed axially as the upstream velocity decreases on approach to the blade disk. This also compresses the scale of turbulent eddies in the axial direction, resulting in a distortion in the character of the inflow turbulence. For full scale wind turbine applications, turbulence characteristics are dictated by upstream atmospheric and meteorological conditions. This means that the scale of turbulence under consideration can be very large, on the order of 140 m. A prediction method has been derived (Glegg *et al.* 1987) utilizing Amiet's (1975) work on the response of an airfoil to a turbulent gust in combination with the Ffowcs Williams and Hawkings equation, but it under-predicts the measured noise levels when atmospheric turbulence scales are used as the length scales. However, the agreement between measurements and predictions substantially improves when smaller turbulence scales, on the order of the blade chord, are used. Glegg suggests that this might occur because the localized unsteady aerodynamic loading on each blade, which propagates to the far-field as sound, is locally influenced by gusts much smaller than the overall scale of atmospheric turbulence. Since wind turbines rotate relatively slowly and because they decelerate the air flowing into and through their blade disc, these local gusts are likely due to the influence of previous blades trailing vortices and wakes (Glegg *et al.*, 1987).

A number of other studies suggest that inflow turbulence contributes significantly to the total far-field noise produced by a wind turbine (Grosveld, 1985, Fuglsang and Madsen 1996). Most importantly, these studies suggest that it is essential to define the inflow turbulence characteristics in order to accurately predict the noise produced by a wind turbine. Fuglsang and Madsen (1996) take both self-noise and inflow turbulence noise into consideration in an effort to accurately predict the noise from two large scale (300kW) wind turbines. They obtained agreement between their predicted spectra and measurements over a range of frequencies from 50 Hz to 10 kHz. They predict that for large scale wind turbines, inflow turbulence is the dominant noise source at lower frequencies while trailing edge noise gradually increases throughout the midrange becoming dominant only at higher frequencies.

Ideally, this measurement of atmospheric turbulence or an upstream turbine wake would be carried out in the field with a full scale wind turbine. However, it is not practical, or at the very least prohibitively expensive, to measure the range of turbulent length scales that a wind turbine sees in the field due to the sheer size of atmospheric boundary layer turbulence and the temporal variability inherent in field measurements. Therefore, it is desirable to first measure and understand the phenomena in a controlled, scaled wind tunnel environment.

A survey of scaled wind turbine experiments, based on data compiled by McTavish *et al.* (2013) is shown in Figure 5 below. Commercial wind turbines typically have a tip Reynolds number on the order of 5×10^6 but there is not yet a formal classification of wind turbine models for testing. McTavish divides scaled wind turbine experiments into three rough categories based on their Reynolds number. Full-sized tests have a Re_{tip} on the order of 10^6 , medium-scale tests have a Re_{tip} on the order of 10^5 and small scale tests have a range of 10^4 or $10^5 Re_{tip}$.



Figure 5: Survey of tip Reynolds number and rotor diameter of scaled wind turbine experiments, based on data from McTavish *et al.* (2013). Triangles indicate commercial and full-scale, squares indicate medium-scale, and circles indicate small-scale experiments. The current experiment is indicated with the black plus signs.

Wind turbine tests conducted in wind tunnels are typically geometrically scaled models of full sized wind turbines that are designed to match tip speed ratio (TSR), and tip Reynolds number, defined in Equation (2) and (3) below. In Equation (2) λ is the tip speed ratio, ω is the rotation rate in radians per second, R is the radius of the rotor, and v is the freestream speed. In Equation (3) Re_{tip} is the tip Reynolds number, U_{tip} is the tip speed, c is the rotor blade chord, and v is the freestream velocity. Another parameter commonly used to describe the operating conditions of rotors is the advance ratio, defined in Equation (4) below, where v is the inflow velocity, n is the rotation rate in revolutions per unit time and D is the diameter of the rotor. The advance ratio will be primarily used in this thesis to refer to the operating condition of the rotor.

$$\lambda = \frac{\omega R}{v} \quad (2)$$

$$Re_{tip} = \frac{U_{tip} c}{v} \quad (3)$$

$$J = \frac{v}{nD} \quad (4)$$

A method has recently been developed by Ryi *et al.* (2014) for estimating the sound produced by a full sized wind turbine from wind tunnel test data of a scaled model and a 2D airfoil section of the blade. This method involves matching the TSR and tripping the flow where transition would occur in the full scale turbine. McTavish *et al.* (2013) found that the thrust coefficient of a geometrically scaled rotor is degraded in low Reynolds number flow, indicating that matching Reynolds number is important for scaled wind

turbine tests. Burdett and Van Treuren (2012) also found that Reynolds number matching is necessary for scaled wind turbine tests. For these reasons, wind tunnel testing of wind turbine models can be valuable and extrapolation of the acoustic results is improved if the model is scaled appropriately. Lastly it should be noted though that the mechanisms of trailing edge noise production are likely to be different between a full sized wind turbine and this rotor. The full scale wind turbine operates at much higher Reynolds numbers which makes it unlikely to experience laminar boundary layer vortex shedding noise. Conversely this rotor is small enough that it is unlikely to have a fully developed turbulent boundary layer at the trailing edge.

Although the rotor in this study is not a geometric model of a wind turbine, it is operating on the same scales and conditions at which previous wind tunnel wind turbine tests have been performed so it is still able to provide insight to the relative dominance of turbulence ingestion vs. self-noise of a braking rotor in a planar boundary layer.

1.6 Previous Rotor Experiments at Virginia Tech

As discussed above, in order to make turbulence ingestion noise predictions for a rotor, the properties of the inflow turbulence must either be assumed, usually to be homogenous and isotropic, or must be completely characterized. A side view of the setup of the previous rotor experiments at Virginia Tech is shown below in Figure 6. The rotor is immersed to approximately half of its blade span in the highly anisotropic thick turbulent boundary layer.

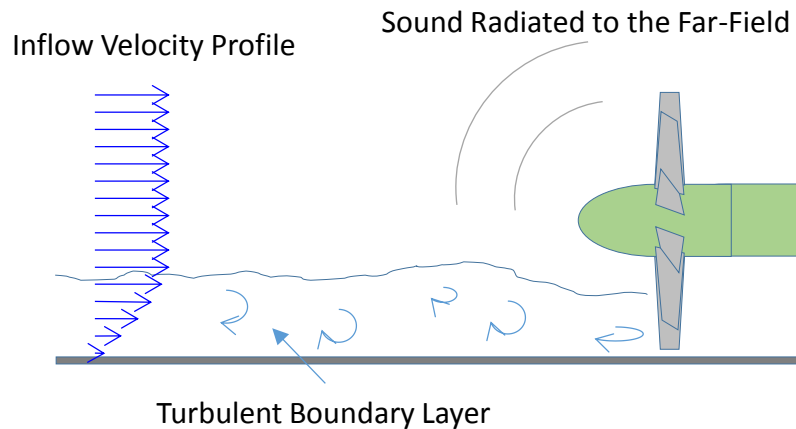


Figure 6: Side view of the rotor partially immersed in a planar turbulent boundary layer near a wall; the configuration studied by Alexander et al. (2013) on the boundary layer characterized by Morton (2012).

The planar turbulent boundary layer used in this experiment had to be completely characterized since it cannot be modeled as isotropic turbulence. The required input to the sound prediction methodologies discussed above is the correlation function in the blade frame of reference. To that end, Morton (2012) completed a measurement of the full 4D space-time correlation function of a thick high Reynolds number equilibrium turbulent boundary layer.

He started the measurement by taking single point hotwire measurements to record the boundary layer profile at a range of operating conditions and upstream trips in order to quantify the conditions of the boundary layer on the wall. He took boundary layer quantification measurements with two separate boundary layer trips, a 9.5mm L-bracket and a double 19mm trip, and three flow speeds, 20, 30 and 55 m/s. Of particular importance are his measurements for the 9.5mm L-bracket and 20m/s case.

The two point velocity correlation measurements that make up the 4D space-time correlation function were only taken with the 9.5mm trip and 30m/s flow speed due to the extensive time required. These measurements were made at two points simultaneously. The three physical dimensions that were varied were the distance from the wall, the distance between probes in the wall normal direction, and the spanwise distance along the wall. Then a time delay was also included which made up the four dimensions of the complete space-time correlation function.

From these measurements Morton confirmed that the boundary layer turbulence was highly anisotropic and found streamwise elongated structures that were inclined at an angle relative to the wall. With these measurements as inputs to the blade response function he was able to compute the full 4D space-time correlation function and then take “slices” of it as a rotor blade would see it in order to predict the sound that the rotor would radiate. He utilized the acoustic prediction methods developed in Glegg *et al.* (2012) and applied them to a 2.25 scaled model of the Sevik rotor, partially immersed in the boundary layer. The rotor was 457-mm in diameter and the boundary layer 101mm thick, the tip gap between the rotor and wall being 20mm. The Sevik rotor was chosen because its simple geometry, a constant chord and square tips, and large number of blades made the acoustic predictions both easier to compute and more likely to contain significant haystacking noise.

Morton’s predictions of the sound the rotor would radiate assumes that the turbulence “seen” by the blade is exactly the same as that measured in the undisturbed boundary layer. Put another way, this means that the effects of the boundary layer turbulence distortion as the inflow is drawn into the rotor are not accounted for. His predictions however still showed that the rotor would have a spectra dominated by the haystacking noise at the blade passage frequencies and likely measureable above the background noise of the tunnel.

This prediction was indeed confirmed during the first rotor experiment at Virginia Tech where Alexander *et al.* (2013) mounted a 2.25 scaled and left handed version of the Sevik rotor in the same thick turbulent boundary layer. The rotor had 10 blades, with a constant 57.2mm chord, square tips, and a diameter of 457.2mm. The blade airfoil section has a maximum thickness of 9.7% of the chord at the tip and 8.4% at the root that is located approximately at midchord. The blade pitch ranges between 55.6° at the root and 21.2° at the tip, and Sevik had suggested that the design advance ratio of this rotor was $J=1.17$. Alexander operated the rotor at advance ratios ranging from zero thrust, ($J=1.44$) to highly thrusting ($J=0.48$) over four inflow velocities, 10, 15, 20, and 30m/s.

He used a single 9.5mm boundary layer trip 4.76m upstream of the rotor to create a turbulent boundary layer that was approximately 101mm thick at the streamwise location of the rotor. Alexander kept the rotor a constant 20.3mm from the wall such that it was immersed up to approximately half the blade span in the boundary layer. Note that this boundary layer was one of the configurations studied by Morton.

He took acoustic measurements at nine microphone angles from 15° to 168° off the rotor’s axis in the xy plane of rotation and measured blade wake profiles 0.64 chords downstream of the blade trailing edge with a quad hotwire. The downstream hotwire measurements were used to infer mean phase locked turbulence characteristics of the blade wake. These measurements showed that there was increased mixing of the blade wake with the boundary layer as the rotor thrust increased.

As predicted by Morton, the far field acoustic measurements showed a strong haystacking pattern and the turbulence ingestion noise easily exceeded the tunnel background noise level. Alexander found that the haystacking pattern from the turbulence ingestion noise increased as the rotor rotation rate

increased. He used the farfield acoustics to develop a novel method to estimate the lateral and streamwise timescales from the acoustic measurements. From this, he found that streamwise timescales approximately doubled over the range of advance ratios considered while lateral timescales remained approximately the same. This suggests that there is a complex distortion and shearing of the boundary layer flow by the rotor.

Alexander’s work in 2013 was followed up by Alexander *et al.* (2014) in which a system of on-blade hotwires was designed and installed on the rotor to measure upwash correlation both spanwise along the blade and on two consecutive blades. Upwash correlation is the driving term in the blade response function which describes the sound produced in the far field. This experiment allowed a measurement of the upwash correlation in the rotating blade reference frame that Morton predicted from his correlation measurements of the boundary layer in the fixed reference frame. This provided a direct way to measure the distortion in the turbulent structures from the boundary layer as they were ingested by the rotor. Unsurprisingly, Alexander found that Morton’s predictions of the blade upwash correlation from his clean boundary layer measurements was accurate at low thrust but that there was a progressive deviation as the thrust was increased. The upwash correlation between each different pair of blade mounted probes is shown for the zero thrust case in Figure 7 below from Alexander *et al.* (2012). The upwash correlation functions for the same probe pairs are then shown for three other thrusting conditions, from advance ratios of 1.05 to 0.52, in Figure 8 below. This deviation of the predictions and the measurements is partially attributed to the distortion of the inflow turbulence by the acceleration of the mean inflow into the rotor.

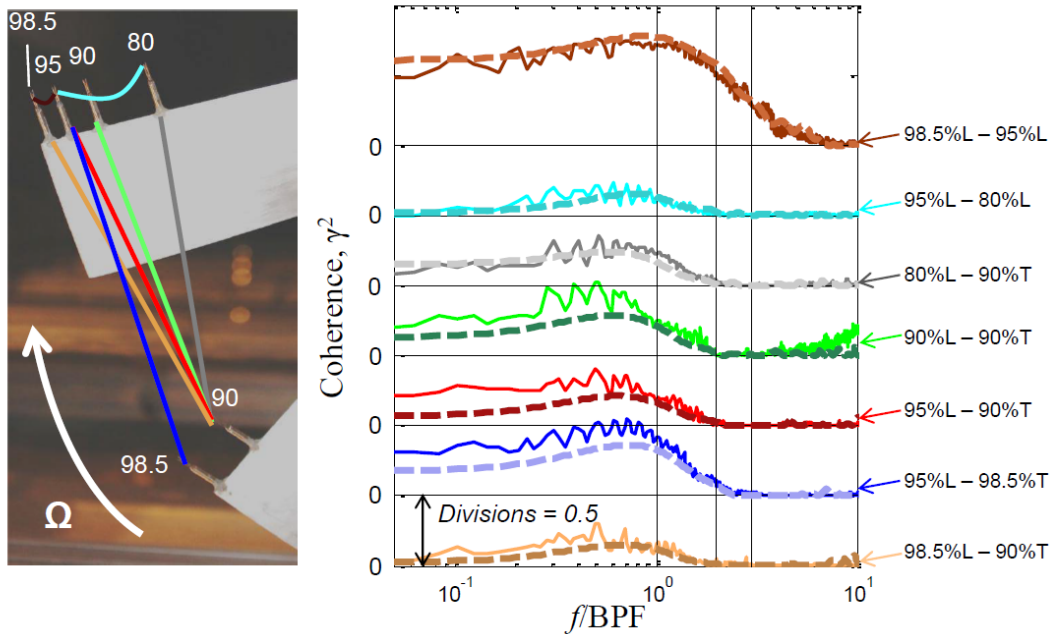


Figure 7: Blade-to-blade coherence measured in Alexander *et al.* 2012 for different probe pairs at a zero-thrust condition, $J=1.44$, 20m/s , 1823RPM . (Predictions shown as dashed lines, L=leading blade, T=trailing blade)

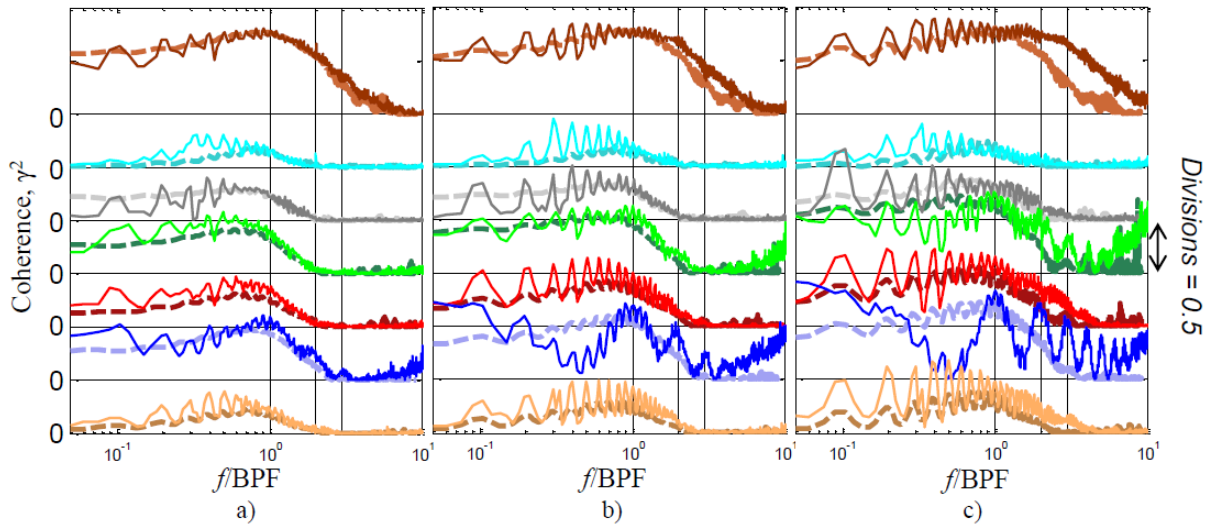


Figure 8: Blade-to-blade coherence for different probe pairs as measured by Alexander et al. (2012) at three thrusting advance ratios. Figure a) is $J=1.05$, 20m/s, 2500RPM, b) is $J=0.79$, 15m/s, 2500RPM, and c) is $J=0.52$, 10m/s, 2500RPM. (Predictions shown as dashed lines, colors correspond to Figure 7)

Figure 8 shows the unexpected haystacking like signature that Alexander observed in the blade to blade upwash correlations in probes near the tips. It should also be pointed out that they became more dominant as the rotor thrust was increased. This indicates that both blades were seeing a very similar flow feature only at frequencies corresponding to the BPF and its harmonics, possibly a separation region between the rotor and wall that increased in strength as the rotor's thrust level increased. The rotating frame measurements also showed that at high thrust, a lateral contraction of the boundary layer turbulence with increasing thrust, as would be expected, was not observed.

The magnitude of sound levels in the far field sound spectra was found to increase proportionally to the boundary layer thickness for low thrust conditions, as would be expected as the rotor ingests more turbulence. However, for high thrust conditions, the haystacking peaks were found to be approximately constant in amplitude, independent of boundary layer thickness. This suggests that the quantity of turbulence entering the rotor near a wall at high thrust has little effect on the noise that it produces, a counter-intuitive result. In order to investigate this further, a tuft flow visualization was used on the wall beneath the rotor. The tuft flow visualization, pictured in Figure 9 below, suggested that there was in fact a separation region below the rotor blades at the highest thrusting conditions.

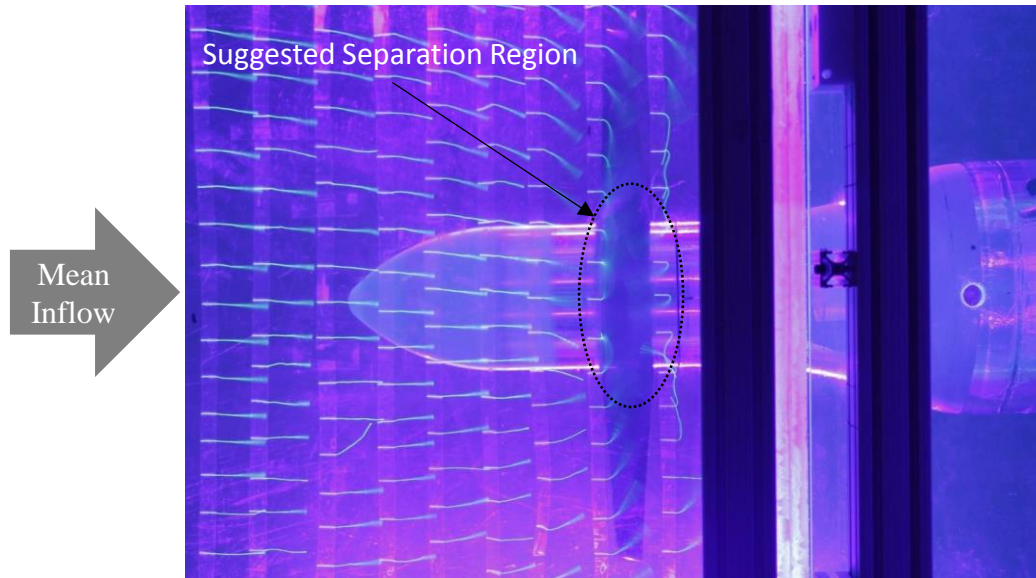


Figure 9: Tuft visualization from Alexander *et al.* (2014) showing the separation region below the rotor for the highest thrust case, $J=0.58$. The image is flipped from the original such that flow is left to right. This picture is taken looking through a transparent wall.

A detailed time domain study of the acoustic signals from the same test rig was completed and presented in Wisda *et al.* (2014). He determined the average acoustic signature of an eddy passing through the rotor using a time delay alignment for multiple microphones and a continuous wavelet for detecting the passages. This revealed that the eddy passages were similar to a cosine wave with a Gaussian window. He also found that the normalized timescales of the eddy signatures remained relatively constant with advance ratio. However, they increased as the freestream velocity was held constant and the rotation rate of the rotor increased. At advance ratios less than 0.6, the eddy signature was found to be dominated by a tonal component which was believed to be caused by the interaction of the blade with the separation region on the wall. In his Master’s thesis, Wisda (2015), also suggests that the blades are interacting with this “Pirouette Effect” flow reversal that is known to form in ships when the propeller is operated close to the hull. The details of the Pirouette Effect will be reviewed in Section 1.8 below.

1.7 Acoustic Predictions for the Rotor in a Turbulent Boundary layer

A new set of acoustic spectra predictions were developed by Glegg for the case of a rotor operating in a turbulent boundary layer near a wall. He matched the operating setup and conditions exactly to those documented in Alexander *et al.* (2013) and (2014) in order to allow a direct comparison and validation of the acoustic predictions. For these predictions, he took advantage of a new time-domain approach, which is detailed in Glegg *et al.* (2015a). Typical acoustic predictions use the inflow turbulence wavenumber spectra as an input to the blade response function and therefore must assume a turbulence model, which is oftentimes inaccurate. Glegg’s model uses the 4D turbulent boundary layer correlation function, which was directly measured by Morton, to determine the unsteady upwash correlation on the blade. This is then taken as the input to the blade response function from which the acoustic spectrum is calculated as an integration over time instead of the summation of infinite series of terms in the frequency domain as was historically done, which is much faster to compute. Glegg found that a time interval of approximately five rotor revolutions is enough to accurately predict the far field spectra. In the original paper explaining this method he also only considers the rotor at zero thrust in order to minimize the effects of the turbulence distortion into the rotor.

The predictions were expanded to thrusting cases between $J=1.44$ (zero thrust) and $J=0.66$ in Glegg *et al.* (2015b). In these predictions Glegg used drift coordinates in an upstream frame of reference to define the eddy correlation function such that any stretching of the eddy by the mean inflow distortion to the rotor is now correctly accounted for. Figure 10 below shows examples of Glegg's new time domain prediction method for a low thrust case and a high thrust case. The predictions are improved from those made by Morton because they now include the effects of eddy distortion and should be able to accurately predict the turbulence ingestion noise for the thrusting rotor. The predictions for the low thrust case do show a high degree of agreement with the measurements. However, at high thrust they deviate significantly from the measurements.

At high thrust conditions, the haystacking response was found to increase significantly more than was predicted both in sound level at the BPF and in the number of harmonics of the BPF seen in the spectra. Reynolds Averaged Navier Stokes (RANS) calculations were also made for the same experimental setup, but modeling the rotor as an actuator disk. The RANS calculations suggested that there was a flow reversal in the tip gap at the highest thrust condition that looped around and formed an arch vortex. This arch vortex was observed in the RANS results to connect between 25 and 40 mm from the wall suggesting that it is likely the blade is interacting with it. Glegg also postulates that the blade/arch vortex interaction could be the cause of the deviations seen between the measurement and predictions at the highest thrust case.

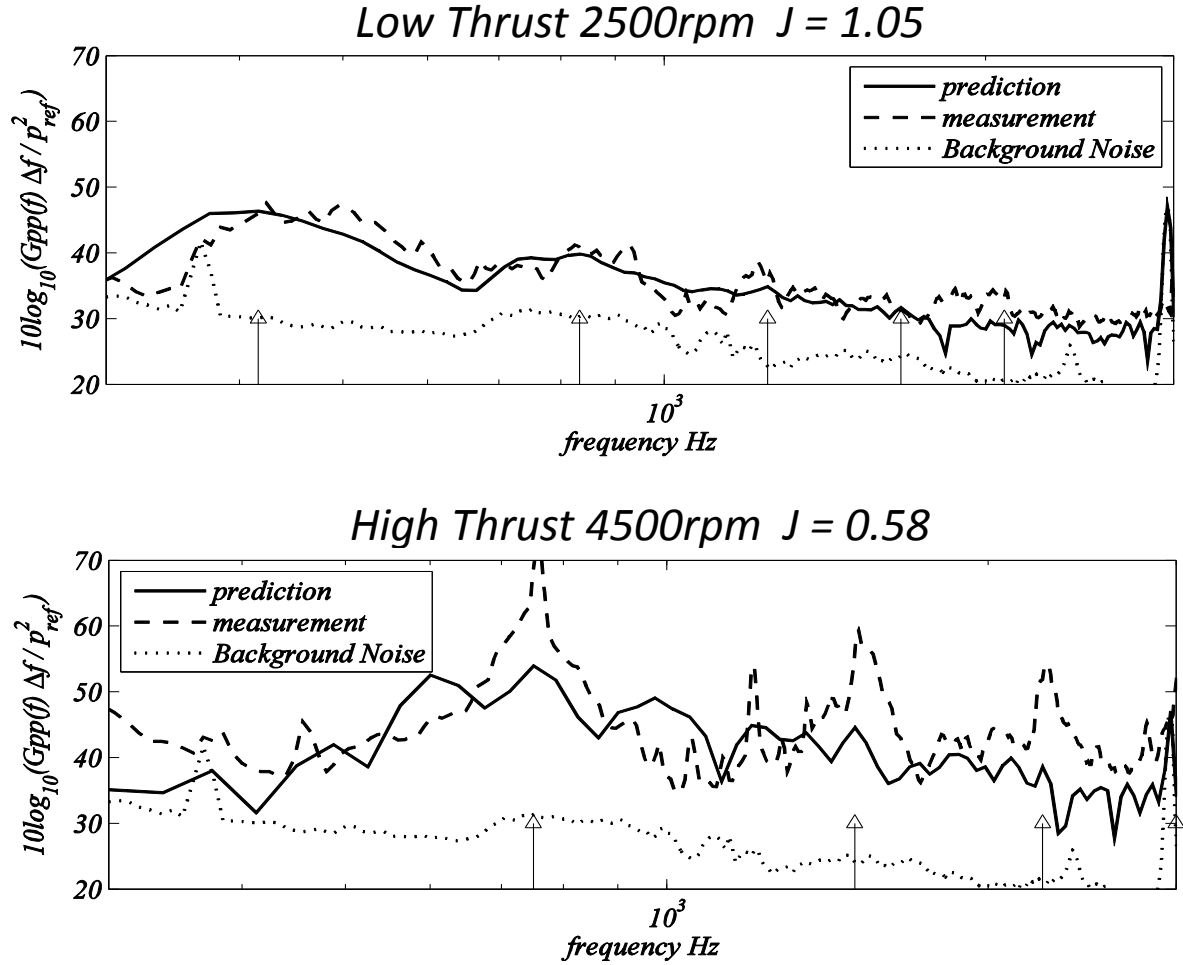


Figure 10: Comparison of spectral predictions and measurements for the rotor in a turbulent boundary layer at high and low thrust conditions. These plots were made by Dr. Glegg as part of the data set published in Glegg *et al.* (2015b) and are used with permission here.

1.8 The Pirouette Effect and the Propeller Hull Vortex

The operating conditions of this test where the deviations mentioned above were found to occur are at high thrust conditions with a small tip gap, near a flat wall. The fluid pattern that arises between a highly thrusting rotor and a near surface is often called a propeller hull vortex (PHV) and was first investigated by Huse (1971). He introduced four hypotheses for the cause of the PHV and found that the pirouette effect was the dominant effect leading to the creation of the PHV. The pirouette effect occurs when a loaded propeller operates near a surface with a small tip gap, which causes the suction side of the blade to be starved of fluid due to inflow restrictions from the nearby surface.

A systematic investigation of the PHV was carried out by Sato *et al.* (1986) with bubble streamlines on a clear, flat surface for a series of six marine propellers at a variety of thrusting conditions and tip gap to rotor diameter ratios. Sato found a series of six common flow reversal patterns that took place over the range of thrust and tip gap conditions. The tip gap ratio and thrust coefficient used by Sato are defined below in Equations (5) and (6). In the equations below, c is the tip gap, D is the diameter of the rotor, T is the thrust produced by the rotor, ρ is the fluid density, and U is the fluid inflow velocity.

$$\text{tip gap ratio} = \frac{c}{D} \quad (5)$$

$$C_T = \frac{8T}{\pi\rho D^2 U^2} \quad (6)$$

When the propeller was far away ($\frac{c}{D} \geq 0.65$) from the plate the bubbles moved uniformly through the tip gap and no flow reversal was observed. As the plate was brought closer ($\frac{c}{D} = 0.30$) flow reversal was occasionally observed but no vortex structure was seen. As the plate is moved to $\frac{c}{D} = 0.20$, a third pattern emerges, a steady vortex just above the propeller, which for a right handed propeller rotates clockwise in the view of the propeller from top down through a transparent wall, as shown below in Figure 11. Sato called this pattern “aft vortex flow.”

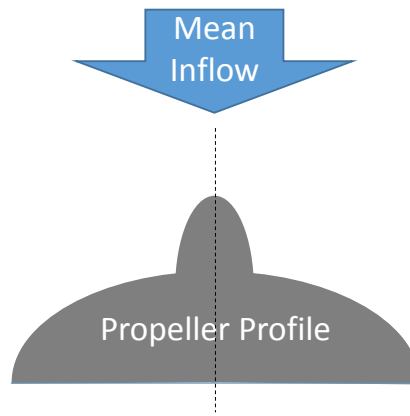


Figure 11: Orientation of the propeller in Sato et al. (1986); visualized looking down at the propeller through a clear panel with flow from top to bottom of the figure.

In the next condition ($\frac{c}{D} = 0.11$) a “double vortex flow” pattern is observed as the plate is brought still closer to the propeller. Two separate counter rotating vortex structures can be seen side by side on the wall. A counter-clockwise vortex appears on the left side of the clockwise vortex and an area of flow reversal presumably occurs between the two vortices. The next pattern occurs at $\frac{c}{D} = 0.06$ and is called “fore vortex flow” according to Sato. This pattern shows the two vortices moving closer together and the counter clockwise vortex appears to absorb the clockwise vortex.

As the plate is moved to its closest position in the study, $\frac{c}{D} = 0.013$, the “splatter flow” pattern emerges. A strong jet is formed on the right side just downstream of the propeller tip as projected on the wall when the tip is very close to the wall. Additionally a strong but small counterclockwise vortex, the “splatter vortex” is generated on the right side of the jet. Sato goes on to say that the upper limit for the splatter flow is $\frac{c}{D} = 0.05$.

The six conditions summarized above are shown as regions in Sato’s plot in Figure 12 below as functions of tip gap and thrust conditions. The tip gap condition for the test conducted by Alexander was at $\frac{c}{D} = 0.044$, situating it squarely in the splatter flow region in Figure 12. The thrust coefficient he examined ranged from the zero thrust case to at least 4.27 in the case of the 4500RPM at 20m/s inflow conditions, meaning that it is in the lower range of the thrust conditions examined by Sato. A qualitative comparison between the limiting streamline measurements made by Sato and the tuft flow visualizations

made by Alexander (Figure 9) at similar operating conditions shows that they both suggest a similar flow pattern upstream of the rotor. Both measurements appear to show that the fluid along the wall is drawn toward the center of the tip gap in a roughly symmetric manner upstream of the rotor blades. Sato's documentation of the bubble trajectories on the plate is lacking downstream of the rotor, implying that not many of the bubbles that were seeded upstream made it behind the rotor. This could be explained by a flow reversal behind and below the rotor like the tuft flow visualization from Alexander suggests.

Note that the blue line in the upper left indicates the operating conditions considered by Alexander with a constant tip gap and a range of thrust conditions from 3.31 N in the nominal zero thrust case at $J = 1.44$ to 171.8 N in the highest thrust case at $J = 0.58$. The thrust value required to calculate the propeller load factor was calculated by JavaProp at the given advance ratios based on lifting line theory with an inflow speed of 10 m/s.

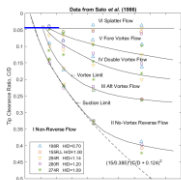


Figure 12: Tip clearance ratio vs propeller load factor and the associated flow patterns in the tip gap for five different right handed marine propellers. The blue line represents the conditions considered in this experiment. Data taken directly from the results of Sato et al. (1986).

Martio *et al.* (2011) followed up Sato's study with a URANS simulation of the same INSEAN E779a propeller that Sato used. They used a tip clearance of $\frac{c}{D} = 0.157$ and examined thrust factors from $C_T = 2.0$ to 531.7 by keeping the rotation rate of the rotor constant and varying the speed of the inflow. They found that visualizing the vortex flow in the tip gap was difficult, but by using the limiting streamlines on the flat surface they could directly compare the flow patterns with Sato's bubble flow visualization measurements. They found six flow patterns which showed reasonable agreement with those observed by Sato at similar thrust conditions and tip gap ratios.

Examining the unsteady thrust of the propeller at the highest thrust conditions they found that it oscillated at the blade passage frequency. Significantly, they found that the PHV in the highest thrust conditions was interacting with both the blades and their tip vortices. At other, lower thrust, conditions they found that the PHV could exist without interacting with the blades.

The purpose of discussing Sato's investigation of the PHV in such detail is to place the operating conditions for the thrusting regime of this experiment in the broader context of near wall thrusting propellers. It also gives an indication of the types of flow structures that we expect to see in the tip gap of this experiment. These structures could be causing the flow reversal observed with tufts in Alexander *et al.* (2014), the deviation of the acoustic predictions found in Glegg *et al.* (2015b), and the deviation of the predicted upwash correlation function from that measured in the rotating frame in Alexander *et al.* (2014).

1.9 Conclusion of Literature Review

There has been substantial progress in the investigation of rotor noise in recent years in both thrusting and braking rotors, however significant gaps in understanding still remain.

In the thrusting conditions, the leading edge noise created by a rotor ingesting isotropic turbulence is relatively well understood and able to be predicted with reasonable accuracy. The radially symmetric, and therefore time invariant, case of a rotor interacting with a fan casing boundary layer is also relatively well understood. Glegg *et al.* (2015b) showed that the noise from a near-wall rotor ingesting anisotropic and inhomogeneous turbulence could be predicted for moderate thrust conditions as long as the inflow turbulence was completely characterized. However, this predictive method deviates from the acoustic measurements at high thrust conditions.

It was suggested in Alexander *et al.* (2013) and (2014) that there is a separate generation mechanism taking place near the wall due the flow reversal pocket that was found at these high thrust conditions. The existence of this flow reversal was suggested by both on-blade hotwires and tuft flow visualization, however the character of this flow reversal has not been quantitatively measured. Measuring and characterizing this flow reversal is a key goal of the present experiment because it will provide insight into how to model and predict this additional blade-vortex or blade-flow reversal interaction noise.

The logical extension of this case, where a rotor in an inhomogeneous and anisotropic turbulent boundary layer is yawed at an angle to the freestream, is also documented and examined in this thesis. As with the previous unyawed rotor tests at Virginia Tech, this test provides a validation to the acoustic predictions methodologies developed in Glegg *et al.* (2015a) applied to the case of a rotor in yaw. These comparisons have been published in Glegg *et al.* (2015b). To the author's knowledge the effects of simultaneously varying rotor thrust and yaw, in an inhomogeneous and anisotropic turbulence inflow, on the far field turbulence ingestion noise have not been experimentally studied.

With regard to the braking cases, the literature has shown that both turbulent ingestion noise and airfoil self-noise are important to the total sound signature of a wind turbine. However, it is not definitively

known which generation mechanism is dominant overall or at what conditions and at what frequencies one generation mechanism becomes dominant over the other.

It has also been shown that scaled models can be used to accurately predict the sound generated by a full scale turbine. The present test was conducted with a rotor diameter and tip based Reynolds number that was between small and medium, approximately 10^5 , when compared to other scaled wind turbine tests in McTavish's survey. Therefore, we believe that the results obtained here might provide insight to the relative dominance of turbulence ingestion and airfoil self-noise. Additionally, the setup of this experiment will allow us to examine, to a limited extent, the question of if a braking rotor near a surface interacts with its own tip vortices in the tip gap as suggested in Glegg *et al.* (1987).

1.10 Objectives of this Thesis

The over-arching goal of this thesis is to use detailed new measurements to reveal the aeroacoustics of an idealized rotor operating next to a wall. In particular, it examines key regions of the flow and operating conditions not studied by previous authors. This work is focused on detailed velocity measurements in the tip gap between the rotor and the wall that reveal the turbulence structure of the flow there and provide insight to the interaction of the rotor with the wall. These velocity measurements are then supported by measurements of the mean wall pressure and far-field sound. Along with Wisda *et al.* (2014), this study extends the previous work of Alexander *et al.* (2013) and (2014) to high advance ratio conditions where the rotor is braking, and to cases where the rotor is yawed relative to the oncoming flow. It should be noted that this experiment also provides acoustic measurements at a systematic and extensive set of rotor thrust conditions and yaw angles to the mean inflow that can be used to validate acoustic predictive codes.

Due to the different applications of the measurements taken in the thrusting and braking flow regimes and their non-overlap in the literature, the goals of this study are split into those two flow regimes.

Specifically, the goals related to the thrusting rotor are:

1. To reveal the impact of the rotor on the wall pressure field and then infer the distortion of the near wall flow approaching the rotor as a function of rotor thrust and yaw angle.
2. To investigate and reveal the time averaged, phase averaged, and instantaneous turbulent vortex structures associated with the hypothesized flow reversal in the tip gap at high thrust conditions.
3. To explain the inability to predict the far field hysteresis response at high thrust with the same method that incorporates the boundary layer turbulence distortion and successfully predicts this response at low thrust.
4. To systematically examine the effects of yaw and thrust condition on the far field noise and fluid flow in the tip gap in an effort to better understand how yawing the rotor affects the far field sound and the flow in the tip gap at high thrust conditions. This provides insight to the range of conditions at which certain aeroacoustic noise generation mechanisms are likely to occur.

And the braking regime the goals are:

1. To determine the relative dominance of turbulence ingestion and trailing edge noise in the far field spectra at a variety of advance ratios and yaw angles.
2. To qualify the extent to which yaw changes the far field spectra.
3. To determine if the blades interact with their own wakes in the tip gap as might occur in full scale wind turbines.

To achieve these goals, an experiment was performed that used a 2.25 scaled model of the Sevik rotor mounted in a 101mm thick turbulent boundary layer 20mm away from a hard wall. The rotor mount

was build such that it could be yawed $\pm 15^\circ$ relative to the mean flow in order to explore the effects of yaw as outlined in the objectives above. This experiment was operated at the same inflow conditions and with the same boundary layer trip as a case measured by Morton and then verified by Alexander *et al.* (2013). When the rotor is unyawed in this test it is in exactly the same configuration as in Alexander's previous experiments at Virginia Tech. A particle image velocimetry system was set up to directly measure the fluid velocity in the tip gap between the rotor and the wall, and an array of static wall pressure taps was installed near the rotor on the wall to infer the near-wall inflow distortion.

The experimental setup, including all details of the testing facility and instrumentation used, is presented in the next chapter. That chapter is then concluded with an explanation of the test conditions and the experimental coordinate system. The third chapter presents the results of this experiment organized by flow regime. The results from the unyawed thrusting conditions are presented first. This is then used as a baseline for the thrusting conditions at yaw. In the final section, the braking conditions, including the effects of rotor yaw, are presented.

Chapter 2: Experimental Setup, Instrumentation, & Conditions

2.1 Virginia Tech Stability Tunnel and Semi-Anechoic configuration

The experiment was performed in the Virginia Tech Stability Wind Tunnel, shown in Figure 13 below. The Stability Tunnel has two interchangeable test sections with extremely low turbulence levels (0.01% to 0.03%). Each test section measures 1.83m square by 7.3m long. The anechoic configuration utilizes tensioned Kevlar fabric for the port and starboard walls of the test section. The Kevlar fabric is acoustically transparent but contains the flow inside the test section. There is an anechoic chamber outside each Kevlar “wall” that sits adjacent to the outer frame of the test section and is lined with acoustic foam wedges to dampen sound reflection. The chambers are anechoic down to 190 Hz. The floor and ceiling of the anechoic test section are made of 0.61m square perforated aluminum panels with Kevlar fabric stretched over them to allow sound to pass through where it is absorbed by acoustic wedges.

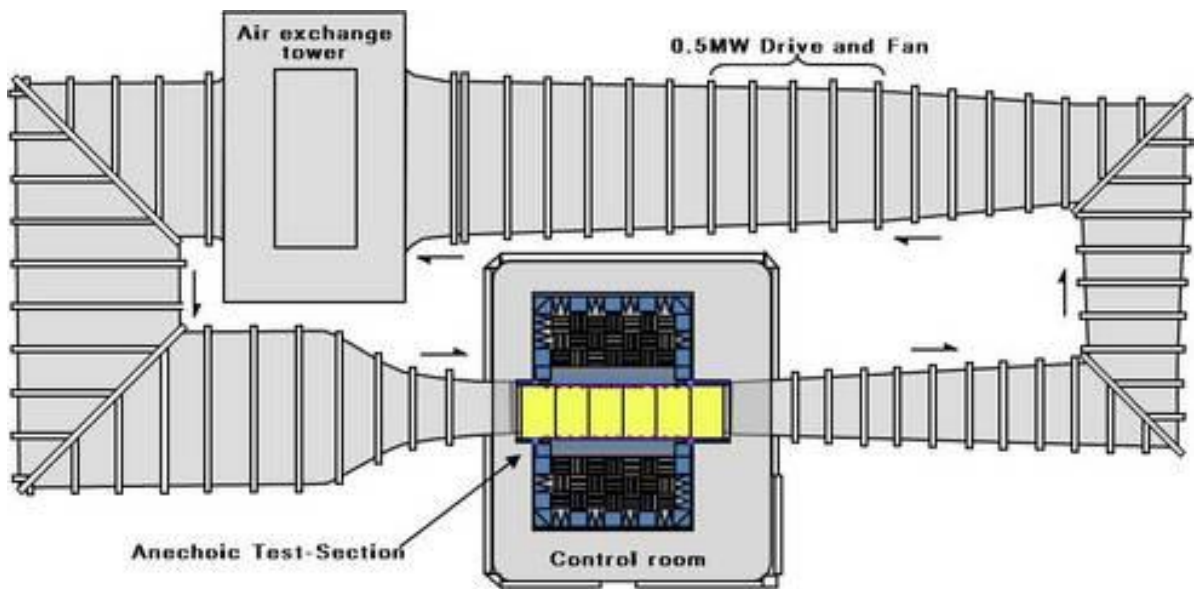


Figure 13: Top down view of the Virginia Tech Stability Wind Tunnel in the full anechoic configuration.

The test was completed in a semi-anechoic configuration, shown in Figure 14 below, for which the starboard Kevlar “wall” is replaced by a movable Lexan wall consisting of six separate panels. This configuration has been documented in several previous experiments (Meyers *et al.* 2015, Morton, 2012, Forest, 2012, and Awasthi, 2012) and can be used to produce a thick, high Reynolds number boundary layer on the Lexan wall. A detailed schematic of the configuration and coordinate system can be seen in Figure 15 below. The Lexan wall extended the entire length of the test section but reduced the width of the test section by 0.12 m. The Lexan wall can be seen on the left in Figure 16.

A modified contraction was installed upstream of the Lexan wall to smoothly transition the flow into the narrower test section. A single 9.5mm tall L-bracket boundary layer trip was placed in the contraction, 4.6m upstream of the rotor, such that the turbulent boundary layer at the rotor was approximately 100mm thick. The Lexan wall panels were adjusted in the y -direction to maintain a zero streamwise pressure gradient in the absence of the rotor. This was achieved by measuring the streamwise static pressure gradient approximately 40cm from the ceiling and floor on each of the panels and sliding them in or out individually to slightly increase or decrease the cross sectional area of the test section at that streamwise location.

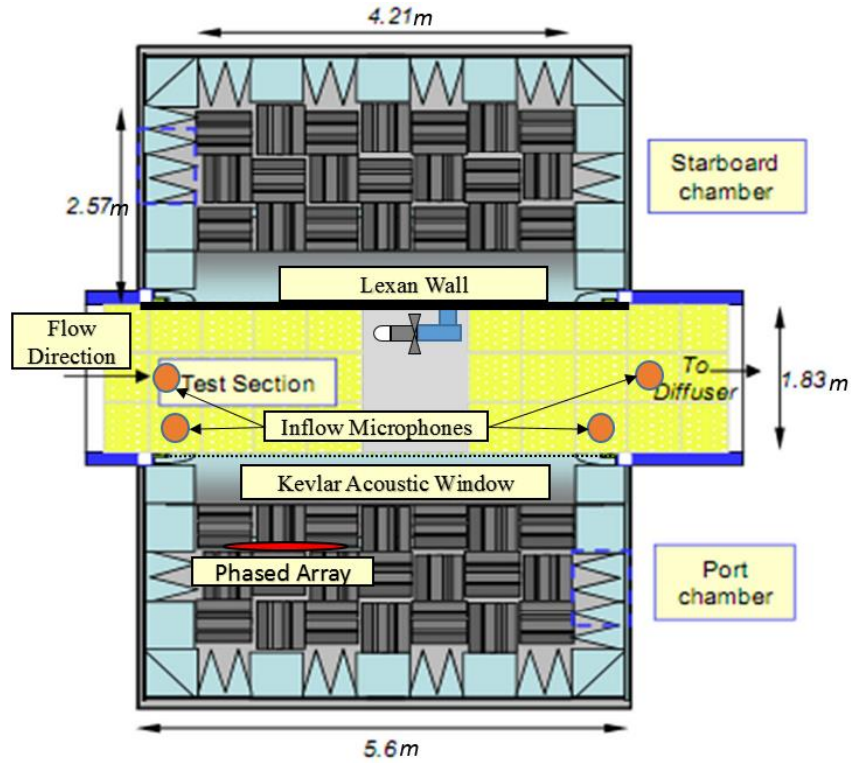


Figure 14: Test section layout for the semi-anechoic configuration.

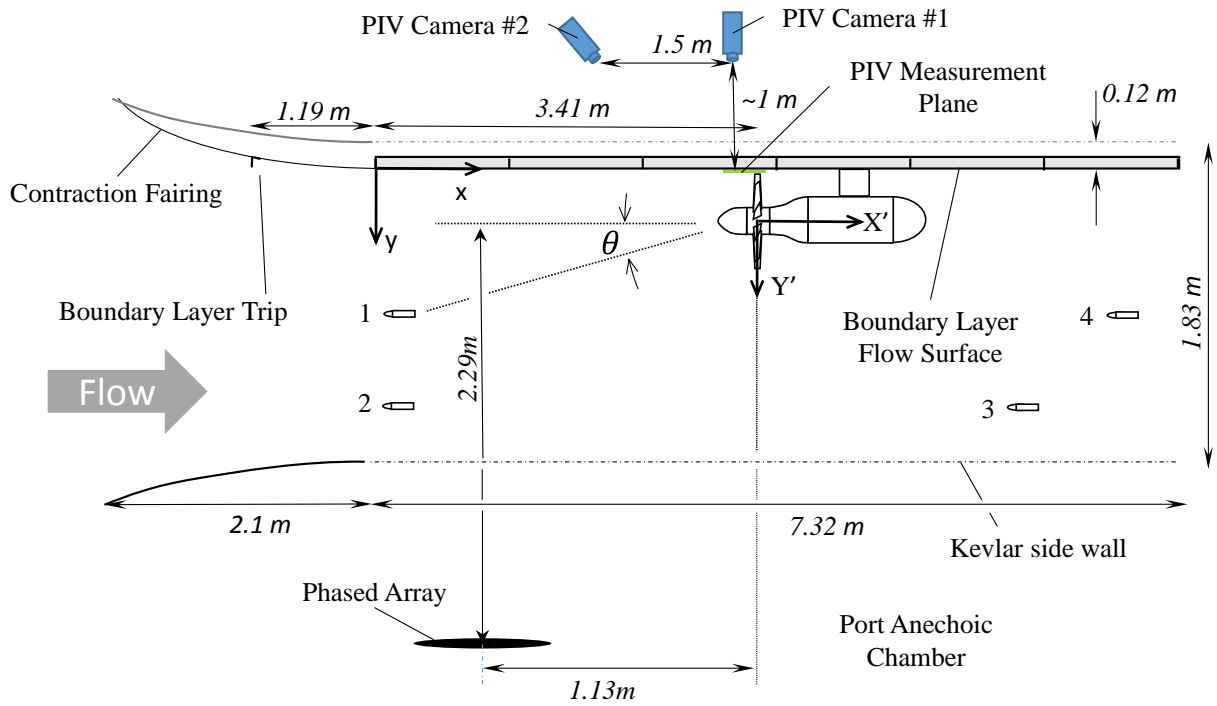


Figure 15: Detailed schematic of the test section setup and instrumentation used in this experiment.

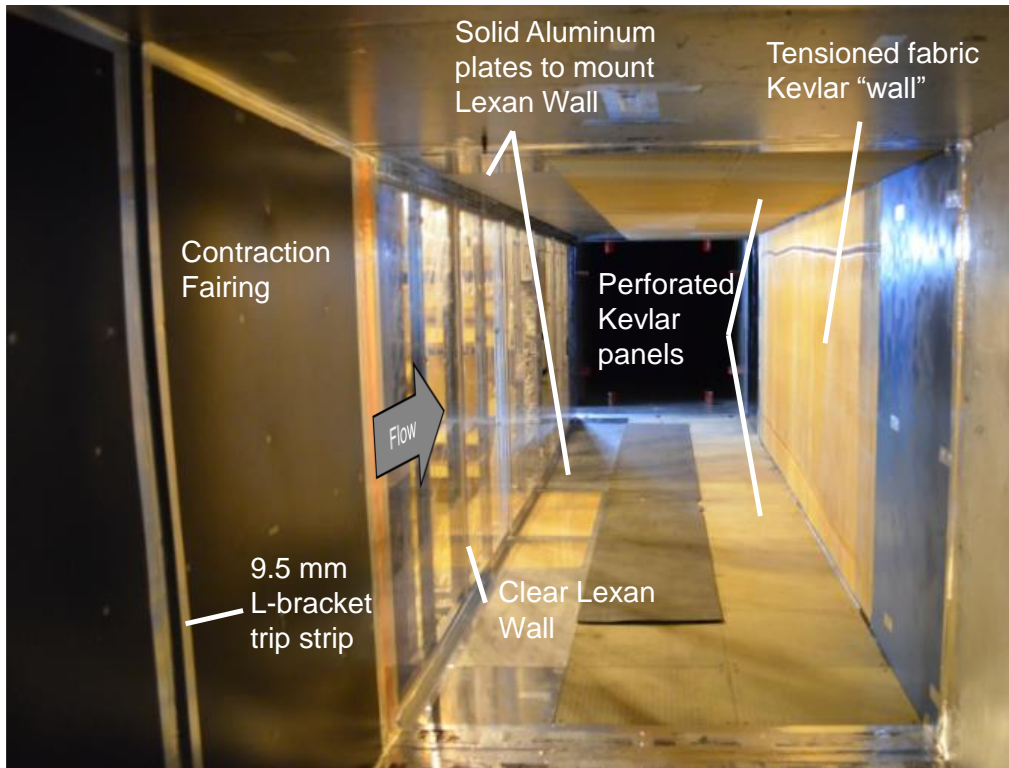


Figure 16: Picture of the empty test section after setting the zero pressure gradient on the Lexan wall.

This setup is identical to one of the configurations used in Awasthi (2012) and verified in Morton (2012). This configuration was also used in Alexander *et al.* (2013) and the turbulence characteristics of the boundary layer were verified to be the same as during Morton’s (2012) experiment. These turbulence characteristics, as measured by Morton, are listed in Table 1. Therefore, the turbulent, high Reynolds number boundary layer utilized in this experiment has been confirmed to be repeatable and is fully characterized and documented. Additionally, the boundary layer profiles measured in this experiment with Particle Image Velocimetry have been verified to match that measured by Awasthi to within experimental uncertainty. This comparison is presented first in the results, Section 3.1.

Table 1. Characteristics of the turbulent boundary layer used in this experiment, as measured by Morton (2012).

Trip (mm)	U_{ref} (m/s)	X (m)	δ (mm)	C_f	δ^* (mm)	Θ (mm)	Re_δ	Re_Θ	H
9.5	20	4.72	101	0.00275	12.0	9.4	122,360	11,457	1.27

2.2 Rotor System

The rotor design used in this experiment is a modified version of the 10-bladed rotor first used in Sevik’s (1974) work in the four-foot water tunnel at the Ordnance Research Laboratory at Penn State. This design has been used in several studies of turbulence ingestion noise (Stephens and Morris, 2009, Wojno *et al.*, 2002, Alexander *et al.* 2013, 2014, Wisda *et al.* 2014, 2015). This rotor also has a simple design and a historical record of research for comparison.

The present rotor is a left handed, 2.25 scaled version of Sevik's initial design and has square blade tips and no skew. The blades each have a constant chord of 57.2 mm and the rotor has a total tip diameter of 457.2 mm. The diameter of the hub was expanded slightly beyond the 2.25 scale to 127 mm by removing 6.35 mm of each blade root such that the outside diameter of the rotor blades was accurately scaled. The blade pitch angle ranges from 21.2° at the tip to 55.6° at the root. The blade airfoil sections have a maximum thickness of 8.4% at the tip and 9.7% at the root, located approximately at the mid-chord. A profile of the blade tip is shown in Figure 18 below. The design advance ratio for the Sevik rotor is 1.17 and the zero thrust condition advance ratio is 1.44, as computed with JavaProp. The JavaProp calculations are explained in detail in Wisda (2015) §2.2.1. A rounded nosecone with a diameter of 127 mm and a length of 216.4 mm extends in front of the hub of the blades and a Kollmorgen AKM-64P-ACCNDA00 servo-motor and S61200 servo-drive is used to power the rotor up to 4500RPM. A picture of the rotor as mounted for this experiment is shown in Figure 19 below.

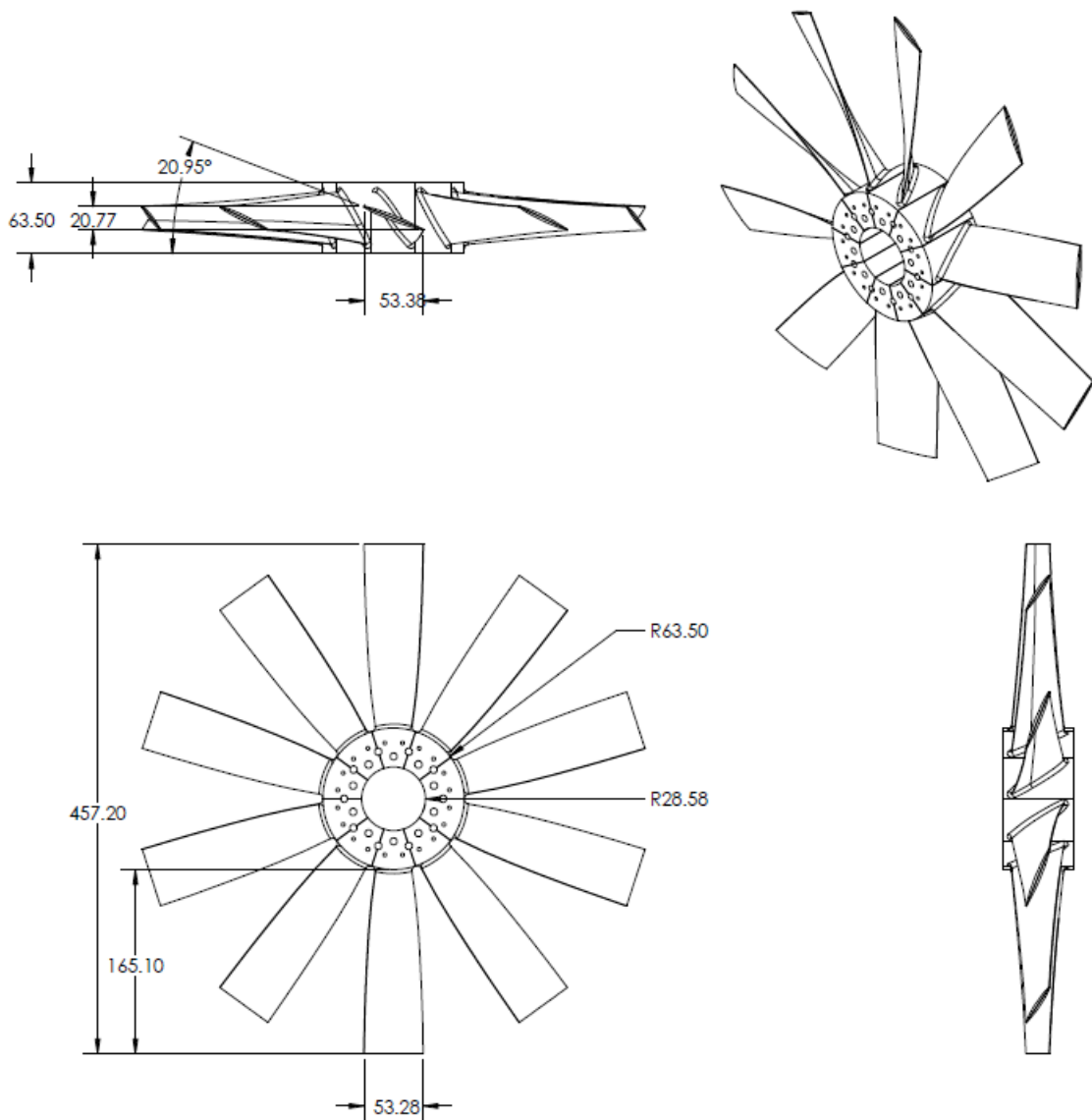


Figure 17: Three view and isometric drawings of the 2.25 scaled Sevik rotor used in this experiment.

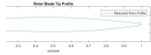


Figure 18: Rotor blade profile at the tip.

The entire rotor housing was mounted from a frame outside the test section that allowed the blade disc plane to be yawed with respect to the freestream, about the Y' axis in Figure 15. The blade disc could be yawed from $+15^\circ$ to -15° in increments of $7.5 \pm 0.05^\circ$, where positive angles are measured as the nose of the rotor was moved in the negative Z' direction. The center of rotation of the rotor and mount was 0.592m downstream of the center of the blades disc along the X' axis when the rotor was unyawed. At each rotor yaw angle, the flat edge of the blade at bottom dead center as kept a constant 20 ± 0.5 mm from the wall. Aerodynamic fairings were utilized in the front and back of the rotor servo housing, and around the support beam of the servo mount to reduce aerodynamic noise. The rotor, mounted at $+7.5^\circ$ yaw, is shown in Figure 19 below and the external supporting structure that was designed to allow the rotor to yaw is shown in Figure 20.

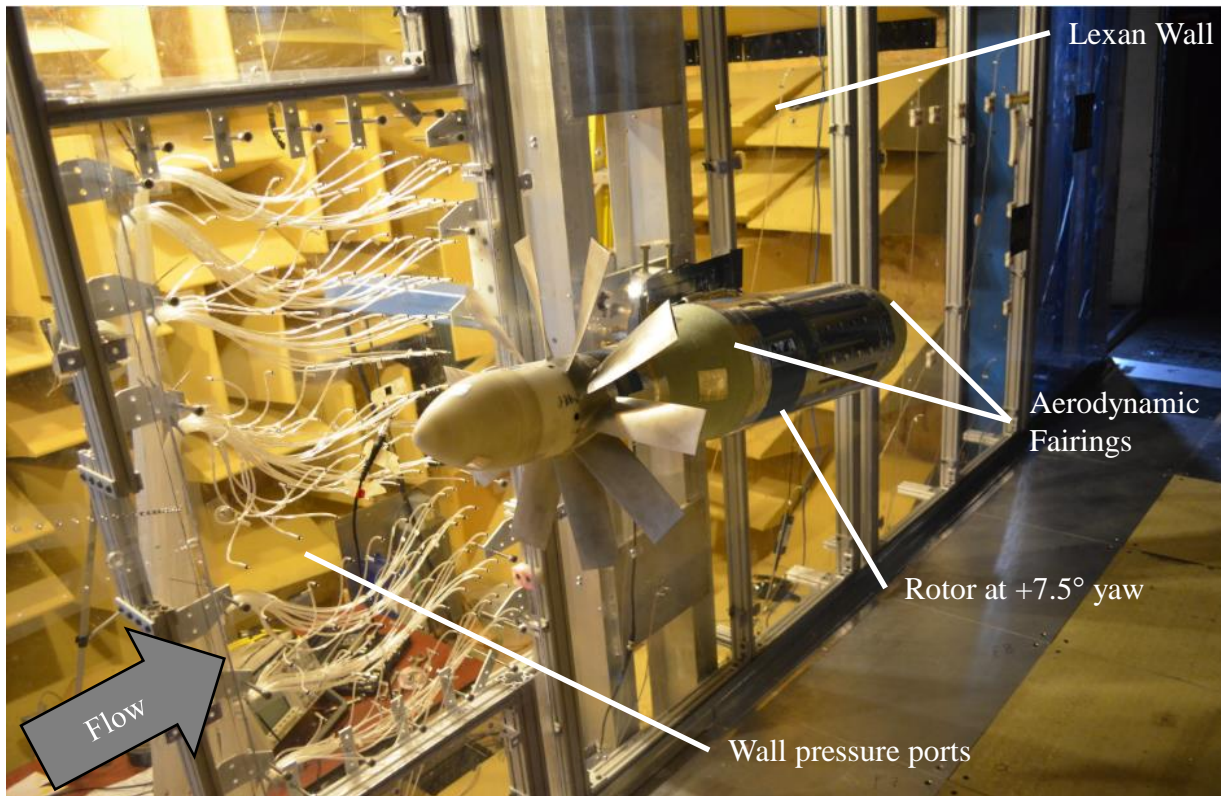


Figure 19: Rotor installed near the Lexan wall in the semi-anechoic configuration.

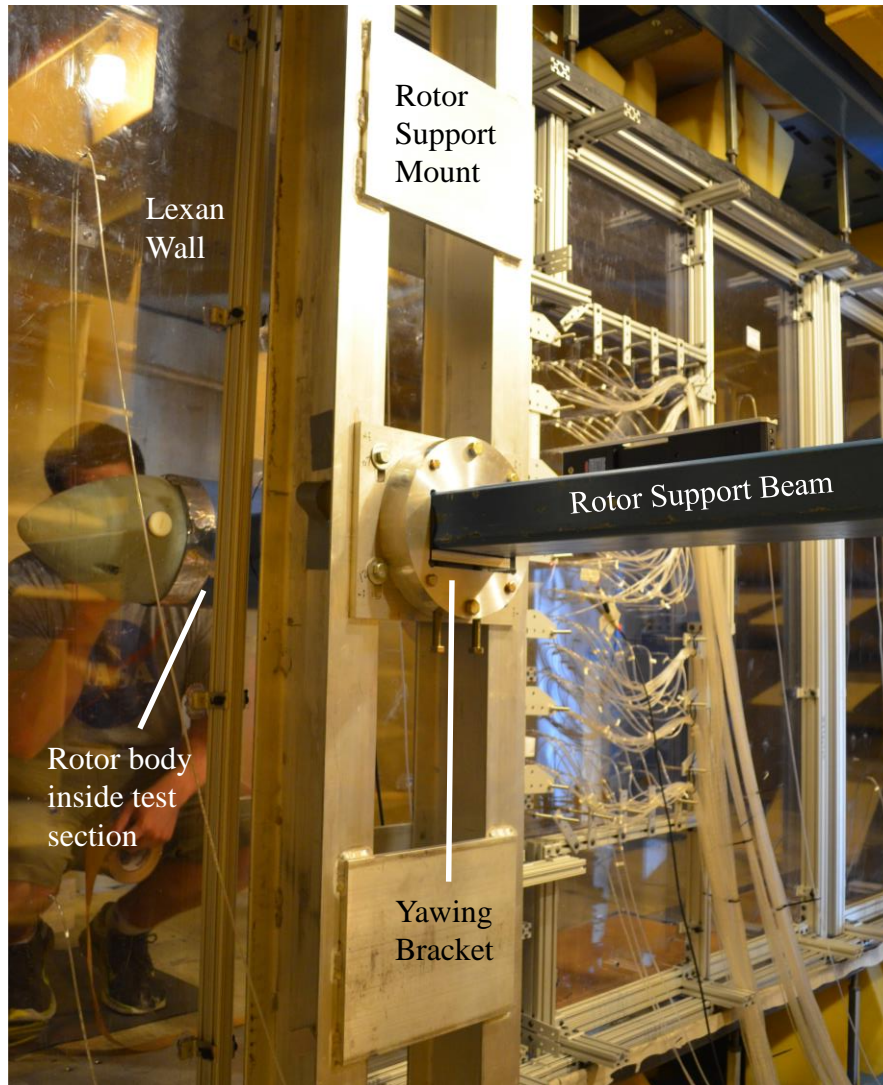


Figure 20: External support structure for mounting the rotor and yawing to +/- 15°.

2.3 Acoustic Measurements: Inflow Microphones

Four Bruel & Kjaer 4190 ½" microphones were used inside the test section to record the noise produced by the rotor from different angles. The B&K 4190 microphone by itself has a flat frequency ($\pm 1\text{dB}$) response between 10Hz and 20kHz. However with frequency response of the microphone is altered slightly by the nose cone and a typical far-field acoustic response can be seen in Figure 21 below. With the nose cone attachment, the microphone has a flat response from 200Hz to 6kHz where it increases to +2dB at approximately 11kHz before rolling off to approximately -5.5dB at 20kHz. This response of the microphone with the bullet nose cone was corrected to remove the artificial inflation and dampening at high frequencies in all the thrusting cases, discussed in §3.2 and §3.3. Note that the braking cases, §3.4, were not corrected for this microphone response because this was above the higher frequency range of the trailing edge noise primarily discussed there.

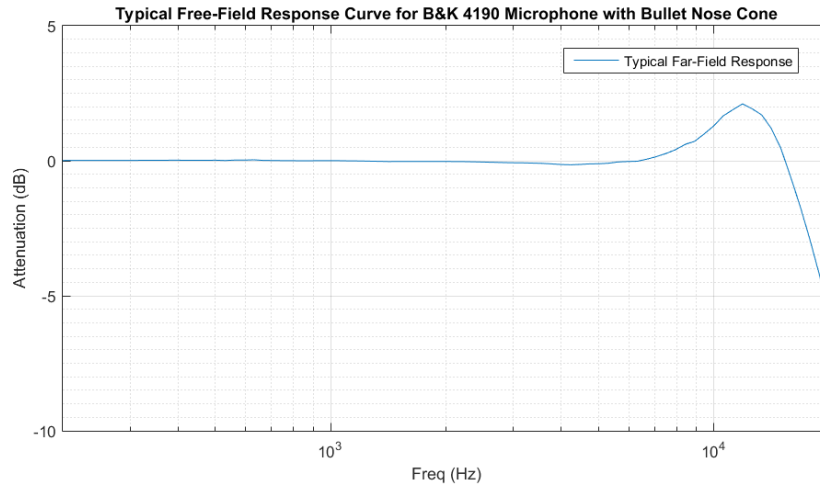


Figure 21: Example free-field response curve of the B&K 4190 microphone with the bullet nose cone.

The microphone arrangement inside the test section is shown schematically in Figure 15 above. Each inflow microphone was aligned axially with the flow and fitted with a Bruel & Kjaer 1/2" bullet nose cap and then mounted on the top of an aerodynamically faired stand designed to produce minimal noise. The stands were bolted to the floor or ceiling and were arranged such that the downstream microphones were not in the wake of any upstream microphones or stands. A picture of the test section showing the configuration of the inflow microphone mounts is below in Figure 22 and a close up of the bullet nose cone is pictured in Figure 23 below.

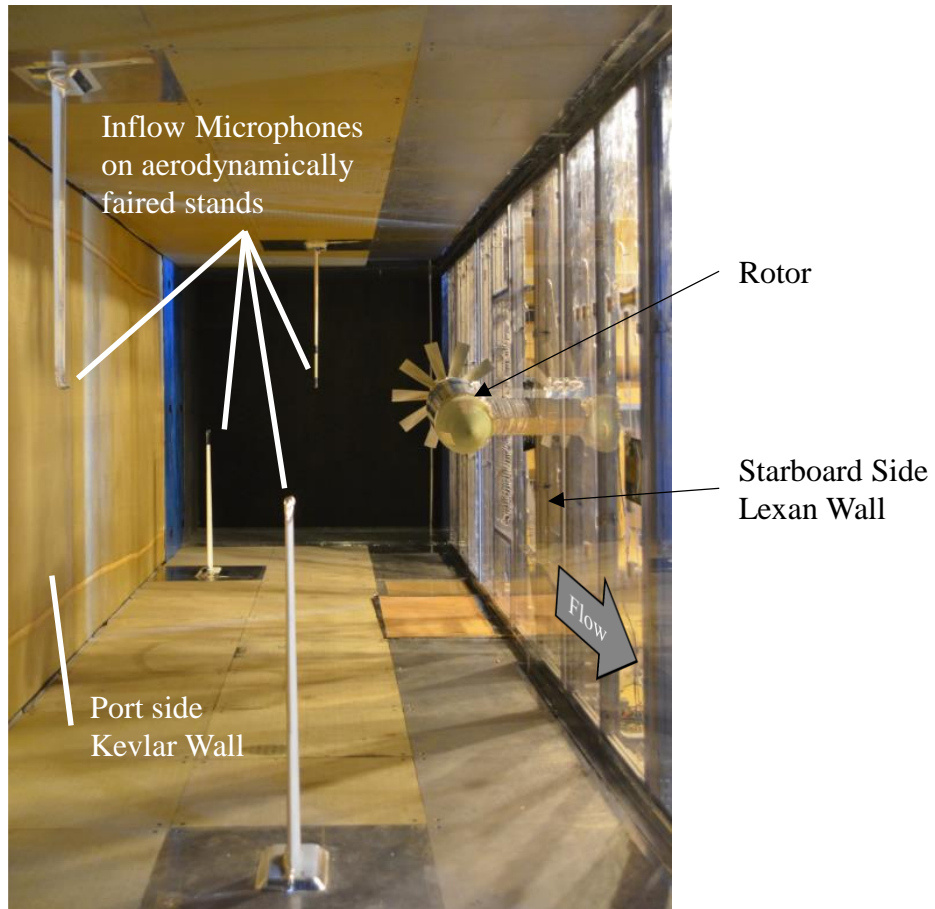


Figure 22: Inflow microphones and rotor in the semi-anechoic configuration, looking upstream.

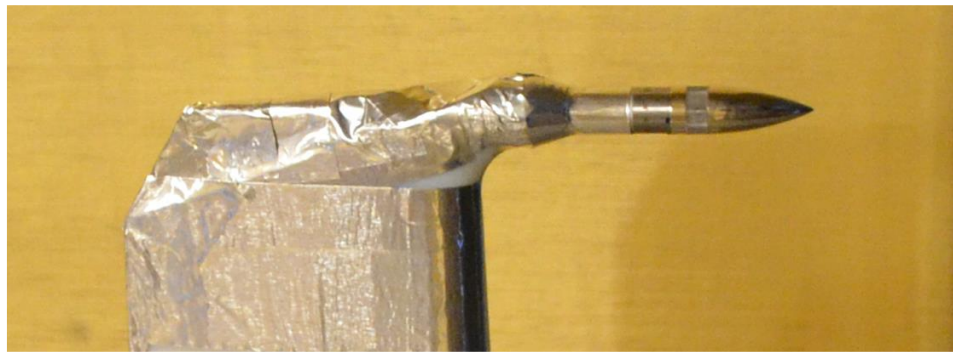


Figure 23: Close up of the B&K 4190 microphone with the bullet nose cone.

The positions of each microphone relative to the center of the rotor in its un-yawed position are given in Table 2 below. The primed coordinate system is shown in Figure 15 and its convention is as follows: positive X' is in the downstream direction, positive Y' is away from and perpendicular to the Lexan wall, and positive Z' is parallel to the Lexan wall, positive down, in accordance with the right-hand rule. The angle θ is measured from the axis of rotation of the rotor to the microphone in the $X'Y'$ plane. The origin of the primed coordinate system is located at $x = 3.41m$, measured downstream of the lower corner of the hard wall, $y = 0.249m$, measured from the wall beneath the rotor to the axis of rotation of the rotor, and $z \cong 0.915m$, such that the rotor is approximately centered in the test section.

Background noise measurements without the rotor installed were made to isolate the noise from the tunnel and microphone stands. The rotor was installed without the blades and then baseline noise measurements were recorded of the motor mechanical noise and the aerodynamic noise of the motor housing at each yaw angle. Inflow microphone data was recorded using four 24 bit B&K 3050-A LXI data acquisition systems sampling at 65,536 Hz for 32 seconds using the Pulse 14 software from B&K.

Table 2. Inflow microphone positions relative to center of rotor.

	X' (m)	Y' (m)	Z' (m)	θ (deg)
Mic 1	-2.234	0.545	-0.025	13.72
Mic 2	-2.165	1.148	0.225	27.94
Mic 3	2.007	1.149	-0.032	150.21
Mic 4	2.676	0.548	0.232	168.42

A planar 117-channel phased array was also mounted 0.58 m from the Kevlar wall in the port anechoic chamber and 1.13 m downstream of the rotor plane, although results from its measurements are not presented here.

2.4 Mean Wall Pressure Measurements

A panel with 131 pressure ports arranged in a radially expanding pattern was installed in the Lexan wall directly upstream of the rotor to measure the pressure distribution. The installed pressure port panel can be seen in Figure 19 above and a schematic of the radially expanding pattern is shown below in Figure 24. The pattern was designed to provide coverage of the wall upstream of the rotor, in the $-X'$ direction, for all the yaw conditions in this test.

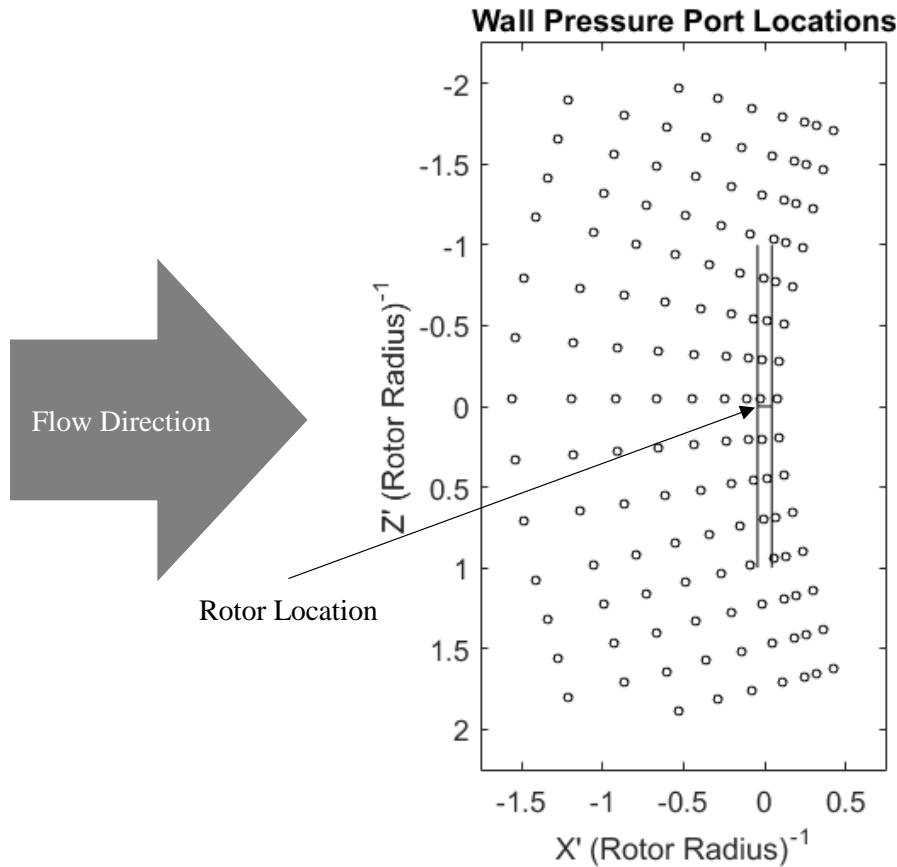


Figure 24: Schematic of wall pressure port locations relative to the projection of the unyawed rotor on the removable panel of the Lexan wall. Note that the primed coordinate system is used and the rotor is centered at the origin.

The mean wall pressure for each port was recorded by an Esterline 9816/98RK pressure scanner with a range of ± 10 in of water and an accuracy of $\pm 0.05\%$ the dynamic range, or ± 0.005 inches of water. The scanner could only simultaneously measure a total of 96 ports, so each run had to be performed twice to obtain the complete pressure distribution. For each run, the scanner took the average of 25 repeated mean pressure measurements for each port.

A mean wall pressure baseline was recorded before the rotor was installed. With the rotor blades installed, mean wall pressure data was recorded at each of the yaw angles listed above and at advance ratios J from 1.44 to 2.19. The specific flow conditions for each rotation rate are listed below in Table 3.

The zero pressure gradient boundary layer utilized in this experiment was measured with a series of pressure taps distributed in the Lexan wall panels along the length of the test section. Each panel had four pressure tap, except the panel with the mean wall pressure array which only had space for two taps. They were located approximately 40cm from both the ceiling and floor and then approximately 30cm from the left and right edges to provide even coverage over the whole panel. The zero pressure gradient boundary layer is discussed in Section 3.1.1 below.

2.5 PIV Measurement System

The Particle Image Velocimetry (PIV) system consisted of two LaVision Imager pro X 4M CCD cameras, each with a resolution of 2048x2048 pixels and equipped with a 50mm lens, a Nd:YAG laser from

New Wave Research, a LaVision Di-Ethyl-Hexyl-Sebacat (DEHS) oil seeder, and a computer running LaVision's DaVis 8.2 software to control and synchronize the laser and camera timing. The cameras averaged only about 3.5 Hz during this experiment so consequently the PIV data is not time resolved. The measurements were double pulse with a time delay of $50\mu\text{s}$ between pulses. This gave a nominal displacement in the freestream flow of 1mm which corresponds to a nominal 6.7 pixel displacement in the measurement images.

The measurement region stretched from approximately 4.6 cm behind the blade trailing edge to approximately 22 cm upstream of the blade leading edge. The measurement region was 28.6 cm wide (in the spanwise Z' direction), centered on the point of closest approach to the wall by the rotor blades. The interrogation windows were sized such that the final vector field was computed with a resolution of 2.23 mm. An outline of the measurement region is superimposed on the rotor for zero degrees yaw in Figure 25 below.

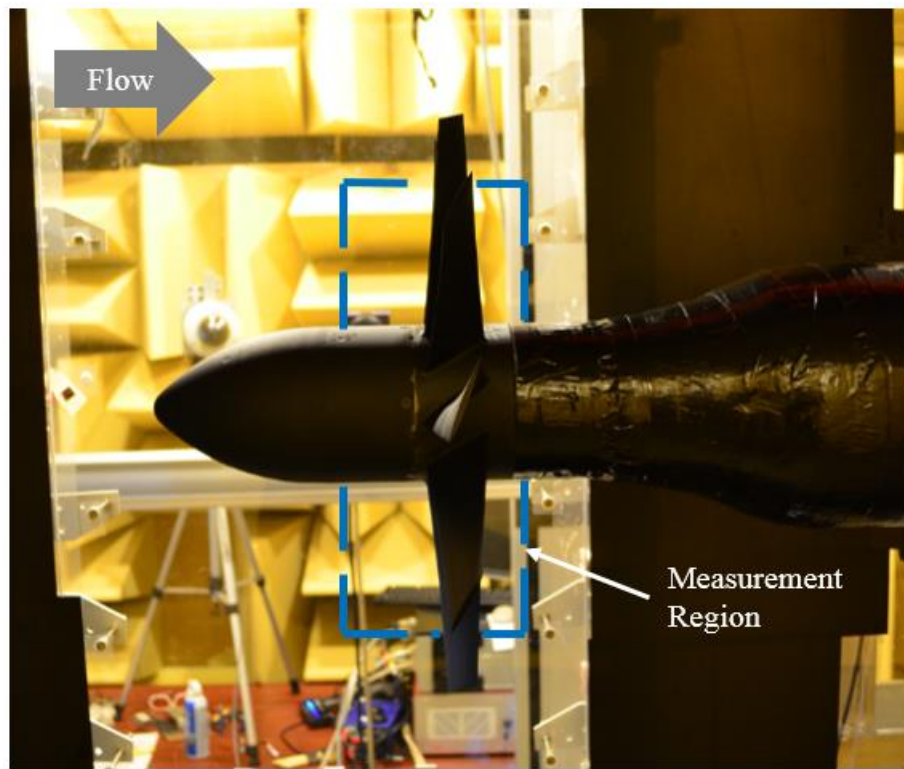


Figure 25: PIV measurement region superimposed behind the unyawed rotor.

The first camera was aligned normal to the measurement region to capture planar images and the second camera focused on the same region but was mounted approximately 1.5m upstream at a 40° angle to the measurement plane. The arrangement of these camera relative to the rest of the experimental setup can be seen in Figure 15 above. This enabled simultaneous stereo images to be recorded, and therefore, in theory, calculation of three component velocity vectors. However, on practice only two component velocity fields were able to be processed accurately. This was due to difficulties separating the effects of the moving rotor blades out of the image background from the upstream camera since it was looking downstream directly at the rotor face.

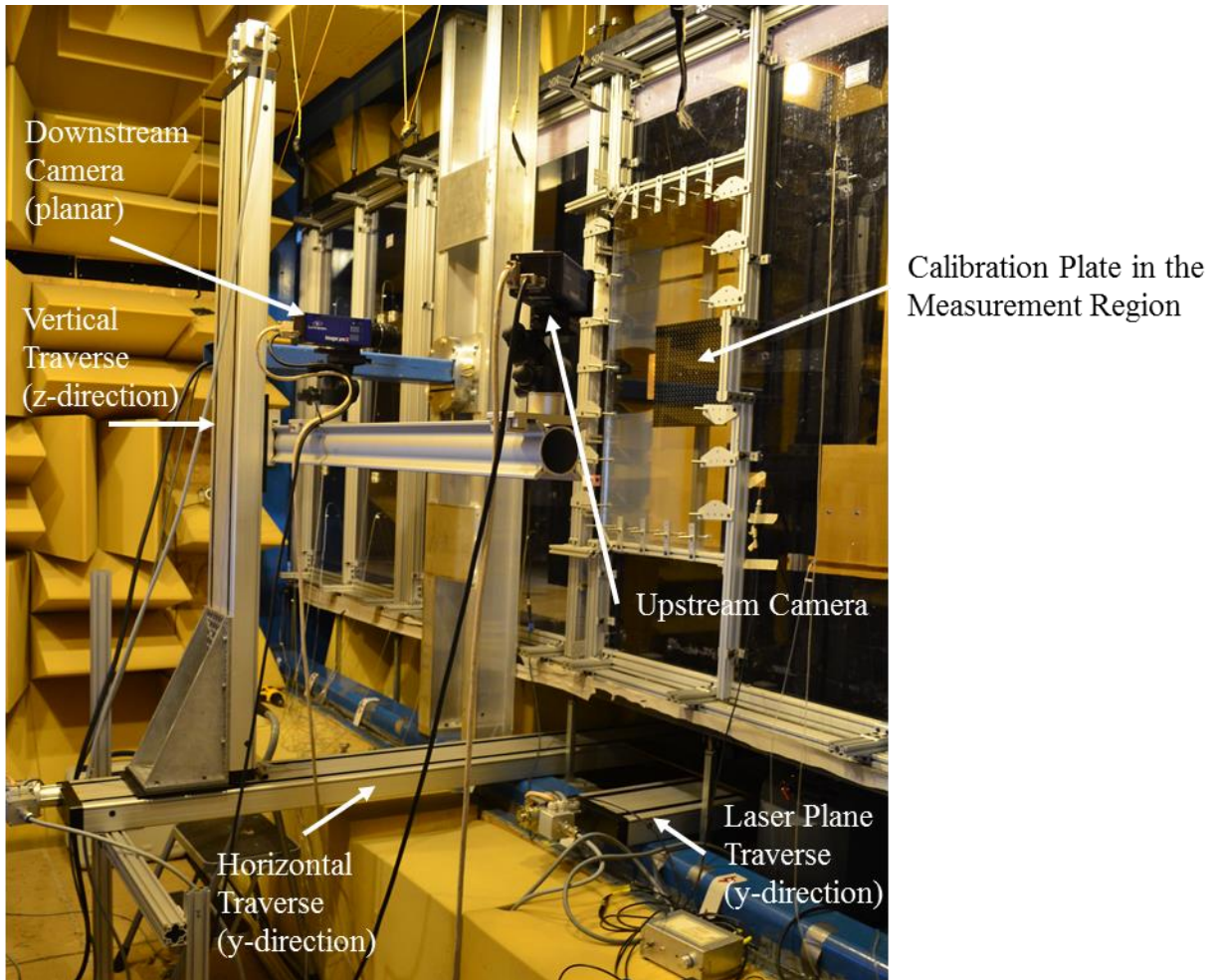


Figure 26: Camera mounts and traverses in the starboard anechoic chamber for the PIV setup.

The cameras were mounted on a two axis traverse system such that they could be moved in tandem with the laser to avoid having to recalibrate the cameras for each plane at a different distance from the wall. The measurement region was a plane parallel to the wall between approximately -137mm and 91mm in the X' coordinate and between ± 228 mm in the Z' coordinate. It was illuminated with a Nd:YAG 532nm Double Pulse Laser rated at 200mJ/Pulse from New Wave Research. The laser was mounted on a single axis traverse below a clear acrylic floor panel, which allowed the laser sheet and the cameras to move in unison. The laser beam was directed, focused, and expanded into a sheet that was parallel with the wall to illuminate the measurement region. A 90° mirror, a +1000mm spherical lens, and a -10mm cylindrical lens respectively were used to condition the beam and form it into the sheet. The thickness of the light sheet in the measurement region was not recorded but is estimated to be approximately 1-2 mm thick. A schematic of the PIV setup, looking downstream into the front of the rotor, is presented in Figure 27 below for clarity.

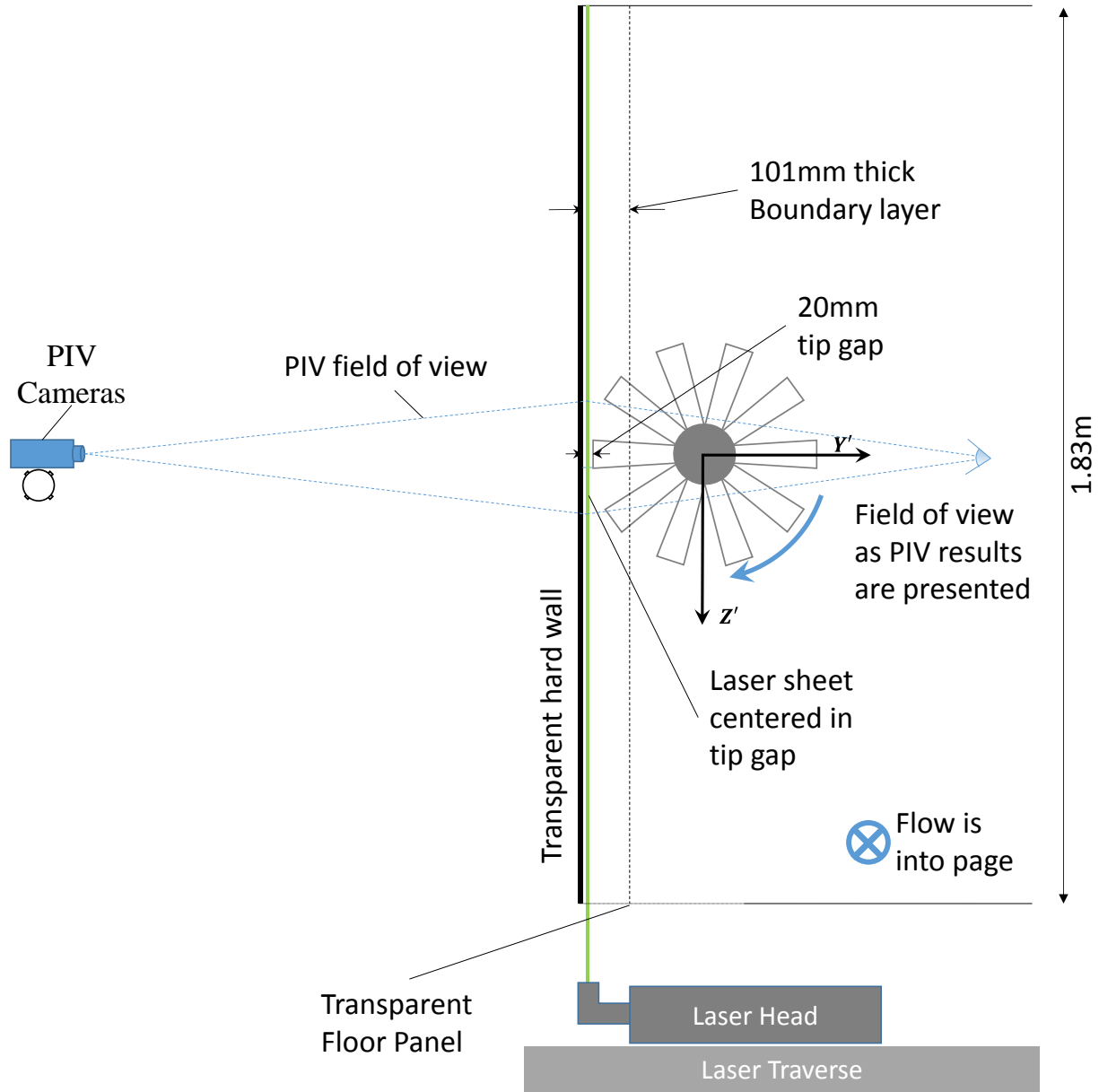


Figure 27: Schematic looking downstream into the rotor face that shows the relative locations of the cameras, the rotor, the laser sheet, the laser, and the field of view as the PIV results are presented in this thesis. Note that the schematic is drawn to scale to show the relative size of the rotor and placement of the PIV equipment.

The laser and cameras were coordinated and controlled with LaVision's DaVis 8.2 software suite. The software suite was used to record, pre-process the raw images, cross-correlate to compute the vector field, and post-process the vector fields. The post processing operations in LaVision are explained in the subsection below. Phase averaging and other additional post processing operations were then performed in Matlab. The Stability Tunnel was seeded directly downstream of the test section with atomized DEHS oil. The oil was atomized in a LaVision atomizer and had a nominal average particle diameter of 1 micron.

A series of 5000 or 1000 image-pairs for each camera, according to the test matrix in Table 4 below, were taken at each case. Additional sets of images were taken of the undisturbed boundary layer, i.e. without the rotor installed, at 5, 10, 23.4, 31.4, 42.9, 65.7, 80, 101, and 125 mm from the Lexan wall to

serve as a baseline and to compare for similarity with the undisturbed boundary layer measurements made by Morton (2012).

2.5.1 Measurement Post-Processing Details in DaVis 8.2 from LaVison

There were a number of difficult factors and complications in these PIV measurements that required extensive post processing extract the true measurements. The laser unevenly illuminated the measurement region, the moving rotor in the background created additional problems in the cross-correlation and reflections into the camera, and the clear acrylic wall the camera was looking through also created additional reflections. In order to mitigate these complications as best as was possible, the image was first preprocessed, then the cross-correlation was performed to identify the vector displacements, and finally post processing steps were taken to remove spurious vectors.

In the preprocessing stage, a subtraction of the sliding background and a particle intensity normalization, both with a scale of 4 pixels were performed. This was designed to reduce the influence of the background and of bright spots that remained stationary over many images and were not a real part of the measurement.

The vector calculation was performed with a multi-pass cross-correlation of decreasing size in the interrogation window. The first two passes used a square window at 64x64 pixels with a 50% overlap and then the next three passes used a circular window at 32x32 pixels with 50% overlap. A multi-pass post processing routine was then employed that consisted of two applications of a median filter and then two applications of a 3x3 smoothing that used the average vector from a 3x3 neighbor region. This smoothing could not be turned off due the use of multi-pass cross-correlation in DaVis. The median filter removed and iteratively replaced vectors that were outside of 2 standard deviations of their neighbors. If the vector was removed and then a vector corresponding to a lower correlation peak at that location was found to be within 3 standard deviations of the neighbors the vector from the lower correlation peak was then included instead.

A second vector post processing step was employed to remove and replace vectors that were unlikely to be realistic representations of the flow. First all vectors with a peak ratio of less than 1.3 were removed. Then four passes of a “strongly remove and iteratively replace” median filter were run on the vector field. Similarly to the median filter described above, vectors that were outside of 2 standard deviations from their neighbors were removed and if a vector corresponding to a lower correlation peak was found to be within 2.5 standard deviations of the neighbors it was included instead. Also note that any missing vectors that were previously found to be unlikely to be realistic were left as blank spaces in order to avoid including interpolations in the measurements.

Lastly a universal outlier detection scheme, called a “space-time median filter,” was applied to the vector field. This filter had a size of 9x9 vectors in the spatial dimension and 1 in the time dimension. The removal threshold was set at 3 standard deviations, the insertion threshold was set at 2 standard deviations and the minimum number of neighbor vectors needed to make the removal or insertion was set at 8. The epsilon term in DaVis for this filter was set to be 0.2.

2.5.2 Estimate of the Particle Response Time Based on Stokes Drag

The DEHS oil droplets form spheres when they are atomized and as such the response time of the particle based on the Stokes drag can be estimated. The Stokes law for spherical particles is given in Equation (7) below where ρ_p and d_p is the density and diameter of the particles of DEHS oil in the flow and μ is the dynamic viscosity of the air.

$$\tau_p = \frac{\rho_p d_p^2}{18\mu} = 2.7\mu s \quad (7)$$

Using a density for the DEHS oil of approximately 900kg/m^3 , a nominal particle diameter of $1\mu\text{m}$, and a typical dynamic viscosity of air of $1.846 \times 10^{-5} \text{ kg/(m s)}$ gives a particle timescale of $2.7\mu\text{s}$ based on the Stokes drag. An estimate of the typical timescale of the flow can be calculated from Equation (8) below based on the flow features desired to be resolved and then the Stokes number can be found from Equation (9).

$$\tau_f = \frac{\text{Typical Vortex Radius}}{U_\infty} = \frac{5\text{mm}}{20\text{m/s}} = 250\mu\text{s} \quad (8)$$

$$\text{Stokes Number} = \frac{\tau_p}{\tau_f} \cong 0.011 \quad (9)$$

Throughout the analysis of the data from this experiment, the flow features found most important to resolve were vortices that were found to form in the tip gap between the rotor and wall for the highest thrust case. These vortices had a typical radius of about 5 mm so this was used as the typical flow length scale and the freestream velocity was used as the typical flow speed to determine the typical flow timescale. This typical flow timescale was $250\mu\text{s}$ which gave a Stokes Number of approximately 0.011. Samimy and Lele (1991) found that a Stokes number of less than 0.1 is required to fully neglect particle slip in a compressible flow. The estimate of the Stokes number for this experiment is on the order of 10 times less than that requirement and therefore the DEHS oil particles are fully expected to faithfully follow the flow in these PIV measurements.

2.6 Definition of Experimental Coordinate System

The coordinate system used in this experiment was defined with the origin at the upstream lower corner of the starboard side wall with the contraction locked in place. This location was slightly inboard of the corner of the test section on account of the contraction thickness. The positive x and y directions were defined as downstream and toward the port wall respectively. Then by the right hand rule, the positive z direction was down through the floor. This coordinate system is labeled on Figure 15 above and was useful for measuring instrument locations during the test.

Since the rotor was the most important piece of equipment in this test, a new more convenient coordinate system with its origin at the center of the rotor blade disc in the unyawed position was defined and is designated the primed coordinate system. The primed coordinate system is in the same orientation as the test section based coordinate system previously described and it is important to note that it does not move as the rotor is yawed. The origin of the primed coordinate system is located at $x = 3.41\text{m}$, measured downstream of the lower corner of the hard wall, $y = 0.249\text{m}$, measured from the wall beneath the rotor to the axis of rotation of the rotor, and $z \cong 0.915\text{m}$, such that the rotor is approximately centered in the test section.

Rotor noise has a strong directivity function so the directivity angle from the rotor, θ , was defined as the angle of the receiver location off the axis of rotation of the rotor, the $-X'$ axis, in all three dimensions. The primed coordinate system and the directivity angle from the rotor are both illustrated in Figure 15 above.

2.7 Test Matrix and Experimental Conditions

The entire test was performed at a freestream flow speed of $U_\infty = 20$ m/s and the rotational speed of the rotor was varied to change its operating condition. The operating conditions for all cases considered in this test is listed in terms of rotor RPM, advance ratio, tip Reynolds number, tip tangential velocity, and tip total velocity relative to the freestream, in Table 3 below. The conditions of a particular result will generally be referred to by the advance ratio of the rotor, J . As previously mentioned, $J = 1.44$ is the zero thrust conditions so all conditions where $J > 1.44$ are in the braking regime and all conditions at which $J < 1.44$ are in the thrusting regime.

In the braking regime, the scale used by McTavish *et al.* (2013) and shown in Figure 5, places the current test at the lower end of the medium sized experiments in terms of tip Reynolds number and rotor diameter. As shown in Figure 12 above, the thrusting condition in this test extends from the no flow reversal region into the splatter flow region defined in Sato (1986).

Measurements were taken with the inflow microphones, and mean wall pressure taps for each of the conditions listed below in Table 3. This test matrix was repeated at each of the 5 yaw angles considered, -15° , -7.5° , 0° , $+7.5^\circ$, and $+15^\circ$.

Table 3: Detailed conditions for each measurement case.

Axial Flow, U_{inf} (m/s)	RPM	J	Re_{tip}	Tangential U_{tip}	U_{tip} rel. to Freestream (m/s)
20	1200	2.19	104,800	28.73	35.00
20	1300	2.02	113,500	31.12	36.99
20	1312	2.00	114,600	31.41	37.24
20	1400	1.88	122,300	33.51	39.03
20	1500	1.75	131,000	35.91	41.10
20	1590	1.65	138,900	38.06	43.00
20	1600	1.64	139,700	38.30	43.21
20	1700	1.54	148,500	40.70	45.35
20	1800	1.46	157,200	43.09	47.51
20	1823	1.44	159,200	43.64	48.01
20	2000	1.31	174,700	47.88	51.89
20	2250	1.17	196,500	53.86	57.46
20	2386	1.10	208,400	57.12	60.52
20	2500	1.05	218,300	59.85	63.10
20	2750	0.95	240,200	65.83	68.80
20	3000	0.88	262,000	71.82	74.55
20	3280	0.80	286,400	78.52	81.03
20	3500	0.75	305,600	83.79	86.14
20	3750	0.70	327,500	89.77	91.97
20	4000	0.66	349,300	95.76	97.82
20	4250	0.62	371,100	101.74	103.69
20	4500	0.58	393,000	107.73	109.57

Due to the much longer time required to take a sufficient number of PIV measurements at each case and the ability to record velocity data at many different distances from the wall, the PIV test matrix was significantly abbreviated from the pressure and acoustic test matrix. Table 4 below describes the advance ratios, yaw angles, and distance from the wall at which PIV measurements were recorded. The bold distances indicate that 5000 image pairs were recorded for that case, otherwise 1000 image pairs were recorded.

Table 4: PIV test matrix, distance from the wall to the measurement plane in mm.

Advance Ratio (J)	Unyawed	-15°, -7.5°, 7.5° Yaw
1.75	10 & 31.43 mm	10 & 31.43 mm
1.44	10 & 31.43 mm	10 & 31.43 mm
1.05	10, 23.4, 31.4, 42.9 , 65.7 & 80 mm	10, 23.4, 31.4 & 42.9 mm
0.58	10 & 31.43 mm	10 & 31.43 mm

PIV measurements could not be completed at +15° yaw due to an equipment malfunction during the test and the -15° yaw case was found to be corrupted and unusable during post processing. Additionally, all planes farther than 20mm from the wall intersected with the blades causing strong laser flare and a multitude of problems with post processing. As a result, for each advance ratio, only the unyawed and ±7.5° yaw cases are presented at 10mm from the wall in this thesis.

Additionally, measurements were taken of the clean wall boundary layer without the rotor installed at nominal distances of 125, 101, 80, 65.7, 42.85, 31.43, 23.43, 10, and 5mm from the wall. These measurements were used to verify the boundary layer mean velocity profile and turbulence characteristics, as explained in Section 3.1.2 below.

2.8 Uncertainty in the Measurement Systems

The uncertainty was examined for each type of measurement utilized in this test and the method by which they were derived is detailed in this section.

Freestream Tunnel Velocity:

The measurement of the freestream velocity of the test section was achieved by measuring the pressure differential in the settling chamber and contraction, applying a calibration to account for the difference in cross sectional area between the measurement in the contraction and the test. The velocity was then calculated with Equation (10) below where ΔP is the pressure differential with the calibration applied and ρ is found with the equation of state, $\rho = \frac{P}{RT}$, using the pressure (P), temperature (T) for the current operating conditions. R is then the specific gas constant for air, 287.058 J/(Kg K). The operating temperature and pressure are measured respectively in the contraction directly upstream of the test section and in the control room.

$$V = \left(\frac{2 * \Delta P}{\rho} \right)^{\frac{1}{2}} \quad (10)$$

The pressure scanner that was used had an uncertainty of ±0.05% of 20 inches of water, the atmospheric pressure was known to within ±0.01 inch of Hg, and the temperature was known to within ±0.2° F. Combining these uncertainties, in the appropriate SI units, with a jitter analysis showed that the uncertainty in the tunnel speed due to measurement error was 0.112m/s. It was also recognized that the

tunnel had to be tuned manually to 20m/s so the uncertainty in this process was estimated to be ± 0.10 m/s. Combining these two sources of uncertainty with the root-sum-square method yields an total uncertainty in the freestream velocity in the tunnel, U_∞ , of ± 0.15 m/s.

Mean Wall Pressure Measurements:

The uncertainty in the wall pressure measurements was also addressed with a similar approach. Equation (12) in the next section was used to calculate the pressure coefficient from the static pressure ports on the wall near the rotor. For this measurement, the static pressure from the ports on the wall were measured with a pressure scanner with a resolution of $\pm 0.15\%$ of 10 inches of water. The atmospheric pressure and temperature were measured with the same instrumentation used to calculate the tunnel velocity and explained in the paragraph above. The uncertainty from the wall pressure measurements and atmospheric pressure and temperature was estimated with a jitter analysis to be 0.0234 for each measurement. The measurements were repeated 25 times for each run so using the standard error of the mean to estimate the uncertainty of the mean wall pressure yields an estimated total uncertainty of ± 0.0047 in C_p for the wall pressure measurements by the rotor.

Acoustic Measurements:

The uncertainty in all the acoustic spectra in this test was calculated based on the processing method used to transform the measurement from the time domain to the frequency domain. A discrete Fourier transform was used in Matlab as part of the `fft()` function to accomplish this. The acoustic signal was sampled by the data acquisition hardware at 65536 Hz for 32 seconds at each operating condition. To improve the accuracy of the spectra, this original time series was divided up into 511 individual records each with a length of 8192 data points with a 50% overlap. These records were then individually transformed to the frequency domain, resulting in a resolution of 8Hz based on their length, and then averaged together to improve the accuracy of the overall spectra. Using the standard error of the mean for the average of the 511 records in decibels in the frequency domain gives an uncertainty of $\frac{20}{\ln(10)\sqrt{N}}$ dB where N is the number of records. Therefore, for this sampling and computation scheme, the error in the averaged acoustic spectra is 0.38 dB.

In order to clearly show areas in the frequency domain effected by background noise, a discretion level of 1dB was used for this subtraction. What this means is that if the spectra from the measurement was less than or within 1dB of the background for that case it was considered to be indistinguishable and the data point at that frequency was removed from the measurement entirely.

Particle Image Velocimetry System:

1) Estimation of Random Error of the Measurement

The uncertainty of each individual vector field was calculated with the Correlation Statistics method as described in Wieneke (2014). A representative vector field was selected that was below average quality in order to provide an upper bound for the uncertainty of processing the raw image pairs into vector fields. The correlation statistics method cannot take into account the bias from peaklocking. However, peaklocking was tested for and we determined that it was not an issue in any of these measurements.

The correlation statistics method is included in DaVis 8.2.2 and can provides an estimate of the error from the PIV cross-correlation process in the form of a bias and standard deviation at each correlation window. The bias and twice the standard deviation, for a 95% confidence interval, were combined with a root-sum-square and then averaged over the region of interest, not including areas where the vectors where

removed or replaced with lower correlation peak vectors that fit the local flow. This gave an estimated worst case 95% confidence bounds of ± 2.10 m/s for each instantaneous PIV measurement in this region under the blades.

If it is assumed that the error of each vector as computed is Gaussian distributed about the true mean, the average two standard deviation interval over the area of interest was ± 3.1 m/s. This was calculated by first computing the standard deviation of a large number of measurements, through time, in the region of interest. These were then averaged and converted to a 95% confidence interval to determine a representative uncertainty about the mean from an individual instantaneous measurement.

The two methods gave slightly different estimates of the uncertainty of the mean from an individual measurement so therefore the more conservative 95% confidence interval of ± 3.1 m/s was used in computing the standard error of the mean.

Each phase averaged velocity field presented had a minimum of 100 independent PIV measurements. The standard error the mean is computed with Equation (11) below. σ_x is the standard deviation of the measurements, N is the number of measurements, and σ_{μ_x} is the standard error of the true mean velocity as estimated by averaging all the measurements in that phase.

$$\sigma_{\mu_x} = \frac{\sigma_x}{\sqrt{N}} \quad (11)$$

This yielded a 95% confidence interval of ± 0.31 m/s for the phase averaged results. The overall mean flow fields are calculated from a series of 5000 measurements in the unyawed cases and 1000 measurements in the yawed case. Averaging all the measurements for each case gives estimates for the 95% confidence interval of the standard error of the mean of ± 0.044 m/s in the unyawed cases with 5000 measurements and ± 0.098 m/s in the yawed cases with 1000 measurements.

2) Estimating the Error from the Measurement System

There were other sources of uncertainty specifically in the PIV measurements due to the experimental setup that should be addressed. The two most important sources are laser misalignment with the wall, and rotation of the measurement region, as defined by the calibration plate, around the Y' axis. PIV measurements of the undisturbed boundary layer were used to bound the uncertainty for the misalignment and rotation.

From an analysis of the measurements of the completely unobstructed, zero pressure gradient boundary layer it was determined that the measurement region was oriented within $\pm 0.75^\circ$ of parallel to the mean flow. This orientation angle offset about the Y' axis would cause a worst case bias error of ± 0.26 m/s in the U and W components of the flow, however the total flow magnitude would be unaffected.

The error in the rotation about the X' and Z' axis was characterized by comparing with Morton's boundary layer and it was determined that the plane was within 0.65° of parallel to the wall. Using Morton's boundary layer profile around 10% of the boundary layer thickness, this could cause a worst case bias error of ± 0.375 m/s in the 10mm plane in the streamwise velocity component.

Lastly it was noticed that the intensity of the raw images tended to correlate to with the velocity measurement. This is a recognized issue with PIV when cross-correlating two low intensity images, as was done here because of the background subtraction preprocessing steps, and to the author's knowledge there is no established way to quantify this error. In this case the error was bounded by comparing the mean

velocity of an adjacent consistently bright and consistently dim spot. This method yielded a velocity difference of 0.16m/s.

These systematic sources of error in the PIV measurements are largely produced and controlled by the calibration procedure. Since, the calibration had to be redone every time the rotor was yawed, a correction factor cannot be directly applied from unobstructed boundary layer measurements to the rest of the measurements to reduce the bias errors.

However, we were unable to set the calibration plate to calibrate the clean boundary layer measurements as exactly as during the rest of the cases due to technical difficulties that arose with the laser and limited testing time. Therefore, we believe that the inaccuracies measured in the clean wall case are representative of an absolute “worst case scenario” for the rest of the measurements. All these sources of error discussed above were combined with a root-sum-square as they applied for each velocity component of each measurement to determine a final uncertainty. The rotational bias about the Y' axis was neglected in the calculation of the velocity magnitude uncertainty because it has an inverse relationship on the U and W velocity components and its effect on the mean is believed to be negligible.

Therefore, the estimates tabulated below are the 95% confidence interval uncertainties in the PIV velocity measurements. The relative uncertainty was found by normalized on the nominal freestream velocity of 20 m/s.

Table 5: PIV Uncertainty Summary

Measurement	Component	95% Confidence Level (m/s)	Relative Uncertainty
Mean Flow (5000 Measurements)	Magnitude	±0.41	± 2.06%
	Streamwise	±0.49	± 2.43%
	Spanwise	±0.26	± 1.32%
Mean Flow (1000 Measurements)	Magnitude	±0.43	± 2.15%
	Streamwise	±0.49	± 2.47%
	Spanwise	±0.28	± 1.39%
Phase Averaged Mean Flow	Magnitude	±0.60	± 2.99%
	Streamwise	±0.57	± 2.85%
	Spanwise	±0.40	± 2.00%

Chapter 3: Experimental Results and Analysis

The results from this experiment are organized into four major sections based on the logical breakdown of the different operating regimes of the rotor. The first section focuses on the unobstructed boundary layer without the rotor present and compares it to previous experiments. The second section focuses on the thrusting regime when the rotor is aligned with the inflow, and the third focuses on the thrusting rotor operating at an angle, or yawed, with respect to the mean inflow. Lastly, the fourth and final section focuses on the braking regime.

3.1 Verification of the Boundary Layer

The first results presented are of the boundary layer verification with previous experiments, which was comprised of two parts. First the zero pressure gradient was verified so that the turbulent boundary layer would develop like that of Awasthi (2012), Morton *et al.* (2012), and Alexander *et al.* (2013 and 2014) and then secondly the boundary layer profile at the measurement region was checked for similarity to these previous experiments.

3.1.1 Zero Pressure Gradient Boundary Layer

The first step in verifying that the boundary layer was identical to the previous experiments is showing that it is indeed a zero pressure gradient. As explained above, this was measured by static pressure ports that were located 40cm from both the floor and ceiling along the length of the test section. These ports were used for feedback to set the wall such that as close to a zero pressure gradient as practically possible was maintained along as much of the wall as possible. After the zero pressure gradient was set, within the practical constraints, two runs of the empty test section were recorded. The pressure coefficient, defined in Equation (12), at each streamwise position was averaged over those two runs and for the top and bottom port and this is plotted in Figure 28 below for a flow speed of 20 m/s. The mean wall pressure measurements recorded by Awasthi (2012) at the same experimental conditions after he had set the wall to a satisfactory zero pressure gradient is also plotted to allow a direct comparison.

Requiring a zero pressure gradient along the wall means that the width of the test section must be slightly increasing downstream. This was physically possible for the first four panels however panels five and six ran into physical constraints and were unable to be widened enough to continue the zero pressure gradient. The second pressure port on panel five was almost two meters downstream of the rotor and the wall pressure there is not believed to significantly affect the boundary layer at the rotor. Additionally, the wall pressure gradient achieved in this experiment is actually closer to zero than the mean wall pressure gradient recorded by Awasthi (2012).

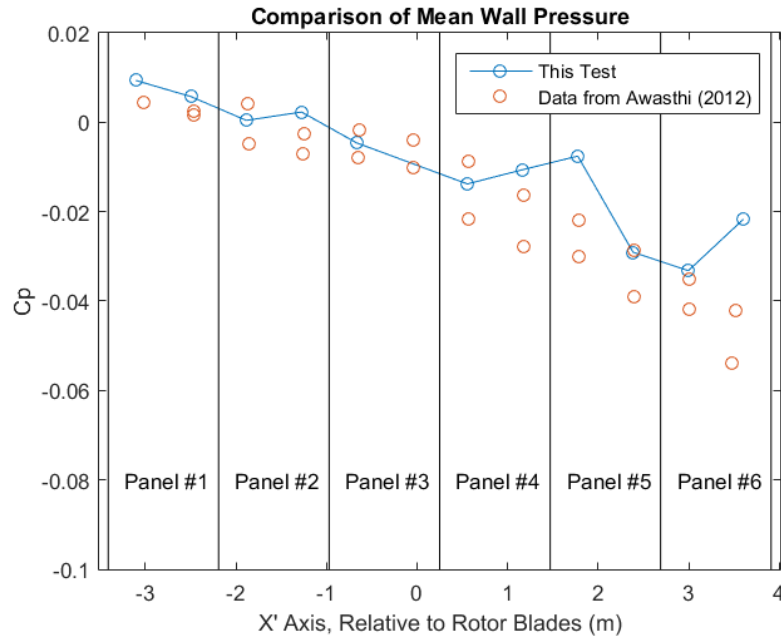


Figure 28: Comparison of mean wall pressure measurements in this test and data taken by Awasthi (2012) for the same boundary layer configurations. Note that the coordinate system is relative to the rotor location and there was no second measurement on panel 3 in this experiment due to the presence of the removable static pressure array there.

3.1.2 Boundary Layer Profile Comparison

The boundary layer profiles were compared to hotwire measurements from Awasthi (2012) with the same flow speed and trip height, 20m/s and 9.5mm respectively. Awasthi recorded his boundary layer profile 4.87m downstream of the trip. The rotor in this test, and therefore also the velocity measurements, were made 4.60m downstream of the boundary layer trip. This corresponds to a location of 0.27m downstream of where the rotor was located in this test. Despite this small streamwise difference the turbulent boundary layer had ample time to develop over the previous 4.6m of wall by the time it reached both measurement regions so Awasthi's measurements will provide a good comparison of the boundary layer shape to conform the repeatability of the boundary layer used in this experiment. Morton (2012) also compared and verified his boundary layer profile with the data set from Awasthi.

The average velocities and turbulence characteristics were calculated from PIV measurements taken at nominal distances of 125, 101, 80, 65.7, 42.85, 31.43, 23.43, 10, and 5mm from the wall. There was significant difficulty in this post processing due to uneven laser illumination in the measurement region. To help mitigate this a spatial average was used over a subset of the measurement region with even laser illumination to calculate the velocity and turbulence quantities shown in Figure 29 below. The boundary layer profile was also normalized on the mean streamwise velocity from the 125mm plane since it is outside of the 101mm boundary layer and provides a direct measurement of the actual wind tunnel flow velocity.

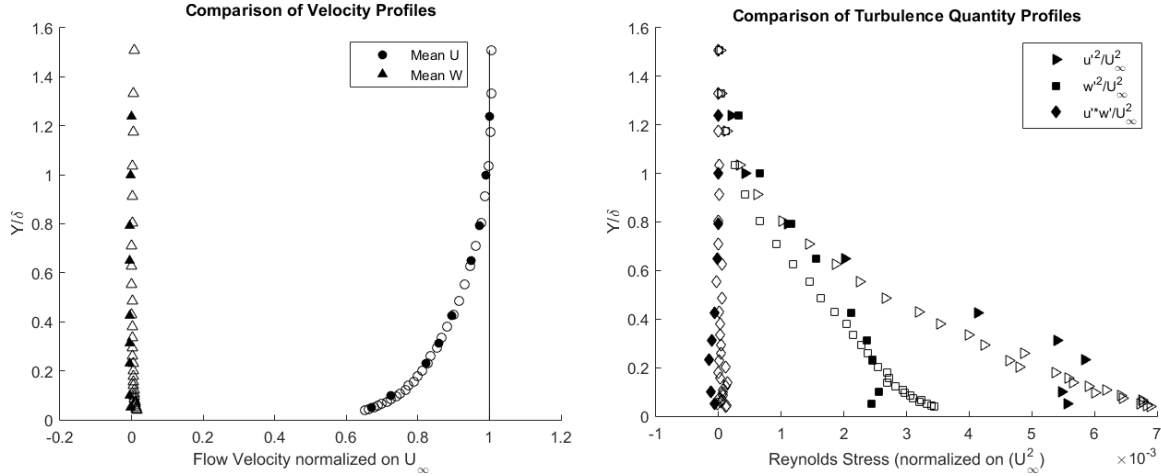


Figure 29: Comparison of velocity and mean Reynolds Stress profiles for the boundary layer in this experiment and that of Awasthi (2012). The filled symbols are spatial averages in planes parallel to the wall from the PIV measurements in this experiment and the open symbols are from a 30 point quadwire statistical measurement made by Awasthi.

The normalized boundary layer mean velocity profiles from this experiment match up well with those from Awasthi in the streamwise (U) and spanwise (W) directions. The streamwise velocities match the 30 point hotwire measurements made by Awasthi to within 1.7% of U_∞ falling slightly below Awasthi's measurements as they approach the wall. The turbulence stress profiles show good agreement above $\frac{y}{\delta} = 0.23$, but deviate below this point with the PIV estimates falling below those from the hot wire. The small discrepancy above $\frac{y}{\delta} = 0.23$ is believed to be due to a possible misalignment of the measurement plane out of parallel with the wall and therefore the inadvertent measurement of fluid lower in the boundary layer than intended in part of the plane. Below $\frac{y}{\delta} = 0.23$ the discrepancy is an underestimate of the streamwise and spanwise components. This is believed to be due to an unintentional and unavoidable spatial filtering by the PIV measurement system. The resolution of the PIV measurement was 2.23 mm so this tended to filter out turbulence scales smaller than this size, which are also more prevalent near the wall. This would help explain the lower Reynolds stresses measured nearest the wall when compared to Awasthi's hot wire measurements. Overall though, the boundary layer measured in this experiment compares well to that measured by Awasthi for the same configuration showing that the creation of this boundary layer is repeatable.

3.2 Thrusting Regime

The next section in the logical breakdown of this experiment is the thrusting regime when the rotor is aligned axially with the mean inflow. A moderately thrusting case is presented and discussed first as an example of the typical flow and acoustics seen in a thrusting rotor ingesting a planar turbulent boundary layer near a wall. This includes haystacking noise due to stretching of boundary layer turbulence and flow distortion seen in near-wall velocity and pressure measurements on the wall. Then, the effects of the rotor advance ratio on the acoustics and flow measurements is compared with the baseline case.

3.2.1 Baseline Case – Moderately Thrusting

The first case that will be presented is that of the moderately thrusting case, where $J = 1.05$, to demonstrate the typical rotor-planar boundary layer interaction in terms of flow and acoustic phenomena.

The mean wall pressure distribution for the moderately thrusting case is shown in Figure 30 a) below. Flow moves left to right and the leading and trailing edge of the rotor blades, as projected onto the wall, are indicated by the overlaid vertical lines centered at the origin. The spacing and height of the lines corresponds to the maximum extent of the rotor disc as projected into the wall. The coordinate system is the primed coordinate system, which is set up such that the origin is below the center of the un-yawed rotor. The pressure coefficient, defined in Equation (12) below, is normalized on the free stream dynamic pressure and referenced to the free stream static pressure measured far upstream of the rotor. As explained in the uncertainty analysis, Section 2.8, the pressure coefficient uncertainty is estimated to be ± 0.0047 .

$$C_p = \frac{p - p_\infty}{\frac{1}{2} \rho_\infty V_\infty^2} \quad (12)$$

The mean wall pressure distribution shows that there is a low pressure region on the wall directly upstream of the rotor centered at $X'/R = -0.3$ on the axis of rotation of the rotor as projected onto the wall. This region has a minimum pressure coefficient of -0.07. This minimum indicates that there is an adverse pressure gradient leading up to the rotor blades, and implies a deceleration in the flow next to the wall as it approaches the rotor. The increasing mean wall pressure leading up to the rotor blades and the decreasing velocity in the tip gap as fluid passes under the blades is believed to be the result of the thrusting rotor contracting the stream tube of air drawn through the blades away from the wall.

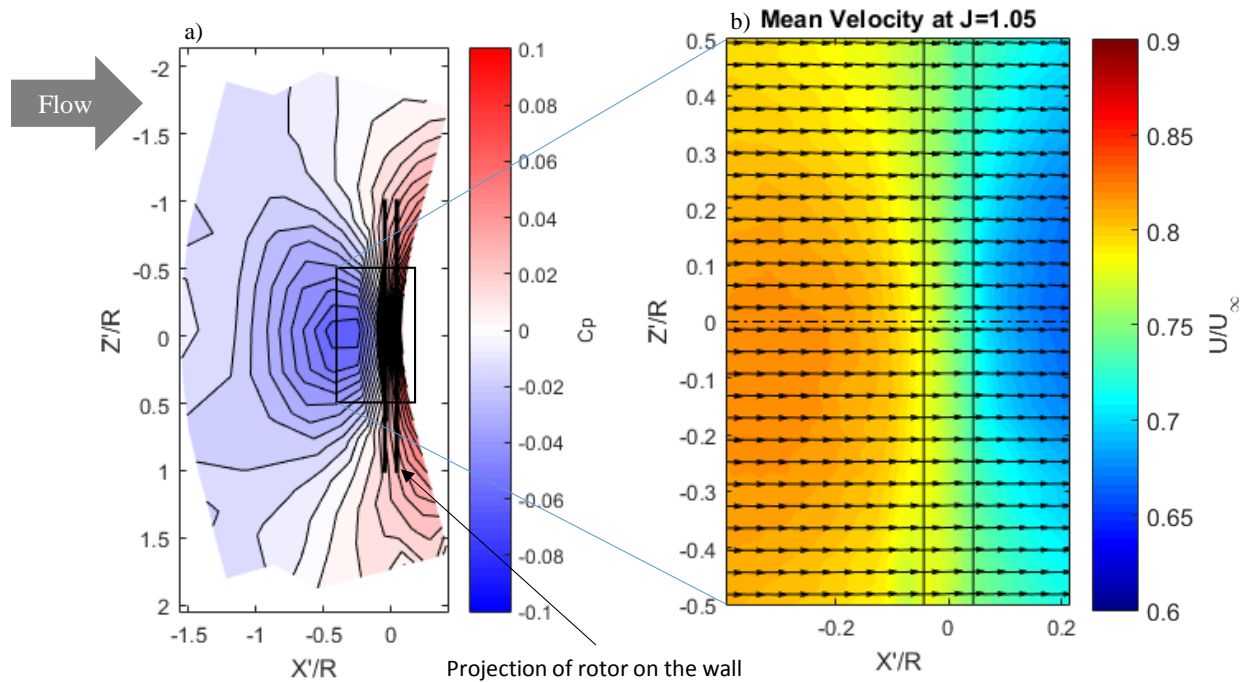


Figure 30: Mean wall pressure distribution, a), and mean velocity in the middle of the tip gap, b), at the moderately thrusting condition of $J=1.05$.

These results are confirmed by measurements of the fluid velocity in the center of the tip gap. The mean near wall velocity map inside the region enclosed by the box in Figure 30 a) is shown in Figure 30 b). Like the velocity field presented earlier flow is from left to right and the two vertical lines mark the projection of the leading and trailing edge of the rotor blades into the measurement plane. The dot-dash line marks the projection of the axis of rotation of the rotor. As described in Section 2.6, the primed

coordinate system is set such that the projection of the center of the rotor blades is centered at the origin, and the dimensions are normalized on the rotor radius.

The mean flow measurements quantify the deceleration that was inferred from the mean wall pressure. They show that the fluid in the tip gap decelerates from $0.79 U/U_{inf}$ to $0.59 U/U_{inf}$ and also that this deceleration is most significant directly below the centerline of the rotor where the tip gap is narrowest.

The phase averaged velocity fields in the tip gap were also examined for the moderately thrusting case. As described in the previous section, this allows the reconstruction of an average blade passage past the wall. Bottom dead center is defined as 0° phase and the blade is approaching the wall at negative phase angles and retreating from the wall at positive phase angles.

Figure 31 shows three evenly spaced and representative phase averages, centered on -12° , 0° , and 12° rotor phase, for the moderately thrusting condition. The markings are the same as in Figure 30 b) however the field of view has changed slightly to better show the blades near bottom dead center. The black oval marks the position of the blade tip as projected into the measurement plane for reference. A consequence of binning the measurements into a two degree bin is that there is some small variation in the actual blade position in each of the measurements averaged together to form the phase average. The projection of the blade oval is plotted at the center of the two degree bin and the actual position of the blade in the measurements is within $\pm 3.95\text{mm}$ or $\pm 0.0173R$ of the plotted position. Note that throughout this thesis the blade phase is designated by the label " $\Omega =$ " above the plot and it is given in either a two degree range of angles or the center angle in a two degree bin although they both mean the same thing.

Examined in succession, these phase averages show that the blade trails a stream of lower velocity fluid, with a minimum magnitude of about $0.56 U/U_{inf}$, in the measurement plane as it passes by bottom dead center which then convects downstream. This stream of lower velocity fluid appears to be the dominant feature in the tip gap at moderate thrust and contributes to the mean slowing of the fluid through the tip gap seen in Figure 30 b). This feature is attributed to part of the blade tip vortex passing through the measurement plane. Since this is a thrusting case, the blades shed a tip vortex that appears as a velocity deficit near the wall. The blade tip vortex is closest to the measurement plane at bottom dead center, which also explains why the wakes appear strongest in the center beneath the rotor. The velocity deficit seen here is consistent with part of a blade tip vortex that is trailing the blade as it passes by the wall and supports the conclusion that that is what causes the wake and could be partially responsible for the lower velocity downstream of the blades observed in the mean flow in Figure 30b).

For the interested reader, each of the phases of the phase averaged velocity fields for the moderately thrusting case and the phase averaged Reynolds stress components at representative phases are presented in Appendix B, in Figure 68 and Figure 69, at the end of this thesis.

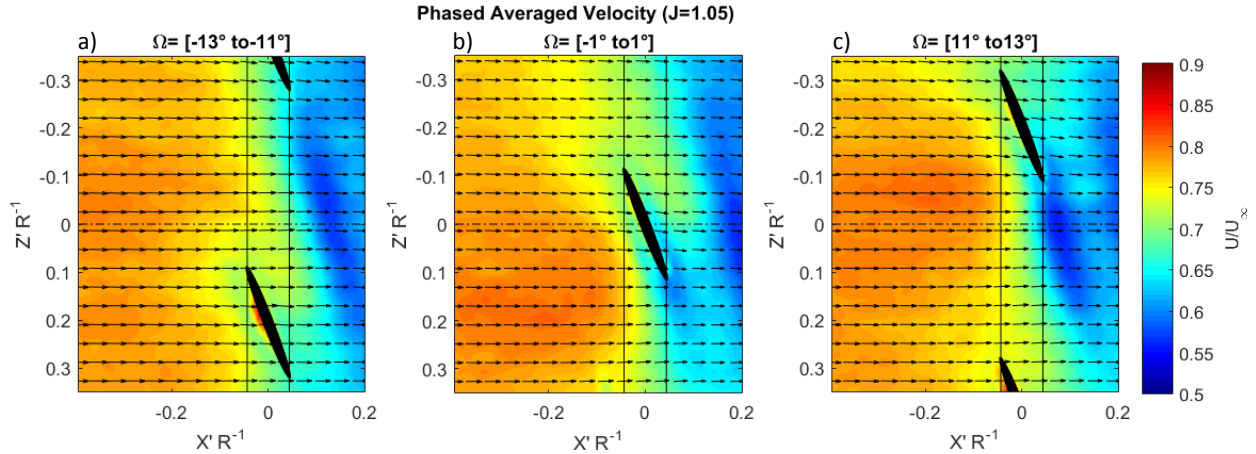


Figure 31: Phase averaged velocity maps in the tip gap for the moderately thrusting case. The three phases shown are (a) as the blade approaches the wall, (b) as the blade is closest to the wall, and (c) as the blade moves away from the wall. Note that the blade trails a velocity deficit in the measurement plane which is carried downstream.

The acoustic power spectral density, as measured from microphone number 1, is shown below in Figure 32 for the moderately thrusting condition ($J = 1.05$, 2500RPM) along with the tunnel background noise. All spectra presented in this thesis are from microphone number 1 because it was the most inline upstream microphone and therefore had the highest signal to noise ratio. This spectra, and all others in this thesis were computed as narrowband spectra with a resolution of 8Hz.

The three vertical lines in Figure 32 below indicate the first three harmonics of the blade passage frequency (BPF), 416.66, 833.33, and 1250 Hz respectively. The spectra for the moderately thrusting condition shows a very high SNR above 300 Hz and all further acoustic analysis in the thrusting regime will be presented from 300 Hz to 20 kHz, with the background noise subtracted. The background subtraction was carried out with a discretion level of 1dB and at any frequencies where the background was larger than or within 1dB of the measurement the spectra is not shown.

The spectra in Figure 32 shows features typical of a thrusting rotor ingesting turbulence in addition to a number of other features common to all farfield acoustic measurements from this experiment. It has a large and broad spectral hump, or haystack, centered just above the first BPF and a smaller haystack centered just above the second BPF harmonic, labeled a). This haystacking phenomena is due to the coherent response of multiple blades cutting the same turbulent eddy as it passes through the blade disc and is the dominant noise source for a thrusting propeller ingesting turbulence.

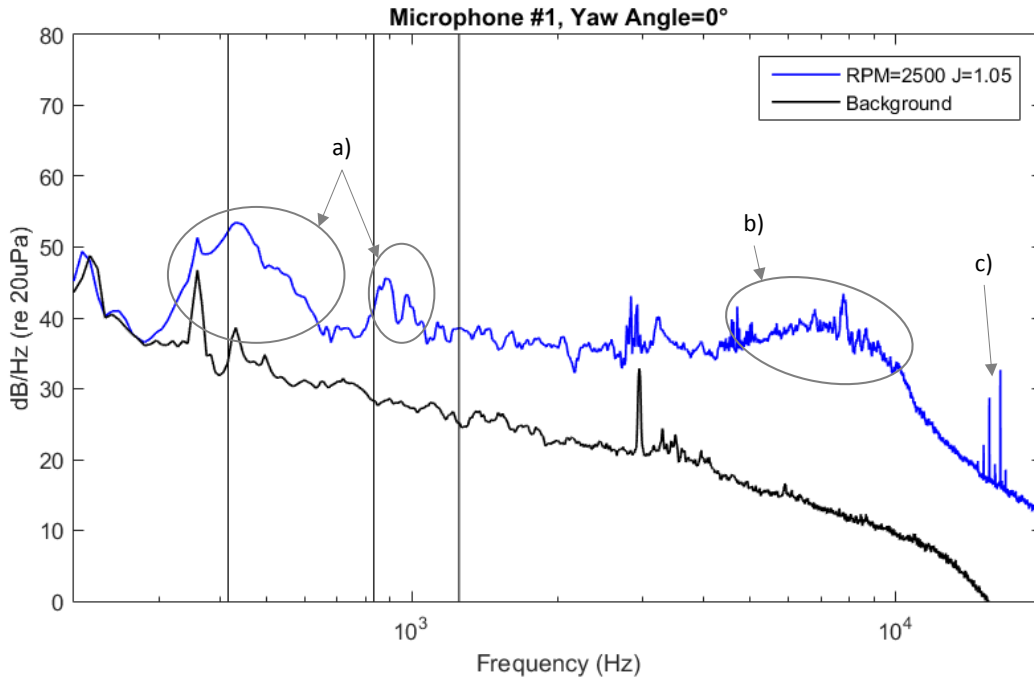


Figure 32: Acoustic spectra from Microphone #1 for $J=1.05$ with background to show the signal to noise ratio. Vertical lines indicate the first, second, and third harmonics of the blade passage frequency for reference. a) haystacking noise centered slightly above the first two blade passage frequency harmonics, b) trailing edge vortex shedding noise, d) high frequency spikes at 10 times the shaft rate attributed to motor whine.

Some of the other features of this spectra that are also seen in the measurements at other advance ratios and yaw angles are listed in the other callouts. In particular, the spectral hump seen between 5 and 10 kHz in this example, labeled b), is attributed to trailing edge vortex shedding noise which occurs when the blade is at low angles of attack. As will be shown later, it occurs in bands that depend heavily on the advance ratio of the rotor so it is clearly an angle of attack dependent phenomena.

The high frequency spikes, between approximately 15 and 17 kHz in this example and labeled c), are spaced at ten times the motor shaft rate and are attributed to motor whine. They appear more prominently in the higher advance ratios (which have a lower SNR) at these same frequencies although they can be seen in all except the lowest three advance ratios. In each instance, they are at ten times the shaft rate, and also only show up around 8.5 kHz and then in the 15 to 17 kHz range.

3.2.2 Effects of Advance Ratio in a Near Wall Rotor

Now that the typical features seen in the acoustic spectra and near wall flow for a thrusting rotor near a wall have been introduced and explained, the effects of changing the rotor rotation rate will be explored. The rotation rate is expressed as the advance ratio, defined in Equation (4), and ranges between highly thrusting ($J = 0.58$) and braking ($J = 2.19$). First the effects in the far-field spectra will be explored and then the mean wall pressure and near wall flow velocity through the tip gap are presented.

3.2.2.1 Far-Field Spectra

The spectral density for all advance ratios considered in this experiment is shown in Figure 33. The two most significant features of this contour plot are the diagonal “stripes” in the bottom left corner and the higher frequency spectral humps, labeled a) and b) respectively. The dashed lines correspond to the four

advance ratio conditions at which velocity measurements in the tip gap were also recorded. For reference, the line labeled c) corresponds to the case shown in Figure 32.

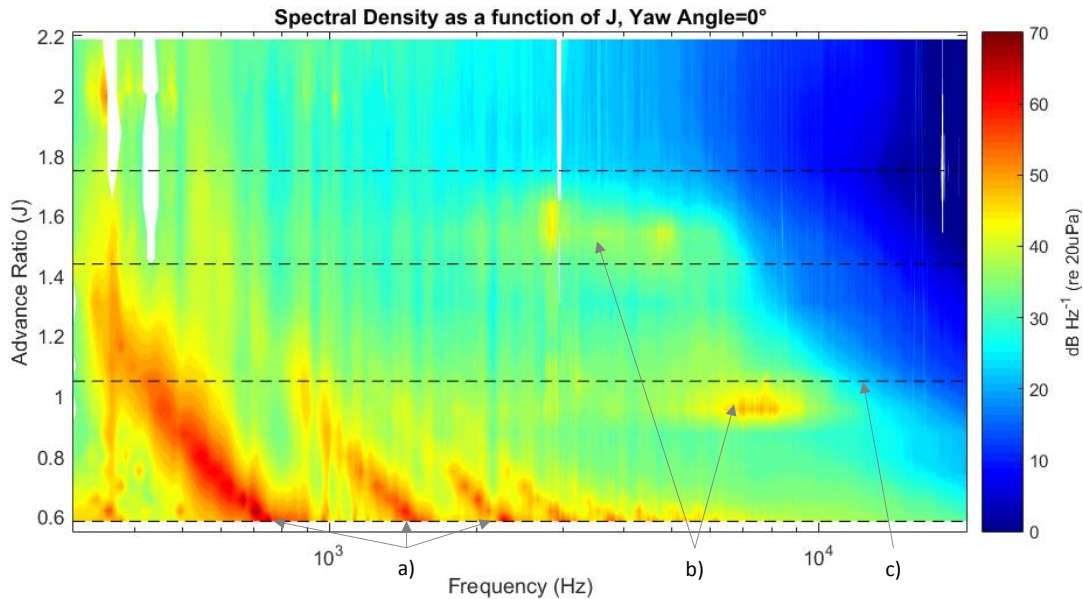


Figure 33: Spectral density contour plot for all advance ratios considered in this experiment. The dashed lines indicate advance ratios of 1.75, 1.44, 1.05, and 0.58 respectively from top to bottom where PIV measurements of the tip gap were also made. The features called out by a) are haystacking noise, b) is trailing edge incoherent vortex shedding noise, and c) indicates the advance ratio $J = 1.05$ which is the primary focus of this section.

This contour plot shows that the trailing edge spectral humps pointed out in Figure 32b) are highly dependent on the advance ratio of the rotor, and therefore local blade angle of attack. They only appear in two distinct bands, between $J = 0.95$ to 1.17 in the thrusting regime, and between $J = 1.44$ and 1.54 in the braking regime.

In Figure 34 the spectra for the four representative advance ratio conditions, and corresponding to the dashed lines in Figure 33, are presented. The first figure, a) shows the spectra plotted without any scaling or normalization for a better direct comparison. In the second figure, b), the overall sound level for each case was scaled on tip velocity to the fifth power, because airfoil self-noise mechanisms have been shown to scale as such, and the frequency is plotted in terms of the Strouhal number based on blade thickness and relative tip velocity.

The collapse of the spectral humps on this scaling for the moderately thrusting condition ($J = 1.05$) and the zero thrust condition ($J = 1.44$) with this scaling, labeled c) in Figure 34, indicates that the two spectral humps, labeled b) in Figure 33, are produced by the same mechanism. This mechanism is strongly suspected to be laminar or transitional trailing edge vortex shedding because of the similarity to the spectral humps seen in Hersh *et al.* (1974). Hersh tested the same Reynolds number range as considered here and saw similar vortex shedding spectral humps at lightly loaded conditions. The frequency of the spectral humps he observed also scaled directly on velocity.

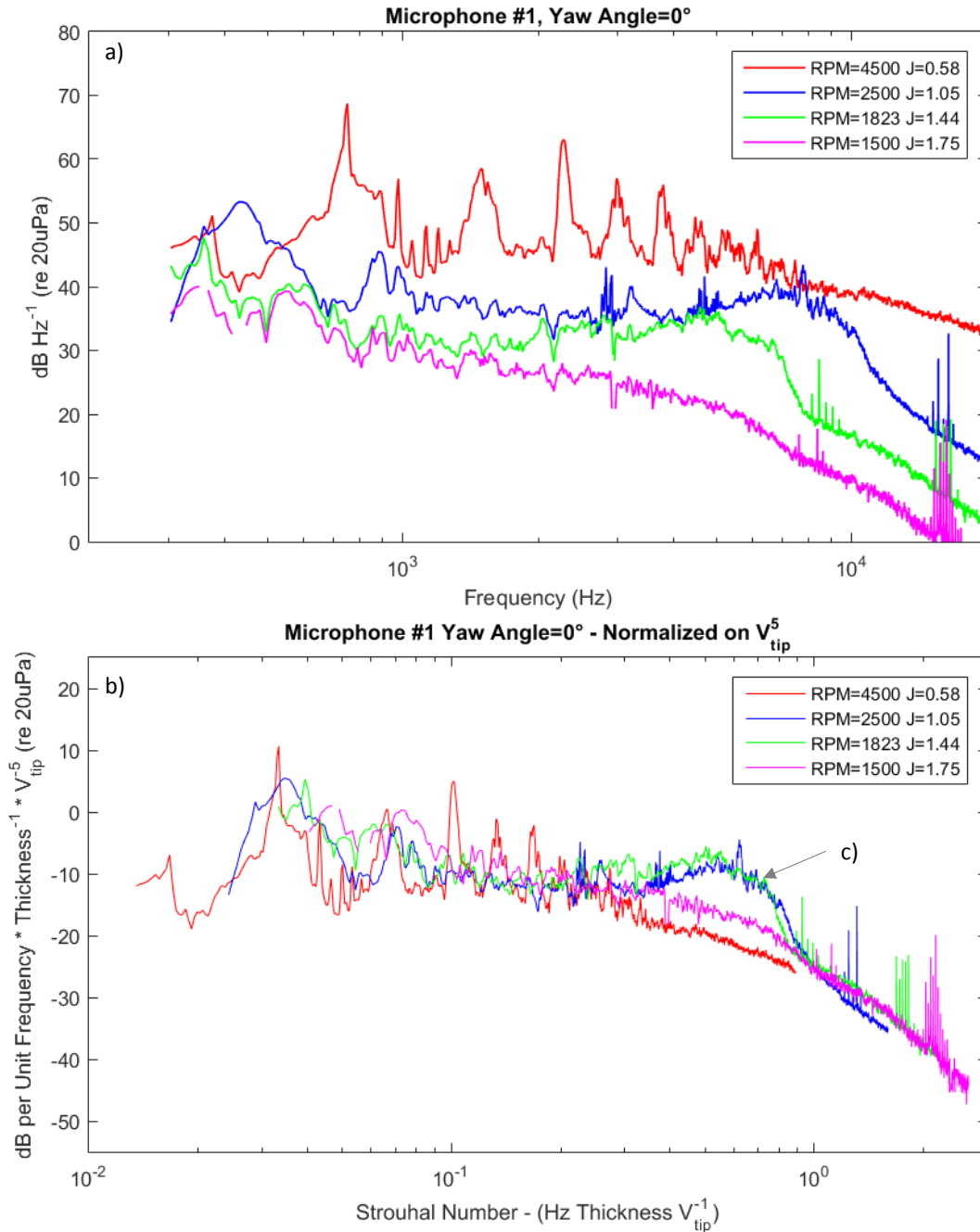


Figure 34: Representative spectra from all four operating regimes considered and where velocity measurements were taken in the tip gap; high thrust ($J=0.58$), moderate thrust ($J=1.05$), no thrust ($J=1.44$), and negative thrust or braking ($J=1.75$). Figure a) is the unscaled spectra and b) is the same spectra normalized on $V_{blade\ tip}^5$ for airfoil self-noise spectral collapse. Note that the spectral humps, labeled c), for the $J=1.05$ and $J=1.44$ conditions collapse very well, indicating that they are produced by the same mechanism.

In Figure 33, the diagonal stripes at lower frequencies and high thrust conditions, low J , are the haystacking peaks at harmonics of the blade passage frequency, as mentioned briefly above. Looking at the entire range of advance ratios considered, it is apparent that the haystacking response is predominantly in the thrusting regime and changes dramatically as the advance ratio decreases. As the rotor spins faster,

and the advance ratio decreases, the haystacking response increases magnitude, each haystack narrows in its frequency range, and the number of haystacks significantly increases.

The change in haystacking response is clearly visualized in Figure 35 as the difference between the spectral density functions at $J = 0.58$ and $J = 1.05$. Figure 35 shows the spectra for the same four representative conditions but normalized on their blade passage frequency so that the blade passage dependent response for each case can be easily compared. The spikes seen between the first and second blade passage frequency in the $J = 0.58$ case also show up at $J = 0.61$, and are at the rotor shaft rate. This leads us to believe that they are due to motor noise or a slight rotor imbalance that becomes significant at high rotation rates and therefore are spurious.

The spectra at $J = 1.05$ displays the expected turbulence ingestion haystacking response however the highly thrusting case, $J = 0.58$, shows significant differences. The “haystacking” peaks in the $J = 0.58$ case are much narrower than in the $J = 1.05$ case and there is also a significant response up to the tenth multiple of the blade passage frequency, compared to just the second multiple in the $J = 1.05$ case. Glegg *et al.* (2015b) made haystacking noise predictions, which accounted for the stretching of boundary layer turbulence, to match the cases studied here. He found that the predictions showed good agreement with the measurements at low thrust conditions ($J = 1.05$) but that the response was far larger, both in magnitude and in number of spectral peaks, than was predicted at high thrust conditions ($J = 0.58$). This lack of agreement suggests that boundary layer turbulence stretching is no longer the dominant cause of the “haystacking” response in a highly thrusting rotor operating near a wall.

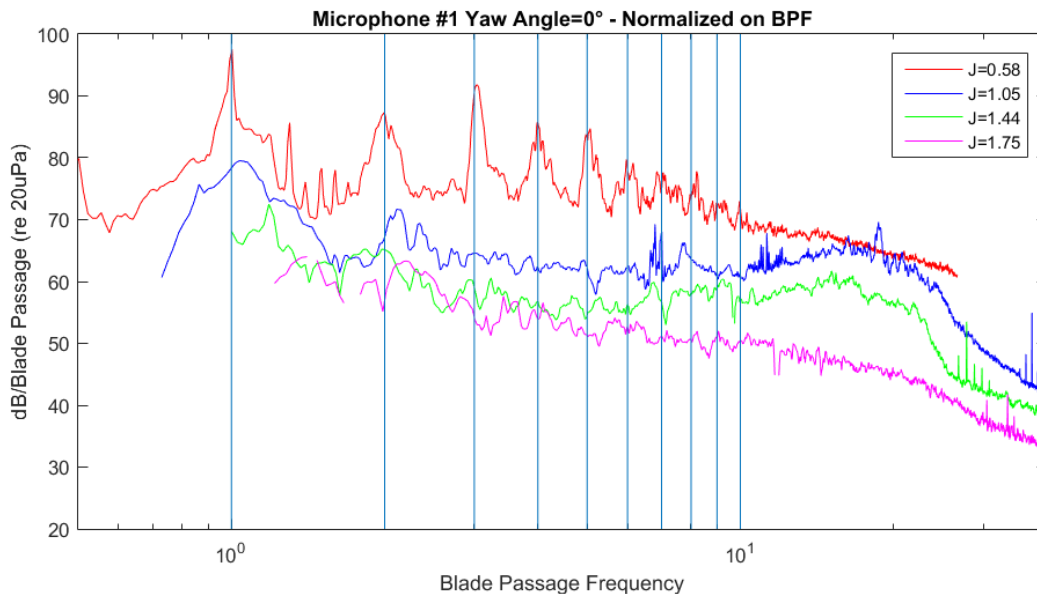


Figure 35: Representative spectra normalized on blade passage frequency from all four operating regimes considered and where PIV measurements were taken in the tip gap. Note that the moderate thrust condition ($J = 1.05$) has two haystacking peaks while the high thrust condition ($J = 0.58$) has 10 distinct peaks aligned with the blade passage frequency. The other two conditions shown have no blade passage dependent characteristics.

3.2.2.2 Mean Wall Pressure Measurements

Mean wall pressure measurements upstream of the rotor, shown in Figure 36 below, also support the conclusion that a different fluid dynamic interaction is taking place at high thrust. The pressure coefficient is defined in Equation (12) above and the mean wall pressure is plotted as a function of advance ratio for a braking case, the zero-thrust case, a moderately thrusting case, and a high thrust case in Figure

36a) through d) respectively. The pressure distributions are very near to symmetric for the thrusting cases but skewed slightly toward the upstroke side, negative Z' , for the other cases. As expected, a region of higher pressure was found upstream of the rotor for the braking case, with a maximum pressure coefficient of 0.09 and a region of lower pressure was found upstream of the moderately thrusting case, with a minimum pressure coefficient of -0.06. Somewhat unexpectedly, the zero thrust case showed a region of slightly higher pressure upstream, 0.04 maximum pressure coefficient, but this just indicates that it was creating a slight blockage in the boundary layer near the wall. The high thrust case, as expected, produces a low pressure region on the wall upstream of the rotor. But with a minimum pressure coefficient of -0.36, it is more than six times as strong as in the moderately thrusting case.

As a consequence of the upstream pressure minimum in the thrusting cases, the wall pressure gradient reverses and becomes unfavorable as the flow along the wall approaches the rotor. The adverse pressure gradient is very strong for the highly thrusting case and suggests that the flow is likely to separate in this region. The most significant finding of the mean wall pressure measurements is that the high thrust case has a separate low pressure region directly beneath the rotor blades along its axis of rotation. The second low pressure region, shown in more detail in Figure 36e), has a magnitude of -0.27 and was not observed in the moderately thrusting case. This region, in conjunction with the fluid velocity measurements presented next, show that the flow has indeed separated in the tip gap in the high thrust case.

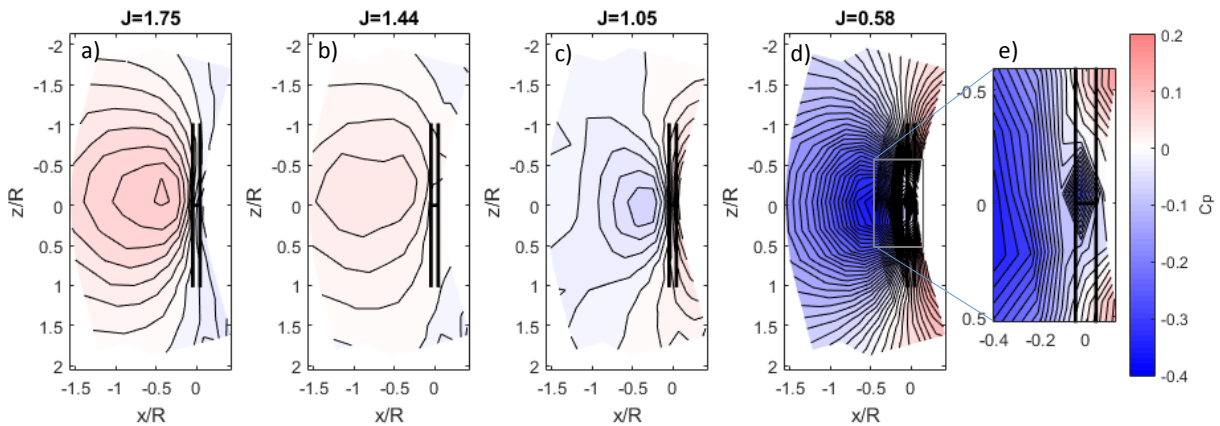


Figure 36: Mean Wall pressure fields at all four operating regimes considered, (a) is a braking condition, (b) is zero-thrust, (c) is moderately thrusting, and (d) and (e) are highly thrusting. The rotor is centered at the origin and the bracket marks the leading edge and trailing edge of the rotor as projected onto the wall. The color scale and contour line interval is the same between all subplots to emphasize the magnitude of the low pressure region upstream of the high thrusting case. Note the second low pressure region in the tip gap shown in (e).

3.2.2.3 Flow Velocity Measurements in Middle of the Tip Gap

Flow velocity measurements were made in the middle of the tip gap; 10mm from both the wall and the rotor blades at bottom dead center, their point of closest approach to the wall. The mean velocity through the tip gap is shown for the zero-thrust case, the moderate thrust case, and the high thrust case in Figure 37a) through c) respectively.

In the zero-thrust case there is very little change in the average velocity through the measurement plane in the tip gap. The moderate thrust case shows a slowing of fluid through the tip gap by approximately $0.2 U/U_{inf}$. The high thrust case however shows strong counter rotating cells, approximately centered at $Z'/R = 0.10$ and -0.15 , which appear to feed an area of reversed flow near the wall downstream of the rotor. This reversed flow then creates a stagnation point in the center of the tip gap directly downstream of the projection of the leading edge plane of the rotor blade. This matches well with the second low pressure

region seen on the wall in the center of the tip gap, Figure 37 e). The mean velocity measurements show that the flow reversal has a maximum velocity of $0.43 U_{inf}$ and is slightly offset toward the upstroke side of the center line, toward positive Z' .

This flow reversal in the mean at high thrust is caused by the presence of the wall. The wall prohibits the natural contraction of the stream tube of air entering from upstream that would occur for an unobstructed rotor. This starves the blade disc of fluid on the wall side, creating a larger pressure differential across the blade disc there that results in a flow reversal in the tip gap. However, this flow reversal is not a steady phenomenon.

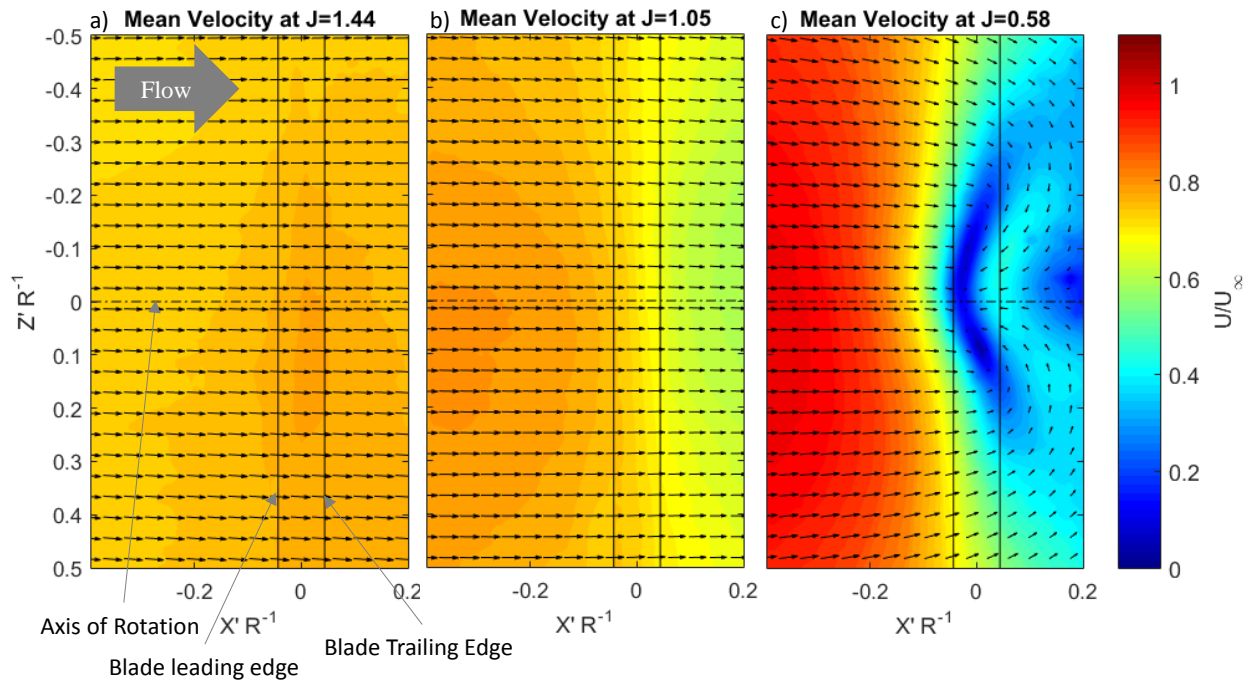


Figure 37: Mean velocity fields in the middle of the tip gap from PIV measurements. Flow is moving left to right, the two vertical lines mark the leading and trailing edge of the rotor blades, and the center line marks the axis of rotation of the rotor all of which are projected onto the measurement plane. a) is the zero-thrust case, b) is moderate thrust, and c) is the high thrust case.

It was not possible to observe an individual blade passage because the velocity field measurements were not time resolved. However, it was possible to reconstruct an average blade passage because the blades were visible in the raw images and could be related to angular position. The phase repeated very 36° owing to the 10 blades of the rotor. After the blade angular position was identified, images were sorted into 18 separate two degree bins. The vector fields in each bin were then averaged together. Each phase average consisted of more than 200 measurements in the unyawed cases.

A sequence of three evenly spaced and representative phase averaged flow measurements in the tip gap for the high thrust case are presented in Figure 38 and the phase angle of each of them is indicated by Ω . The zero phase angle is defined when the center of the blade is closest to the wall at bottom dead center (BDC) and Ω is oriented positive in the direction the rotor is spinning. In these plots, the blades are moving upward, in the negative Z' direction, as the phase angle increases. At negative phase angles the blades are approaching the wall and at positive phase angles they are retreating from it. The black oval indicates where the projection of the blade tip would fall in the measured plane to provide a frame of reference for the blade phase.

When compared to the moderately thrusting case previously discussed, there is no velocity deficit downstream that would suggest the presence of tip vortices. The flow in the tip gap for this high thrust case appears to be dominated by the flow reversal instead of the blade tip vortex. The phase averaged position of the counter rotating cells in the measurement plane appear to fluctuate slightly as the blade passes by the wall but the overall flow reversal pattern is constantly present throughout all phases of rotation. As the blade reaches bottom dead center, Figure 38b), the flow reversal tends to be strengthened by a jet of fluid in the tip gap traveling perpendicular to the blade chord and displacing part of the stagnation region. This jet of fluid is believed to be caused by the pressure differential between the pressure and suction sides of the blade. As the blade moves past bottom dead center and away from the wall, Figure 38c), the higher velocity jet of reversed flow remains near the center of the tip gap. This boosts the total reversed flow, Figure 38a), and the stagnation region returns to its original state. These phase averaged velocity fields suggest that the flow reversal pattern observed in the mean is fed by periodic jets of fluid that coincide with the tip of the blades passing closest to the wall.

For the interested reader, each of the phase averaged Reynolds stress components at these three phases are shown in Appendix B, in Figure 70, at the end of this thesis.

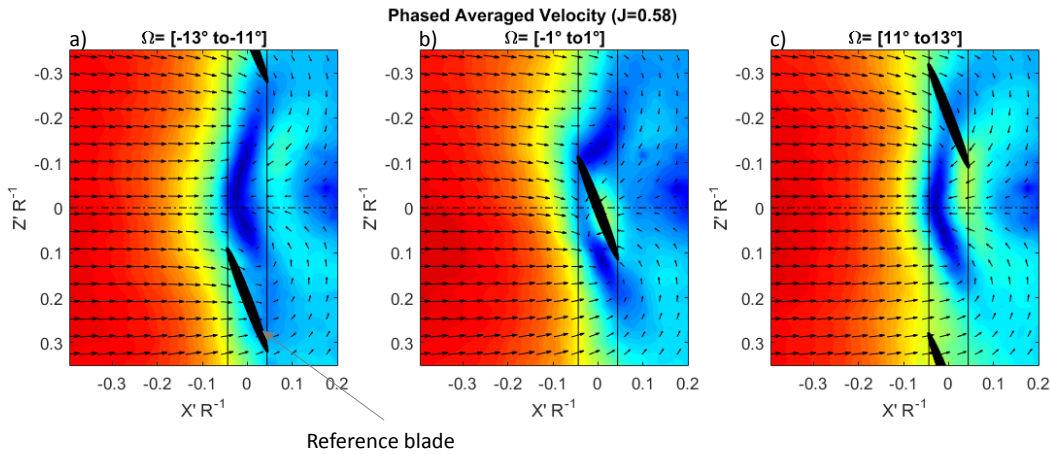


Figure 38: Phase averaged velocity measurements in the tip gap of the high thrust case. The three phases shown are a) the blade approaching the wall, b) the blade closest to the wall, and c) the blade moving away from the wall. The black ovals designate the projection of the blade tip into the measurement plane. Note that there is a stagnation region under the blades and also a strong consistent flow reversal behind the rotor, regardless of blade phase.

To gain a more complete understanding of the flow in the tip gap next to a highly thrusting rotor, the unsteady features of the flow also need to be examined. To that end, three representative instantaneous velocity fields for the $J = 0.58$ case are shown in Figure 39a) through c) with the same field of view as the phase averaged results discussed above and plotted on contours of vorticity. For the interested reader several more instantaneous velocity fields for this case are shown in Appendix B, Figure 71, at the end of this thesis. Two typical examples from the moderately thrusting case are included in Figure 72 to show that the vortices only appear in the highest thrust case.

Figure 39a) and b) shows the double vortex pattern but there is considerable variation in the location of the vortex centers. In a) the vortex pair is skewed toward the upstroke side of the rotor and there appears to be another clockwise vortex core just above the outline of the blade. All three vortices are also of approximately equal magnitude. The vortex pair in Figure 39b) is very close to the centerline and there is also another clockwise vortex center of approximately half the magnitude as that pair above the upper blade.

The final example Figure 39c) shows a single clockwise vortex slightly to the upstroke side of the centerline and with approximately double the maximum magnitude of the vortex pairs previously examined. Although an example is not pictured there were also other instantaneous velocity fields that showed a strong flow reversal but no clear vortex structure.

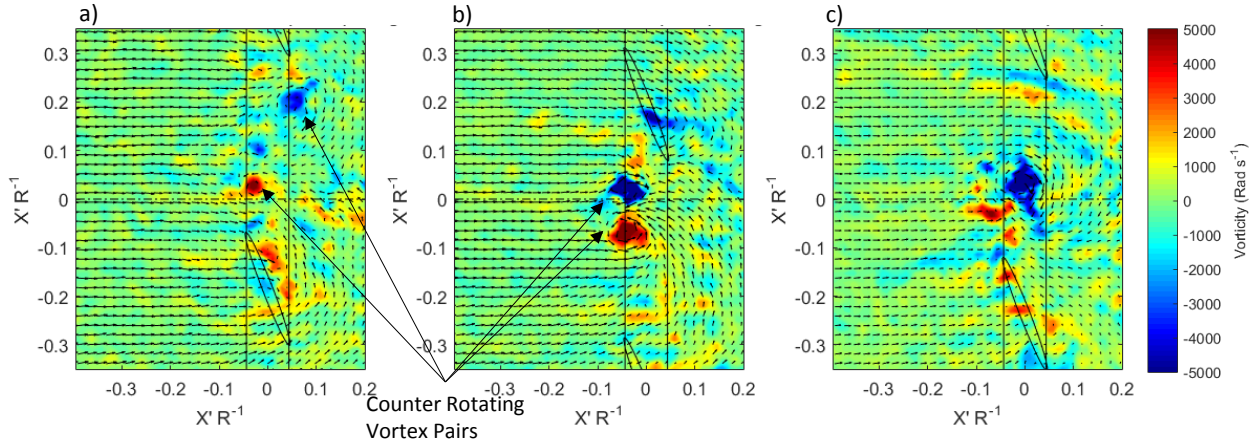


Figure 39: Instantaneous vector fields from the high thrust ($J = 0.58$) case, showing examples of a double vortex of uneven strength at different locations (a) and (b), and a single strong counterclockwise vortex (c). Note that the few gaps where vectors could not be reliably resolved during post processing were interpolated over to better show the vortex structures here. The oval shows the projection of the blade tips into the measurement region.

It is important to note that none of the instantaneous measurements closely resemble the time or phase averaged results. This suggests that the presence of the counter rotating cells is highly unsteady, since a single vortex pattern is also frequently observed. The instantaneous flow in the tip gap appears to take on several of the characteristic patterns documented in Sato *et al.* (1986) in a thrusting marine propeller near a wall, including the double vortex, the fore or aft vortex, and the splatter flow. Sato categorized the different near wall flow patterns as a function of the rotor tip gap to diameter ratio and thrust coefficient. However, this work suggests that the near wall flow for a high thrust rotor, with a low tip gap to diameter ratio, is highly unsteady and switches between several distinct flow patterns.

Since the flow reversal in the tip gap was found to be extremely unsteady, the Reynolds stress tensor was also examined. The Reynolds stress in the streamwise and spanwise directions, τ_{11} and τ_{33} respectively, is normalized on U_∞^2 and is shown in Figure 40a) and b). The Reynolds Stress was computed as defined in Equation (13) below where $\langle \rangle$ indicates the time average at a particular spatial location and u'_i is mean subtracted velocity component in the i^{th} direction as defined by: $u'_i = u_i - \langle u_i \rangle$.

$$\tau_{ij} = \langle u'_i * u'_j \rangle \quad (13)$$

The peak turbulent stresses in the high thrust case are approximately twenty times the magnitude of the peak turbulent stress in the moderate thrust case, which are not shown. In the high thrust case τ_{11} reaches a maximum of 0.25 and τ_{33} reaches 0.1 which confirms that the flow is highly unsteady. The τ_{11} component, Figure 40a), is largest in a crescent region directly below the rotor blade and between $z R^{-1} = -0.2$ and $+0.2$, where the maximum is skewed toward the down stroke side at $z R^{-1} = 0.07$. Figure 40b) shows that τ_{33} is largest in a similarly located but elliptical region and is also skewed toward the down stroke side of the rotor with a maximum at approximately the same location. The maximum Reynolds stresses measured in the tip gap are also 40 times the levels in the undisturbed boundary layer.

The down stroke skew of the peak for both Reynolds stress components agrees with on-blade hot wire measurements for this rotor published in Alexander *et al.* (2014). The hotwire measurements showed that upwash intensities were higher on the down stroke than on the upstroke side. Taken together these results indicate that the unsteady aspects of the flow reversal do not behave symmetrically and that the direction of rotation of the rotor is very significant. This could be a consequence of the increased prevalence of vortices on the downstroke side, as will be explained in §3.2.3 below.

The same components of the Reynolds stresses are presented for the moderately thrusting case to emphasize the extreme level of velocity fluctuations that are present in the highest thrust case. Also note that the moderate thrust case is plotted on a scale that is only 40% that of the high thrust case. The moderate thrust case shows that in general the streamwise velocity fluctuations decrease below the blades and then the spanwise velocity fluctuations increase downstream of the rotor in the tip gap, likely due to the blade wakes that are found there.

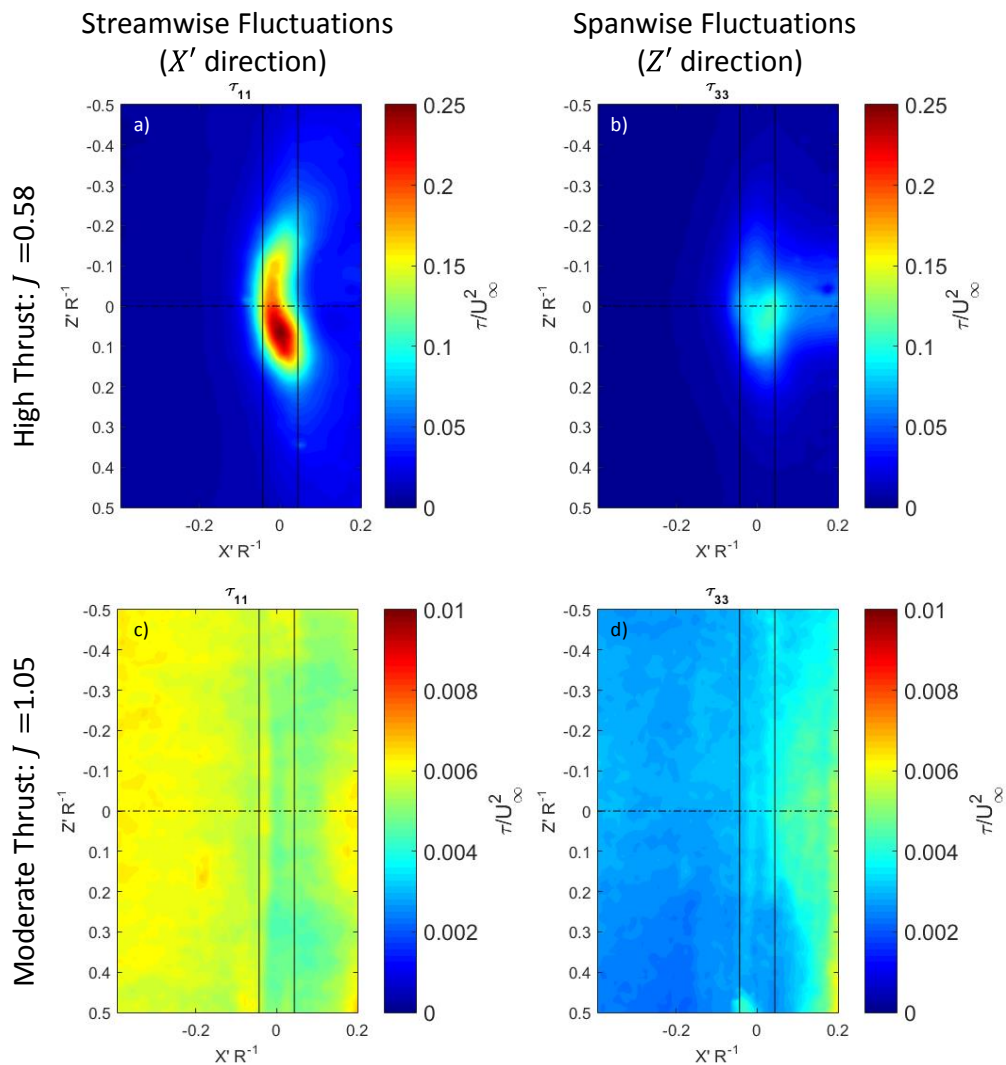


Figure 40: Streamwise and spanwise components of the Reynolds stress tensor for the high thrust ($J = 0.58$) and moderate thrust ($J = 1.05$) case, (a) and (b) and then (c) and (d) respectively. Note the strong skew toward the down stroke side in both components in the . The velocity fluctuations in both directions are greatest in the center of the rotor disc and at approximately $Y' R^{-1} = 0.06$.

Although the velocity measurement plane is outside of the rotor blade disc, it still allows us to infer the kind of structures that the blade encounters as it sweeps by the wall. Relating the far field spectral and velocity measurements, the presence of flow separation from the wall in the tip gap was accompanied by a strong acoustic signal at the blade passage frequency. This is believed to be caused by the interaction of the blade with the stalled and highly unsteady reversed flow in the tip gap. The increase in tonal spikes at the blade passage frequency for the high thrust condition can be thought of as a result of the blade interacting with a large mean velocity change as it passes by the wall while the widening of those peaks is the result of the interaction of the blade with the fluctuating velocity component of this flow reversal. In other words, the blade sees a large but unsteady angle of attack change around the blade disk. This accounts for the strong acoustic signature at the blade passage frequency in the highest thrust case and indicates that additional investigation is needed and a new methodology is required for accurate predictions of a highly thrusting rotor near a wall where flow reversal is present.

3.2.3 Vortex Identification and Quantification in Instantaneous Velocity Fields

In order to help develop that new methodology for predicting the blade-vortex interaction noise, a detailed analysis of the vortex structures in the tip gap was performed. This analysis aimed to quantify the locations and strengths of the strong vortex structures frequently observed in the instantaneous velocity field measurements when the rotor was at the highest thrust conditions.

The analysis presented in this section was based on the “Q-criterion” for the definition of a vortex in a field of planar velocity data originally developed in Hunt *et al.* (1988) and further explained in Haller (2005). There had been significant discussion on the exact mathematical definition for the objective identification of a vortex in recent years and Haller (2005) provides a good review and summary. The Q-criterion was selected because it was the first method developed and for its simplicity and ease of implementation with this data set.

The Q-criterion is a measure of the relative strengths of the vorticity tensor (Ω) and strain tensor (S) at every point in the velocity field and has units of $\frac{1}{s^2}$. The Q-criterion is defined in Equation (14) below where $\Omega = \frac{1}{2}[\nabla V - (\nabla V)^T]$, $S = \frac{1}{2}[\nabla V + (\nabla V)^T]$ and where $|x|$ indicates the Euclidian norm of the matrix x and V is the velocity field. In the two dimensional plane of data examined here Ω and S reduce to the 2x2 matrices shown in Equations (15) and (16) below.

$$Q = \frac{1}{2}(|\Omega|^2 - |S|^2) > 0 \quad (14)$$

$$\Omega = \frac{1}{2} \begin{bmatrix} 0 & \frac{\partial V_x}{\partial y} - \frac{\partial V_y}{\partial x} \\ \frac{\partial V_y}{\partial x} - \frac{\partial V_x}{\partial y} & 0 \end{bmatrix} \quad (15)$$

$$S = \frac{1}{2} \begin{bmatrix} 2 \frac{\partial V_x}{\partial x} & \frac{\partial V_x}{\partial y} + \frac{\partial V_y}{\partial x} \\ \frac{\partial V_y}{\partial x} + \frac{\partial V_x}{\partial y} & 2 \frac{\partial V_y}{\partial y} \end{bmatrix} \quad (16)$$

The conditions where the inequality is true, $Q > 0$, indicate that the vorticity tensor is dominant over the strain tensor and that a vortical flow is occurring in this region. In this analysis the Q-criterion is used in a qualitative sense to identify the spatial location of vortex centers based on local maxima in the Q-criterion scalar field. Several example of instantaneous velocity measurements from the center of the tip gap for the highest thrust condition are plotted over contours of the Q-criterion and shown below in Figure

41. Note that the small gaps in the data were filled by 2D linear interpolation because this analysis relied on a finite difference evaluation of the derivative and any small gaps created large holes in the Q-criterion which was problematic.

The examples in Figure 41 show the utility and accuracy of the Q-criterion in identifying vortex patterns. There were however three specific challenges that were overcome in developing an automated method of identifying and extracting the center location of each vortex based on the Q-criterion. The basis of this method is to extract the locations of Q-criterion maxima for each velocity field measurement, which corresponds to the center of the vortex. The three challenges in implementing this were: 1) establishing a lower limit for what qualified as a vortex 2) ensuring that two adjacent local maxima in the Q-criterion that are part of the same vortex are only flagged as a single vortex, and 3) making sure that vector fields without any strong vortices were flagged as such.

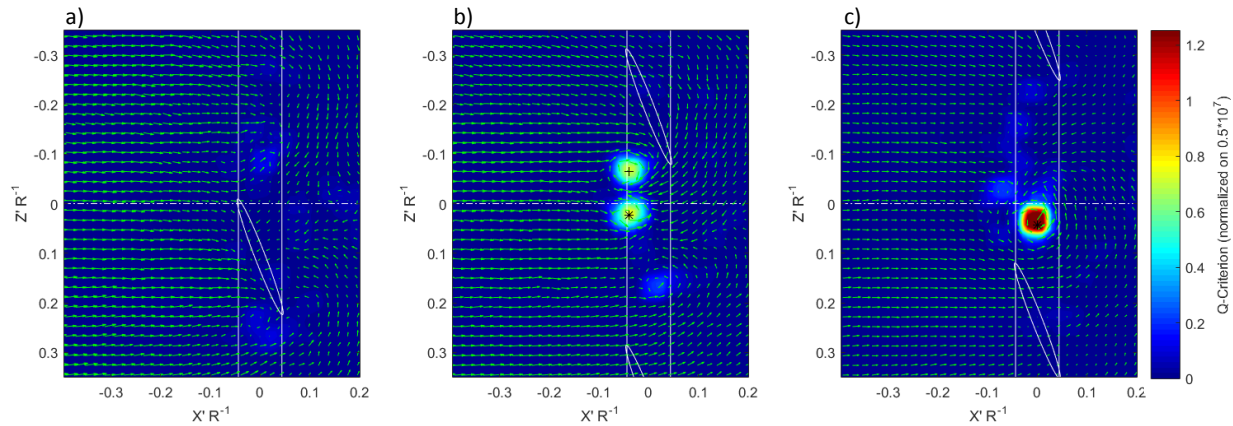


Figure 41: Three example instantaneous velocity fields overlaid on the Q-criterion. Note that b) and c) are the same measurements shown in Figure 39 b) and c) to allow comparison of the Q-criterion and the vorticity fields.

The second challenge was solved by implementing two separate methods. The first was that the Q-criterion scalar field was first smoothed before its local maximums were recorded. It was found that a 5x5 data point mean smoothing, which is a spatial area of 11.07x11.07mm, worked best for this. The other method was to check that no maxima were within 10mm of each other. If they were the larger Q-criterion would be taken as the vortex center. These two methods appeared to successfully avoid double identification of vortex centers.

The third challenge was solved by setting an absolute minimum cutoff level in the Q-criterion. This level was based on an analysis of 26 example vector fields like Figure 41a). Between all of them, there was only one or two strong vortices. A trade study was run on the 26 example vector fields where this threshold level was varied between 0.5 and 0.95, normalized on the typical Q-criterion level of 0.5×10^7 . A plot of the average number of vortices identified per vector field analyzed for each cutoff level is shown below in Figure 42. This trade study indicated that a minimum cutoff level of 0.3 and 0.35, normalized on 0.5×10^7 , returned the fewest false positives while still identifying the one to two strong vortices in this example data set. Therefore an absolute level of 0.3, normalized on $0.5 \times 10^7 \frac{1}{s^2}$, (which gives $0.15 \times 10^7 \frac{1}{s^2}$) was selected because it was the least restrictive level that resulted in the fewest false positive identifications.

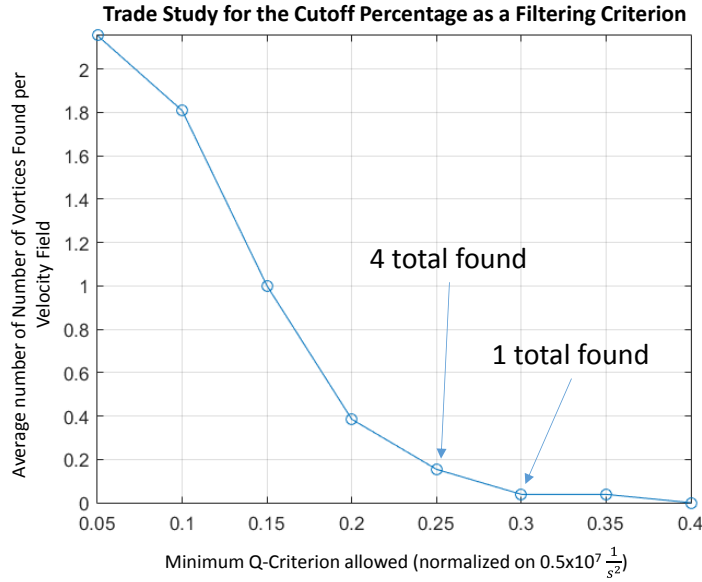


Figure 42: Trade study of absolute cutoff level of the Q -criterion in 26 example vector field with one to two strong vortices in total.

Lastly, the first challenge of setting a cutoff level for the vector field was solved by setting a floating minimum level that was a percent of the absolute maximum Q -criterion for each vector field. This approach was taken because it was qualitatively observed that each measurement, if it had multiple vortices, would tend to have one or two vortices of similar strengths and then multiple weaker vortical structures. The floating minimum level insured that these multiple weaker vortical structures were not counted relative to the one or two strong structures even if they passed the minimum Q -criterion level described above. This analysis was done objectively by running a trade study where the cutoff level was varied between 5% and 95% of the maximum and the number of vortices found in a subset of the dataset was tracked. Initially this method suggested that a value of 60% was the best choice. However, that was revised to 25% after the analysis was rerun with the other criteria explained above as they were found to be fairly restrictive already. All in all, this particular filtering criteria will have minimal effect on the vortices identified however it was still used in order to possibly filter out any outliers.

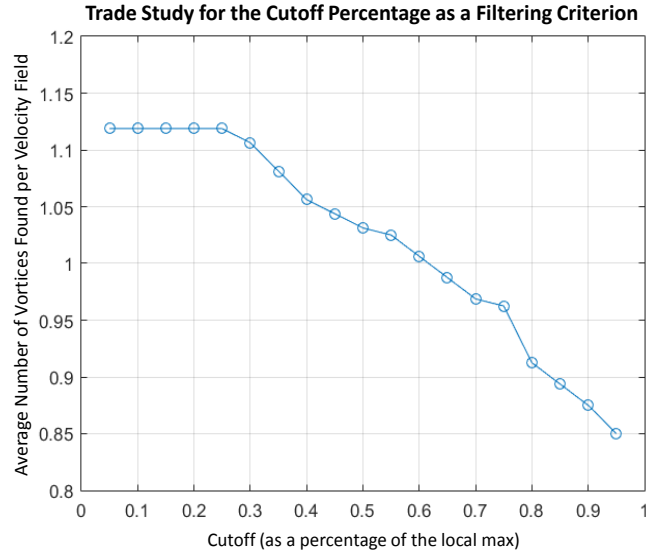


Figure 43: Trade study of the Q-criterion cutoff percentages on the average number of vortices found per measurement in a sample of the data. All other criteria described above were also applied and this study shows that a level of 25% is the maximum possible before large numbers of vortices are eliminated.

Using these filtering criteria; 5x5 smoothing of the Q-criterion, an absolute minimum of $0.15 \times 10^7 \frac{1}{s^2}$ in the Q-criterion, a cutoff of 25% of the maximum Q-criterion in that vector field, and requiring that vortex centers be more than 10mm apart, the entire unyawed dataset was evaluated. These criteria were deliberately set to be restrictive because it was reasoned that the blade interaction with the strong vortices would cause the most noise so they were therefore the most important. Additionally, it is better to miss some medium or low strength vortices than to allow false positives through because the location of the vortex center is not weighted on the strength of the vortex and false positives are difficult to detect.

A probability density function of the measured locations of the vortex centers is plotted in Figure 44a) below. The probability represents the chances of seeing a vortex in a 19.5 mm^2 area in any measurement taken during this experiment. This resolution is a consequence of the spatial resolution of the velocity measurement itself.

This analysis confirms the qualitative observation from instantaneous velocity measurements that the vortices are primarily located directly beneath the blades at their point of closest approach. It also shows that the vortices tend to be more often located on the downstroke than the upstroke side. Figure 44b) shows the averaged Q-criterion for the 5000 velocity field measurements recorded in this case and also suggests that the vortices on the downstroke side might be stronger than those on the upstroke side. In the unyawed case the total integrated probability, or the chance of finding at least one vortex in the tip gap region for any measurement of this thrust case is 77.56%. The probability of finding at least two vortices is 28.00% and that of finding three vortices is 0.54%. Overall the spatial distribution and the mean Q-criterion agrees well with the streamwise Reynolds stress in the tip gap (Figure 40a) which found that the highest level of velocity fluctuations was also skewed toward the downstroke side.

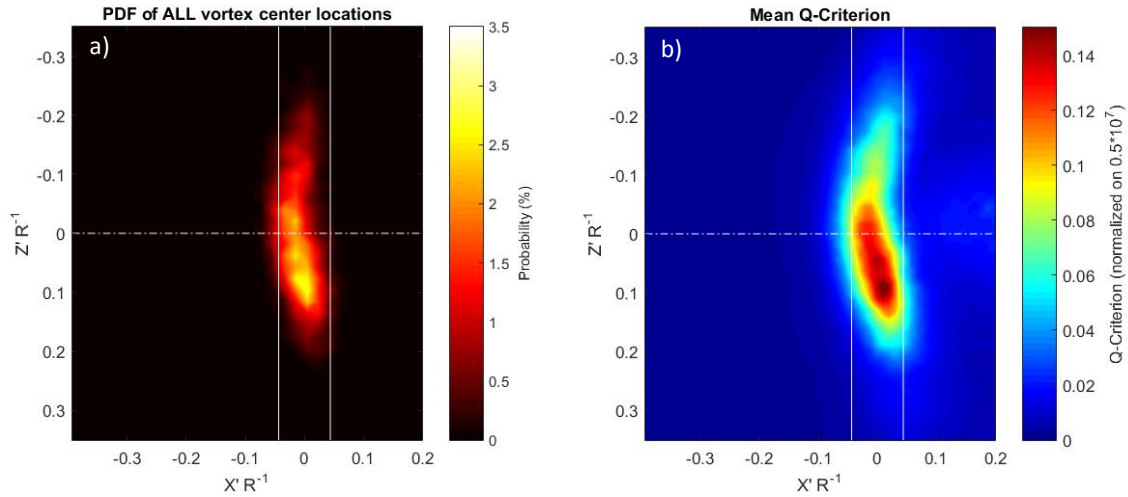


Figure 44: Quantification of the location of vortices in the tip gap in a) a probability density function and b) the mean of the Q-criterion. Each point represents the probability of finding a vortex center in a 4.43mm by 4.43mm area surrounding that point.

The probability density function is broken up into the components representing clockwise and counterclockwise eddies in Figure 45a) and b) respectively based on the sign of the vorticity at each vortex core. Separating them in this way shows that the clockwise vortices tend to be found on the upstroke side while the counterclockwise vortices tend to be found on the downstroke side. This is consistent with the two counter rotating vortices seen in the mean flow for this case, shown in Figure 37c). The integrated probability of finding a clockwise vortex in the tip gap in any arbitrary measurement is 39.74% and the integrated probability of finding a counterclockwise vortex is 66.36%.

It is significant that the counterclockwise vortices are in general more likely to be seen in the tip gap. In the context of that observation it should be noted that the sign of the bound circulation on the blades, projected into the measurement plane is counterclockwise as well. If the vortices observed in the tip gap were caused only by the flow reversal it is expected that clockwise and counterclockwise vortices would appear in approximately equal prevalence. The increased prevalence of the counterclockwise oriented vortices then suggests that they are partially the result of blade tip vortices shed by the blades passing close to the wall. Since vortex lines in a fluid do not end, and there is a disproportionately large number of counterclockwise vortices passing through the measurement plane, they are likely coming from the blade tip and connecting with the wall in the tip gap region.

The probability density functions for each phase of the rotor's rotation were also explored in an effort to determine if the spatial locations of the vortices tended to depend on the angular position of the rotor's blades. It was found that the spatial distribution of vortex centers and the increased likelihood of the counterclockwise vortices was relatively constant through the entire sweep of rotor phase angles. This indicates that the uneven distribution is not caused by an asymmetry associated with the blades approaching the wall vs moving away from the wall. This finding then supports the explanation that the counterclockwise vortices are fed by the blade tip vortex in addition to the flow reversal in the tip gap. A series of plots of the probability density functions and mean Q-criterion for phases throughout the rotor's rotation can be found in Appendix C.

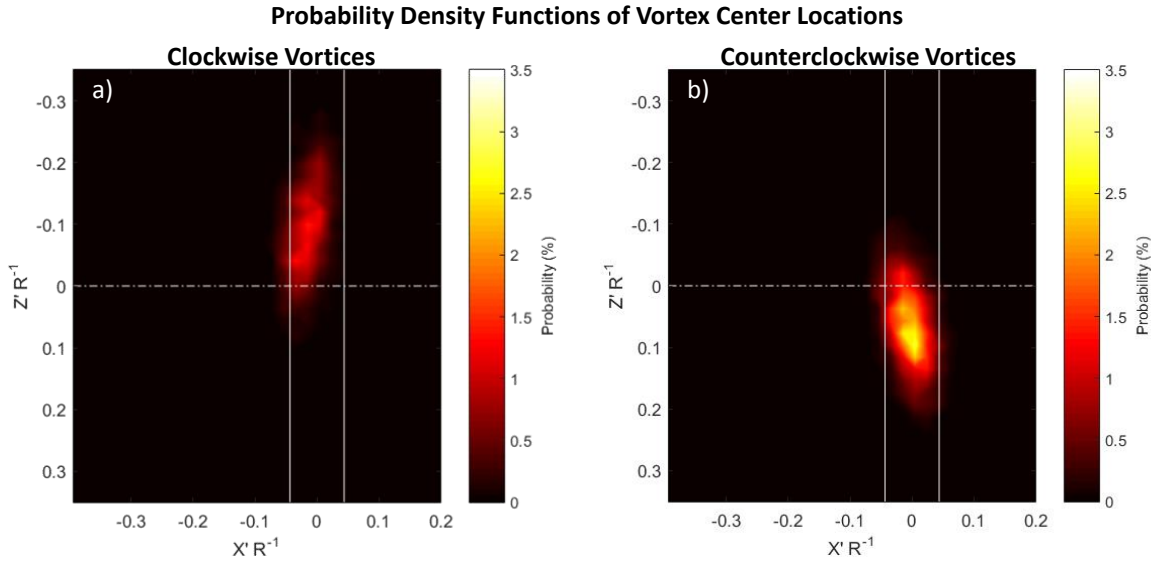


Figure 45: Probability Density Function of the locations of vortex centers relative to the rotor blades and sorted into clockwise and counterclockwise vortices.

3.3 The Effects of Yaw on a Thrusting Rotor

In this section the acoustic and tip gap flow effects resulting from yawing the thrusting rotor are discussed in detail. The geometric results of yawing a rotor near a wall are first presented for background information and to help explain some of the flow effects that were observed. Then the effects of yaw on the inflow distortion are discussed. That is followed by separate discussions of the non-flow-reversal regime and the flow-reversal regime on the farfield noise, and tip gap velocity measurements, as a function of rotor yaw.

3.3.1 An Explanation of the Geometric Consequences of Rotor Yaw

Yawing the rotor with respect to the freestream creates off-design operating conditions that change for each blade as it rotates. Yawing creates local cyclic variations in the speed of the tip-relative freestream velocity seen by the blade since it is now moving back and forth in the freestream direction as well. This contributes to local angle of attack variations for each blade section over the course of its rotation. However, a larger factor in the angle of attack variation of a blade section comes directly from the geometry of yawing the rotor.

At a fixed point in the blade rotation, take the point closest to the wall. Yawing the rotor will either increase or decrease the blade angle of attack of that blade section at that point in the rotation. This effect is illustrated in Figure 46 below. In the case of this experiment, where the rotor interaction with the boundary layer and other near-wall effects is of primary concern, yawing the rotor in the positive direction results in a decrease in blade section angle of attack near the wall. The inverse is also true, yawing the rotor in the negative direction results in an increase in the local blade section angle of attack near the wall relative to the unyawed case.

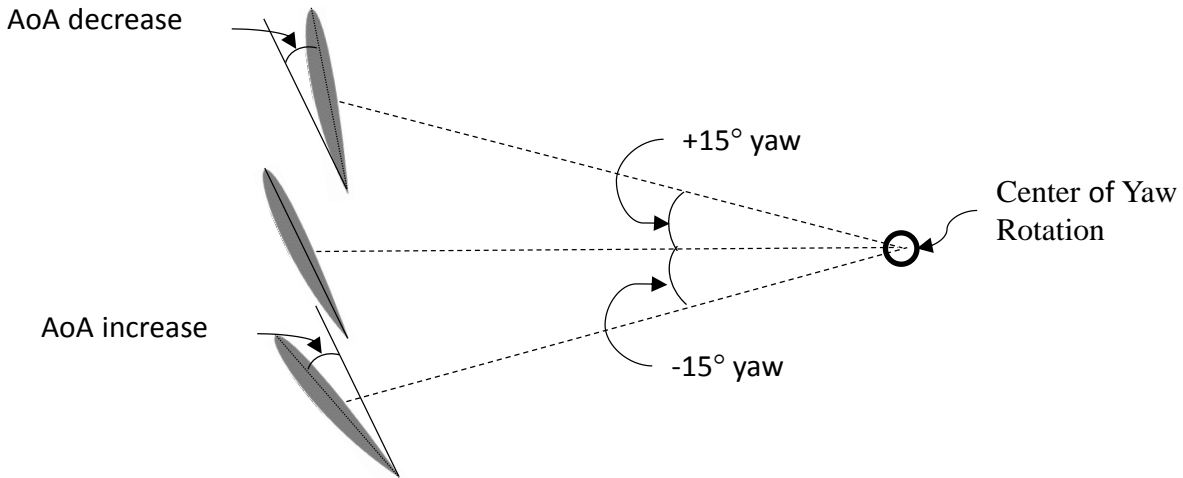


Figure 46: Illustration of the change of blade section angle of attack as it passes by the wall solely due to rotor yaw.

The drawing above serves to illustrate the situation in an intuitive way however it also slightly oversimplifies the effects of yawing the rotor on the blades nearest the wall. When the rotor is yawed at -15° the blade is also moving upstream due to the angle of the rotor blade disc, and the opposite is true when the rotor is yawed at $+15^\circ$. This effect is shown in the drawing of the velocity triangles that the blade sees in Figure 47 below. It is difficult to see the actual undistorted angle of attack, α , change in these drawings but for the moderately thrusting case ($J = 1.05$, 2500RPM) yawing the rotor from $+15^\circ$ to -15° creates an increase of 1.49° . At the high thrust case ($J = 0.58$, 4500RPM) yawing the rotor over the same range only creates a difference of 0.48° in the geometric angle of attack. This is due to the increased dominance of the rotational component in determining the blade angle of attack and will be important in the results presented below.

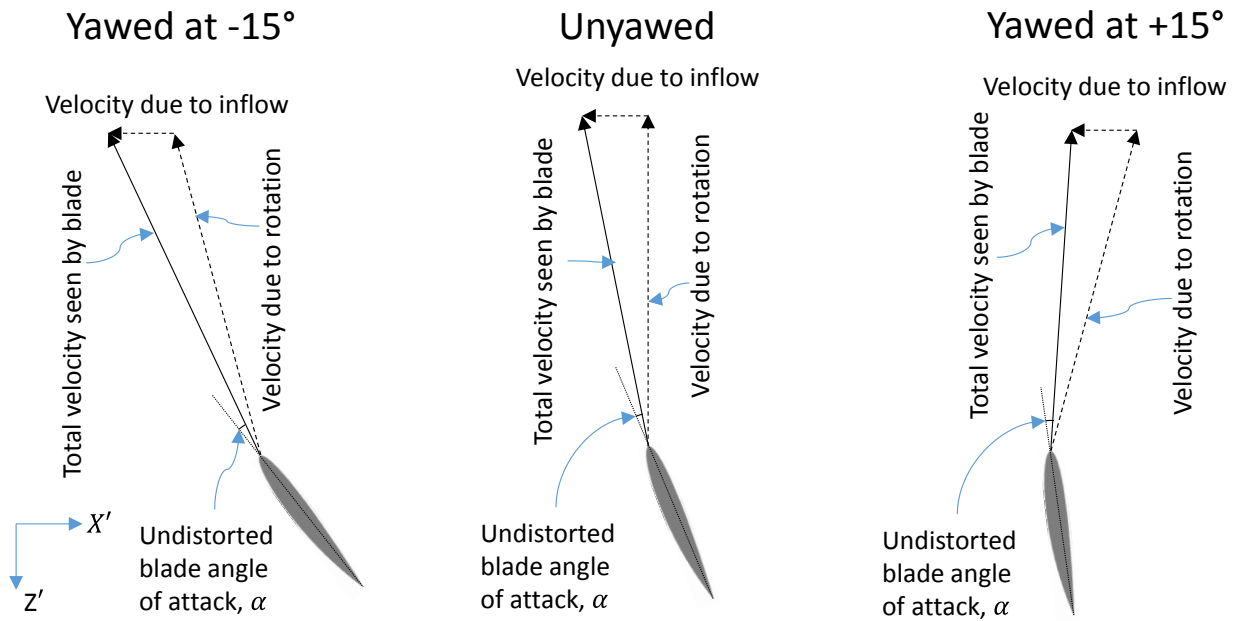


Figure 47: Diagram of velocity triangles seen by the blade at the range of yaw angles considered in this experiment. Note that they are drawn relative to the primed coordinate system which is shown in the bottom left of the figure.

This effect was found to provide explanations for many of the effects that were observed to occur as the rotor was yawed. The first was the obvious asymmetry in the inflow with respect to yaw that could be seen in the mean wall pressure measurements and tip-gap mean velocity measurements. The near-wall blades in the negative yaw cases create more thrust in the boundary layer than when unyawed. The opposite is true for the positive yaw cases and these differences can be seen in the mean wall pressure and mean flow through the tip gap, Figure 48 and Figure 49, below at each of three representative thrust cases shown.

3.3.2 A Discussion of Flow Measurements as a Function of Rotor Yaw

First the effects of yawing the rotor on the mean flow near the wall and in the tip gap will be discussed. This will lead into an explanation of two distinct flow and acoustic patterns that will then be discussed in the subsequent sections.

The mean flow near the wall will be explained first using the mean wall pressure measurements and then this will be compared to and verified with the mean flow measurements in the tip gap. In the zero thrust case the asymmetry in the inflow wall pressure, between Figure 48a) and e), and the tip gap velocity measurements, between Figure 49a) and c), is especially pronounced. This is because when this case is unyawed the blades are actually producing a slight blockage effect, as seen in Figure 48c). However in the negative yaw case, the blades near the wall are at an increased local angle of attack and the low pressure region ahead of the rotor there, Figure 48a), suggest that that part of the rotor is actually slightly thrusting. The converse is true in the positive yaw case, Figure 48e), where the high pressure region expands suggesting that the blockage effect is increased. The mean flow through the tip gap, Figure 49a) through c), suggests the same conclusions. Specifically when compared to the freestream the increased velocity ahead of the rotor in Figure 49a) and the decreased velocity ahead of the rotor in Figure 49c) indicates that the yaw causes a decrease and increase respectively in the blockage effect caused by the rotor near the wall.

A similar same effect happens in the moderately thrusting case. Yawing the rotor in the negative direction causes a larger low pressure region upstream of the rotor when compared to the unyawed case, Figure 48f) vs h). This implies that the rotor thrust near the wall is increased as the local blade angle of attack there increased. This is also supported by the larger velocity differential through the tip gap when compared to the unyawed case, Figure 49d) vs e). As before, the opposite is true for the positive yaw case. When the moderately thrusting rotor is positively yawed, the upstream low pressure region is weaker, Figure 48j), and the velocity differential is less, Figure 49f), than the unyawed case. The velocity differential along the centerline in the measurement region was 27% of freestream for the -7.5° yaw case, 20% of freestream at 0° yaw, and 15% of freestream at $+7.5^\circ$ yaw. As first explained in §3.2.1 the slowing of fluid through the tip gap for the thrusting case is believed to be due to the contraction of the streamtube downstream of the rotor and the blade wakes in the tip gap for the moderately thrusting case, which increase in strength proportionally to the pressure difference across the bladed. A larger velocity differential in the tip gap therefore indicates that the rotor is producing more thrust in that region.

Results for the same yaw angles at the highest thrust condition show a very different story. The mean wall pressure distribution in Figure 48k) through o) shows a strong low pressure area directly upstream of the rotor independent of its yaw angle. The low pressure region stays upstream of the rotor and slightly toward the $Z'/R = 0$ line as the rotor yaws. The minimum of the low pressure region is 0.4 rotor radii upstream of the front of the rotor face in the unyawed case, Figure 48m). In each of the $\pm 15^\circ$ yaw cases the minimum is approximately 0.3 rotor radii upstream along the axis of rotation so it is slightly closer to the rotor face but the location is almost exactly symmetric with respect to yaw in terms of location. The magnitude of the minimum pressure coefficient upstream of the rotor is larger for the yawed cases than

for the unyawed case. Specifically, it is -0.46 and -0.40 for the -15° and $+15^\circ$ cases respectively compared to -0.37 for the unyawed case.

Mean velocity flow maps show that the flow reversal pattern changes dramatically between the unyawed cases and the $\pm 7.5^\circ$ cases. In the unyawed case, Figure 49h), the flow reversal occurs almost symmetrically about the $Z'/R = 0$ line. However in the yawed cases, Figure 49g) and i), the flow reversal turns into a cross flow that is traveling in the same direction that the rotor is yawed directly downstream of the rotor blades. The approximate magnitude of this crossflow is $0.80 U_\infty$ and $0.60 U_\infty$ for the negative and positively yawed cases respectively, compared to $0.42 U_\infty$ for the unyawed case. The crossflow appears to feed into a stagnation region that extends under the rear part of the downstream side of the rotor and trails off out of the measurement region. This is in contrast to the flow reversal feeding a small stagnation region directly under the center of the rotor in the unyawed case. It should also be noted that, as with the mean wall pressure results, the location of the features in the crossflow pattern appears very closely symmetric with respect to yaw.

The reason that the high thrust case shows less variation with yaw angle is that as the rotor spins more quickly the blade angle of attack becomes dominated by the rotational component. This makes the variation caused by the geometry of the rotor with respect to the inflow, as explained in Figure 46 above, far less significant. The opposite is true at low rotation rates, which is why the inflow pressure field changes significantly for the zero thrust case.

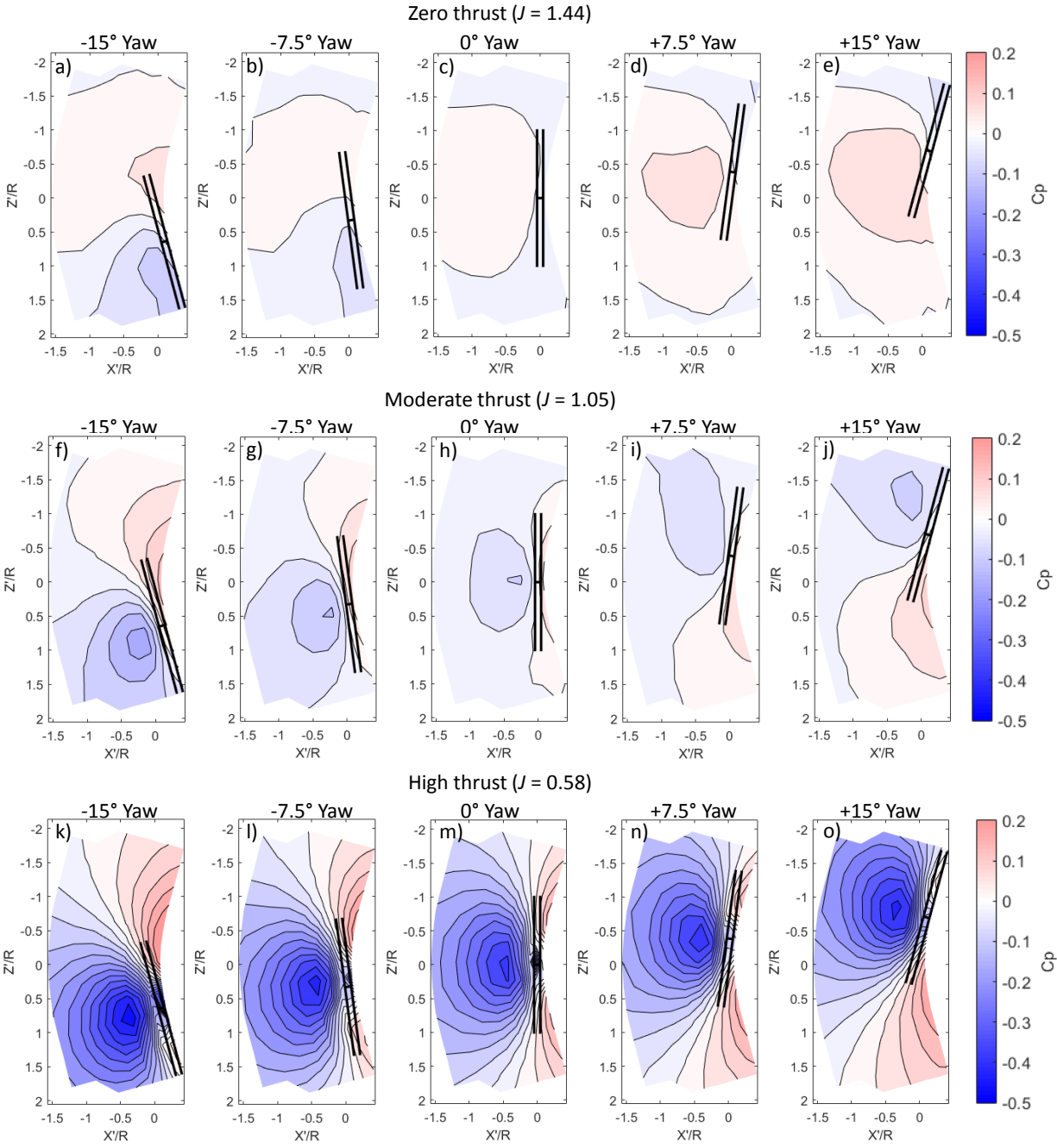


Figure 48: Mean wall pressure measurements as a function of rotor yaw angle for three representative advance ratios, zero thrust, moderate thrust, and high thrust. Note that each contour line is a constant 0.0368 C_p to emphasize the magnitude of the low pressure region in the high thrust case. Also note the asymmetry with respect to yaw and that it is more significant at higher advance ratios (lower rotor rotation rates).

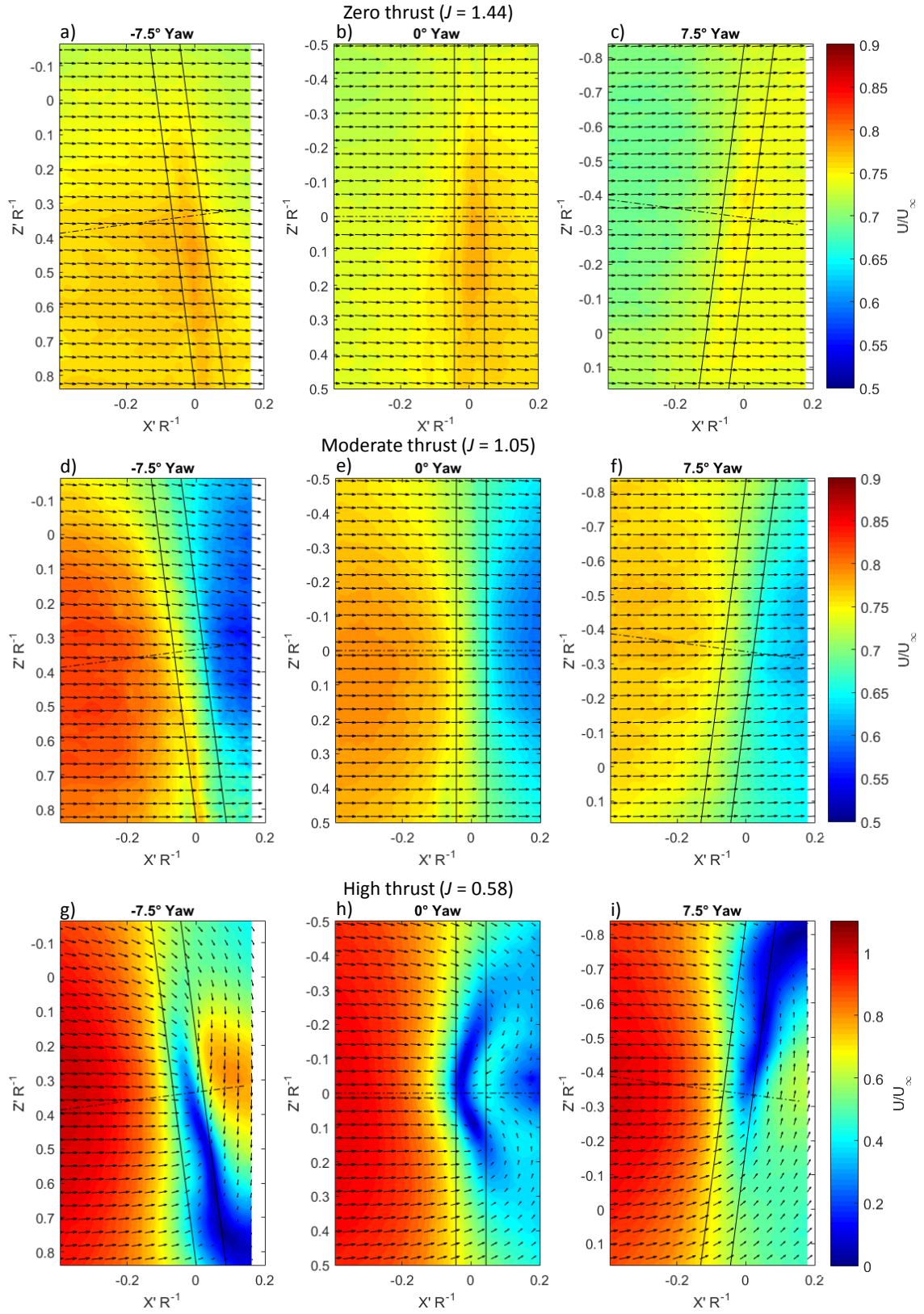


Figure 49: Mean velocity contour maps through the tip gap for the three representative thrust conditions ($J = 1.44$, 1.05 , and 0.58) and at three rotor yaw angles (-7.5° , 0° , and $+7.5^\circ$).

3.3.3 Evidence of the Stagnation Region in Mean Wall Pressure Measurements

Upon further examination of the mean wall pressure fields it was found that there was a reversal in the pressure gradient directly under the rotor blades in the high thrust cases. An example of this reversal and secondary lower pressure region under the blades was discussed in §3.2.2.2 and is shown in Figure 36e). In the unyawed case, this reversal was found for all $J < 0.65$. Thus this is an indication that the same flow reversal seen in the mean velocity field at $J = 0.58$ was also present for runs where $J < 0.65$. Noting the presence of this feature at all yaw angles examined in this experiment allowed the construction of a “front” where it is believed that the conditions for the flow reversal were met.

This front is plotted with the circles in Figure 50 below. The dotted horizontal and vertical lines indicate yaw angle and advance ratio conditions from the test matrix and the filled region represents the conditions where the pressure gradient reversal was observed. The pressure gradient reversal appears to show up at higher advance ratios, lower rotation rates, in the negatively yawed cases. This is believed to be related to the higher angle of attack of blades sections near the wall due to the geometry of the negatively yawed rotor.

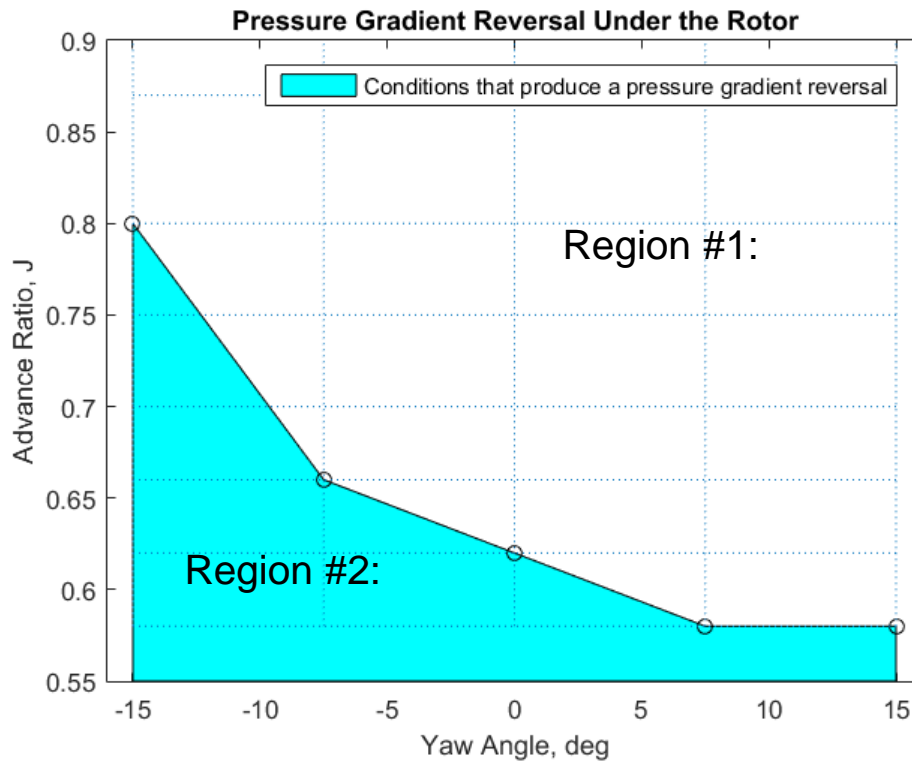


Figure 50: Yaw and advance ratio conditions at which pressure gradient reversal was observed on the wall below the rotor. Note that negative yaw increases the local blade angle of attack near the wall.

The rest of this section will be broken up into two types of cases; those where this pressure gradient reversal was not observed (Region #1), implying that there is no flow reversal, and where it was observed, (Region #2), implying that flow reversal could be present. The cases without the pressure gradient reversal are addressed first to show the effects of yaw on haystacking noise due to turbulence distortion. Using the unyawed case as a baseline, the thrusting, non-flow reversal region were defined for experiment as $0.70 \leq J \leq 1.31$. Following that discussion, the effects of the blade interaction with the inferred flow

reversal as a function of yaw are explored. Again using the unyawed case as a baseline, this region was loosely defined as where $J < 0.66$.

3.3.4 Acoustic Effects of Yaw in Region #1: No Pressure Gradient Reversal

Comparing the spectra from the same thrust condition across yaw angles, allows the effects of yawing the rotor on the haystacking pattern to be explored. For the interested reader, the contour plots of the spectra as a function of advance ratio for each of the rotor yaw conditions, like shown in Figure 33 for the unyawed case, are presented in Appendix B, in Figure 73 and Figure 74, at the end of this thesis. However this section will focus on the two acoustic patterns in regions 1 and 2 as introduced above.

A typical comparison that clearly illustrates the yaw angle dependence of the haystacking peaks in Region #1 is shown below in Figure 51. This is a thrusting condition so it clearly shows the haystacking pattern, but the pressure gradient reversal was not seen at any yaw angles at this thrust level.

As explained before, yawing the rotor in the negative direction increases the angle of attack of the blades near the wall and as a result increases the thrust in that region. Since this region is near the wall, this acts to increase the stretching and organization of boundary layer turbulence which causes an increased response in the farfield spectra at frequencies slightly above the blade passage frequency. The opposite is true for the positive yaw case. This effect causes an increased haystacking response of the order of 5 to 10 dB for the -15° case when compared to the $+15^\circ$ case. The yaw cases in between show a clear monotonic decrease as the yaw angle increases at frequencies above the first haystack peak. The same arrangement is generally true for the low frequencies, below the 5th blade passage frequency. This conclusion is bolstered by the discussion in §3.3.2 above and the observation that the velocity differential across the moderately thrusting rotor was largest for the negatively yawed case and smallest for the positively yawed case. This effect can be seen for $J = 1.05$ in Figure 49 d) through f).

It should also be noted that trailing edge noise shows up here in the higher frequencies, from 6kHz to 20kHz. The trailing edge noise levels appear to be relatively constant as a function of yaw angle from -15° to 0° yaw in the example shown here but then increase as the rotor is yawed toward $+15^\circ$. The exact reason this occurs is not currently fully understood. When all the spectra are plotted together for each operating condition at all of the advance ratios, the high frequency regions of trailing edge noise appear to spread out in the advance ratio dimension. This is shown in Figure 73 and Figure 74 in Appendix B.

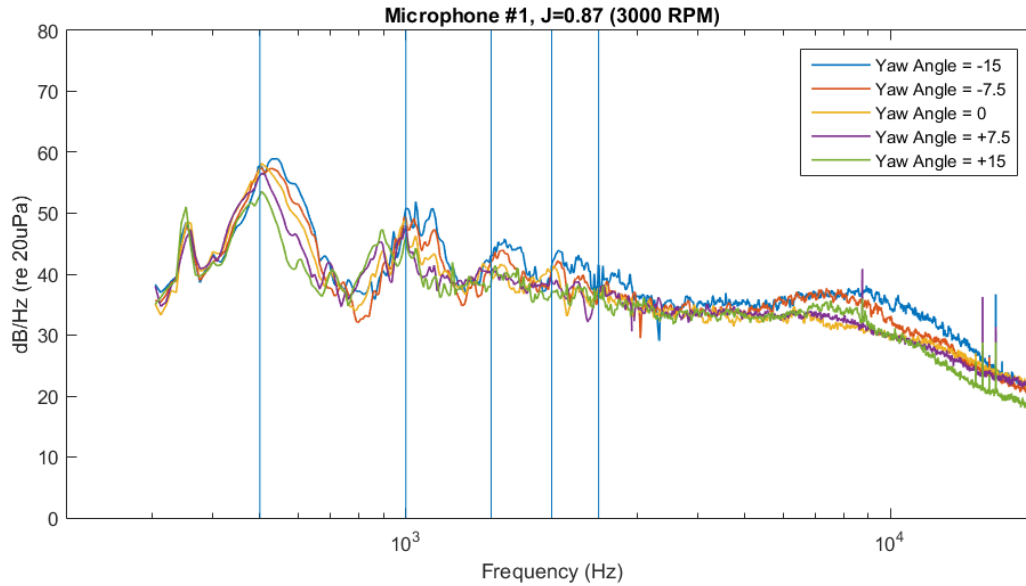


Figure 51: Comparison for spectra for a high thrust condition, without the inferred flow reversal, at all yaw angles studied. The vertical lines indicate the first five harmonics of the BPF for reference to the haystacking peaks.

3.3.5 Acoustic Effects of Yaw on Region #2: Pressure Gradient Reversal Observed

When the rotation rate of the rotor is increased however we see a different pattern emerge in the haystacking peaks. At the highest thrust conditions the “haystack” peaks shift to line up exactly with the BPF, instead of being centered on a slightly higher frequency, and they simultaneously become less rounded and very sharp. The other change is that the unyawed case becomes the loudest at the haystacking peaks, instead of the -15° yaw case above. An example of these effects is shown below in Figure 52a) for $J = 0.62$. Although it is difficult to see because the peaks are so narrow, the unyawed case is 6dB louder than the -15° yaw case and 9dB louder than the $+15^\circ$ yaw case at the first blade passage frequency. The unyawed case is louder than or approximately as loud as all the other cases at the blade passage frequency harmonics up until approximately the 8th harmonic.

Another case that exhibits this trend is the highest thrust case examined in this study, $J = 0.58$. This case was observed to have the pressure gradient reversal underneath the rotor at all yaw conditions and the unyawed case was also observed to have the strong flow reversal in the tip gap, Figure 49h). The far field spectra for this highest thrust case, Figure 52b) shows that the unyawed case is loudest at the BPF. At the first blade passage frequency it is dominant by 5dB and 7dB over the -15° and $+15^\circ$ yaw cases respectively. The same is the case at all other BPF except the second. The narrow spikes between the first and second BPF are spaced at exactly 13, 14 and 15 times the rotor shaft rate and are loudest at $+15^\circ$ yaw with peaks that monotonically decrease as the rotor yaw decreases. The cause of these spike is currently unknown.

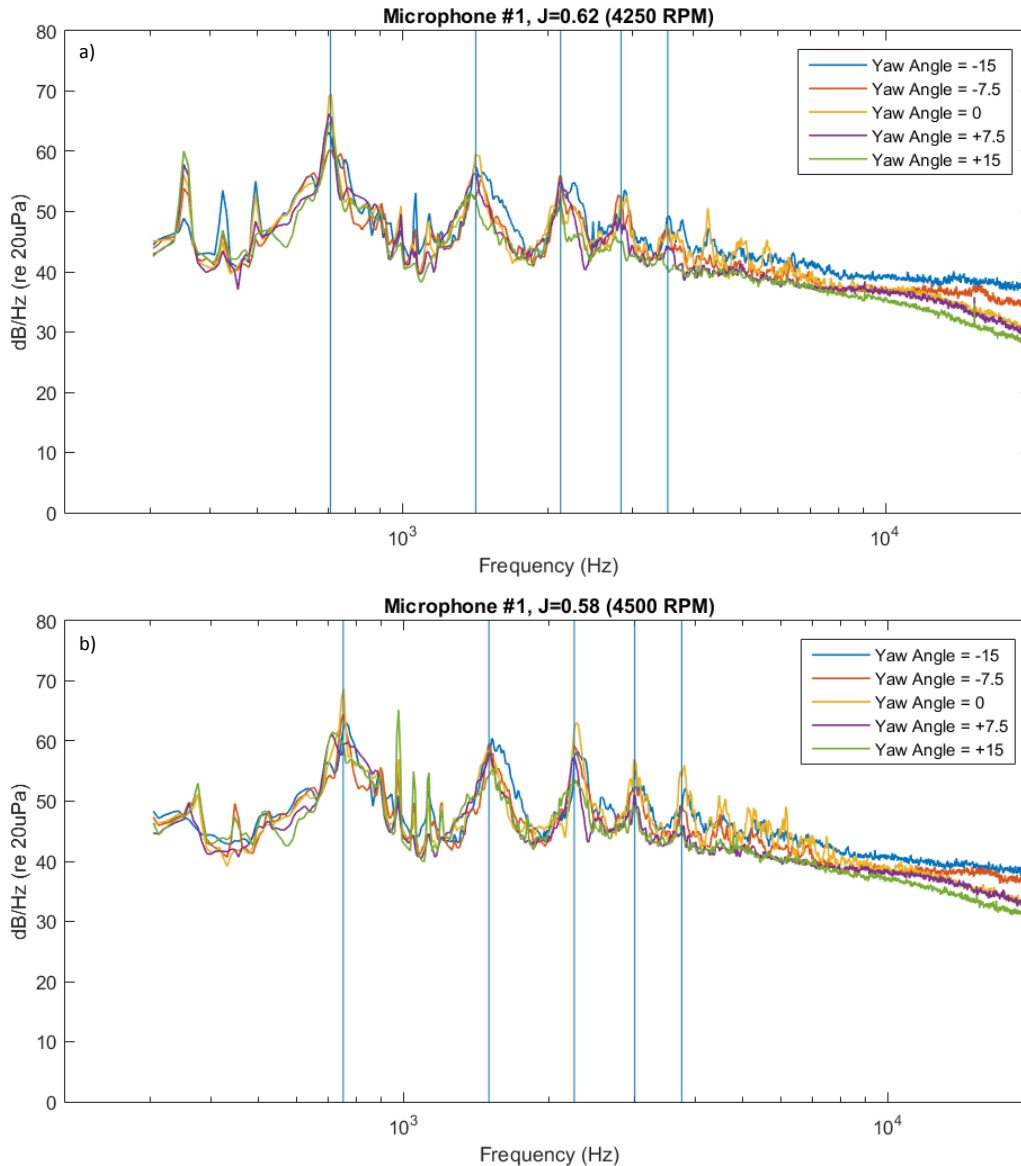


Figure 52: Comparison of spectra at all yaw angles examined for two high thrust conditions ($J = 0.58$ and $J = 0.62$ where flow reversal was inferred to have occurred).

The trend in Region #2, at the very highest thrust conditions ($J < 0.66$), of the unyawed case being the loudest at the BPF and its harmonics suggests that the blade interaction with the flow reversal is dominant over the noise of turbulence ingestion. As the rotor is yawed, the falloff of the peaks at the BPF harmonics indicates that the blades interact less consistently with the unsteady flow in the smallest part of the tip gap. This is believed to be because yawing the high thrust rotor to one side more easily allows fluid to come in around the other side to the center where it is starved because of the wall. Yawing the rotor causes a less unsteady and weaker flow pattern which results in less interaction with the blades and therefore less of a response at the BPF in the farfield acoustic spectra. A comparison of the fluctuations in the tip gap for the different yaw cases can be seen in the Reynolds stresses below in Figure 53.

3.3.6 Reynolds Stress and Phase Averaged Velocity Measurements as a Function of Yaw

The Reynolds stresses in the tip gap for the unyawed case were discussed at the end of Section 3.2.2.3 above and are reproduced for easier comparison in Figure 53c) and d) below. The maximum velocity fluctuations in the streamwise direction, Figure 53a), c) and d), are $8.5\% U_\infty^2$ and $7.5\% U_\infty^2$ for the -7.5° and $+7.5^\circ$ yaw cases respectively compared to $25\% U_\infty^2$ in the unyawed case. Put another way, the maximum τ_{11} for the unyawed case is three times larger than the yawed cases. Similarly, the maximum velocity fluctuations in the spanwise direction, seen in Figure 53b), d), and f), is also largest in the unyawed case. It is $9.1\% U_\infty^2$ and $6.4\% U_\infty^2$ in the -7.5° and $+7.5^\circ$ yaw cases, compared to $10.7\% U_\infty^2$ in the unyawed case. The maximum τ_{33} in the unyawed case are only slightly larger than the maximum found in the -7.5° case and almost double the maximum found in the $+7.5^\circ$ case.

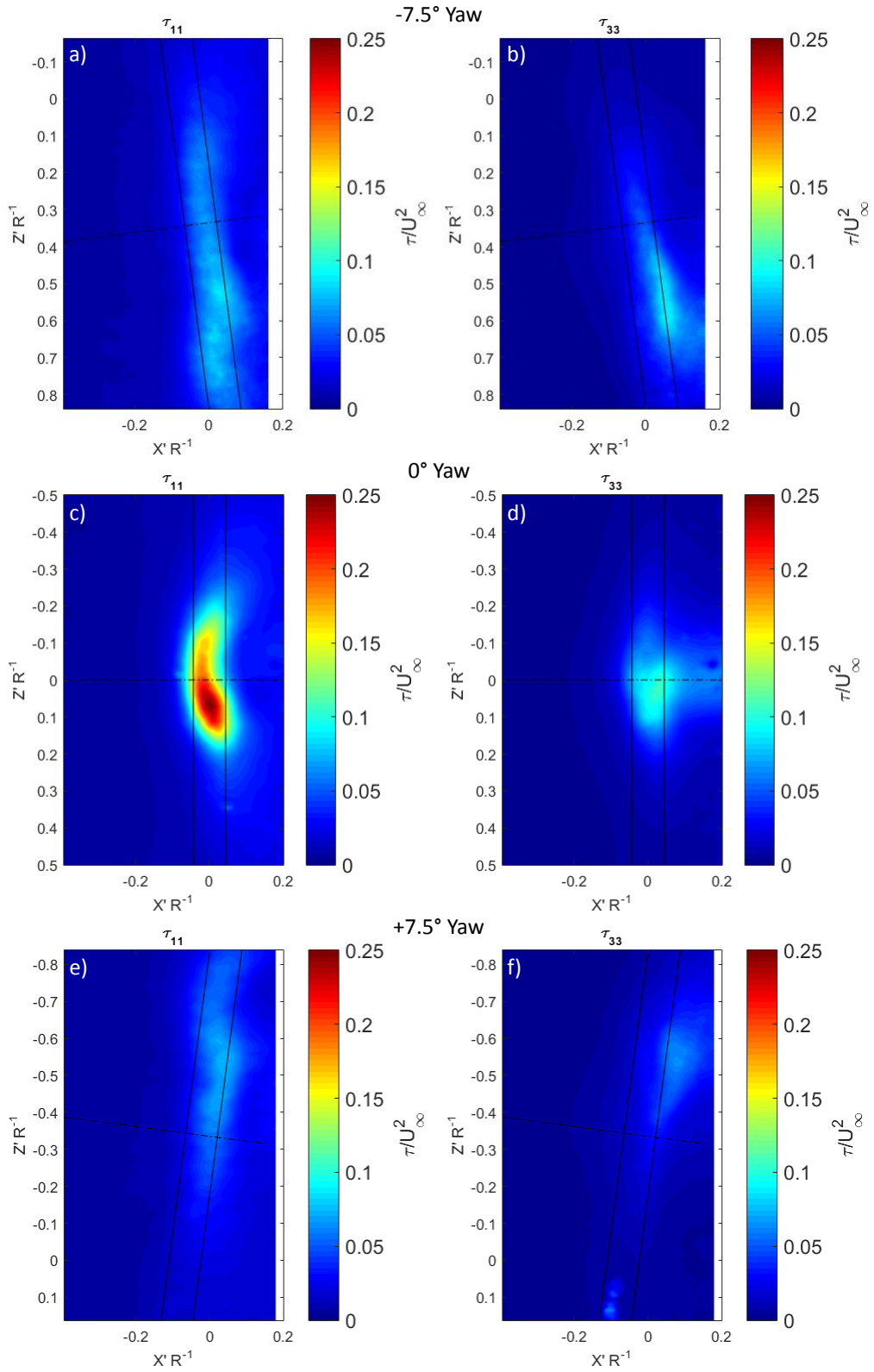


Figure 53: Normal components of the Reynolds stress tensor in the measurement plane for the $\pm 7.5^\circ$ yawed cases.

The distribution of the areas of higher Reynolds stress in the yawed cases closely matches the stagnation regions found in Figure 49g) and i). This indicates that although those look like areas of low fluid velocity in the mean, they are actually the regions of highest velocity fluctuations.

In order to better understand what happens in the tip gap when the blades from the yawed rotor pass by the wall, representative phase averaged velocity fields are plotted below in Figure 54. For the interested reader, the rest of the phases for each yaw angles are presented in Appendix B in Figure 75, Figure 76, and Figure 77. The phase average process is explained in §3.2.2.3 and each two degree increment contains approximately 50 measurements for each yawed case while the unyawed case is from over 200 measurements. Figure 54a) through c) is the -7.5° case, d) through f) is the unyawed case, which is repeated from a previous figure to provide a comparison, and g) through i) is the $+7.5^\circ$ case.

In the -7.5° case the stagnation region is on the downstroke side of the blades and appears to be swept up across the projection of the centerline of the rotor. In contrast, in the $+7.5^\circ$ case the blade appears to have minimal effect on the tip gap flow before it reaches bottom dead center. At bottom dead center however the blade appears to induce a separate stagnation region in the center of the tip gap which sweeps up and then combines with the main stagnation region located under the upstroke side of the blades and seen in the mean flow for this case. Also, in the negative yaw case the main stagnation region underneath the downstream side of the rotor extends across the projection of the axis of rotation of the rotor, where it does not in the positive yaw case.

The phase averages for the yaw cases also show that, unlike in the unyawed case, the flow reversal or crossflow is not fed by what is believed to be tip leakage into the tip gap. The crossflow behind the rotor at yaw also looks relatively independent of the blade phase, unlike the flow reversal in the unyawed case. This supports the inference from comparing the far field spectra at different yaw angles that the rotor blades in the unyawed case interact with the flow reversal more strongly than in the yawed cases.

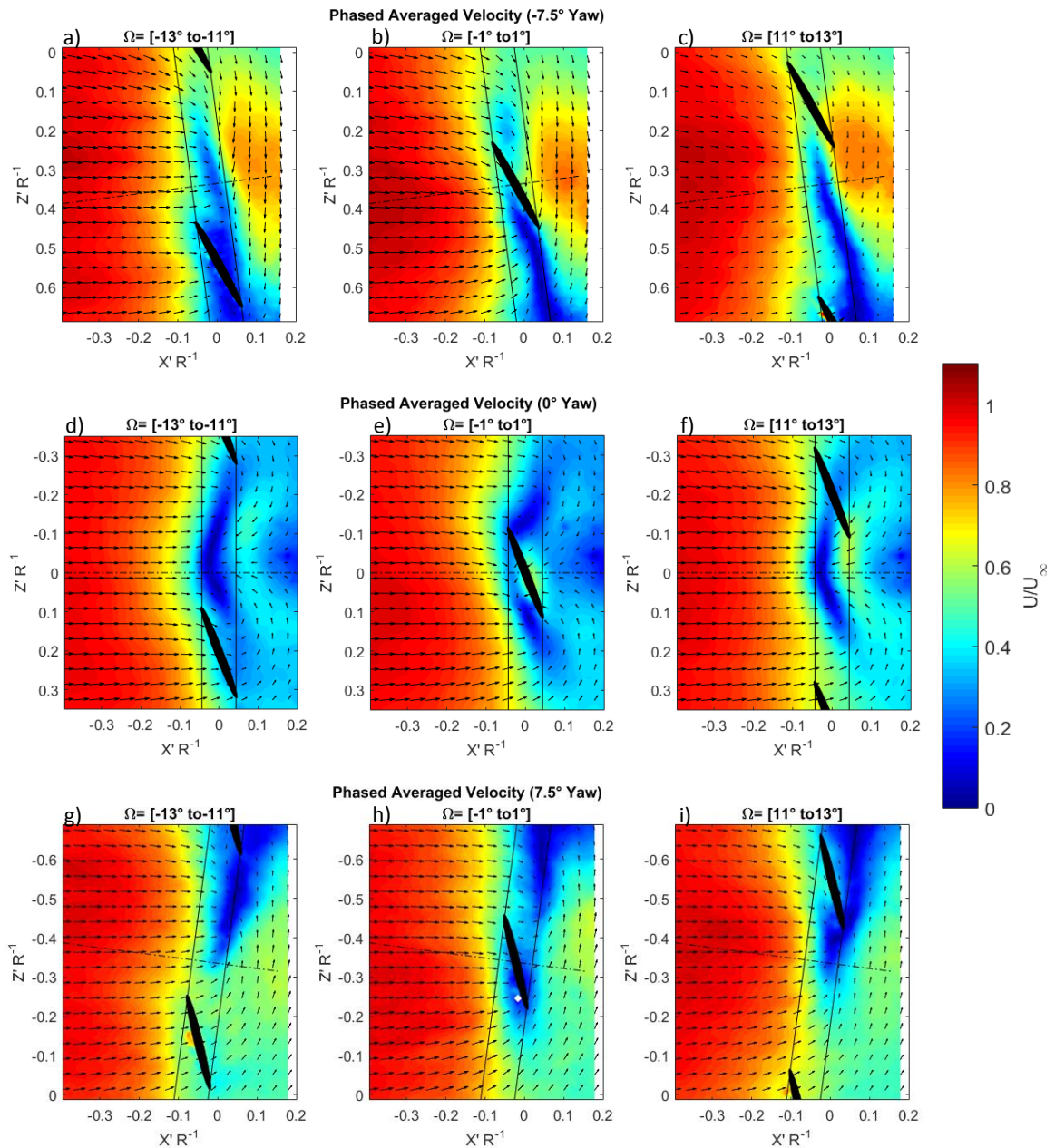


Figure 54: Representative phase averaged velocity fields for the high thrust condition ($J = 0.58$) of the rotor at yaw.

3.3.7 Vortex Identification in the Yawed Rotor at High Thrust

The same vortex identification process used in the unyawed case, and explained in detail in §3.2.3 was also applied to the yawed case. Three examples of instantaneous vector fields for each of the -7.5° and $+7.5^\circ$ cases are shown together in Figure 55 below.

The instantaneous vector fields are also plotted over contours of the Q-criterion, like the unyawed case shown in Figure 41. For the interested reader, several more typical examples of the instantaneous vector fields plotted on Q-criterion contours for each yaw angle considered, -7.5° , 0° , and $+7.5^\circ$, are shown

in Appendix B, in Figure 78, Figure 79, and Figure 80 respectively, at the end of this thesis. When the rotor is yawed it is much less likely to exhibit the strong vortex or double vortex structures often seen in the unyawed case. The Q-criterion here is plotted on the same scale as in the unyawed case (Figure 44b) to emphasize how much weaker the vortex formations in the tip gap are when the rotor is yawed. Most of the instantaneous measurements show no obvious vortex structures in the tip gap. In the few measurements that do show the presence of a vortex it is important to note that more than one vortex is very rarely seen, the double counter rotating vortex formation seen in the unyawed case was never observed in the yawed cases.

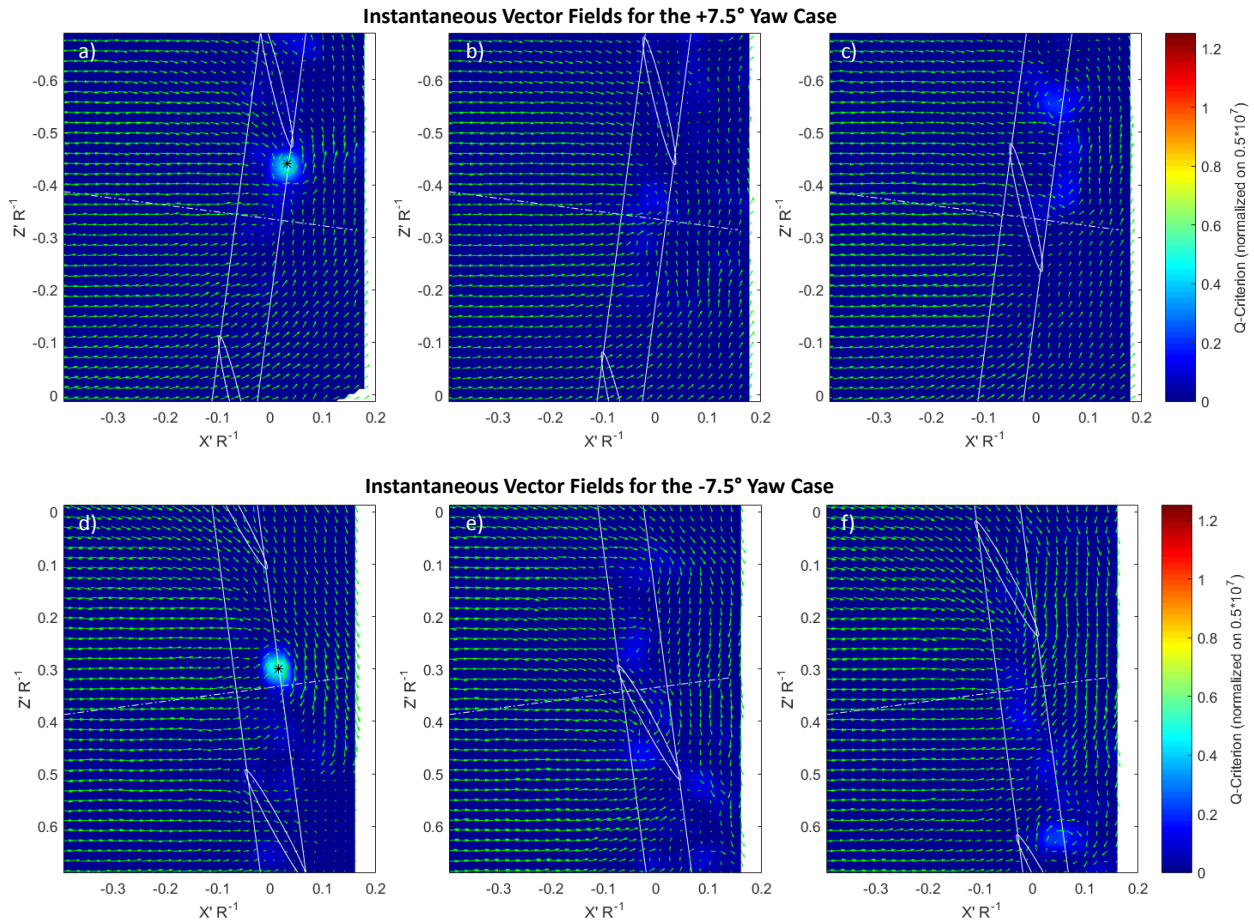


Figure 55: Representative instantaneous vector fields for the $+7.5^\circ$ and -7.5° cases at high thrust ($J = 0.58$) plotted over contours of vorticity to highlight vortex formations. Note that they are plotted on the same scale as those in the unyawed case, Figure 41, to show how much weaker the vortex formations are when the rotor is yawed.

The automated vortex identification process was run with the same cutoff criteria as used in the unyawed case in order to directly and consistently compare to the yawed cases. This analysis found that there were many less vortices in the tip gap region when the rotor was yawed as compared to the unyawed case and this difference was quantified in Table 6 below. The probability density function of the location of vortex centers for the yawed cases, and the unyawed cases to provide a comparison, is shown below in Figure 56. The probability density function is binned and normalized such that each point represents the likelihood of finding a vortex center in a spatial area of 4.43mm by 4.43mm or $\sim 20\text{mm}^2$ in any measurement that was taken.

It is significant that unlike in the unyawed case, where vortices occurred on both the upstroke and downstroke side of the rotor, the positive yaw case only sees vortices on the upstroke side and the opposite is true for the negative yaw case. When the vortices are further sorted by their handedness, the positive yaw case shows that predominantly counter-clockwise vortices are found. Again, the opposite is true in the negative yaw case where predominantly clockwise vortices are found. This is in sharp contrast to the unyawed case where both clockwise and counter-clockwise vortices are likely to be found in the tip gap.

The fact that vortices of one handedness dominate in each yawed case implies that in these cases the vortices tend to be formed by the interaction of the crossflow downstream of the blades and the mean inflow on the side the rotor is yawed toward. This is in contrast to the unyawed case where the higher prevalence of the counter-clockwise vortex suggests that the blade tip vortex tends to interact with the wall through the measurement region.

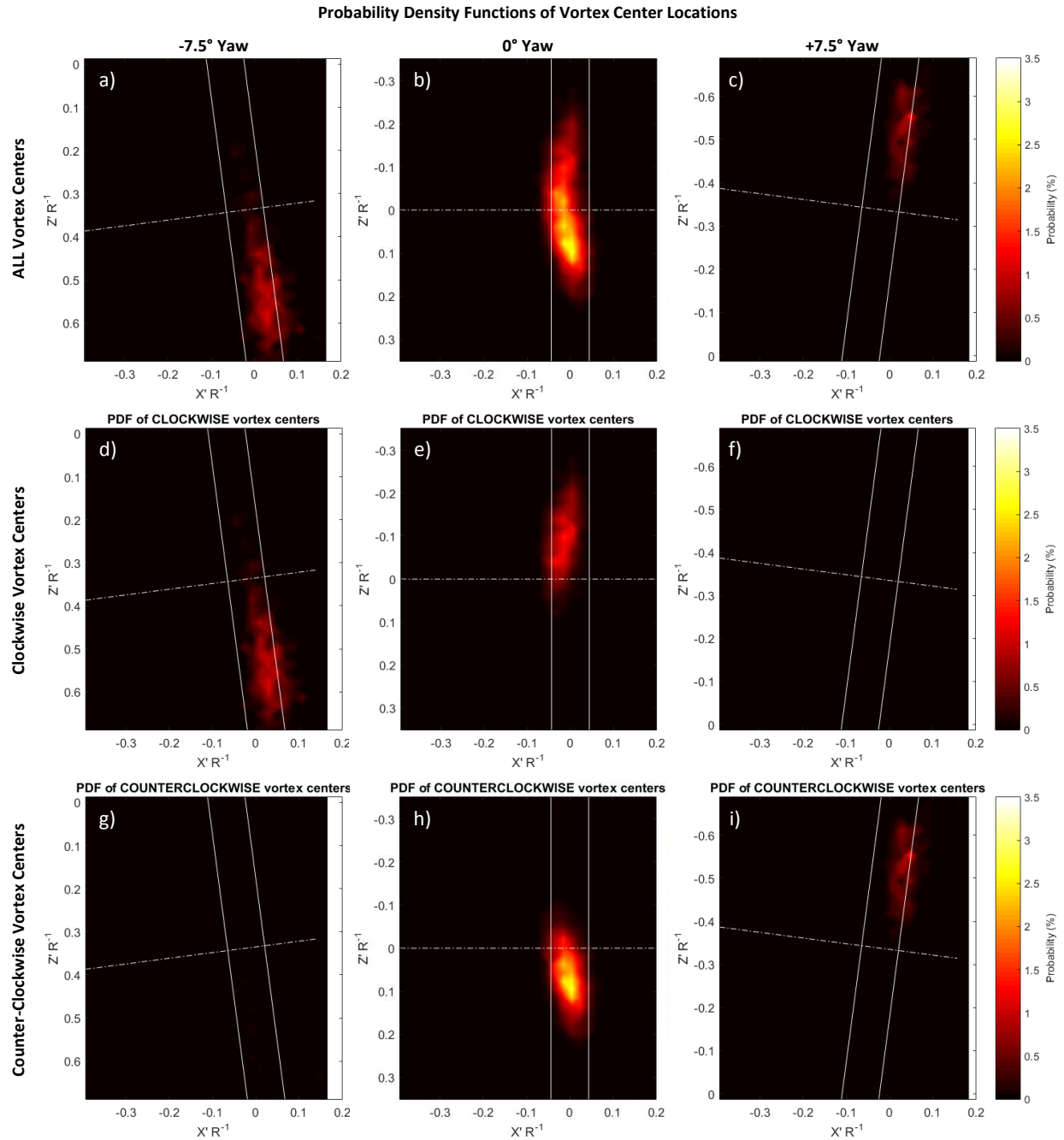


Figure 56: Probability Density Functions of the locations of vortices in the tip gap when the rotor is at high thrust ($J = 0.58$) and at yaw to the mean inflow. Each point represents the probability of finding a vortex center in a 4.43mm by 4.43mm area surrounding that point.

The total probability of finding a vortex in the tip gap region for any arbitrary measurement was computed and compiled for each handedness and yaw case in Table 6 below. Note that the probability given is the probability of finding at least one vortex of that handedness, or just one or more vortices in general for the overall probability, in any arbitrary measurement for each yaw angle. As previously commented on, the counterclockwise vortices were much more numerous in the unyawed case. The yawed cases showed a very heavy skew toward the clockwise orientation for the -7.5° case and towards the counterclockwise orientation for the $+7.5^\circ$ case. One would expect that the yawed cases might be biased

to produce vortices in opposite handedness however it would also be expected that the $\pm 7.5^\circ$ cases would do so in equal proportions. However, it is interesting to note that this is not the case and taken together the yawed cases are 7% to 8.4% more likely to produce clockwise oriented vortices than counterclockwise vortices.

Table 6: Integrated probability of a vortex in the tip gap for different yaw angles at the high thrust condition.

	-7.5° Yaw	Unyawed	+7.5° Yaw
Overall Probability	38.3%	77.56%	37.2%
Clockwise Vortex	36.7%	39.44%	9.5%
Counterclockwise Vortex	2.5%	65.58%	28.3%

Lastly, a comparison of the average Q-criterion for the unwyawed and yawed cases is presented below in Figure 57. The Q-criterion can be used as a qualitative measure of the strength of vortex-like formations at each spatial point and allows the comparison of this quantity between yawed and unwyawed cases. The average Q-criterion shows that the unwyawed case definitely tends to have the strongest vortices. The yawed cases have approximately 50% of the maximum Q-criterion found in the unwyawed case. They also show that the fluid underneath the downstream side trailing edge of the rotor has the highest average Q-criterion as opposed to the fluid at the centerline, where the blades make their closest approach to the wall, as in the unwyawed case. When compared with the $+7.5^\circ$ case, the -7.5° yaw case also had a higher average Q-criterion in this region. This suggests that yawing the rotor toward the downstroke side increases the presence and strength of vortices there due to the higher thrust near the wall.

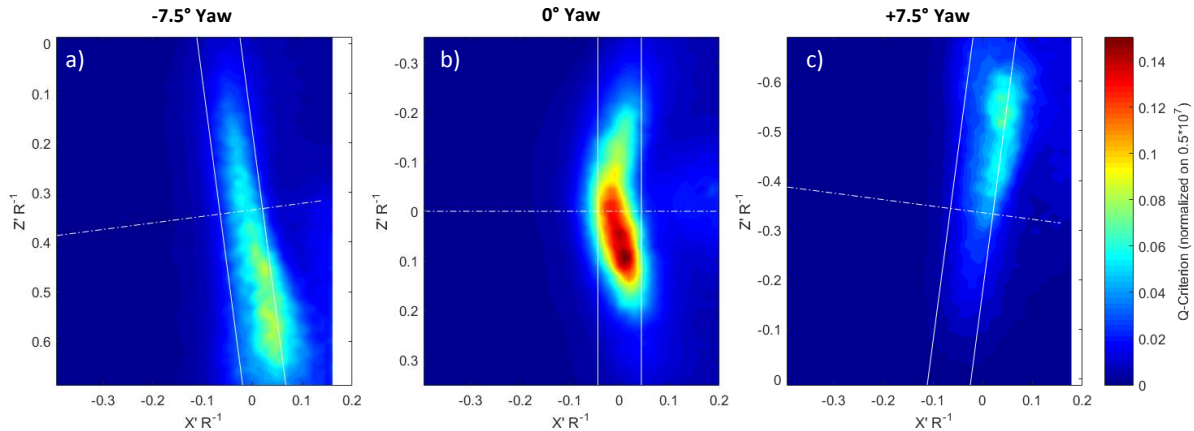


Figure 57: Average Q-criterion for the yawed and unwyawed cases at high thrust ($J = 0.58$) shows the relative strengths of the vortex flow structures found in the tip gap across yaw conditions.

The most important conclusion from this analysis though is that the unwyawed case tends to create many more vortices in the tip gap and they tend to be much stronger than those created by the rotor in the yawed case. Taken together with the acoustic results seen in Sections 3.3.4 and 3.3.5, this analysis shows that the presence of more vortices in the tip gap in the unwyawed case coincides with a larger acoustic response at the blade passage frequencies at this high thrust condition suggesting that a blade interaction with the vortices, and the increased interaction in the unwyawed condition, is responsible for the additional noise at the blade passage frequencies.

3.4 Braking Regime

The operation of the rotor in the braking regime is very different than its operation at high thrust. The measurements taken in the braking regime will be presented by first exploring the acoustic measurements in an effort to answer the questions about the relative dominance of leading edge vs trailing edge noise and the effects of yawing the rotor. Then the results of the mean wall pressure measurements and tip gap velocity measurements will be presented in an effort to explain how the inflow is distorted.

3.4.1 Acoustic Measurements of the Braking Rotor

The acoustic power spectral density from microphone 1 is shown in Figure 58 below at five advance ratios between zero thrust ($J = 1.44$) and heavily braking ($J = 2.19$) along with the background noise from the wind tunnel. Microphone 1 is the most upstream inline microphone from Table 2 above. The spectra are plotted between 200 Hz and 20 kHz and this frequency range was considered because the anechoic chambers are anechoic down to 190 Hz and the upper limit of the microphones is 20 kHz.

There is a signal to noise ratio of approximately 3-5 dB for the quietest case at all frequencies above 300 Hz except for three spikes in the background tunnel noise. The background noise for each yaw angle was subtracted from the measured acoustic spectra with a discretion level of 1 dB and as in the thrusting cases discussed previously, all subsequent spectra are presented between 300 Hz and 20 kHz and are background subtracted.

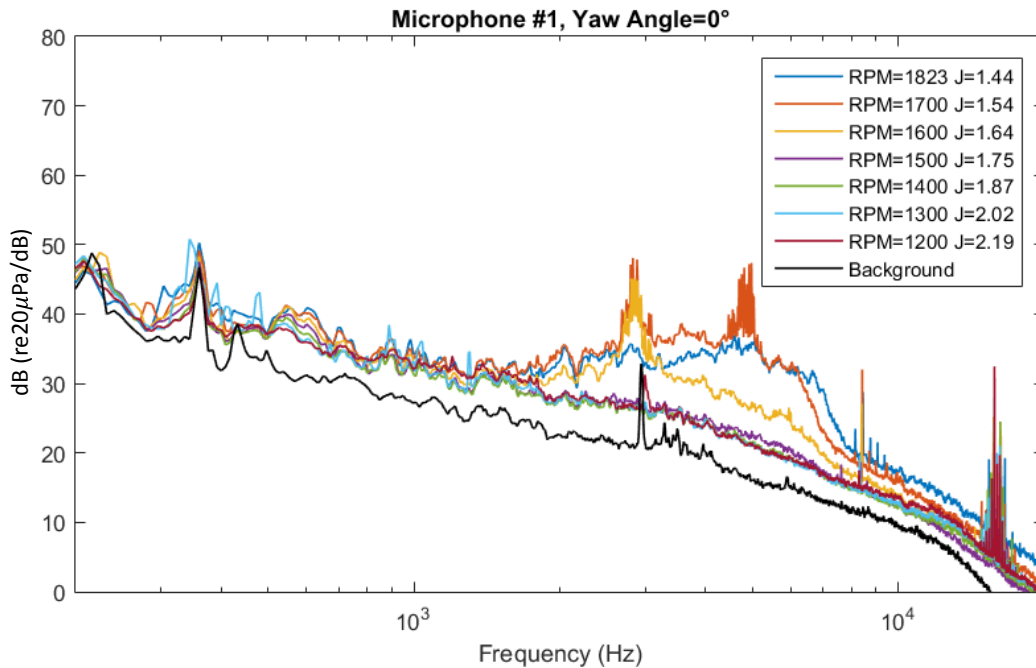


Figure 58: Spectra for the most inline upstream inflow microphone, microphone #1, for each advance ratio at 0° yaw, including background noise to show the signal to noise ratio over the whole frequency range.

3.4.1.1 Microphone Spectra for the Unyawed Rotor

In the unyawed case, Figure 59 b), the acoustic spectra display roughly the same behavior for frequencies below about 1200Hz. This portion of the spectra is believed to be predominantly caused by ingestion of the boundary layer turbulence. Spectral shapes show an approximate f^{-1} dependence here interrupted by diffuse humps at frequencies of about 350 and 500Hz. Even though these frequencies are of

the same order as the blade passing frequency and its first harmonic (BPF = 304 Hz at $J = 1.44$ and 200 Hz at $J = 2.19$), the frequency of the peaks shows no evidence of varying in proportion to the rotor speed associated with the advance ratios. We therefore conclude that these are not haystacking peaks associated with blade to blade correlation of the turbulence of the type seen at lower advance ratios (Wisda, 2015). Instead, the spectral levels show a gradual decline as the advance ratio is increased, the $J = 2.19$ spectrum sitting about 6dB below that for $J = 1.44$. This drop is quite close to that predicted (-6.9 dB) if we assume that the sound spectrum level is reduced as the 5th power of the tip relative flow speed, as would be expected for leading edge noise.

At frequencies between 1500 Hz and 6 kHz, the spectra measured at advance ratios greater than $J = 1.75$ appear to continue the behavior seen at lower frequencies, characterized by a f^{-1} dependence and a gradual decline in levels with decreasing rotation rate. Those measured at $J \leq 1.64$, however, display a broad hump that raises spectral levels at 5 kHz almost 15 dB above those seen at other conditions. This feature is believed to be the result of trailing edge noise from the rotor-blades enhanced by laminar or transitional blade boundary layers and/or vortex shedding. These conditions occur at low Reynolds numbers and angles of attack. Blade chord Reynolds number is approximately 160,000 at these advance ratios. Interestingly, the second lowest advance ratio ($J = 1.54$) has the highest sound levels over this frequency range. This may be because the $J = 1.54$ case has an angle of attack distribution that is more conducive to transitional or laminar trailing edge noise generation. The cause of the two rooster-tail peaks in the spectra for $J = 1.54$, centered at approximately 2.8 kHz and 4.8 kHz, is not fully understood at this time.

Hersh *et al.* (1974) observed boundary layer vortex shedding noise from an airfoil centered on Strouhal numbers of between 0.24 and 0.31 based on trailing edge thickness augmented by both trailing edge boundary layer thicknesses. They found signs of shedding to occur despite the fact that both boundary layers were believed turbulent at the trailing edge. For the present rotor, a frequency of 5 kHz, the tip relative flow velocity of 45 m/s (as at $J = 1.54$) and a Strouhal number of 0.28 imply an effective trailing edge thickness of approximately 2.5 mm, which is a seemingly reasonable value given the maximum blade thickness is only 4.8 mm.

The tonal spikes that occur in each spectrum around 8.5 kHz and then between 14 and 17 kHz are believed to be noise related to motor whine. They were investigated and found to predominantly show up in lower signal to noise ratio cases over the entire range of conditions tested. They were also found to be spaced at exactly ten times the motor shaft rate for each different case. The rotor has ten blades which would imply that it was related to the blade passage rate however the motor also has ten poles so it is difficult to pin down the source of this high frequency tonal noise. The bearings used on the shaft have nine balls so they could be eliminated as the source.

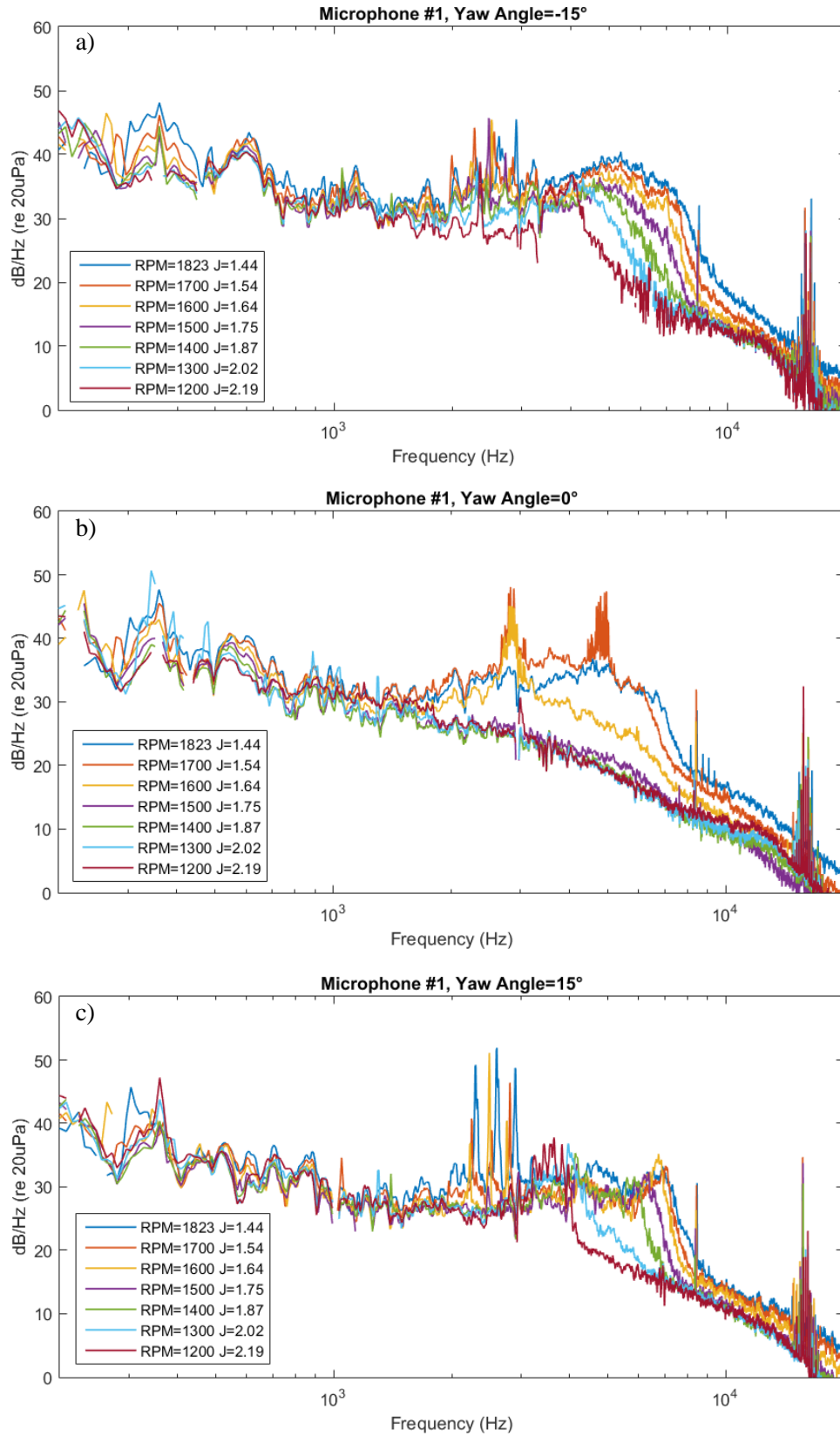


Figure 59: Background subtracted acoustic spectra as a function of advance ratio and frequency from inflow microphone #1.

3.4.1.2 Acoustic Spectra for the Yawed Rotor

The spectra for the same seven advance ratios when the rotor is yawed at -15° are shown in Figure 59 a). The spectra at low frequencies (<1500 Hz) appear quite similar to those at zero yaw with the exception that the reduction in spectral levels with increase in advance ratio is less clear at frequencies around 1kHz. At high frequencies, however, evidence of trailing edge noise is seen at all advance ratios. This may indicate that negative yaw creates particularly favorable conditions for this noise source by decreasing the local blade angle of attack near the wall. Noise levels drop off above 4 kHz for all the spectra as a function of their advance ratio. The highest braking condition, with an advance ratio J of 2.19, starts to drop off at 4 kHz followed by each consecutive lower advance ratio at increasing frequencies.

Laminar or transitional boundary layer trailing edge noise is typically created only at low angle of attack and the frequency and loudness of the broadband noise increases as the inflow velocity increases (Moreau *et al.*, 2012). As the advance ratio of the rotor decreases the rotational speed increases and the local angle of attack on each blade section changes. It is straightforward to compute the rotor blade geometric angle of attack at each point in the blade disc due to the freestream inflow, the rotor rotation, and the mean boundary layer profile. The rotor geometric angle of attack is shown below in Figure 60 for a braking case and the zero thrust case. Such predictions differ, of course, from the actual angles of attack experienced by the blades because of the distortion of the inflow by the rotor. Wisda (2015) shows that such predictions agree well with actual angle of attack measurements from Alexander *et al.* (2014) for the minimally distorted nominal zero thrust condition. While predictions at other braking conditions are likely to substantially overestimate angle of attack magnitude, these still provide insight to the rotor operating conditions at yaw. Figure 60 a) and c), and f) and h), show geometric angles of attack for the rotor for the -15° yaw and unyawed cases, respectively, for advance ratios of 1.75 and 1.44, respectively. When the rotor is negatively yawed, regions of comparatively low angle of attack appear and grow over the lower half of the rotor disk increasing, presumably, the proportion of the rotor likely to experience laminar or transitional boundary layer trailing edge noise.

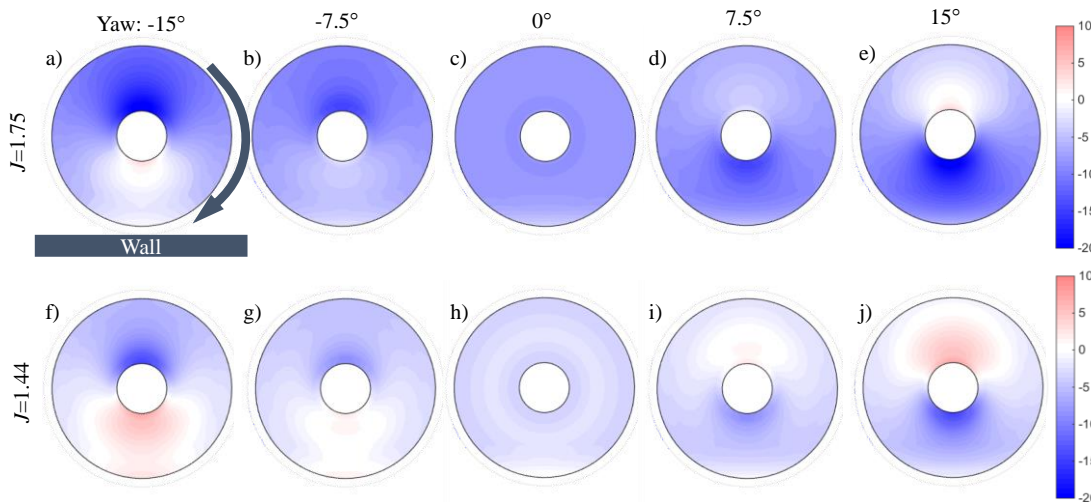


Figure 60: Undistorted angle of attack distribution across the rotor disc for $J=1.75$ (top row) and $J=1.44$ (bottom row) as a function of yaw angle. From left to right: -15° , -7.5° , 0° , 7.5° , and 15° yaw angle. The wall is below the rotor disc plane and it is rotating clockwise, as shown in a). Note that zero degrees angle of attack is white, fading to red and blue at positive and negative angles of attack respectively.

The spectra for each advance ratio with the rotor yawed at positive 15° are shown in Figure 59 c). In this case there appears to be no clear sound level dependence on advance ratio at low frequencies

(<1500Hz), even though the spectra in this range retain the same overall form and f^{-1} dependence seen at the other yaw angles. At higher frequencies, the high frequency spectral humps indicative of trailing edge noise again appear at all advance ratios, and again the upper limit of these humps is a function of the advance ratio.

Lastly, we note that in both the 15° and -15° yaw cases the spectra show series of sharp peaks at between 2 and 3 kHz whose cause is currently unknown. The frequencies of these features do not appear to be multiples of the blade passage rate. At -15° yaw, 5 peaks are seen at $J=1.44$ and 1.54 , decreasing slightly in frequency as the rotor speed is reduced between these two advance ratios. For the 15° yaw case there are only three spikes and they only show at the two lowest advance ratios. However, the frequencies of these peaks line up almost exactly with the frequencies of the three middle spikes in the -15° yaw case. This suggests that they are the result of the same phenomenon that is at least partially symmetric with the rotor yaw but more prevalent at the negative yaw angle. Additionally, the fact that the frequency shifts down as the advance ratio increases indicates that it is a rotation rate dependent phenomenon.

The acoustic spectra for a moderate braking case, ($J = 1.75$), is directly compared as a function of yaw angle in Figure 61 below. Below 2 kHz, each of the yawed cases have a very similar spectral shape. The spectra exhibit a loose dependence on yaw with the $+15^\circ$ yaw case producing the least noise and the -15° yaw case producing the greatest low frequency sound levels.

All of the yawed cases show evidence of trailing edge noise above 2 kHz. The noise appears about 5 dB louder in this region at -15° yaw than at 15° yaw, and the spectra have a quite different form. The trailing edge noise signature for the $\pm 7.5^\circ$ yaw cases peaks at lower frequencies than for the $\pm 15^\circ$ cases and they also have different spectral shapes. This asymmetry in spectral shape with respect to yaw angle presumably results from the high directionality of trailing edge noise and the changing orientation of the rotor relative to the microphone as a result of yaw.

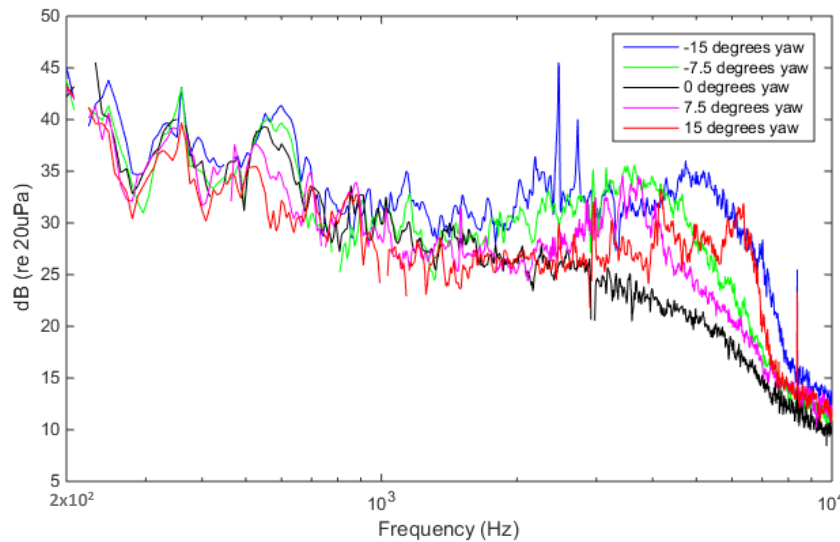


Figure 61: Background subtracted sound spectrum as a function of rotor yaw angle from inflow microphone 1 at $J = 1.75$.

3.4.2 Wall Pressure Measurements

The inflow distortion to the rotor is presented in two ways. First, the effect of the advance ratio was examined for the unyawed case and second the effect of yaw was explored for two specific advance

ratios. The pressure coefficient is defined in Equation (12) and the contour map range is different from the mean wall pressure measurements presented in previous sections.

First the effect of the advance ratio on the inflow distortion is examined for the unyawed rotor. Mean wall pressure coefficient contours for this case are shown in Figure 62 for advance ratios of 2.02, 1.75, 1.54 and 1.44. As before, flow is from left to right and distances are normalized on the rotor radius, equal to 229 mm and equivalent to approximately two boundary layer thicknesses or just over 11 times the tip gap. The coordinate system is the primed coordinate system which is centered at the rotor disc. The measurements are plotted in the $X'Z'$ plane, as projected against the wall, with X' measured axially downstream and Z' spanwise across the boundary layer. Note that Z' decreases upward in the figure, and that the blade tips sweep upward in the negative Z' direction through the boundary layer. The two parallel black lines represent the leading and training edge of the rotor blades as projected onto the wall.

For all advance ratios, the pressure field on the wall reaches a maximum just upstream of the rotor face. The maximum pressure coefficients are 0.11, 0.09, 0.06 and 0.04 for advance ratios J of 2.02, 1.75, 1.54 and 1.44 respectively. This shows that as the advance ratio of the rotor is reduced toward zero thrust, the deceleration of the flow ahead of the rotor also reduces. The inflow pressure coefficient distributions are also not quite symmetric about the rotor axis of rotation. The plane of symmetry of the pressure distribution actually appears to be slightly skewed toward the upstroke side at $Z'/R \approx -0.1$, presumably as a consequence of the blade rotation. As the advance ratio is varied, the location of the maximum holds constant at $X'/R = -0.45$ for all advance ratios except $J=1.44$ where it moves upstream to an $X'/R = -0.91$.

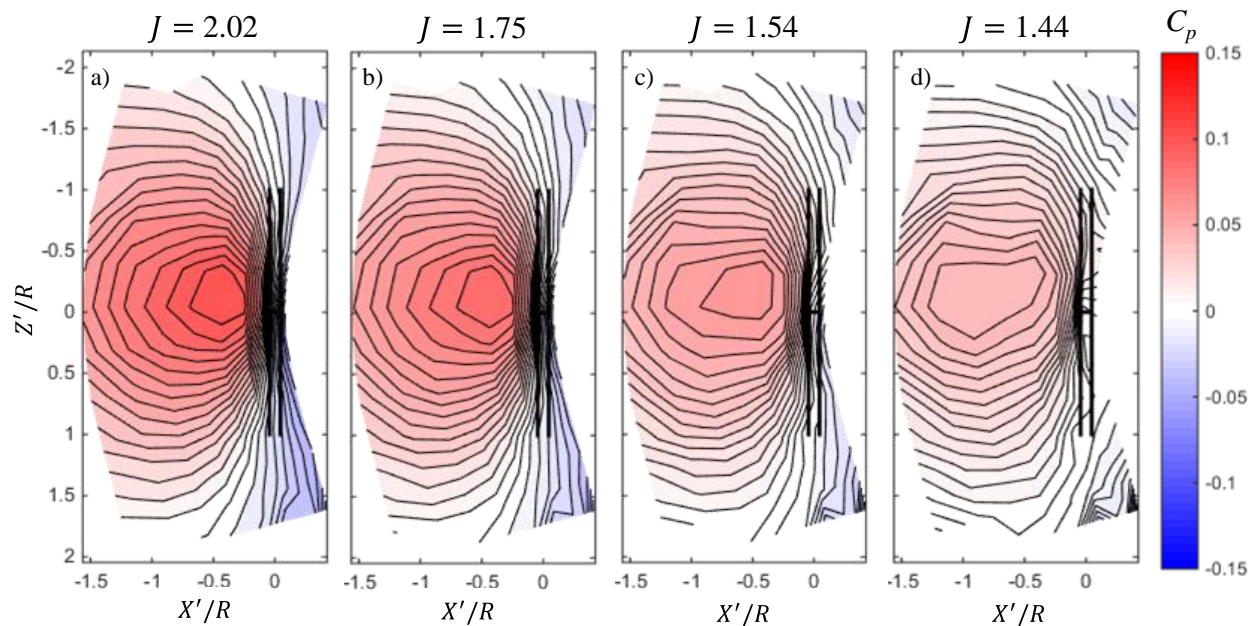


Figure 62: Mean wall pressure measurements for the unyawed rotor in a range of advance ratios.

Next, the effects of yaw is examined for two advance ratios; a braking case at $J=1.75$ and the nominal zero thrust case at $J=1.44$, shown in Figure 62 below. In both cases, the surface pressure contours show that the rotor heavily distorts the flow upstream. The pressure field, and therefore near-wall velocity field, is also not symmetric about the rotor center line with respect to yaw angle at any advance ratio tested.

At negative yaw and $J=1.75$ a large high pressure region forms directly upstream of the rotor disc (Figure 62a) and b)) due to the overall slowing of the flow here. The wall pressure coefficient in front of and on the downstroke side of the rotor is negative, indicating that the flow here is speeding up as it approaches this side of the rotor disc and passes through the tip gap. The asymmetry of the pressure field in the Z' direction appears entirely due to the yawing of the blockage effect created by the rotor, and not due to the implied angle of attack distribution (Figure 60), which remains left-right symmetric, regardless of yaw.

As the advance ratio is reduced to the nominal zero thrust case $J=1.44$ at negative yaw (compare Figure 63f) and a) for -15°) substantial changes are seen, with the high pressure region moving to the right of, and slightly behind the rotor. The low pressure region in front of and to the left of the blade disk also grows in strength and extent. This can be seen as an effect of the higher local angle of attack of the blades near the wall, which are actually predicted to be thrusting through the entire boundary layer region in Figure 63f). The thrusting portion of the blades sucks in air near the wall therefore causes the lower pressure coefficient. The effect is reduced at -7.5° yaw but the low pressure region is still evident in the same location, Figure 63g). This is explained by the slight positive local blade angle of attack next to the wall in the undistorted predictions shown in Figure 60g).

At positive angles of yaw (right hand side of Figure 63) the rotor produces a strong high pressure region that sits about half a radius upstream and to the left of the center of the rotor. As with the unyawed cases, the strength of the high pressure region increases with the advance ratio and is an indication of how the rotor is distorting the inflow near the wall. The rotor blade geometric angles of attack (Figure 60) are negative throughout the lower half of their rotor disk, explaining the consistent high pressure region upstream of the positively yawed rotor. The low pressure corner above the rotor is believed to be due to the flow accelerating through the tip gap and around the rotor, as also seen in the unyawed case.

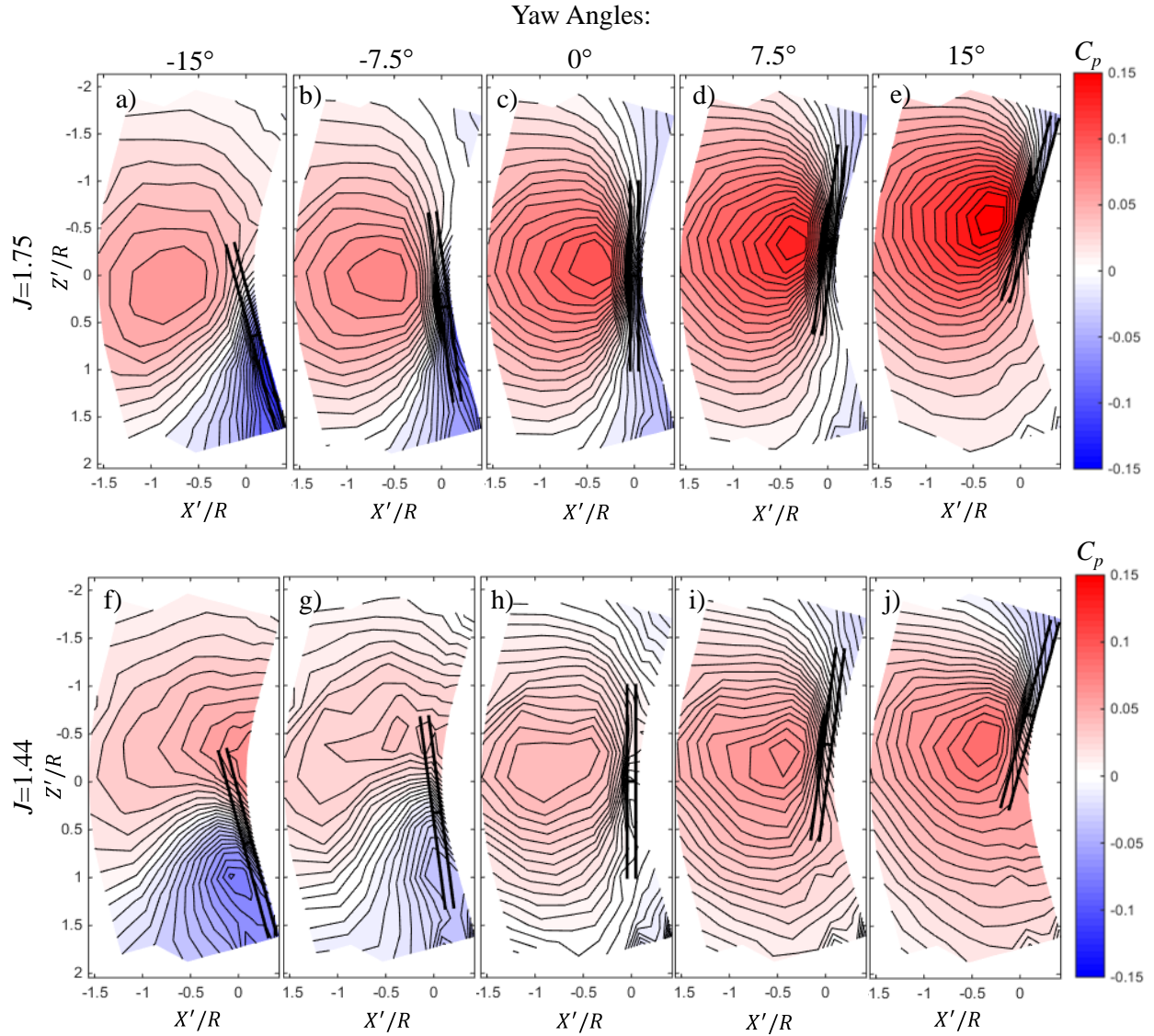


Figure 63: Mean wall pressure as a function of yaw angle at $J=1.75$, a) through e), and $J=1.44$, f) through j). From left to right, -15° , -7.5° , 0° , 7.5° , and 15° yaw angle.

3.4.3 Near Wall Fluid Flow Measurements

In this section fluid velocity measurements from the middle of the tip gap are presented and discussed for three yaw angles, -7.5° , 0° , and 7.5° , and at two advance ratios, $J = 1.44$ and $J = 1.75$. Instantaneous velocity fields were analyzed as well as mean and phase averaged measurements. The phase averaged velocity fields were calculated by computing the phase angle of the rotor from the raw image and then binning the angles into 18 two degree bins and then averaging. Mean flow measurements are presented first followed by phase averaged measurements of the fluid in the tip gap to investigate the development of the blade wake as it passes by the wall.

3.4.3.1 Mean Flow in the Tip Gap

Contour maps overlaid with velocity vectors to show the flow direction are presented in Figure 64 below for $J = 1.75$ and 1.44 . As in the previous sections, the fluid flow is left to right and the plot axis are the X' and Z' axis from the unyawed rotor centered coordinate system. To help locate the relative position

of the rotor blades in the measurement region, the location of the leading and trailing edge of the blades, as projected onto the measurement plane, are shown by the two vertical black lines. The center line is the projection of the axis of rotation of the rotor. The uncertainty in the mean flow measurements for the unyawed cases, with 5000 measurements each, is ± 0.41 m/s or $\pm 2.06\%$ of the freestream and for the yawed cases, with only 1000 measurements each, it is ± 0.43 m/s or $\pm 2.15\%$ of the freestream. The derivation of these uncertainties is described in §2.8 above and listed in Table 5.

Measurements of the fluid velocity in the tip gap for the braking case ($J = 1.75$) in Figure 64a) show that the flow midway in the tip gap approaches the rotor at approximately 70% of freestream and then accelerates through the tip gap, reaching 80% of freestream directly behind the rotor. This is due to the fluid accelerating around the blockage created by the rotor operating in a braking condition and through the tip gap. It should also be noted that the velocity vector arrows are pointed slightly away from the centerline. This also indicates that the fluid in the tip gap is spreading around the rotor, although the relative magnitude is much less than that of the axial velocity.

The higher velocity upstream of the blades on the down stroke side appears to confirm the maximum wall pressure coefficient skew toward the upstroke side in the unyawed case, shown in Figure 62e). The non-smooth streamwise velocity contours between the blade leading and trailing edge may be influenced by the laser sheet reflections from the blade tips interfering with the measurements in this location. However both of these features are less than the measurement uncertainty ($\pm 2.06\%$ freestream).

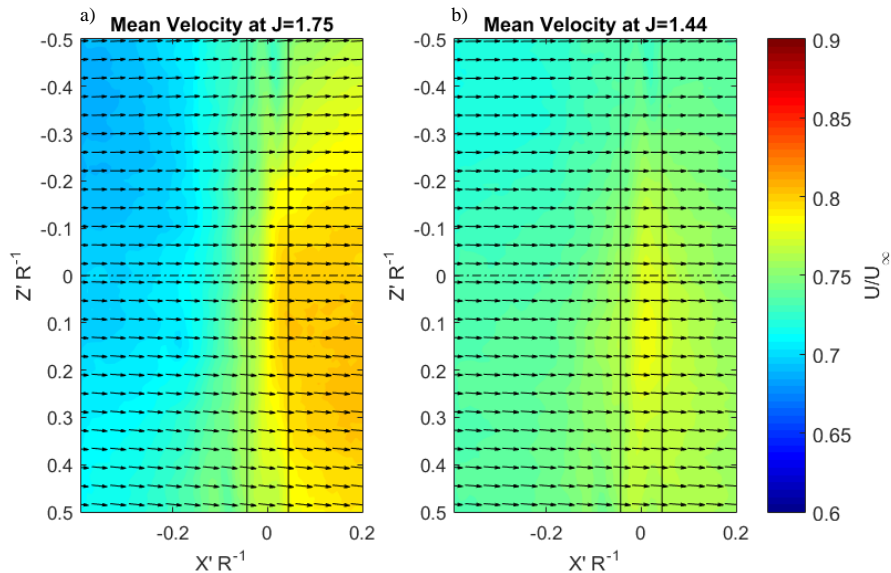


Figure 64: Mean velocity contour maps for the braking a) and zero thrust cases b). Flow is coming left to right. The vertical and horizontal lines indicate the projected leading edge, trailing edge, and centerline of the rotor on the measurement plane. The vectors are diluted 1:4 in both the vertical and horizontal directions for clarity.

The mean velocity field of the nominal zero thrust condition is shown in Figure 64b). The scale, axis, and uncertainty are the same as above. The small net acceleration of the fluid through the tip gap along the projected rotor rotation axis indicates that the real zero thrust condition is actually at a slightly lower advance ratio because the acceleration of the flow through the tip gap indicates that the nominal zero thrust condition is actually slowing the flow in the boundary layer and forcing it around the rotor.

3.4.3.2 Mean Velocity Measurements in the tip gap at Yaw

The braking condition was examined at three yaw angles, -7.5° , 0° , and 7.5° and the mean flow through the tip gap for each case is shown in Figure 65 a) through c) respectively below. Figure 64 a) is reproduced in the middle for reference with the yawed cases.

In the negative yaw case Figure 65 a) the angle of attack of the blades near the wall is increased resulting in less acceleration of the fluid through the tip, a higher velocity in the center of the tip gap, and less slowing of the fluid upstream of the rotor when compared to the unyawed case. Exactly the opposite is true in the positive yaw case, Figure 65 c). Positive yaw for this left handed rotor decreases the angle of attack of the blades near the wall and results in a higher net blockage effect near the wall where the measurement is located.

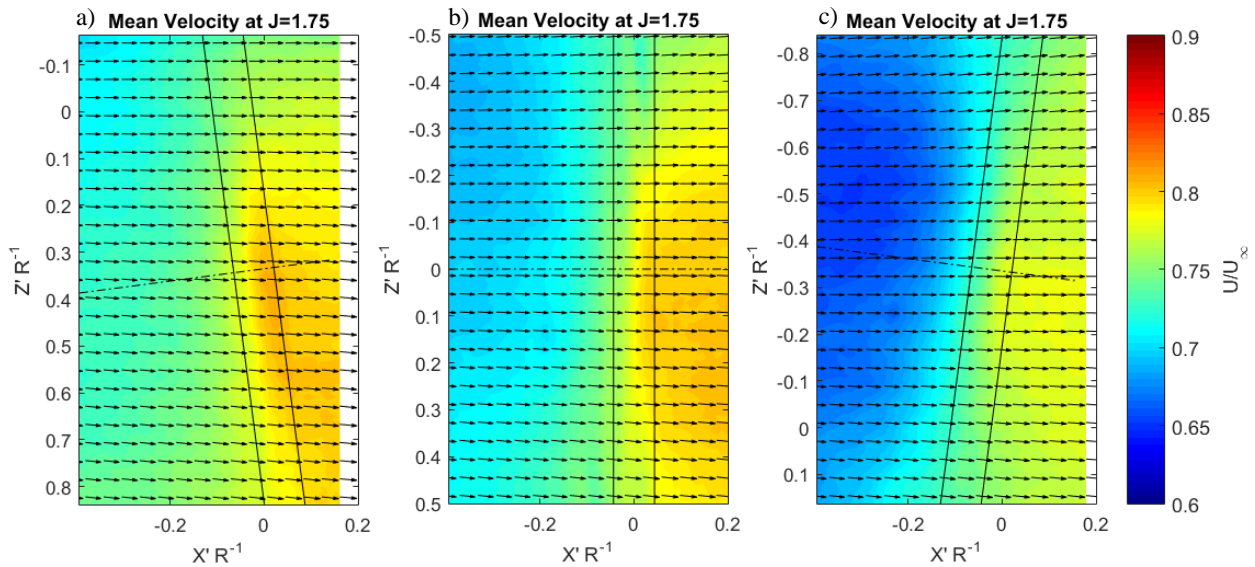


Figure 65: Mean flow in the tip gap for a braking rotor in yaw. Reference lines are the same as above and vectors are again diluted 1:4 for clarity.

3.4.3.3 Reynolds Stresses in the Tip Gap

Reynolds stresses were calculated in an effort to develop an insight to the distortion of the boundary layer turbulence as it passes through the tip gap in all three of the yaw conditions. The in-plane Reynolds normal stress components in the streamwise (τ_{11}) and spanwise (τ_{33}) directions, and, corresponding to the X' and Y' directions respectively, for the braking case are shown in Figure 66 normalized on the freestream velocity squared. The flow is left to right and the origin is at the center of the rotor projected onto the measurement plane and normalized on the rotor radius.

Upstream of the rotor, the τ_{11} component dominates the flow, decreasing slightly as the flow passes through the tip gap and then returning to its upstream value by 0.2 rotor radii downstream. The decrease is presumably due to the distortion of the inflow turbulence as the flow is accelerated through the tip gap and is centered on the projection of the axis of rotation of the rotor where the tip gap is smallest and the streamwise acceleration is greatest. Upstream of the rotor, the τ_{33} component, shown in Figure 66 b), is very close to half the τ_{11} component. However downstream of the rotor it increases to about 75%, showing that moving through the tip gap increases the spanwise velocity fluctuation. In the nominal zero thrust case, not shown here, the streamwise Reynolds stress is again approximately double the spanwise Reynolds stress

but no significant changes are seen as the flow negotiates the rotor, consistent with a much lower distortion in this case.

Yawing the rotor toward the downstroke side appears to reduce the streamwise Reynolds stress behind the rotor compared to the unyawed and upstroke side yawed case. Yawing toward the upstroke side appears to have a minimal effect of the overall streamwise Reynolds stress levels relative to the position of the rotor.

Yawing the rotor to either side also appears to reduce the spanwise Reynolds stress overall in the tip gap. It is interesting to note that yawing the rotor toward the upstroke and downstroke side has a similar effect of reducing the level of spanwise fluctuations in the tip gap. This was unexpected because the local blade angle of attack near the wall changes as the rotor is yawed and this was expected to effect the Reynolds stresses as well. It should also be noted that the high spots in the τ_{33} measurement in figures e) and f) is extraneous and due to a reflection of the blade at that location.

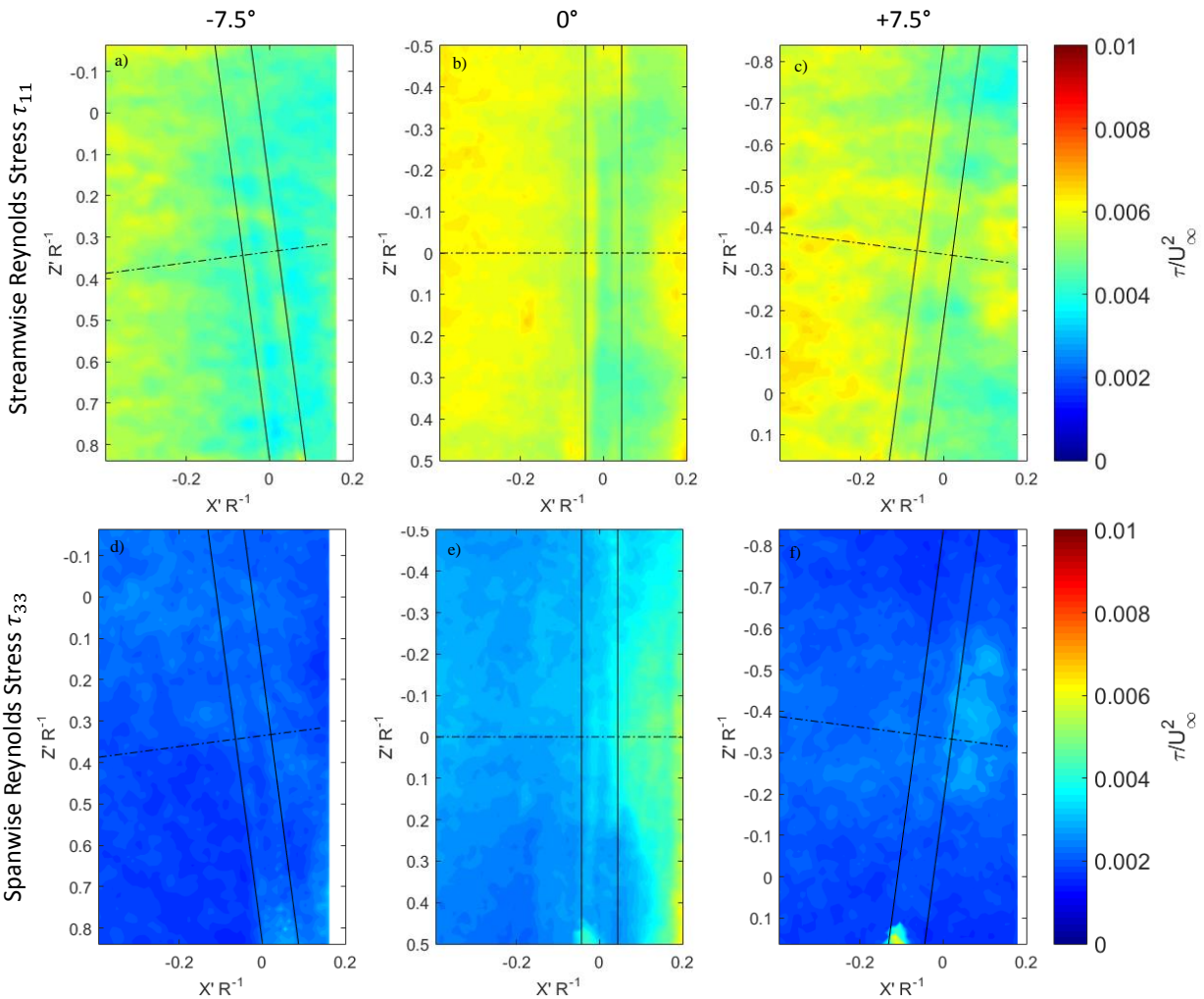


Figure 66: Reynolds Stresses for the braking case ($J = 1.75$) in the streamwise, a) through c), and spanwise, d) through f), directions for all three of the yaw conditions.

In the unyawed case the Reynolds stresses were within $\pm 0.5 \times 10^{-3}$ of the normalized levels from hotwire measurements of the unobstructed boundary layer taken by Morton (2012). This indicates that for

both cases tested, at 0.1 of the boundary layer thickness, the rotor minimally affects the normal Reynolds stresses upstream of 0.2 radii.

3.4.3.4 Phase Averaged Flow in the Tip Gap

The phase averaging process is explained in §3.2.2.3 and it allows the average blade passage to be reconstructed since the phase angle of the rotor could be determined from the raw measurement. Plots a) through c) in Figure 67 are at $J=1.75$ and d) through e) are at $J=1.44$. As before, the flow is moving left to right and the lines marking the blades leading edge, trailing edge, and rotor centerline are unchanged. The black oval indicates where the projection of the blade tip would fall in the measured plane to provide a frame of reference for the blade phase.

Three phase averaged velocity fields for the braking case, $J=1.75$, are plotted in Figure 67a) through c) with 12° of rotor rotation between each plot. For the interested reader, all the phase averaged velocity fields for the zero thrust and braking conditions are presented in Appendix B, in Figure 81 and Figure 82 respectively. The velocity fields upstream of the rotor show no strong dependence on the blade phase and the velocity increase at the tip gap, as seen in the mean flow measurements in Figure 64, starts at the leading edge of the rotor blades as projected into the measurements plane. Most significantly, it shows that as each blade passes through the boundary layer and by the wall, it trails a stream of higher velocity fluid behind it. This stream is following the trailing edge of the blade and the fluid in it is moving in the positive X' and negative Z' direction, indicating that it is likely part of a tip vortex shed from the blade at negative angle of attack as it passes by above the measurement plane. At this advance ratio, the rotor is braking, so the upstream side of the blade is the pressure side and the downstream side is the suction side.

The phase averaged velocity measurements for the zero thrust condition, Figure 67d) through f) reveals that the phase of the blades has very little effect on the flow through the tip gap. It appears that the blades slightly disturb the flow in that region but do not produce the strong periodic fluctuations like seen in the $J=1.75$ braking case.

The difference in the appearance of the blade tip vortex between cases is due to the different operating conditions of the rotor and the increase in tip vortex strength with increased blade loading. At the $J=1.75$ braking condition the rotor blades near the wall are at a negative angle of attack resulting in a noticeable tip vortex that trails downstream of the blades through the tip gap. Since the pressure side is upstream, the vortex appears in the measurement plane as an area of higher streamwise velocity. It is important to note that the blade tip vortex appears to convect downstream through the tip gap with the mean flow before the next blade reaches it suggesting that the rotor in this configuration does not interact with its own blade tip vortex in the tip gap.

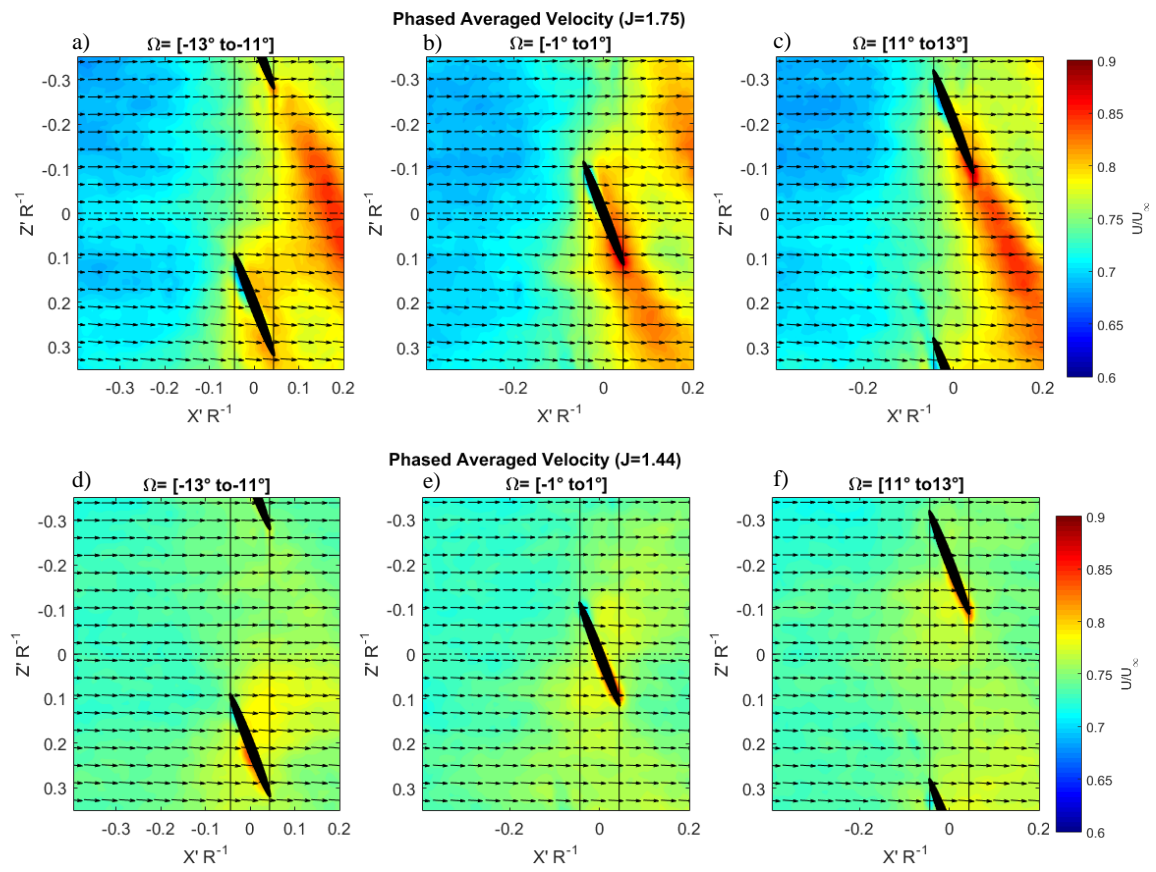


Figure 67: Phase averaged mean flow contour maps at $J= 1.75$ and $J=1.44$ for select blade phase angles (Ω). The black ovals indicates the projected profile of the blade tip into the measurement region. The vectors are diluted 1:4 in both directions for clarity.

Chapter 4: Conclusions

The interaction of an idealized rotor with a turbulent boundary layer near a wall has been studied at a large variety of rotation rates and at yaw angles from -15° to $+15^\circ$ to the mean inflow. Rotation rates in the thrusting regime were in an advance ratio range of $0.58 < J < 1.44$ and in the braking regime the advance ratios considered were between $1.44 < J < 2.19$. Acoustic measurements were recorded with inflow microphones in the test section, mean wall pressure measurements were taken on the wall next to the rotor and turbulence measurements were taken in the tip gap between the rotor and wall. Each of these different types of measurements are aggregated together to build a coherent picture of the interaction of the rotor with the inflow turbulence and the wall.

The overall conclusions from this work are presented in three sections below according to their operating conditions. First, the effect of rotation rate in the thrusting rotor is considered for the case of the rotor aligned axially with the mean inflow. Second, the effects of yawing the rotor are presented. Lastly conclusions from the braking case are summarized.

4.1 Unyawed Thrusting Conditions:

- Humps centered at the Blade Passage Frequency (BPF) harmonics in the acoustic spectra, or haystacking noise, were more pronounced and showed up at a larger number of BPF harmonics in the high thrust conditions ($J < 0.65$) than would be explained by the stretching of inflow turbulence into the rotor, the expected generation mechanism.
- Far-field sound spectra for the high thrust conditions also do not show the right skew in the haystacking peaks that would be expected and is observed in the moderate thrust ($0.65 < J < 1.44$) case.
- Mean wall pressure and velocity measurements in the tip gap for the high thrust condition revealed a separation region in the tip gap and strong reverse flow downstream of the rotor, confirmed the hypothesis of Alexander *et al.* (2014).
- Reynolds stress fields quantified the unsteadiness in the tip gap and showed that the streamwise component, τ_{11} , in the highest thrust case peaks at 0.25 of U_∞^2 and the spanwise component, τ_{33} , peaks at approximately 0.12 of U_∞^2 .
- Additionally this analysis of the Reynolds stress showed that both the streamwise and spanwise components, τ_{11} and τ_{33} respectively, in the tip gap are twenty times larger than measured at the moderate thrust case and 40 times larger than the Reynolds stresses measured in the undisturbed boundary layer at the same height above the wall.
- In the highest thrust case, both streamwise and spanwise velocity fluctuations are larger on the down stroke side of the axis of rotation of the rotor, which is consistent with on-blade hotwire measurements made in Alexander *et al.* (2014)
- Instantaneous velocity measurements in the tip gap frequently showed unsteady counter rotating vortex pairs, single vortices of both handedness and, in much lesser frequency, no vortex flow reversal. The vortices in the tip gap for the unyawed case should be discussed in reference to the handedness of the blade's bound circulation because they are believed to be strongly influenced by the shed vorticity from the blade.
 - An analysis of the locations of vortex centers and the mean Q-criterion shows that the vortices tend to be located in the center of the tip gap although they are significantly skewed both in location and strength toward the downstroke side of the rotor centerline.

- At least one vortex was found in the tip gap in 79% of the measurements made. A vortex with the opposite handedness of the bound circulation in the blade (clockwise in the measurement region) was found in 39% of the measurements and a vortex with the same handedness of the bound circulation in the blade (counterclockwise) was found in 66% of the measurements.
- Vortices with the opposite handedness of the bound circulation in the blade were almost always found to be on the upstroke side and those with the same handedness were more numerous and almost always found on the downstroke side of the measurement region.
- The fact that the vortices with the same handedness as the bound circulation in the blade (counterclockwise) were more numerous indicates that the blade tip vortex tends to extend through the measurement region in the tip gap and presumably link up with the wall since vortex lines in a fluid can only terminate at a surface.
- In summary, separation from the wall and flow reversal in the tip gap was accompanied by a strong acoustic signature at the BPF which is the result of a periodic interaction between the blades and the highly unsteady flow reversal. Specifically, at this highest thrust condition the interaction of the blade tips and the vortices that were commonly found to form in the tip gap is believed to be responsible for this additional noise.

4.2 Thrusting Rotor at Yaw to the Mean Inflow

In interpreting the conclusions below it is important to note that the local blade angle of attack near the wall increases at negative yaw and decreases at positive yaw for this experiment. This is a direct consequence of the geometry of the left handed rotor used in this study and this effect can be generalized for a rotor of either handedness. Yawing a rotor near a wall toward the side where the blades are approaching the wall, the downstroke side, will increase the angle of local attack of the blades near the wall and yawing the rotor the other way, toward the upstroke side will decrease the local angle of attack of the blades near the wall.

- The consequence of the change in the local blade angle of attack near the wall is that there is an asymmetry in the upstream mean wall pressure field and in the mean velocity through the tip gap. This asymmetry is less obvious at lower advance ratios (higher rotation rates) because the rotational component becomes dominant in determining the local blade angle of attack.
- A reversal in the wall pressure gradient is found on the wall directly adjacent to the rotor for unyawed cases where $J < 0.65$ suggesting that the rotor is inducing the same flow reversal at this case as seen in the PIV measurements at $J = 0.58$.
 - The reversal of the wall pressure gradient was found at higher advance ratios for the cases yawed towards the downstroke side, and lower advance ratios for the cases yawed toward the upstroke side. This suggests that yawing the rotor towards the downstroke side causes the stagnation region on the wall at higher advance ratios, lower rotation rates. Since the rotor blades nearest the wall have an increased local angle of attack at this yaw condition this is consistent with the blades producing more thrust in the boundary layer.
- For the unyawed, non-flow-reversal thrusting cases, $0.70 \leq J < 1.31$, yawing toward the downstroke side increases thrust near the wall and therefore the organization and stretching of the boundary layer turbulence in the inflow, which results in an increased haystacking response at the blade passage frequency.
 - This is shown in the magnitude of the BPF peaks which are directly related on the rotor yaw; the -15° yaw case, downstroke side, is the loudest and the sound level drops by 10dB over the entire spectrum as the rotor is yawed to $+15^\circ$, the upstroke side.

- The increased thrust near the wall for the case yawed toward the downstroke side is seen in the mean flow velocity in the tip gap at low thrust, $J = 1.05$, as in increase in velocity differential across the rotor at yaw toward the downstroke side and a decrease at yaw toward the upstroke side.
- At high thrust conditions when flow reversal is present in the unyawed case, approximately $J < 0.66$:
 - Mean velocity fields at $J = 0.58$ shows that there is a region of cross flow downstream of the rotor approximately perpendicular to the mean inflow, and crossing the X' axis in the same direction as the rotor yaw. It is also found to be stronger in the yaw condition toward the downstroke side and this is attributed to the local angle of attack increase in that condition
 - This crossflow results in a region of low mean velocity that extends under the downstream side of the rotor blades, expanding away from the projection of the rotor axis of rotation and appears to trail off downstream out of the measurement region.
 - Rotor-phase averaged velocity field further shows that the region of low mean velocity is not fed by the blade tip vortex in the center of the tip gap, as happens for the unyawed case, but by the cross flow behind the rotor observed in the mean.
 - The blades draw this region across the centerline in cases yawed toward the downstroke side whereas they sweep it back away from the centerline in the cases yawed toward the upstroke side.
 - The haystacking peaks are highest and most numerous for the unyawed spectra and fall off as a function of absolute value of the yaw angle suggesting that blade interaction with the vortices in the tip gap is the dominant noise source.
 - Maximum Reynolds stress in the tip gap is largest for the unyawed case, three times either of the $\pm 7.5^\circ$ cases in the streamwise (τ_{11}) direction and only slightly larger in the spanwise direction (τ_{33}) for the -7.5° case (downstroke side) and almost double for the $+7.5^\circ$ case (upstroke side).
 - An analysis of the locations and relative strengths of the vortices found in the tip gap revealed that the vortices are far more numerous and stronger in the unyawed case than in the yawed cases. Yawing -7.5° (toward the downstroke side) only produces vortices in 38.3% of measurements while yawing $+7.5^\circ$ (toward the upstroke side) produces vortices in 37.2% of measurements.
 - When the rotor is yawed the vortices tend to only form under the trailing edge of the downstream side of the rotor. Additionally, the case yawed toward the downstroke side, negative yaw, was found to predominantly form vortices opposite the direction of the bound circulation in the blade (36.7% of measurements compared to 2.5%). The case yawed toward the upstroke side was the opposite and found to predominantly form vortices of the same handedness at the bound circulation in the blade (28.3% of measurements compared to 9.5%). This suggests that when the rotor is yawed the vortices tend to form as a result of the downstream crossflow, not from the bound circulation in the blade or the blade tip vortex as in the unyawed case.
 - The average Q-criterion was used to compare the relative strengths of vortex like fluid structures in the tip gap across cases and it was found that the unyawed case had double the maximum of the average Q-criterion in the tip gap of either of the yawed cases. The mean q criterion also shows that the area and strength of the

vortex like fluid structures in the tip gap is larger in the case yawed toward the downstroke compared to the case yawed toward the upstroke side. This is likely a result of the stronger crossflow behind the rotor in the case yawed toward the downstroke side.

- Yawing the rotor at moderate thrust operating conditions, but not the highest thrust, results in an increase in the total noise component from trailing edge noise. This is seen in a “spreading” of the trailing edge noise region across a larger range of advance ratios because yaw produces more variation in the local blade angle of attack, which in turn increases the range of advance ratios for which the low angle of attack trailing edge vortex shedding noise occurs at some point in the rotor’s rotation.

4.3 Braking advance ratios:

- Turbulence ingestion noise was found to dominate low frequencies and trailing edge noise dominated high frequencies, when it was present. This confirms the predictions made by Fuglsang and Madsen (1996) and confirms trends predicted for isotropic turbulence ingested by a rotor.
- The high frequency, laminar/transitional trailing edge noise depended heavily on the rotation rate of the rotor, and therefore the local blade angle of attack. It would switch on suddenly between $J = 1.75$ and 1.54 (1500 and 1700 RPM) for the unyawed case. For yawed cases the transition was more gradual over the range of advance ratios tested due to the greater variation of blade angle of attack when the rotor was at an angle to the mean inflow.
- The turbulence ingestion noise level monotonically increased as the rotor RPM increased for -15° through 0° yaw but not in the cases yawed toward the upstroke side. This suggests a dependence on local thrust levels in the boundary layer for the cases yawed toward the downstroke side and a larger response at the blade passage frequency harmonics as the rotation rate increases in the unyawed case, as would be expected for turbulence ingestion noise.
- Phase averaged near wall flow measurements of the tip gap shows the blade tip vortex is carried downstream through the tip gap suggesting that the blade does not interact with its own tip vortex as a source of leading edge noise.
- Minimal change in the upstream Reynolds stresses up to $0.3 R$ upstream of the rotor were observed, suggesting the inflow near the wall is minimally distorted by the braking rotor.

Chapter 5: References

- Alexander, W. N., Devenport, W., Morton, M. A., and Glegg, S. A. L., "Noise from a Rotor Ingesting a Planar Turbulent Boundary Layer", 19 AIAA/CEAS Aeroacoustics Conference, May 27-29, 2013, Berlin, DE, AIAA-2013-2285.
- Alexander, W. N., Devenport, W., Wisda, D., Morton, M., and Glegg, S. A. L., "Sound Radiated from a Rotor and Its Relation to Rotating Frame Measurements of Ingested Turbulence", 20 AIAA/CEAS Aeroacoustics Conference, Atlanta, GA, July 16-20, 2014, AIAA-2014-2746.
- Amiet, R.K., "Acoustic Radiation from an Airfoil in a Turbulent Stream", *Journal of Sound and Vibration*, 1975: 407-420.
- Awasthi, M. A., 2012 "High Reynolds Number Turbulent Boundary Layer Flow over Small Forward Facing Steps", Master's Thesis, AOE Department, Virginia Tech, Avail: <http://theses.lib.vt.edu/theses/available/etd-06292012-120614/>
- Blake, W. *Mechanics of Flow Induced Sound and Vibration*. Academic Press, New York, 1986. §12.6.2. Print.
- Brooks, T. F., Pope, D. S., and Marcolini, M. A., "Airfoil Self-Noise and Prediction," NASA-RP-1218, 1989.
- Burdett, T. A., and Van Treuren, K. W., (2012, 11-15 June). "Scaling Small-Scale Wind Turbines for Wind Tunnel Testing," *ASME Turbo Expo 2012* (GT2012-68359). Retrieved February 23, 2014 from ASME Digital Collection.
- Catlett M R, Anderson, J M, and Stewart D O, "Aeroacoustic Response of Propellers to Sheared Turbulent Inflows", 18th AIAA/CEAS Aeroacoustics Conference, Colorado Springs, CO, June 4-6, 2012, AIAA-2012-2137.
- Dean, L.W., "Broadband Noise Generation by Airfoils in Turbulent Flow", AIAA 4th Fluid and Plasma Dynamics Conference, Palo Alto, CA, June 21-23, 1971, AIAA Paper No. 71-587.
- Williams, JE Ffowcs, and L. H. Hall. "Aerodynamic sound generation by turbulent flow in the vicinity of a scattering half plane." *Journal of Fluid Mechanics* 40.04 (1970): 657-670.
- Forest, J., 2012, "The Wall Pressure Spectrum of High Reynolds Number Rough-Wall Turbulent Boundary Layers", Master's Thesis, AOE Department, Virginia Tech, Avail: <http://scholar.lib.vt.edu/theses/available/etd-02022012-152048/>.
- Fuglsand, P., and Madsen, H A, "Implementation and Verification of an Aeroacoustic Noise Prediction Model for Wind Turbines", Riso National Laboratory, Riso-R-867(EN), Roskilde, DK, 1996.
- Ganz, Ulrich W., et al. "Boeing 18-inch fan rig broadband noise test." NASA/CR-1998-208704. (1998).
- Glegg, S., and N. Walker. "Fan Noise from Blades Moving Through Boundary Layer Turbulence." *5th AIAA/CEAS Aeroacoustics Conference*. Bellevue, WA, 1999.
- Glegg,S., Devenport, W.J., Alexander, N., "Broadband rotor noise predictions using a time domain approach", *Journal of Sound and Vibration*, v. 335(2015) pp115-124.

- Glegg, S., Bruono, A., Grant, J., Lachowski, F., Devenport, W., "Sound Radiation from a Rotor Partially Immersed in a Turbulent Boundary Layer." 21st AIAA/CEAS Aeroacoustics meeting, Dallas, Texas, June 22-26, 2015b, AIAA-2015-2361.
- Glegg, S. A. L., Baxter, S. M., and Glendinning, A. G., "The Prediction of Broadband Noise from Wind Turbines", *J. Sound Vibration*, vol. 118 (2), 1987, pp. 217-239.
- Grosveld, F. W., "Prediction of Broadband Noise from Horizontal Axis Wind Turbines", *J. Propulsion*, vol. 1 (4), 1985, pp. 292-299.
- Haller, George. "An objective definition of a vortex." *Journal of fluid mechanics* 525 (2005): 1-26.
- Hanson, D. "Spectrum of Rotor Noise Caused by Atmospheric Turbulence." *Journal of the Acoustical Society of America*, 1974: 110-126.
- Hersh, A S, Soderman, P T, and Hayden R E, 1974, "Investigation of Acoustic Effects of Leading-Edge Serrations on Airfoils", *Journal of Aircraft*, vol. 11(4), pp. 197-202.
- Hunt, Julian CR, A. A. Wray, and Parviz Moin. "Eddies, streams, and convergence zones in turbulent flows." Center for Turbulence Research, Proceedings of the Summer Program 1988. (1988).
- Huse. (1971) 'Propeller-Hull Vortex Cavitations'. Norw. Ship Model Exp. Tank Publ. 106, May 1971.
- Liepmann, H. W. "Extension of the statistical approach to buffeting and gust response of wings of finite span." *Journal of the Aeronautical Sciences* (1955).
- Majumdar, S., and N. Peake. "Noise Generation by the Interaction between Ingested Turbulence and a Rotating Fan." *Journal of Fluid Mechanics*, 1998: 181-216.
- Martinez, R. "Asymtotic Theory of Broadband Rotor Thrust, Part II: Analysis of the Right Frequency Shift of the Maximum Response", *Journal of Applied Mechanics*, March 1996, vol. 63, pp. 143-148.
- Martinez, R. "Broadband Sources of Structure-Borne Noise for Propulsors in "Haystacked" Turbulence." *Computers and Structures*, 1997: 475-490.
- Martio, J., Sipila, T., Sacher-Caja, A., Saisto, I., Siikonen, T., 2011, "Evaluation of the Propeller Hull Vortex Using a RANS Solver," Second International Symposium on Marine Propulsors smp'11, Hamburg, Germany, June 2011
- McTavish, S., Feszty, D., and Nitzsche, F., "Evaluating Reynolds Number Effects in Small-Scale Wind Turbine Experiments", *J. Wind Engineering and Industrial Aerodynamics*, vol. 120, 2013, pp. 81-90.
- Meyers, T., Forest, J., Devenport, W., "The wall-pressure spectrum of high-Reynolds-number turbulent boundary-layer flows over rough surfaces", *Journal of Fluid Mechanics*, 2015, vol. 768, pp. 261-293.
- Minniti, R. J., W. K. Blake, and T. J. Mueller. "Inferring propeller inflow and radiation from near-field response, Part 1: Analytic development." *AIAA journal* 39.6 (2001a): 1030-1036.
- Minniti, R. J., W. K. Blake, and T. J. Mueller. "Inferring propeller inflow and radiation from near-field response, Part 2: Empirical application." *AIAA journal* 39.6 (2001b): 1037-1046.

- Moreau, Danielle J., Laura A. Brooks, and Con J. Doolan. "The effect of boundary layer type on trailing edge noise from sharp-edged flat plates at low-to-moderate Reynolds number." *Journal of Sound and Vibration* 331.17 (2012): 3976-3988.
- Moreau, S., Roger, M., Jurdic, V., "Effect of Angle of Attack and Airfoil Shape on Turbulence-Interaction Noise", 11th AIAA/CEAS Aeroacoustics Conference, Monterey, CA, May 23-25, AIAA 2005-2973.
- Morton, M. A., Devenport, W. J., and Glegg, S., 2012, "Rotor Inflow Noise Caused by a Boundary Layer: Inflow Measurements and Noise Predictions", *18th AIAA/CEAS Aeroacoustics Conference*, Colorado Springs, Colorado, June 4-6. AIAA 2012-2120.
- Murray, H., Wisda, D., Alexander, W., Nelson, M., Devenport, W., Glegg, S., "Sound and Distortion Produced by a Braking Rotor Operating in a Planar Boundary Layer; with Application to Wind Turbines" *to be presented at the 21st AIAA/CEAS Aeroacoustics meeting in Dallas, Texas June 22-26, 2015.*
- Paterson, Robert W.; Vogt, Paul G.; Fink, Martin R.; and Munch, C. Lee: Vortex Noise of Isolated Airfoils. *J. Aircr.*, vol. 10, no. 5, May 1973, pp. 296-302.
- Paterson, Robert W.; Amiet, Roy K.; and Munch, C. Lee: Isolated Airfoil-Tip Vortex Interaction Noise. AIAA Paper No. 74-194, Jan. Feb. 1974.
- Ryi, J., Choi, J-S., Lee, Seunghoon, and Lee, Soogab, "A Full-Scale Prediction Method for Wind Turbine Rotor Noise by Using Wind Tunnel Test Data", *J. Renewable Energy*, vol. 65, 2014, pp. 257-264.
- Sato, R., Tasaki, R., and Nishiyama, S., 1986. "Observation of Flow on a Horizontal Flat Plate above a Working Propeller and Physics of Propeller-Hull Vortex Cavitation". Proceed. Internat. Symposium on Propeller and Cavitation, Wuxi, China.
- Sears, William R. "Some aspects of non-stationary airfoil theory and its practical application." *Journal of the Aeronautical Sciences* 8.3 (1941): 104-108.
- Samimy M, Lele S (1991) Motion of particles with inertia in a compressible free shear layer. *Phys Fluids* A 3:1915
- Sevik, M., "Sound Radiation from a Subsonic Rotor Subjected to Turbulence", *Fluid Mech., Acoustics, and Design of Turbomachinery, Pt. 2*, NASA SP-304, 1974 pp 493-512.
- Sharpf D., Mueller T., "An Experimental Investigation of the Sources of Propeller Noise Due to the Ingestion of Turbulence at Low Speed." *Experiments in Fluids*, Vol. 18, No. 4, 1995, pp. 277-287
- Stephens, D., and C. Morris, 2009, "Sound Generation by a Rotor Interacting with a Casing Turbulent Boundary Layer." *AIAA Journal*, vol. 47, pp. 2698-2708.
- Wagner, S., Bareiss, R., and Guidati, G., *Wind Turbine Noise*, Springer, Berlin, 1996.
- Wieneke, B., 2014, Generic a-posteriori uncertainty quantification for PIV vector fields by correlation statistics", 17th International Symposium on Applications of Laser Techniques to Fluid Mechanics, Lisbon, Portugal, July 07-10, 2014

- Wisda, D., Murray, H., Alexander, W., Nelson, M., Devenport, W., Glegg, S., .”Flow Distortion and Noise Produced by a Thrusting Rotor Ingesting a Planar Turbulent Boundary Layer” *21st AIAA/CEAS Aeroacoustics meeting in Dallas, Texas June 22-26, 2015.*
- Wisda, D., 2015, “Noise from a Rotor Ingesting Inhomogeneous Turbulence”, Master’s Thesis, AOE Department, Virginia Tech
- Wisda, D., Alexander, W. N., Devenport, W., and Glegg, S. A. L., “Boundary Layer Ingestion Noise and Turbulence Scale Analysis at High and Low Advance Ratios”, 20 AIAA/CEAS Aeroacoustics Conference, Atlanta, GA, July 16-20, 2014, AIAA-2014-2746.
- Wojno J., Mueller T., and Blake W., 2002, “Turbulence Ingestion Noise, Part 1: Experimental Characterization of Grid-Generated Turbulence”, *AIAA Journal*, vol. 40, pp. 16-25.
- Wojno J., Mueller T., and Blake W., 2002, “Turbulence Ingestion Noise, Part 2: Rotor Aeroacoustic Response to Grid Generated Turbulence”, *AIAA Journal*, vol. 40, pp. 26-32.

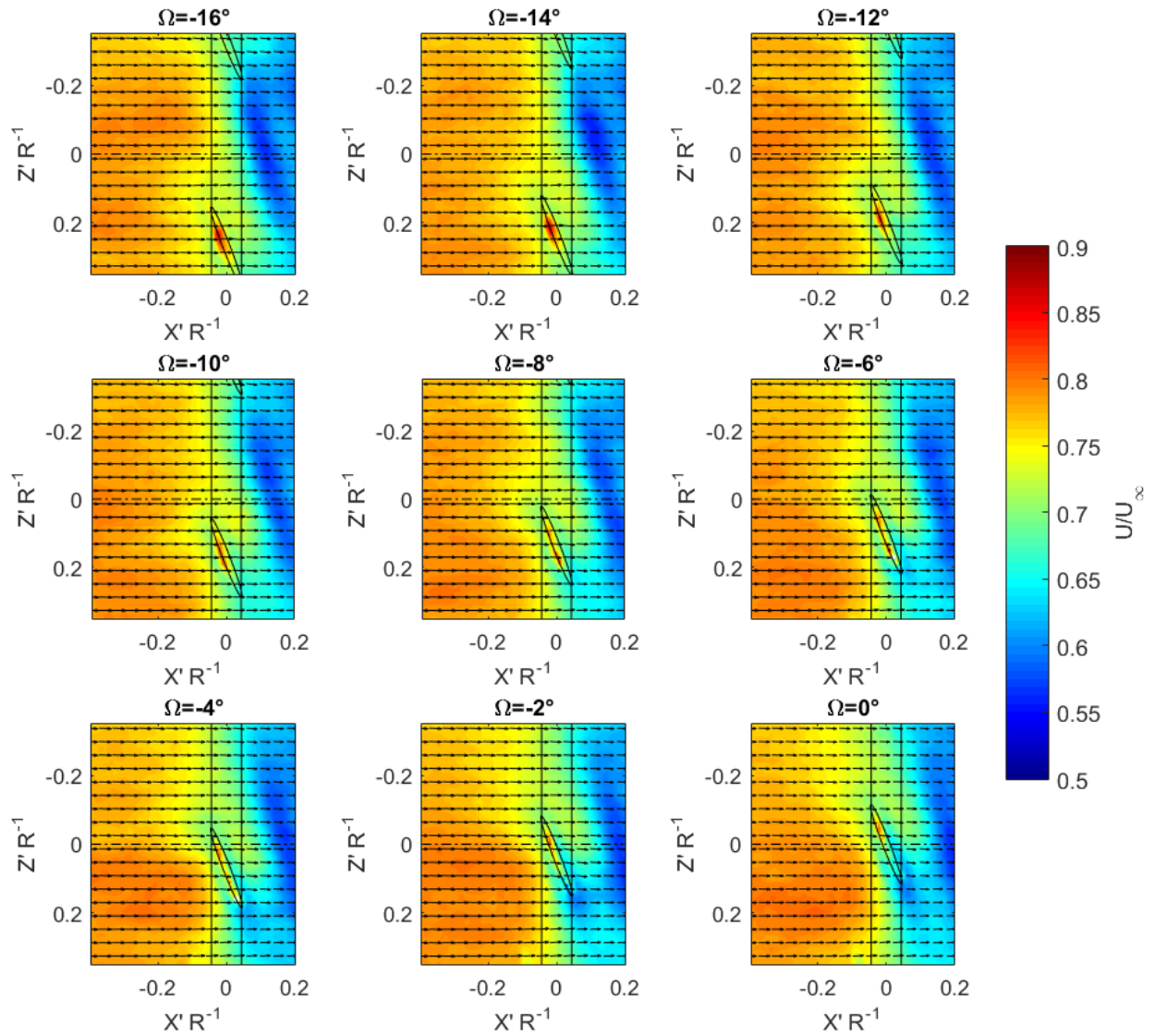
Appendix A – Annotated List of Figures

Figure 1: Diagram of a spanwise oriented gust impacting a 2D airfoil.	2
Figure 2: Illustration of the haystacking pattern in an example acoustic measurement of the rotor.....	5
Figure 3: Example of bias in the blade interaction with skewed eddies in the boundary layer.	6
Figure 4: The distortion and axial elongation of atmospheric turbulence into a stationary thrusting rotor ..	7
Figure 5: Survey of tip Reynolds number and rotor diameter of scaled wind turbine experiments, based on data from McTavish et al. (2013).....	9
Figure 6: Side view of the rotor partially immersed in a planar turbulent boundary layer near a wall.....	10
Figure 7: Blade-to-blade coherence measured in Alexander et al. 2012 for different probe pairs at a zero-thrust condition	12
Figure 8: Blade-to-blade coherence for different probe pairs as measured by Alexander et al. (2012) at three thrusting advance ratios	13
Figure 9: Tuft visualization from Alexander et al. (2014) showing the separation region below the rotor for the highest thrust case, $J=0.58$	14
Figure 10: Comparison of spectral predictions and measurements for the rotor in a turbulent boundary layer at high and low thrust conditions.	16
Figure 11: Orientation of the propeller in Sato et al. (1986).....	17
Figure 12: Tip clearance ratio vs propeller load factor and the associated flow patterns in the tip gap for five different right handed marine propellers.	18
Figure 13: Top down view of the Virginia Tech Stability Wind Tunnel in the full anechoic configuration.	22
Figure 14: Test section layout for the semi-anechoic configuration.....	23
Figure 15: Detailed schematic of the test section setup and instrumentation used in this experiment.	23
Figure 16: Picture of the empty test section after setting the zero pressure gradient on the Lexan wall. ...	24
Figure 17: Three view and isometric drawings of the 2.25 scaled Sevik rotor used in this experiment.....	25
Figure 18: Rotor blade profile at the tip.....	26
Figure 19: Rotor installed near the Lexan wall in the semi-anechoic configuration.	26
Figure 20: External support structure for mounting the rotor and yawing to $\pm 15^\circ$	27
Figure 21: Example free-field response curve of the B&K 4190 microphone with the bullet nose cone. .	28
Figure 22: Inflow microphones and rotor in the semi-anechoic configuration, looking upstream.	29
Figure 23: Close up of the B&K 4190 microphone with the bullet nose cone.	29
Figure 24: Schematic of wall pressure port locations relative to the projection of the unyawed rotor on the removable panel of the Lexan wall.	31
Figure 25: PIV measurement region superimposed behind the unyawed rotor.	32
Figure 26: Camera mounts and traverses in the starboard anechoic chamber for the PIV setup.	33
Figure 27: Schematic looking downstream into the rotor face that shows the relative locations of the cameras, the rotor, the laser sheet, the laser, and the field of view as the PIV results are presented in this thesis.	34
Figure 28: Comparison of mean wall pressure measurements in this test and data taken by Awasthi (2012) for the same boundary layer configurations.....	43
Figure 29: Comparison of velocity and mean Reynolds Stress profiles for the boundary layer in this experiment and that of Awasthi (2012).....	44
Figure 30: Mean wall pressure distribution, a), and mean velocity in the middle of the tip gap, b), at the moderately thrusting condition of $J=1.05$	45
Figure 31: Phase averaged velocity maps in the tip gap for the moderately thrusting case.....	47

Figure 32: Acoustic spectra from Microphone #1 for $J=1.05$ with background to show the signal to noise ratio.	48
Figure 33: Spectral density contour plot for all advance ratios considered in this experiment.	49
Figure 34: Representative spectra from all four operating regimes considered.....	50
Figure 35: Representative spectra normalized on blade passage frequency from all four operating regimes considered	51
Figure 36: Mean Wall pressure fields at all four operating regimes considered.....	52
Figure 37: Mean velocity fields in the middle of the tip gap from PIV measurements.	53
Figure 38: Phase averaged velocity measurements in the tip gap of the high thrust case.....	54
Figure 39: Instantaneous vector fields from the high thrust ($J =0.58$) case	55
Figure 40: Streamwise and spanwise components of the Reynolds stress tensor for the high thrust ($J =0.58$) and moderate thrust ($J =1.05$) case.....	56
Figure 41: Three example instantaneous velocity fields overlaid on the Q-criterion.	58
Figure 42: Trade study of absolute cutoff level of the Q-criterion in 26 example vector field with one to two strong vortices in total.....	59
Figure 43: Trade study of the Q-criterion cutoff percentages on the average number of vortices found per measurement in a sample of the data. All other criteria described above were also applied and this study shows that a level of 25% is the maximum possible before large numbers of vortices are eliminated.	60
Figure 44: Quantification of the location of vortices in the tip gap in a) a probability density function and b) the mean of the Q-criterion.....	61
Figure 45: Probability Density Function of the locations of vortex centers relative to the rotor blades and sorted into clockwise and counterclockwise vortices.	62
Figure 46: Illustration of the change of blade section angle of attack as it passes by the wall solely due to rotor yaw.	63
Figure 47: Diagram of velocity triangles seen by the blade at the range of yaw angles considered in this experiment.....	63
Figure 48: Mean wall pressure measurements as a function of rotor yaw angle for three representative advance ratios, zero thrust, moderate thrust, and high thrust.....	66
Figure 49: Mean velocity contour maps through the tip gap for the three representative thrust conditions ($J= 1.44, 1.05,$ and 0.58) and at three rotor yaw angles ($-7.5^\circ, 0^\circ,$ and $+7.5^\circ$).	67
Figure 50: Yaw and advance ratio conditions at which pressure gradient reversal was observed on the wall below the rotor.	68
Figure 51: Comparison for spectra for a high thrust condition, without the inferred flow reversal, at all yaw angles studied.....	70
Figure 52: Comparison of spectra at all yaw angles examined for two high thrust conditions ($J =0.58$ and $J =0.62$ where flow reversal was inferred to have occurred.....	71
Figure 53: Normal components of the Reynolds stress tensor in the measurement plane for the $\pm 7.5^\circ$ yawed cases.	73
Figure 54: Representative phase averaged velocity fields for the high thrust condition ($J = 0.58$) of the rotor at yaw.....	75
Figure 55: Representative instantaneous vector fields for the $+7.5^\circ$ and -7.5° cases at high thrust ($J = 0.58$) plotted over contours of vorticity to highlight vortex formations.....	76
Figure 56: Probability Density Functions of the locations of vortices in the tip gap when the rotor is at high thrust ($J = 0.58$) and at yaw to the mean inflow.	78
Figure 57: Average Q-criterion for the yawed and unyawed cases at high thrust	79
Figure 58: Spectra for the most inline upstream inflow microphone.....	80

Figure 59: Background subtracted acoustic spectra as a function of advance ratio and frequency from inflow microphone #1.	82
Figure 60: Undistorted angle of attack distribution across the rotor disc	83
Figure 61: Background subtracted sound spectrum as a function of rotor yaw angle from inflow microphone 1 at $J = 1.75$	84
Figure 62: Mean wall pressure measurements for the unyawed rotor in a range of advance ratios.	85
Figure 63: Mean wall pressure as a function of yaw angle at $J=1.75$, a) through e), and $J=1.44$, f) through j).	87
Figure 64: Mean velocity contour maps for the braking a) and zero thrust cases b).	88
Figure 65: Mean flow in the tip gap for a braking rotor in yaw.....	89
Figure 66: Reynolds Stresses for the braking case ($J = 1.75$) in the streamwise, a) through c), and spanwise, d) through f), directions for all three of the yaw conditions.	90
Figure 67: Phase averaged mean flow contour maps at $J= 1.75$ and $J=1.44$ for select blade phase angles (Ω).	92
Figure 68: All phases of the phase averaged mean velocity fields in the center of the tip gap when the rotor is operating at a moderately thrusting condition, $J = 1.05$ or 2500RPM.....	105
Figure 69: Phase averaged Reynolds stress fields for the moderately thrusting case, $J=1.05$ or 2500 RPM.	106
Figure 70: Phase averaged Reynolds stress fields for the moderately thrusting case, $J=0.58$ or 4500 RPM.	107
Figure 71: Six additional examples of the instantaneous velocity fields at the highest thrust case, $J=0.58$ or 4500RPM.	108
Figure 72: Example of two typical instantaneous vector fields from the moderately thrusting case, $J=1.05$	109
Figure 73: Contour plot of the spectra as a function of advance ratio for the negative yawed cases.	110
Figure 74: Contour plot of the spectra as a function of advance ratio for the positive yawed cases.	111
Figure 75: All phases of the phase averaged mean velocity fields in the center of the tip gap when the rotor is at -7.5° yaw.	113
Figure 76: All phases of the phase averaged mean velocity fields in the center of the tip gap of the unyawed rotor.....	115
Figure 77: All phases of the phase averaged mean velocity fields in the center of the tip gap when the rotor is at $+7.5^\circ$ yaw.	117
Figure 78: Example instantaneous velocity fields plotted on Q-criterion contours for the -7.5° yaw case.	118
Figure 79: Example instantaneous velocity fields plotted on Q-criterion contours for the unyawed case.	119
Figure 80: Example instantaneous velocity fields plotted on Q-criterion contours for the $+7.5^\circ$ yaw case.	120
Figure 81: All phases of the phase averaged mean velocity fields in the center of the tip gap when the rotor is operating at the nominal zero thrust condition, $J = 1.44$ or 1823 RPM.....	122
Figure 82: All phases of the phase averaged mean velocity fields in the center of the tip gap when the rotor is operating at the nominal zero thrust condition, $J = 1.75$ or 1500 RPM.....	124
Figure 83: All phase averaged probability density functions (left column) and mean Q-criterion (right column).	130
Figure 84: All phase averaged probability density functions for the clockwise (left column) and counter-clockwise (right column) vortex center locations.	136

Appendix B – Extra Figures



Note: Figure is continued on next page.

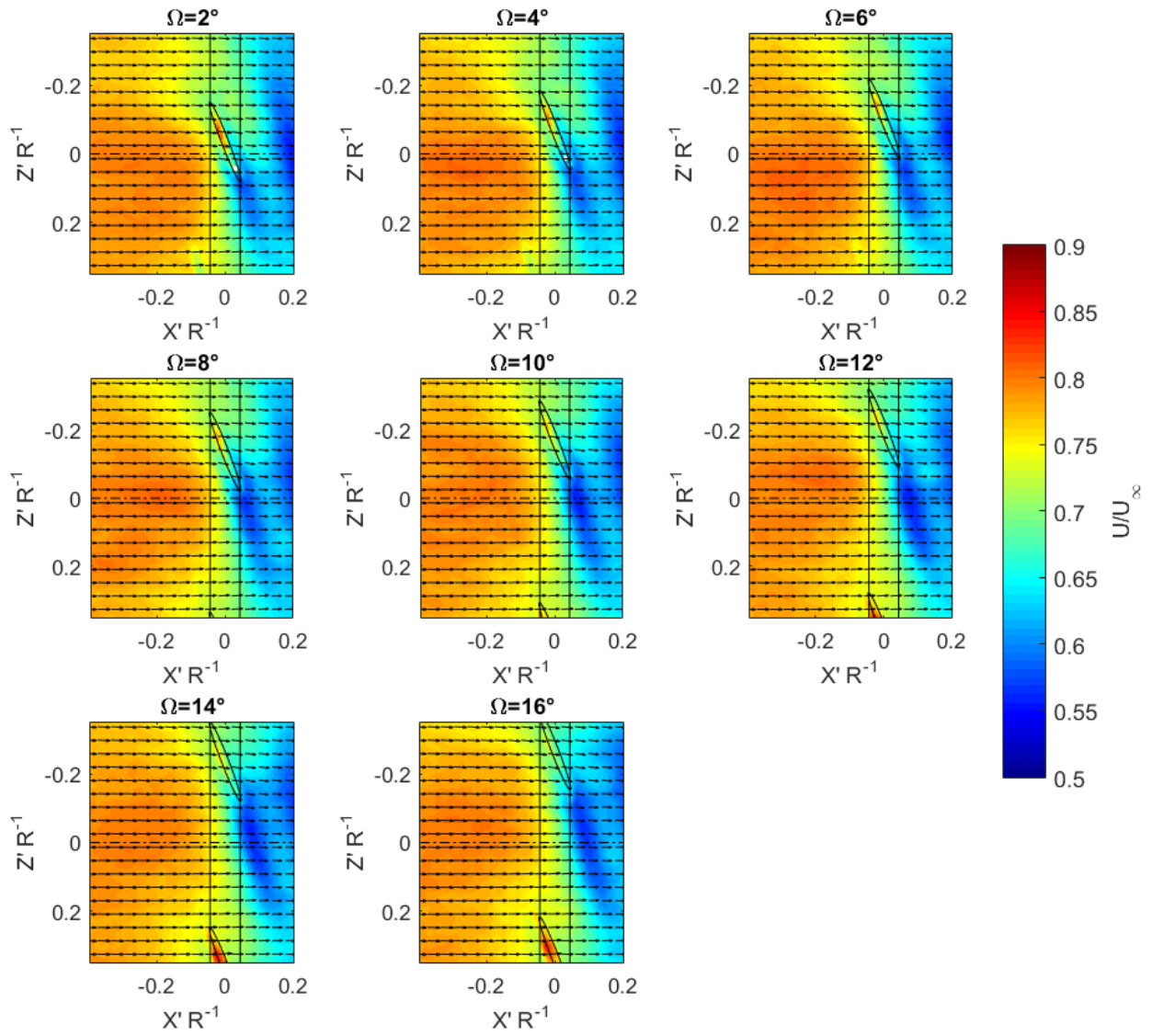


Figure 68: All phases of the phase averaged mean velocity fields in the center of the tip gap when the rotor is operating at a moderately thrusting condition, $J = 1.05$ or 2500RPM.

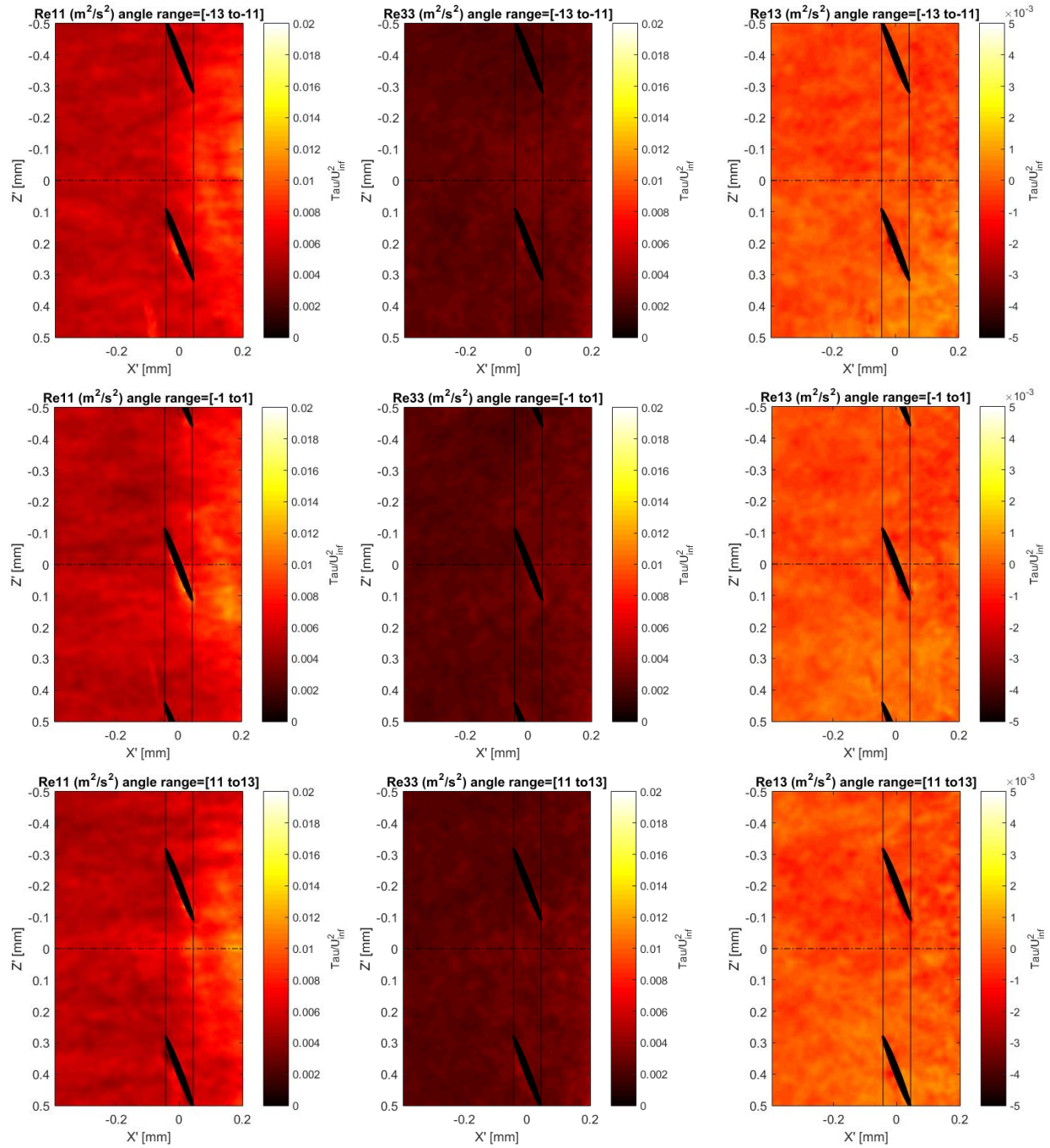


Figure 69: Phase averaged Reynolds stress fields for the moderately thrusting case, $J=1.05$ or 2500 RPM.

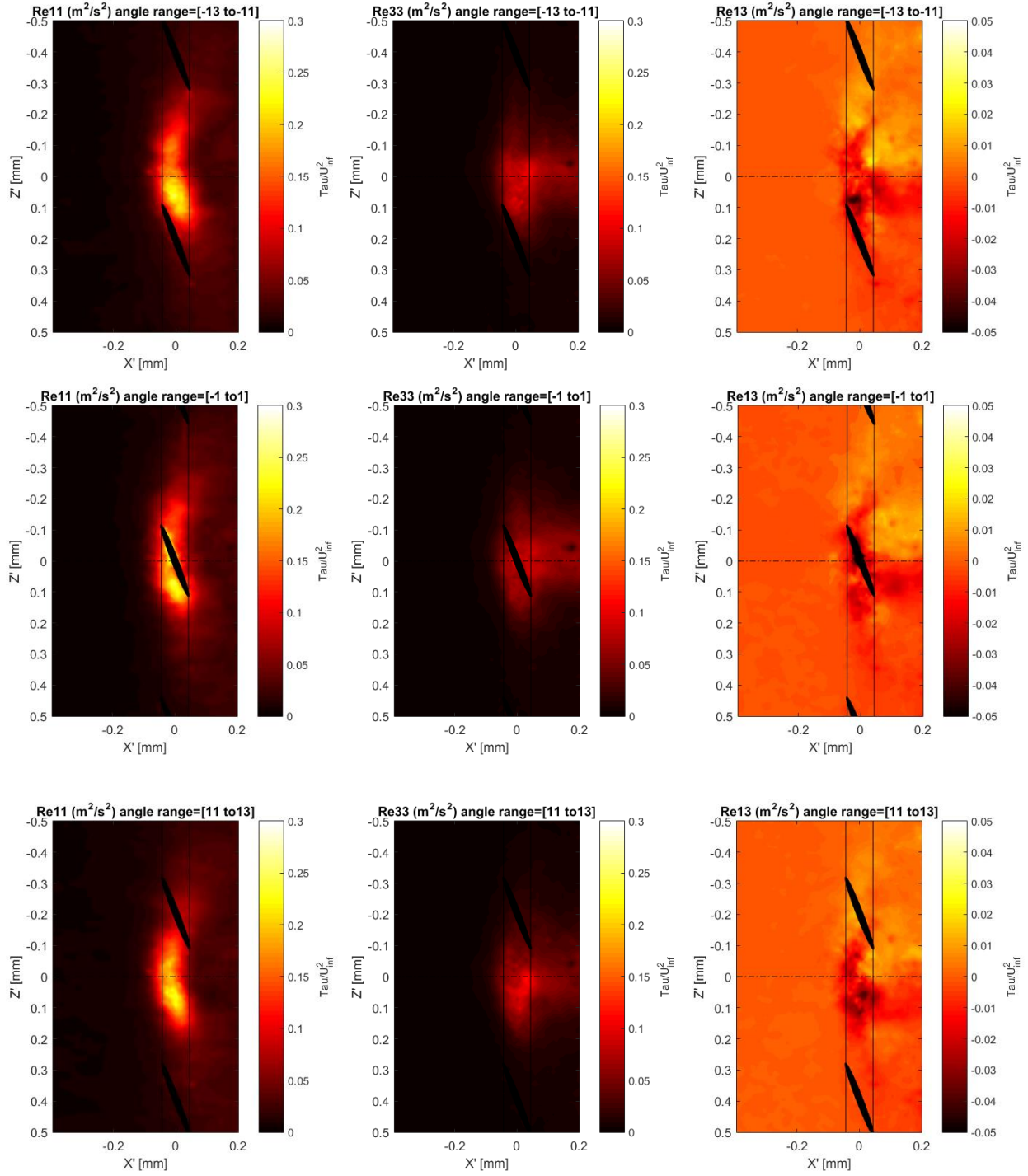


Figure 70: Phase averaged Reynolds stress fields for the moderately thrusting case, $J=0.58$ or 4500 RPM. Note the change of scale from Figure 69 of the moderately thrusting case above.

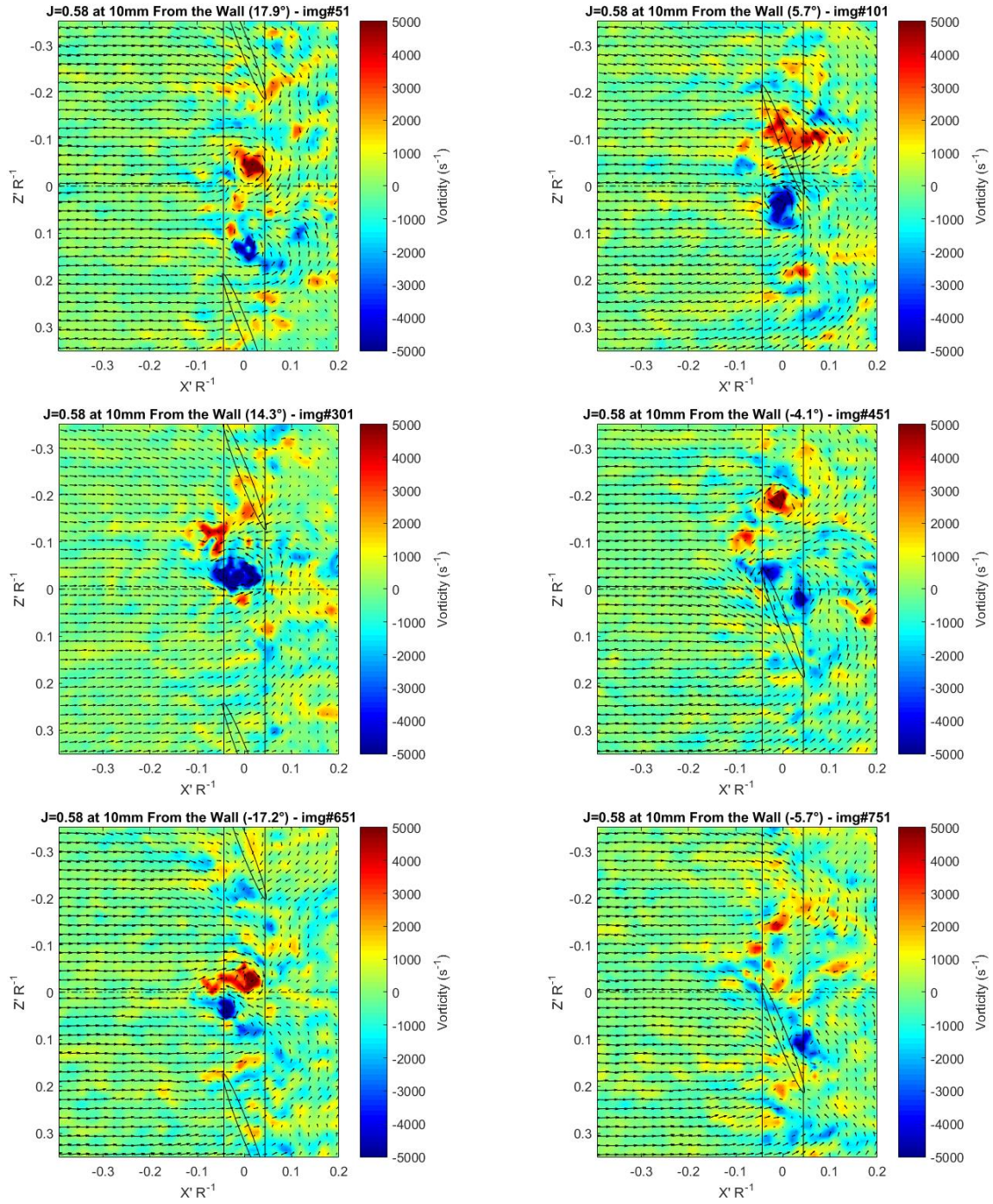


Figure 71: Six additional examples of the instantaneous velocity fields at the highest thrust case, $J=0.58$ or 4500RPM.

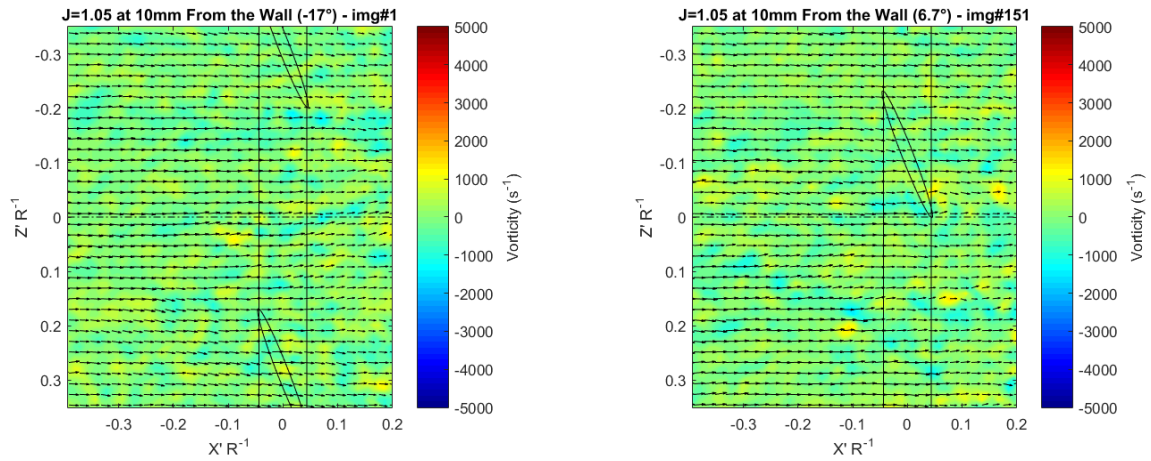


Figure 72: Example of two typical instantaneous vector fields from the moderately thrusting case, $J=1.05$, plotted on contours of vorticity to compare to the instantaneous vector fields at the highest thrust case, shown in Figure 71 above.

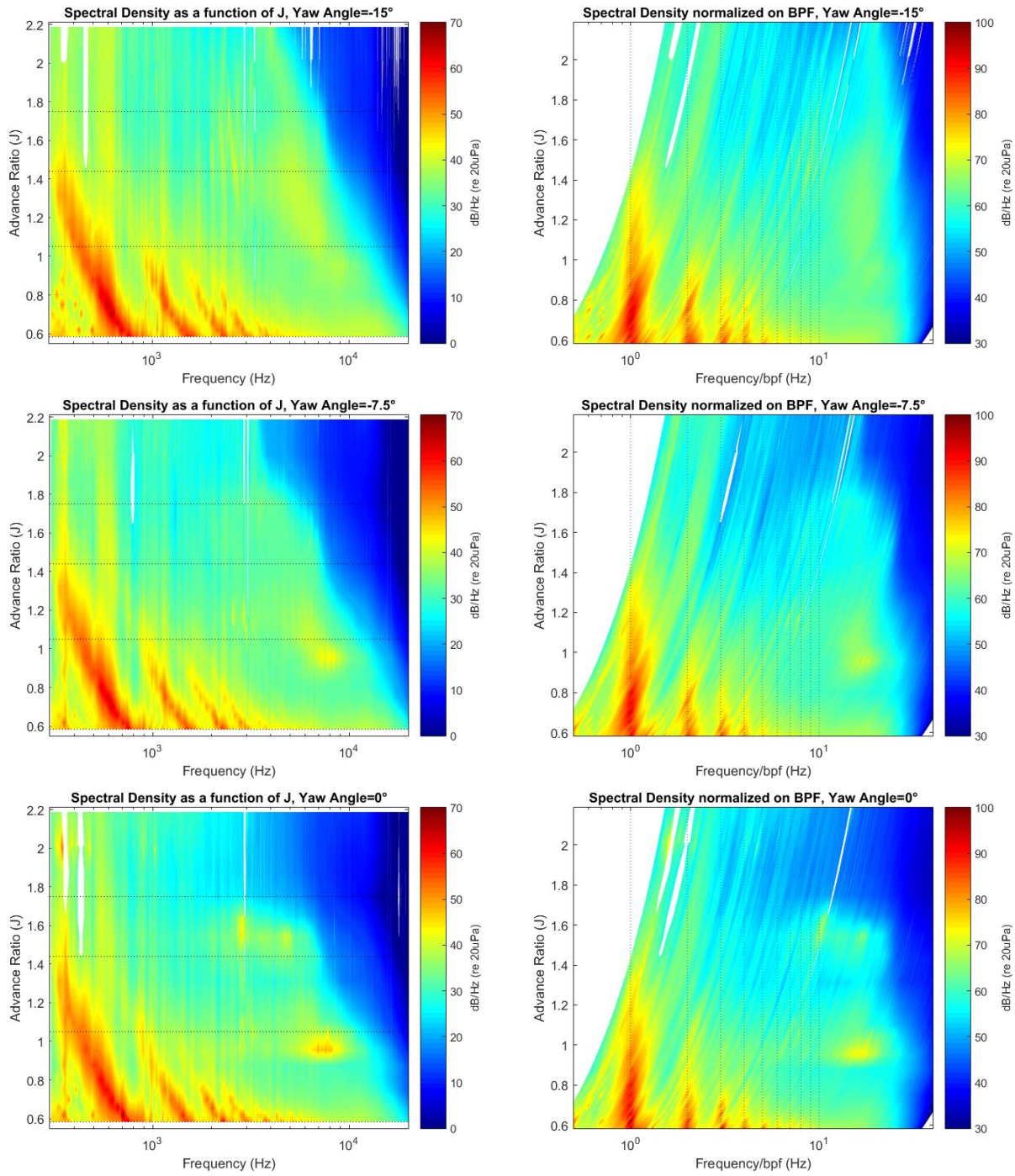


Figure 73: Contour plot of the spectra as a function of advance ratio for the negative yawed cases.

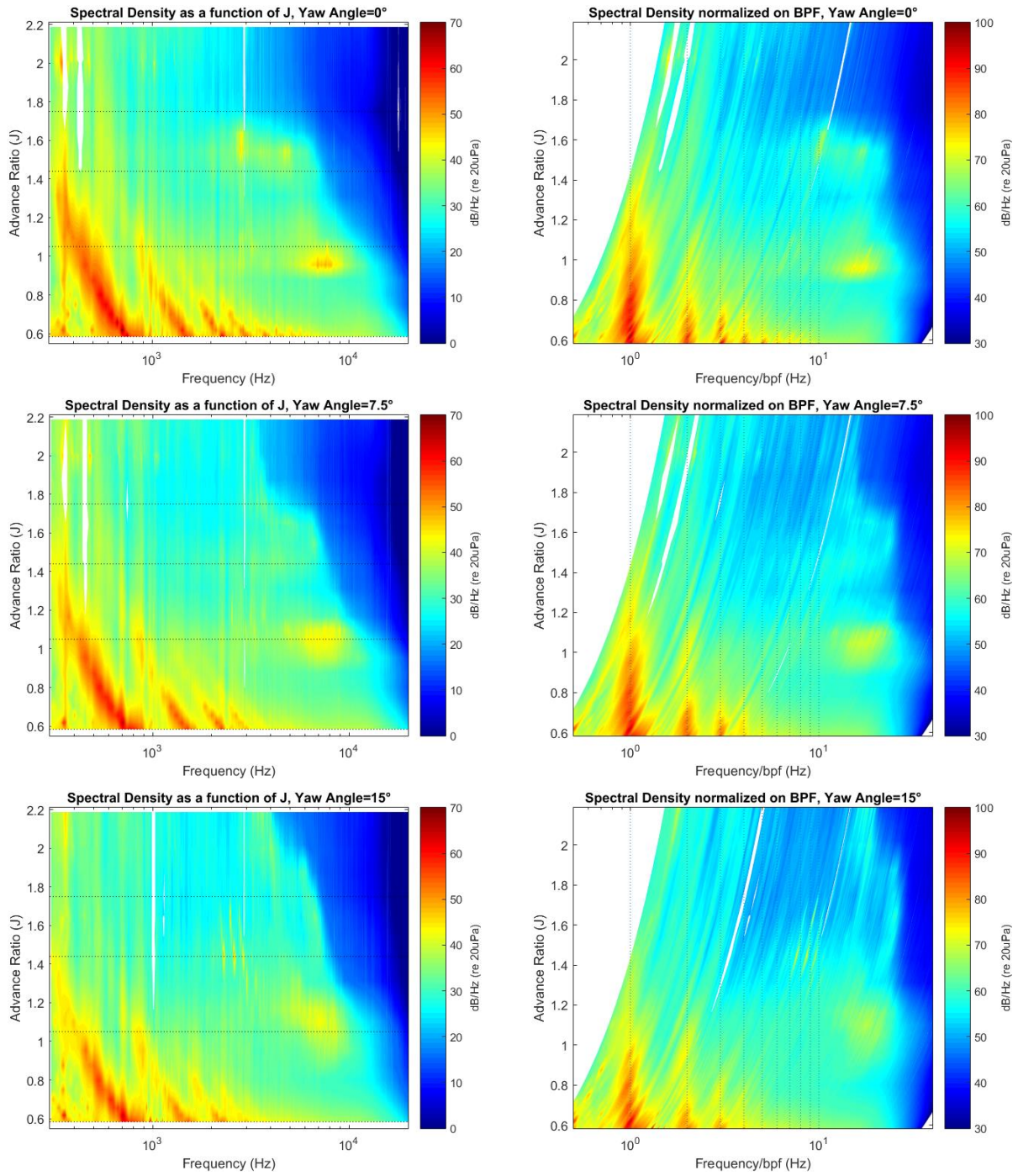
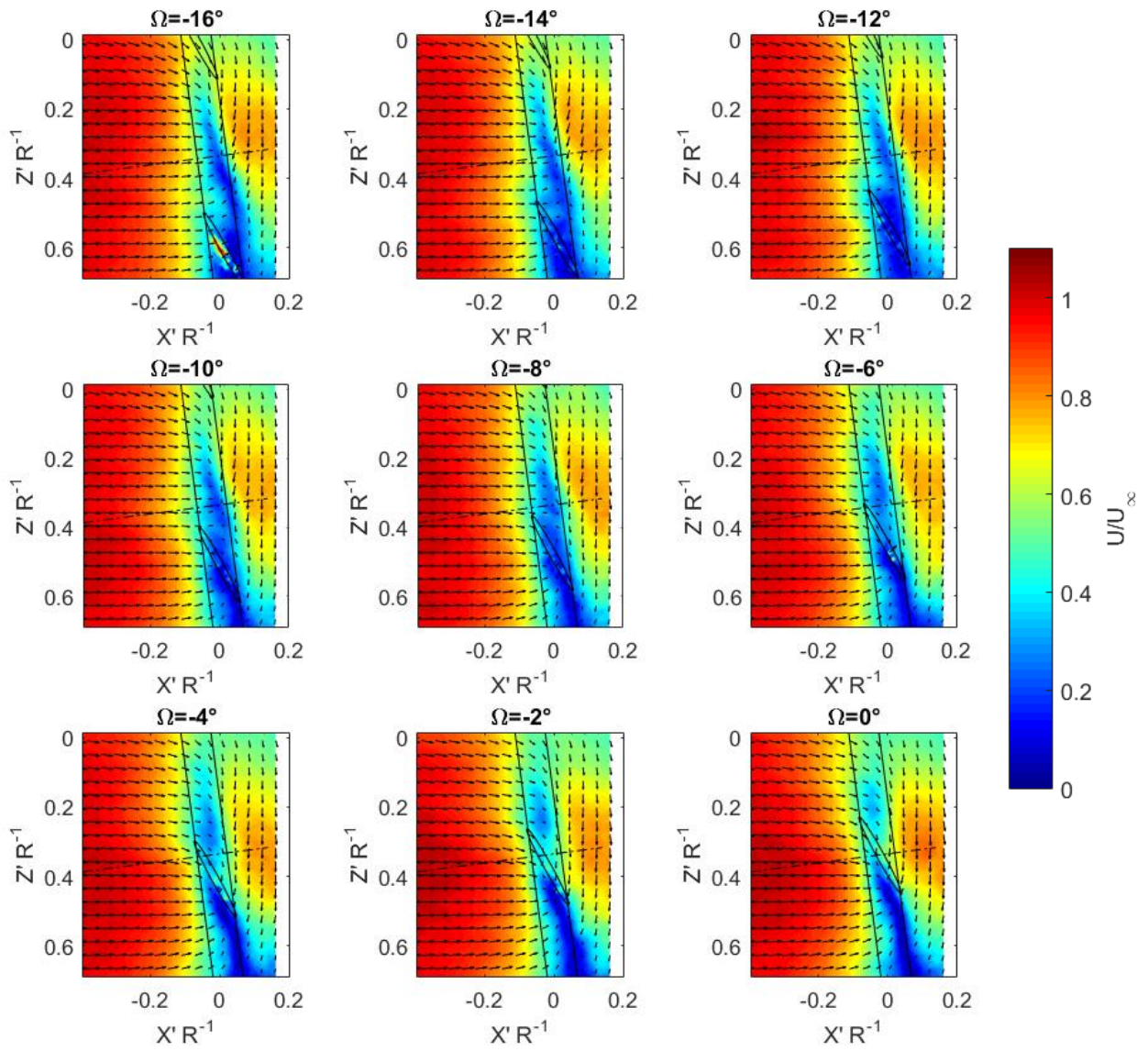


Figure 74: Contour plot of the spectra as a function of advance ratio for the positive yawed cases.



Note: Figure is continued on next page.

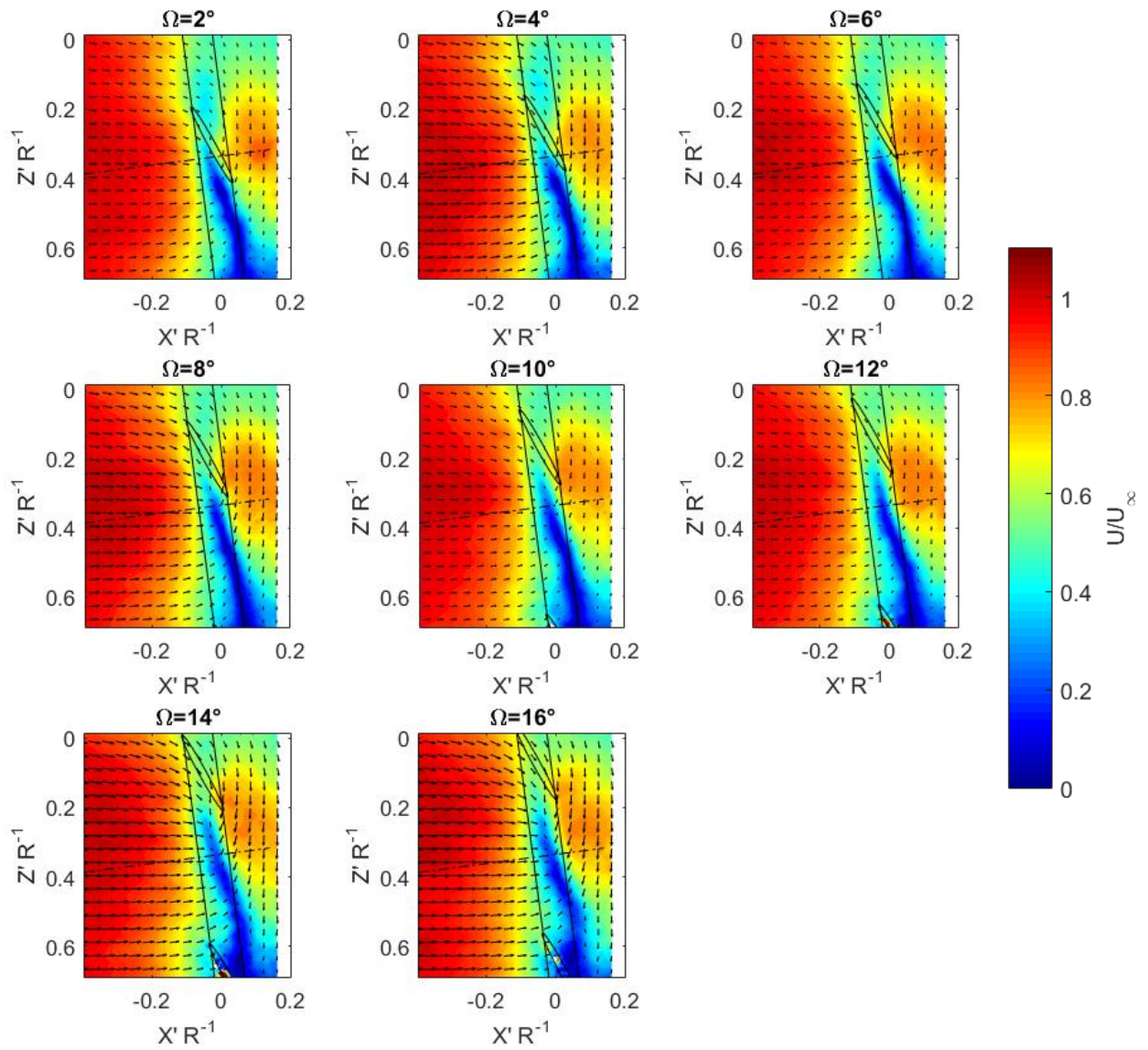
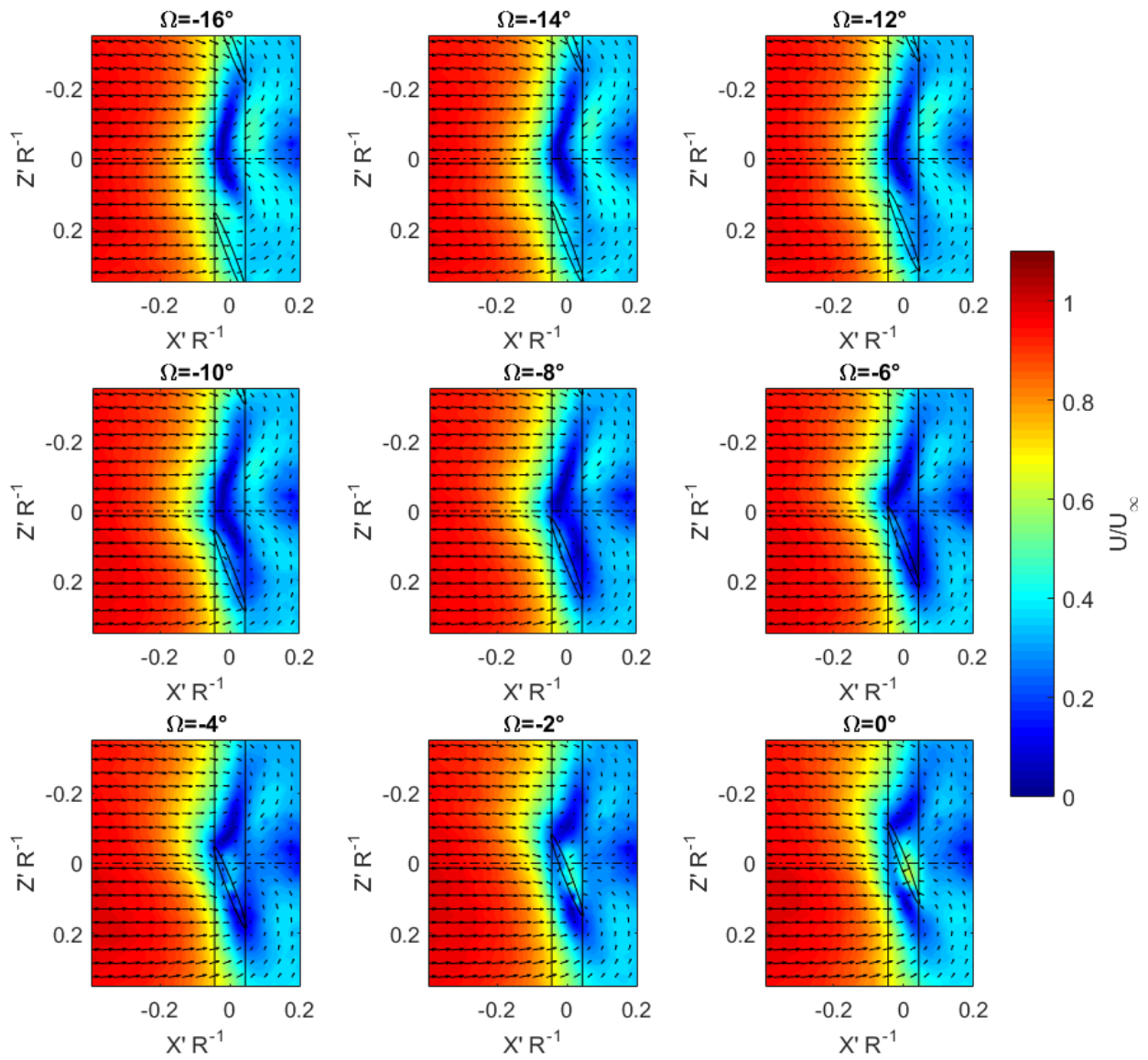


Figure 75: All phases of the phase averaged mean velocity fields in the center of the tip gap when the rotor is at -7.5° yaw.



Note: Figure is continued on next page.

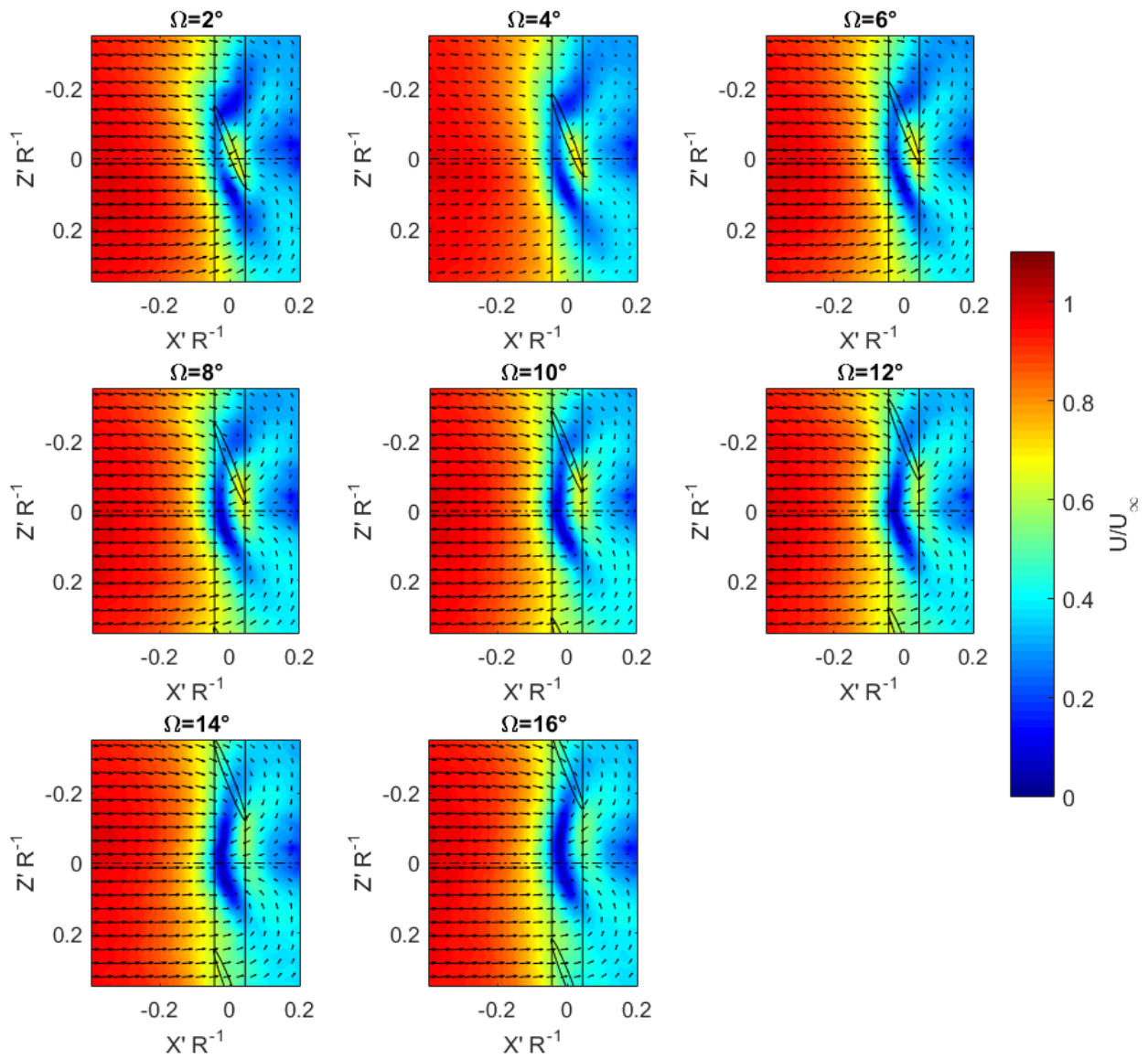
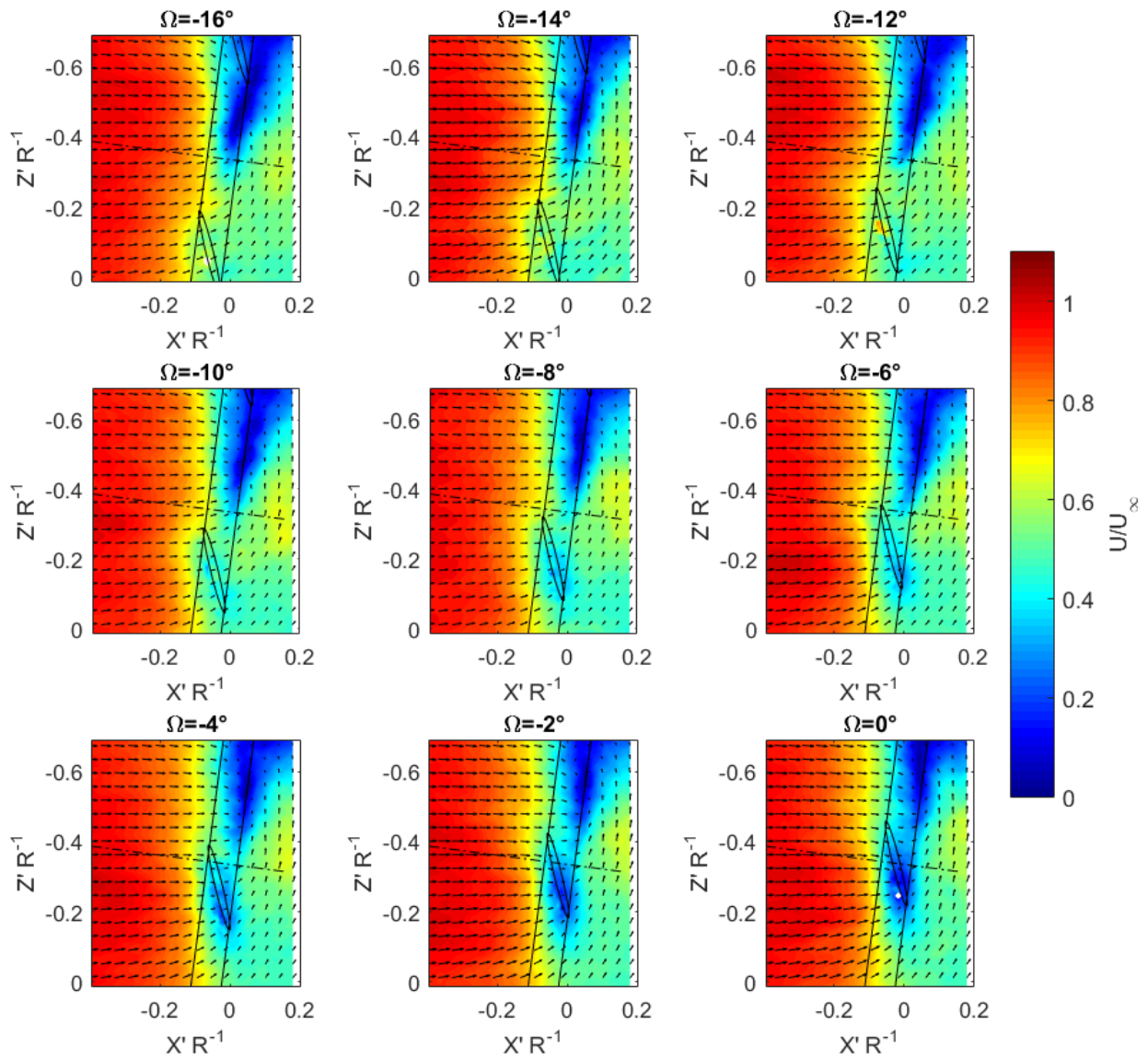


Figure 76: All phases of the phase averaged mean velocity fields in the center of the tip gap of the unyawed rotor.



Note: Figure is continued on next page.

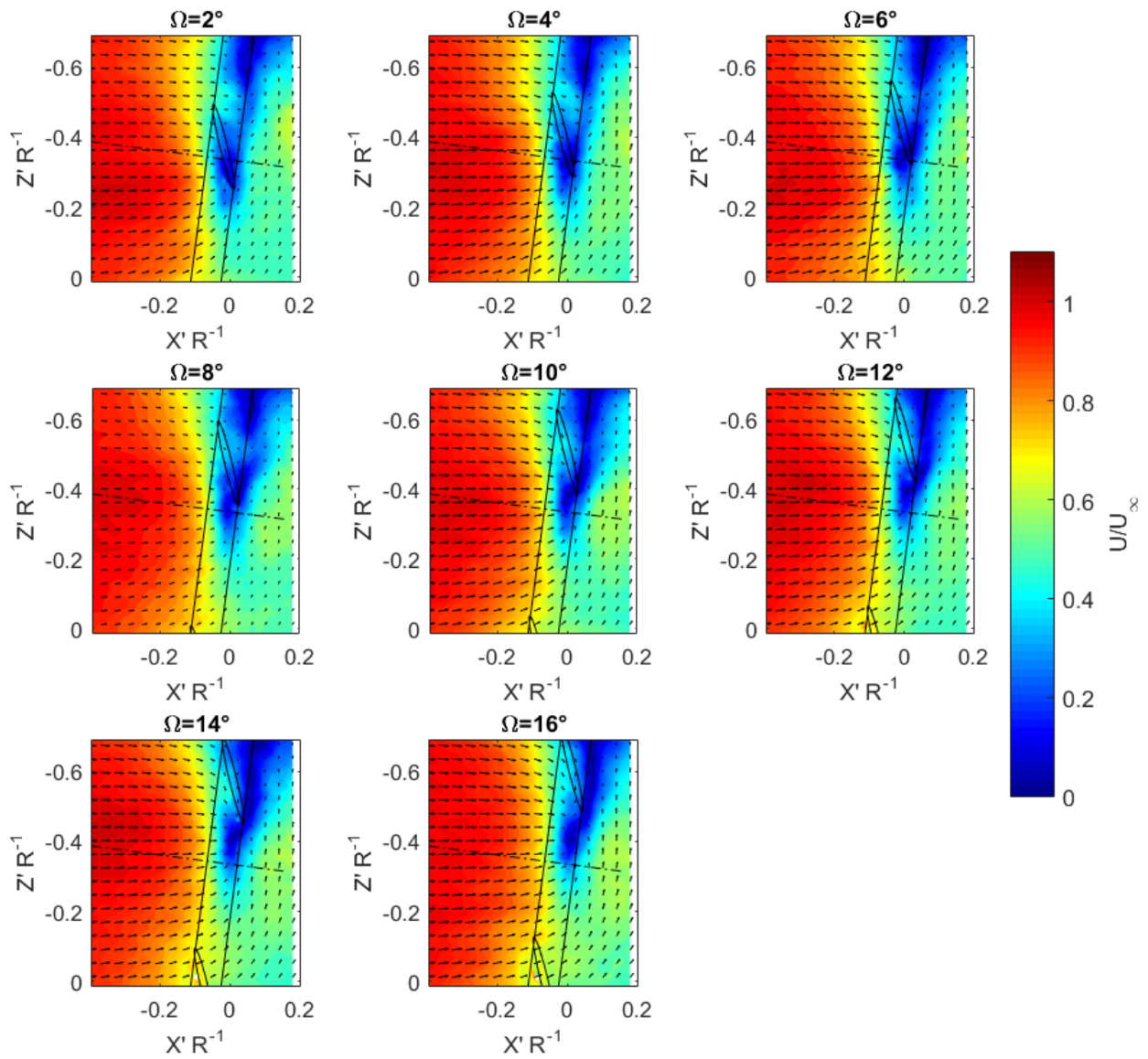


Figure 77: All phases of the phase averaged mean velocity fields in the center of the tip gap when the rotor is at +7.5° yaw.

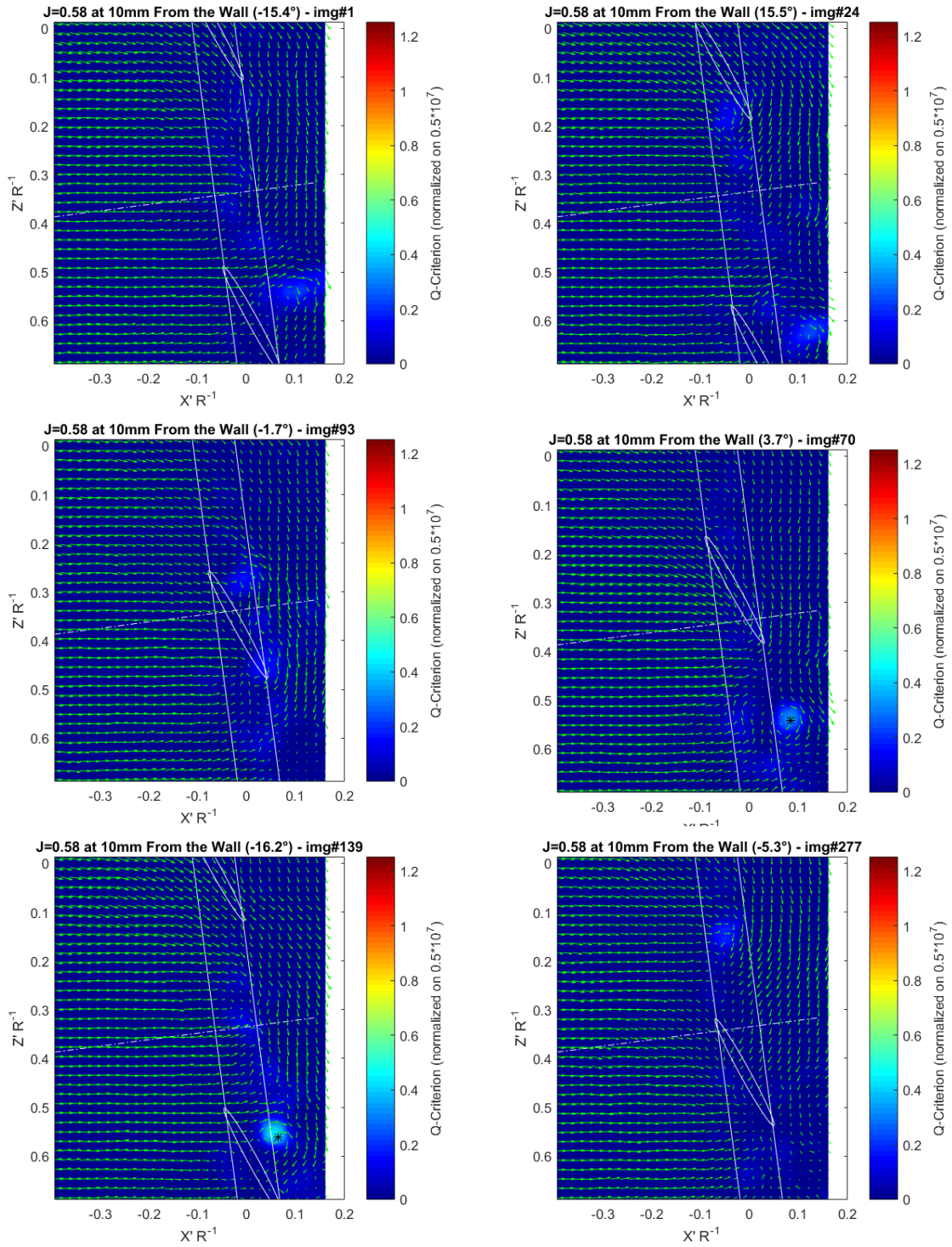


Figure 78: Example instantaneous velocity fields plotted on Q -criterion contours for the -7.5° yaw case.

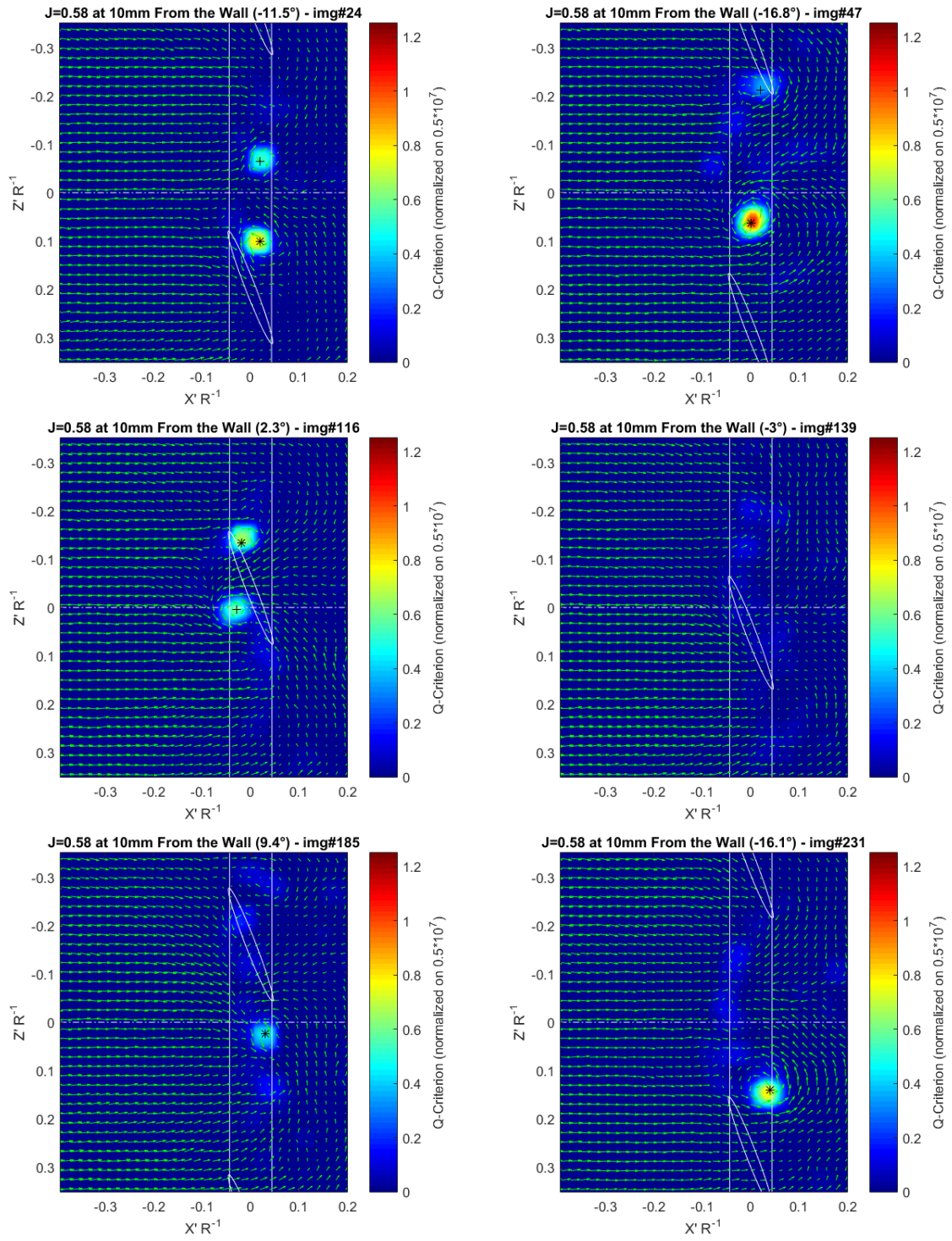


Figure 79: Example instantaneous velocity fields plotted on Q -criterion contours for the unyawed case.

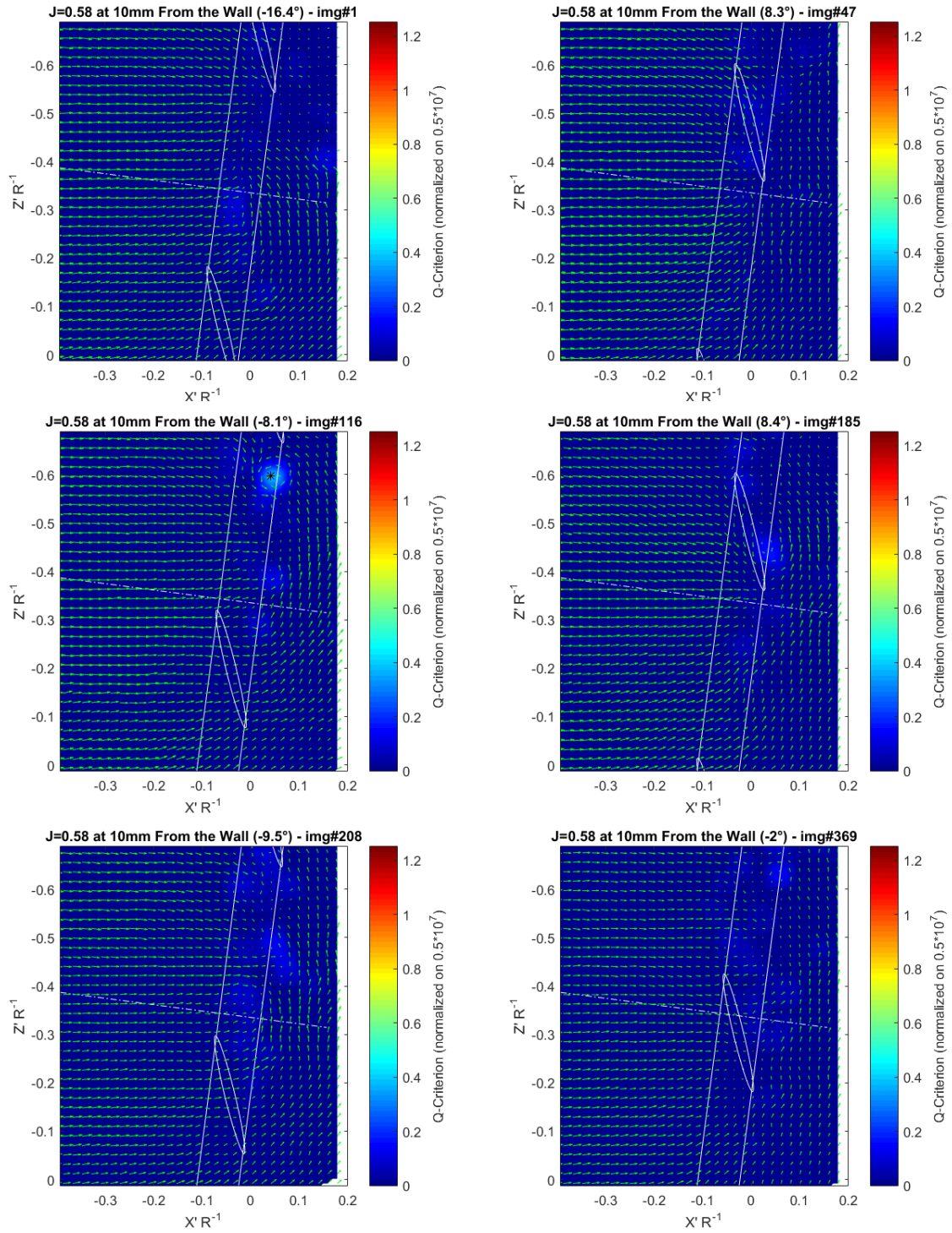
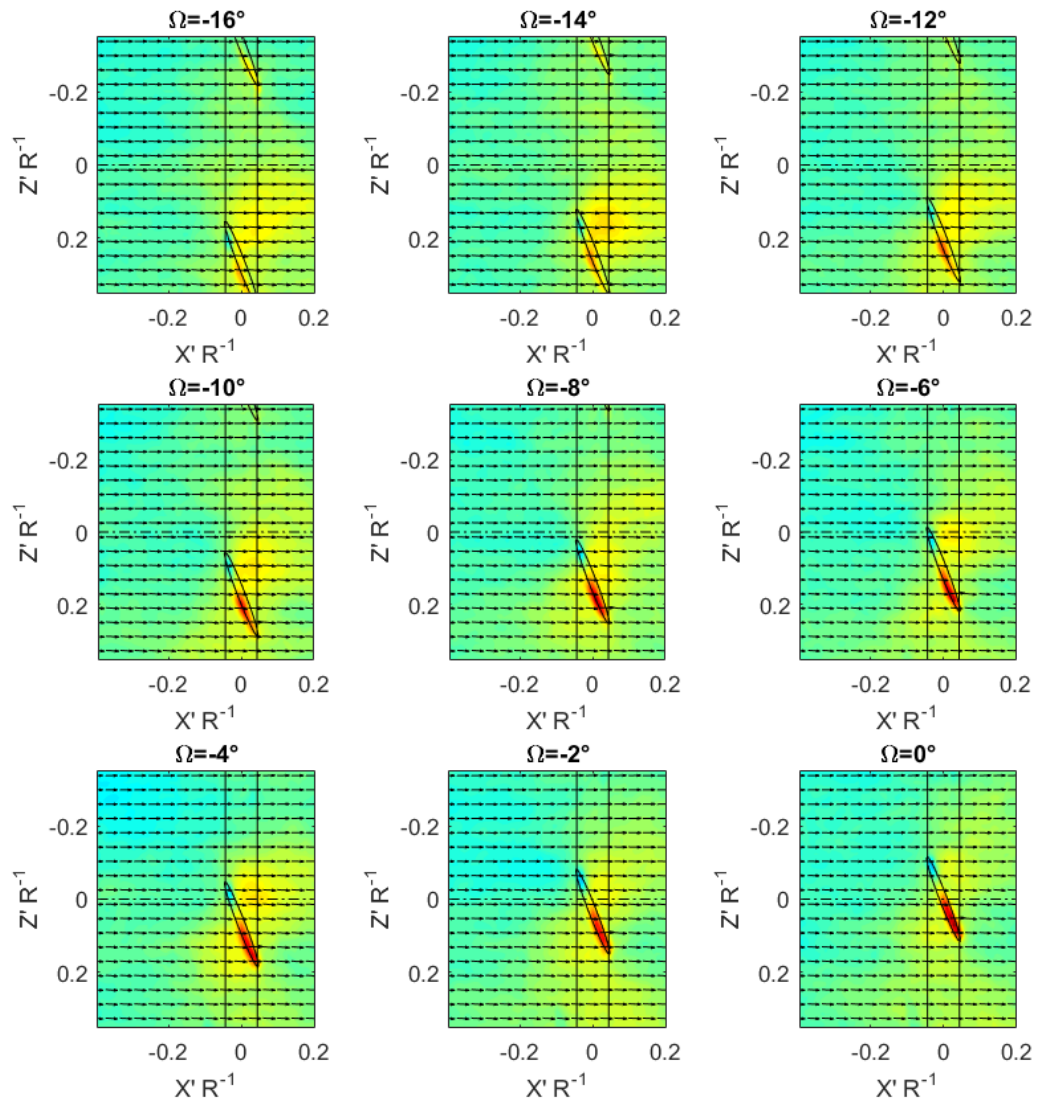


Figure 80: Example instantaneous velocity fields plotted on Q -criterion contours for the $+7.5^\circ$ yaw case.



Note: Figure is continued on next page.

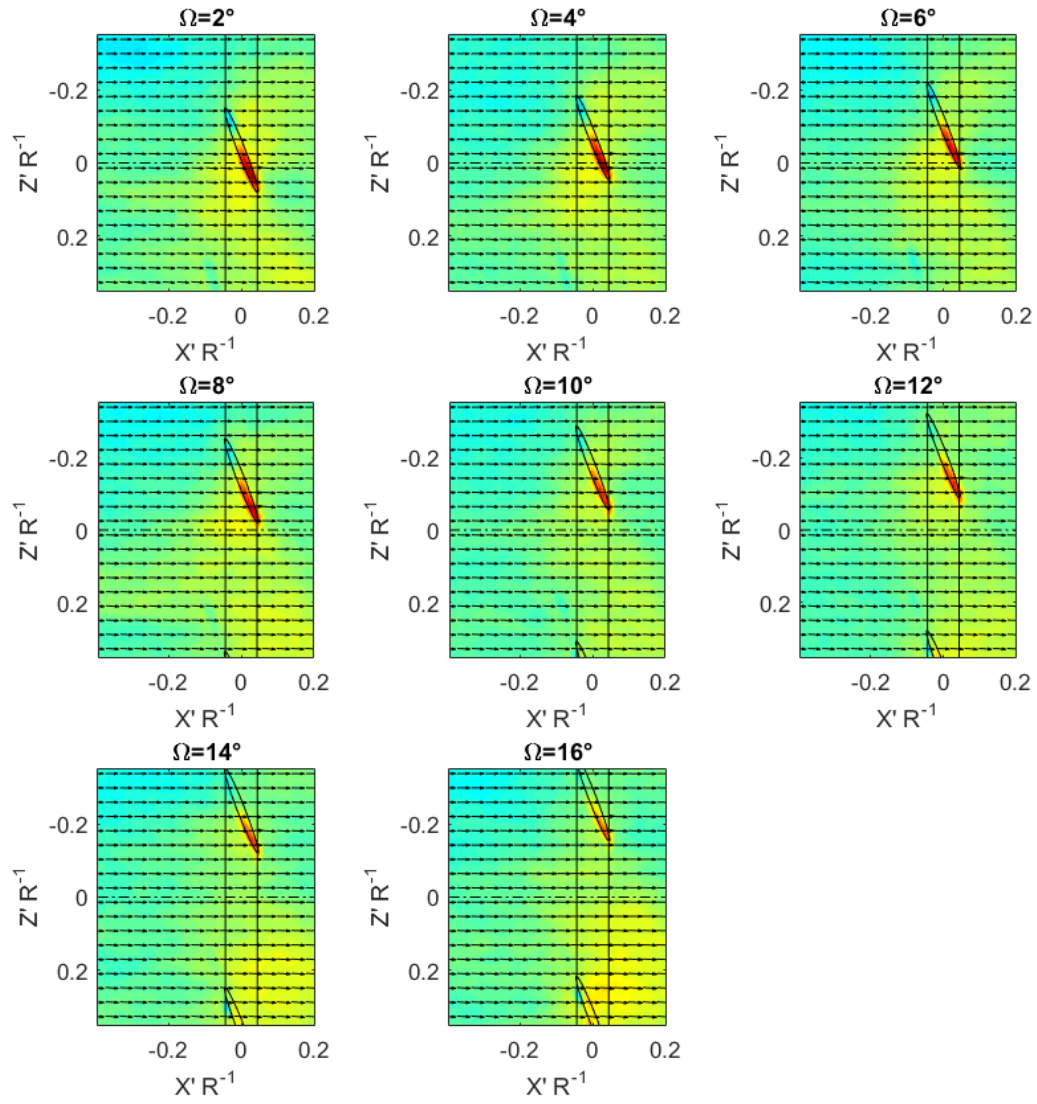
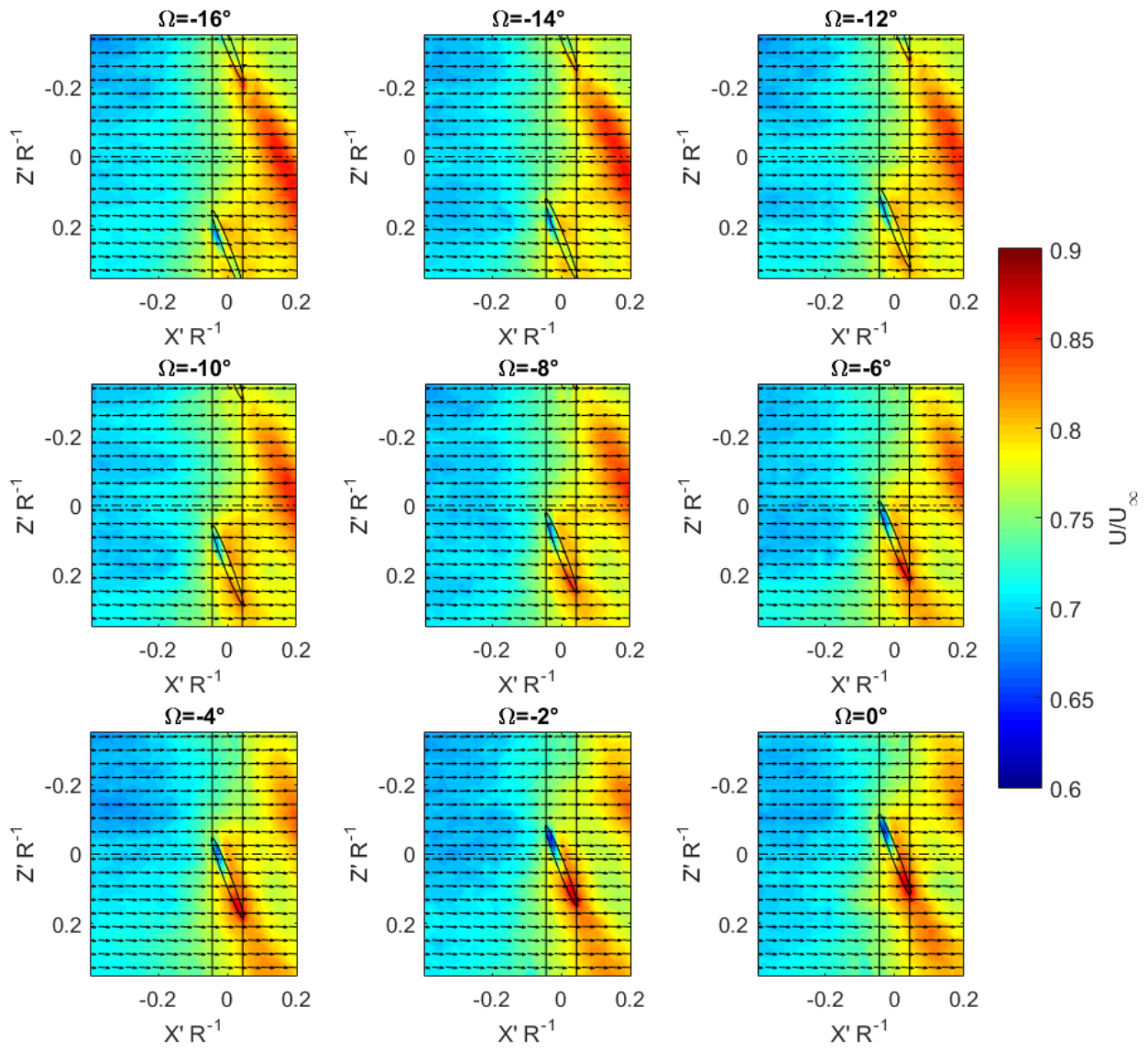


Figure 81: All phases of the phase averaged mean velocity fields in the center of the tip gap when the rotor is operating at the nominal zero thrust condition, $J = 1.44$ or 1823 RPM.



Note: Figure is continued on next page.

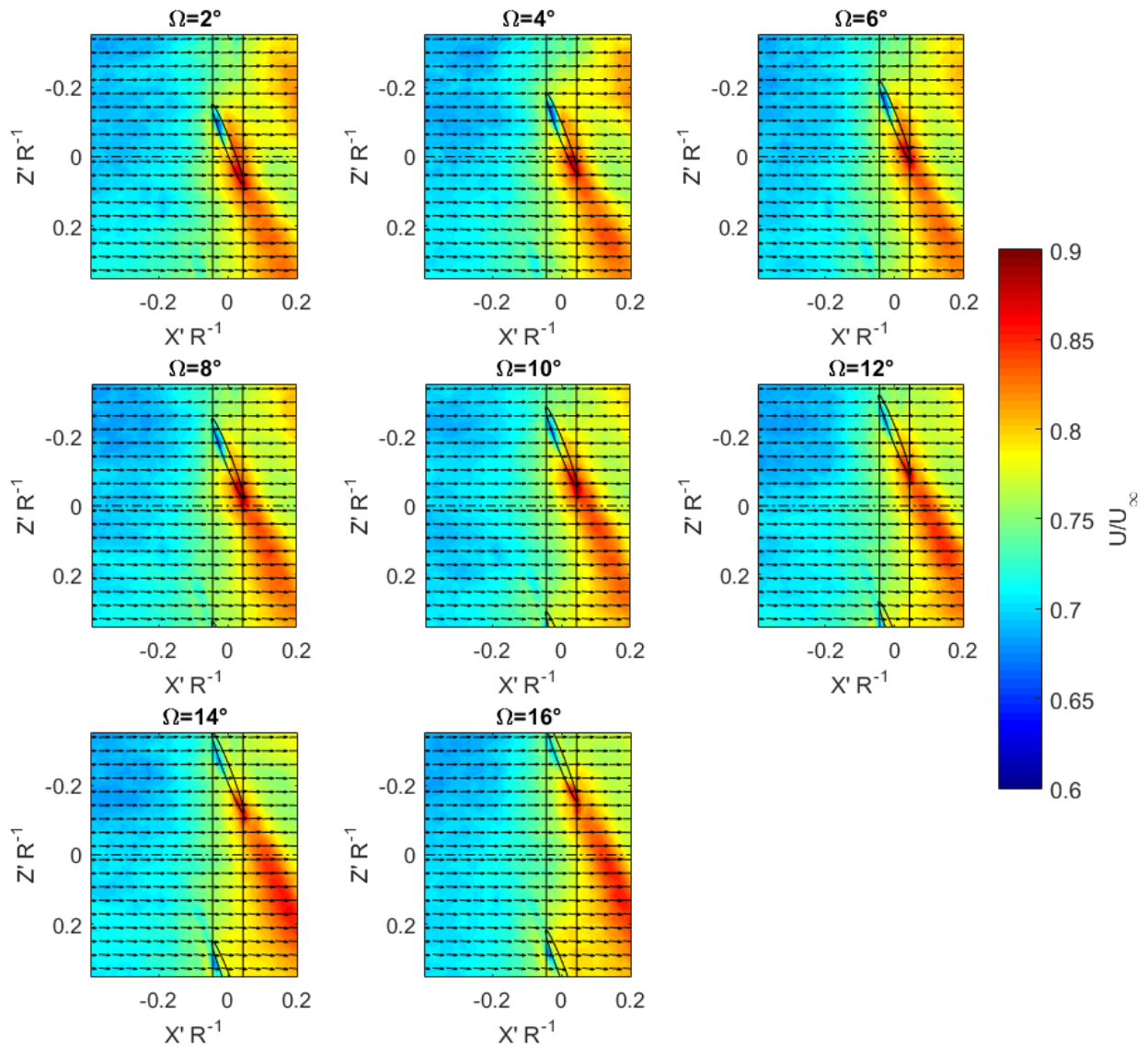
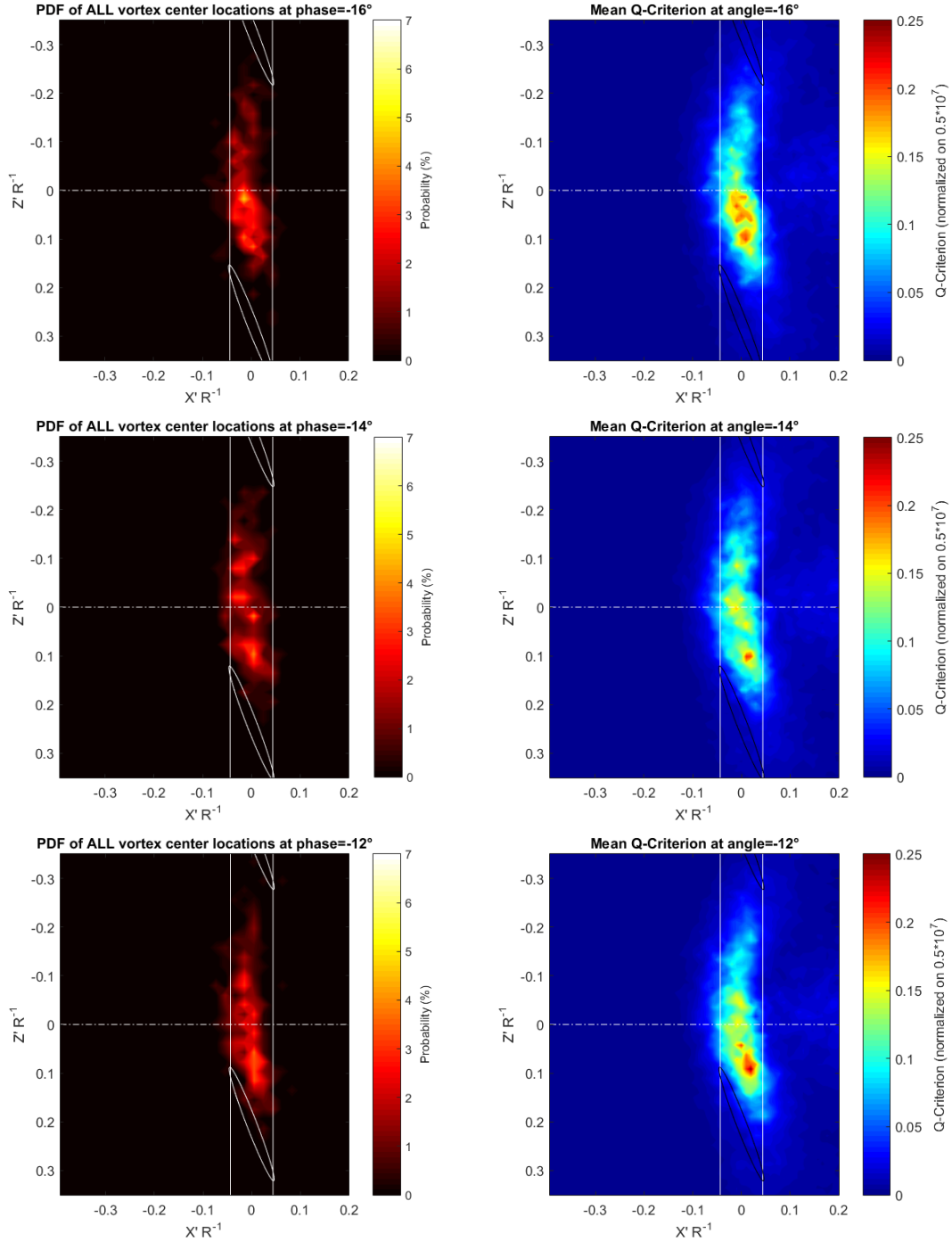


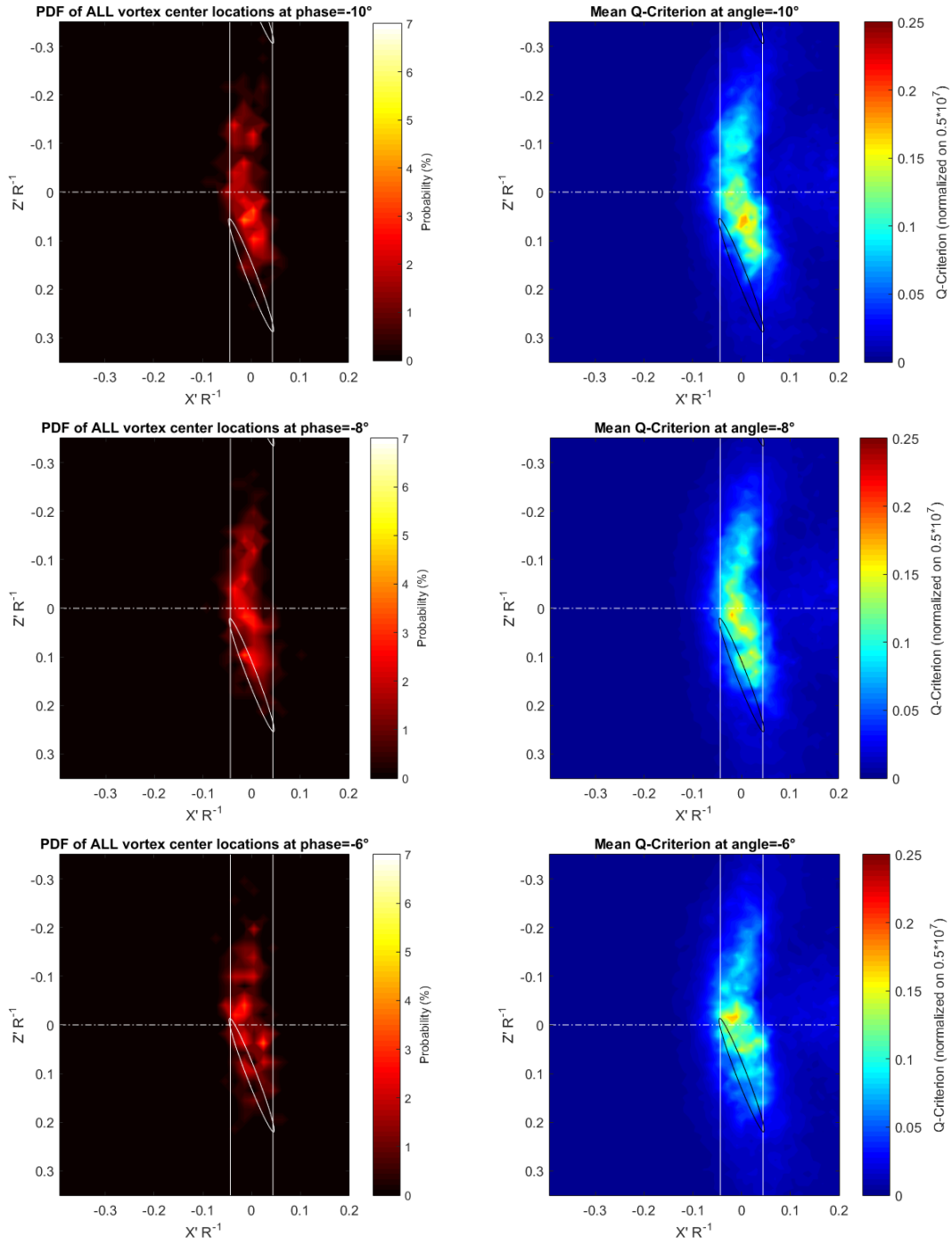
Figure 82: All phases of the phase averaged mean velocity fields in the center of the tip gap when the rotor is operating at the nominal zero thrust condition, $J = 1.75$ or 1500 RPM.

Appendix C – Vortex Identification as a function of rotor phase

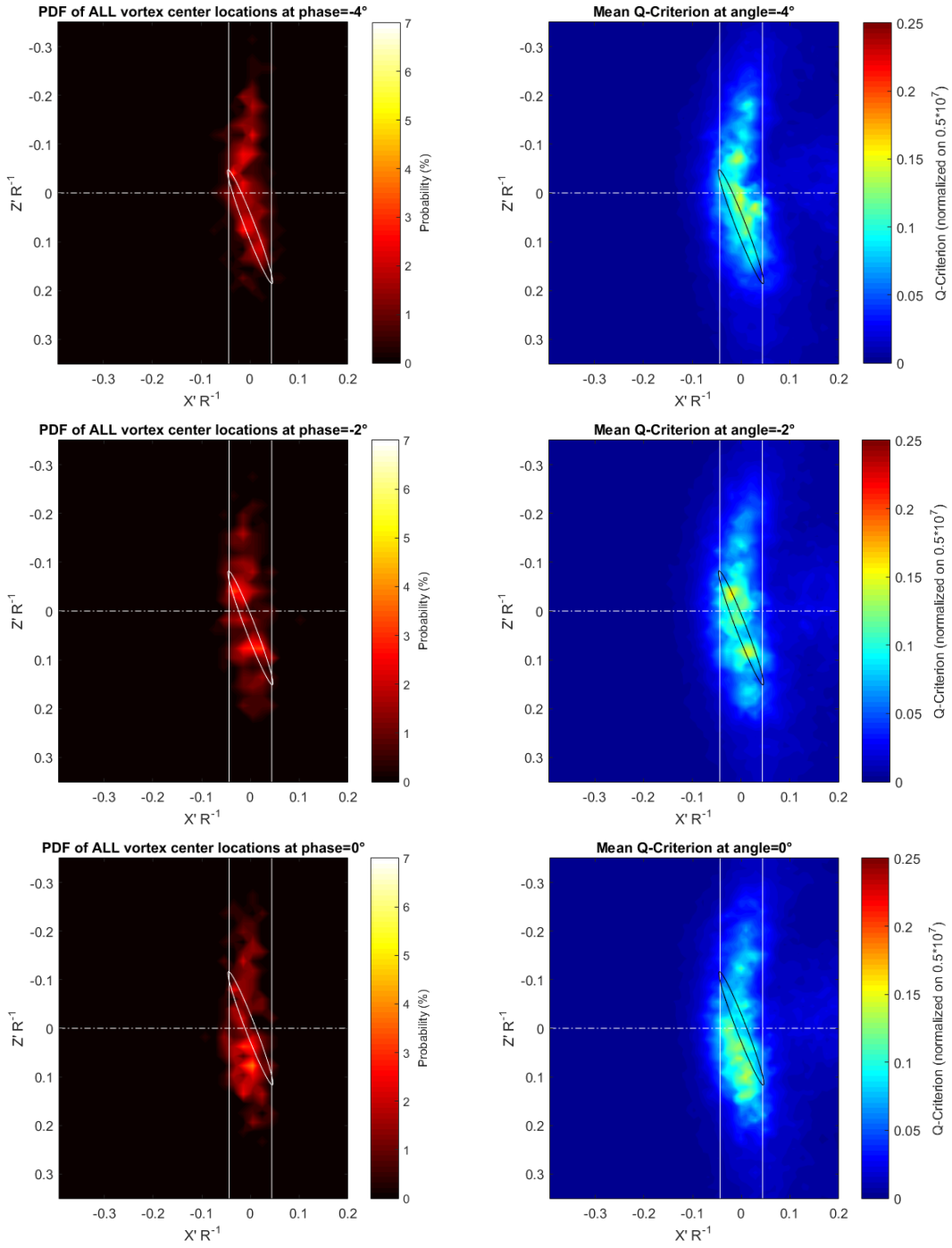
Sweep of Vortex Centers and Mean Q-Criterion



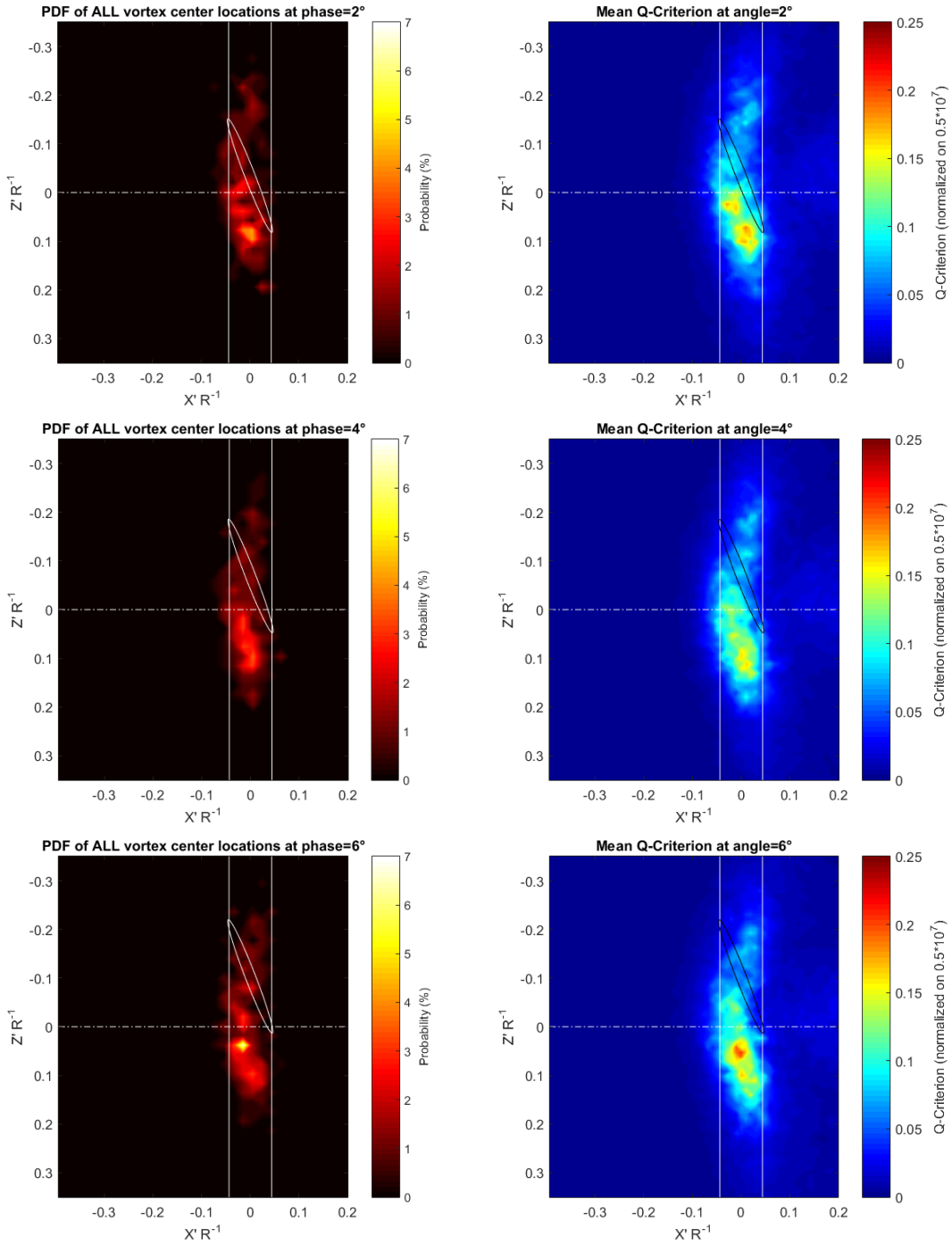
Note: Figure is continued on next page.



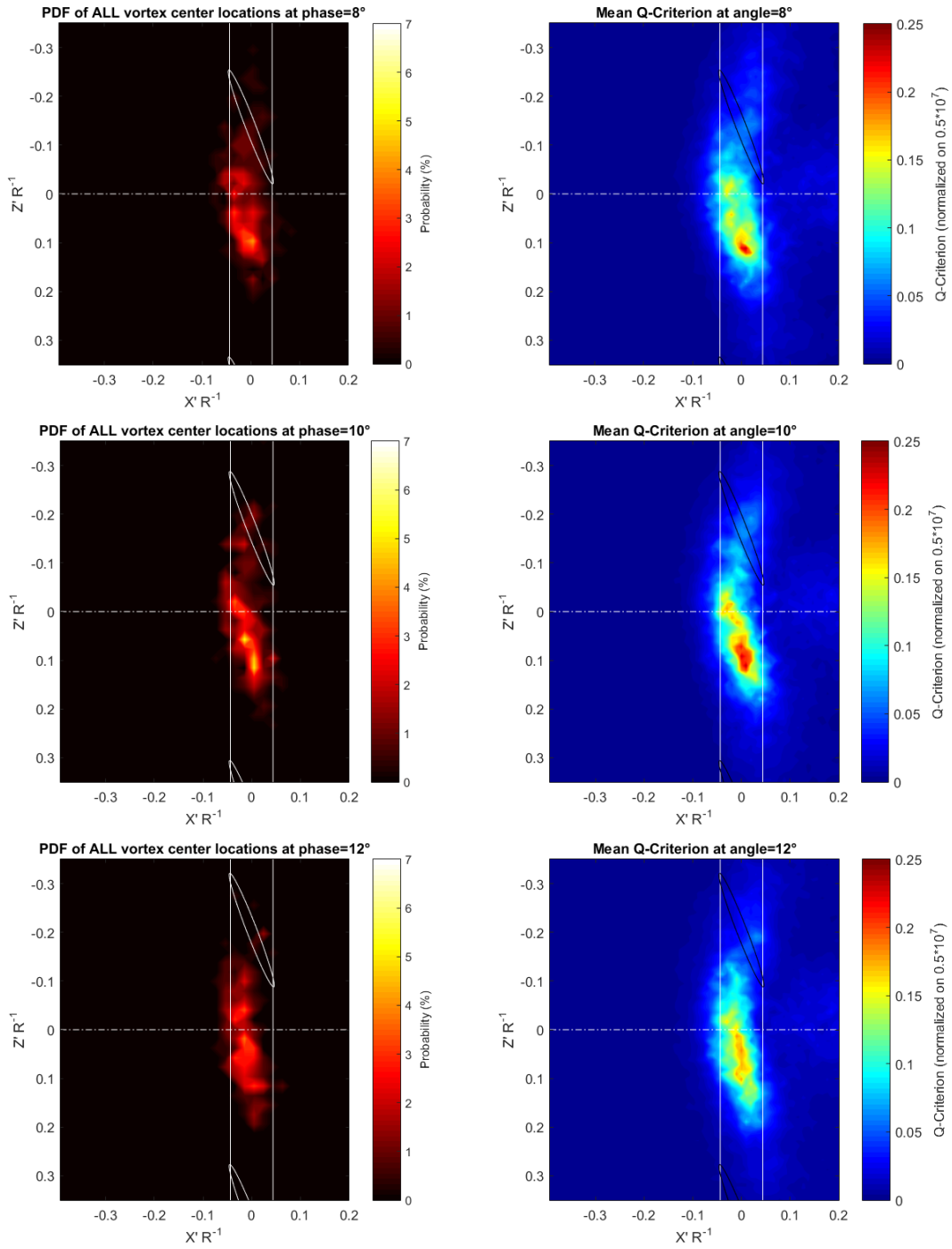
Note: Figure is continued on next page.



Note: Figure is continued on next page.



Note: Figure is continued on next page.



Note: Figure is continued on next page.

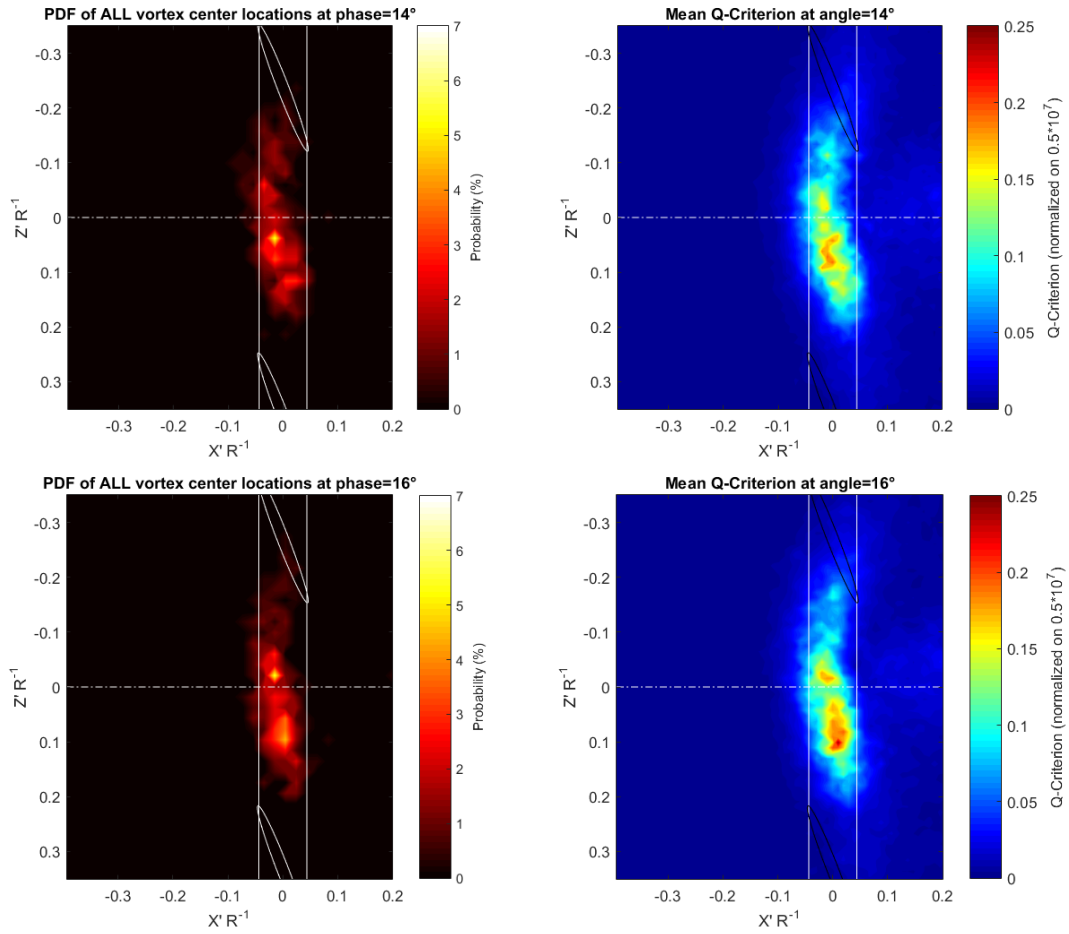
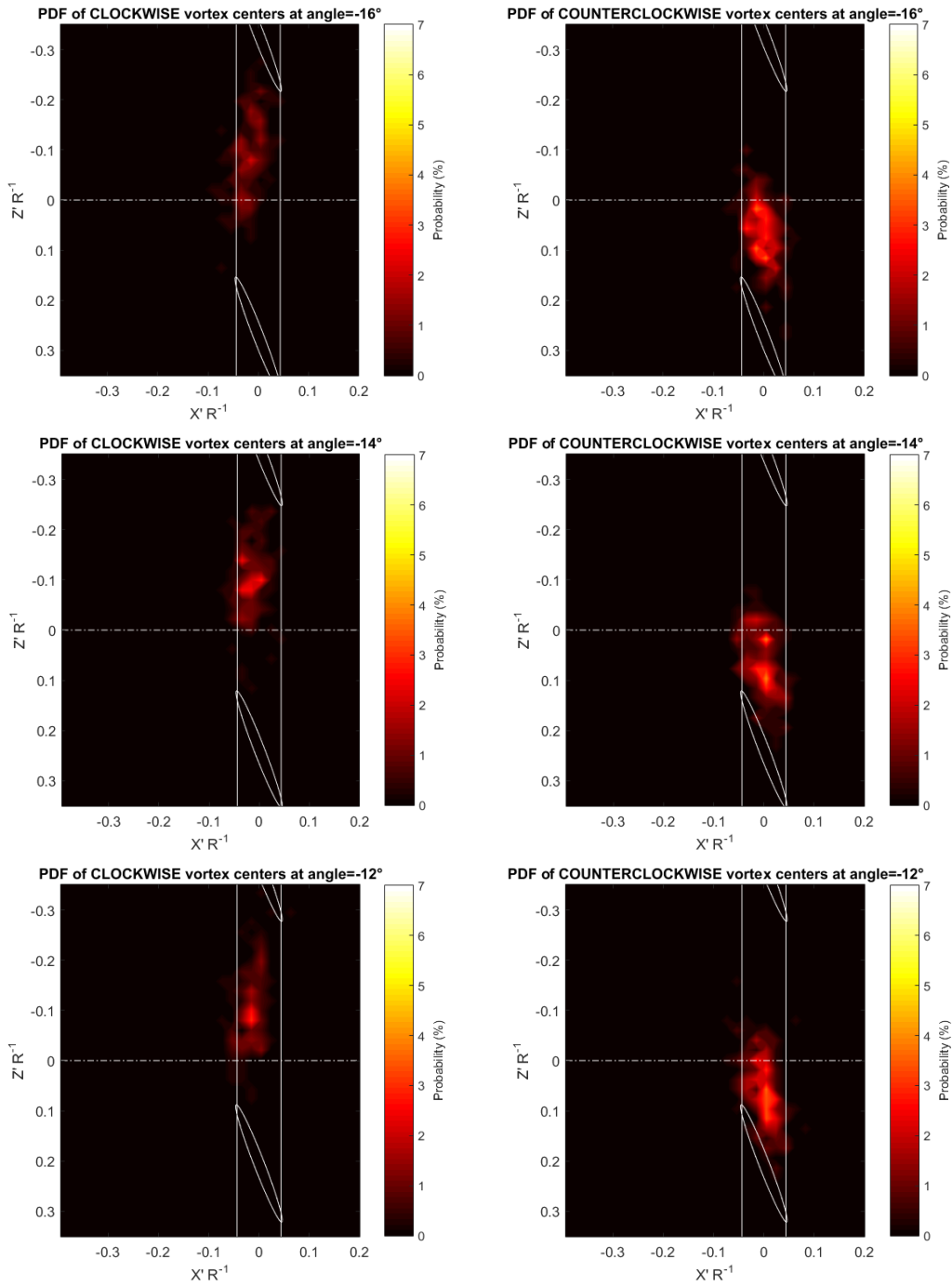
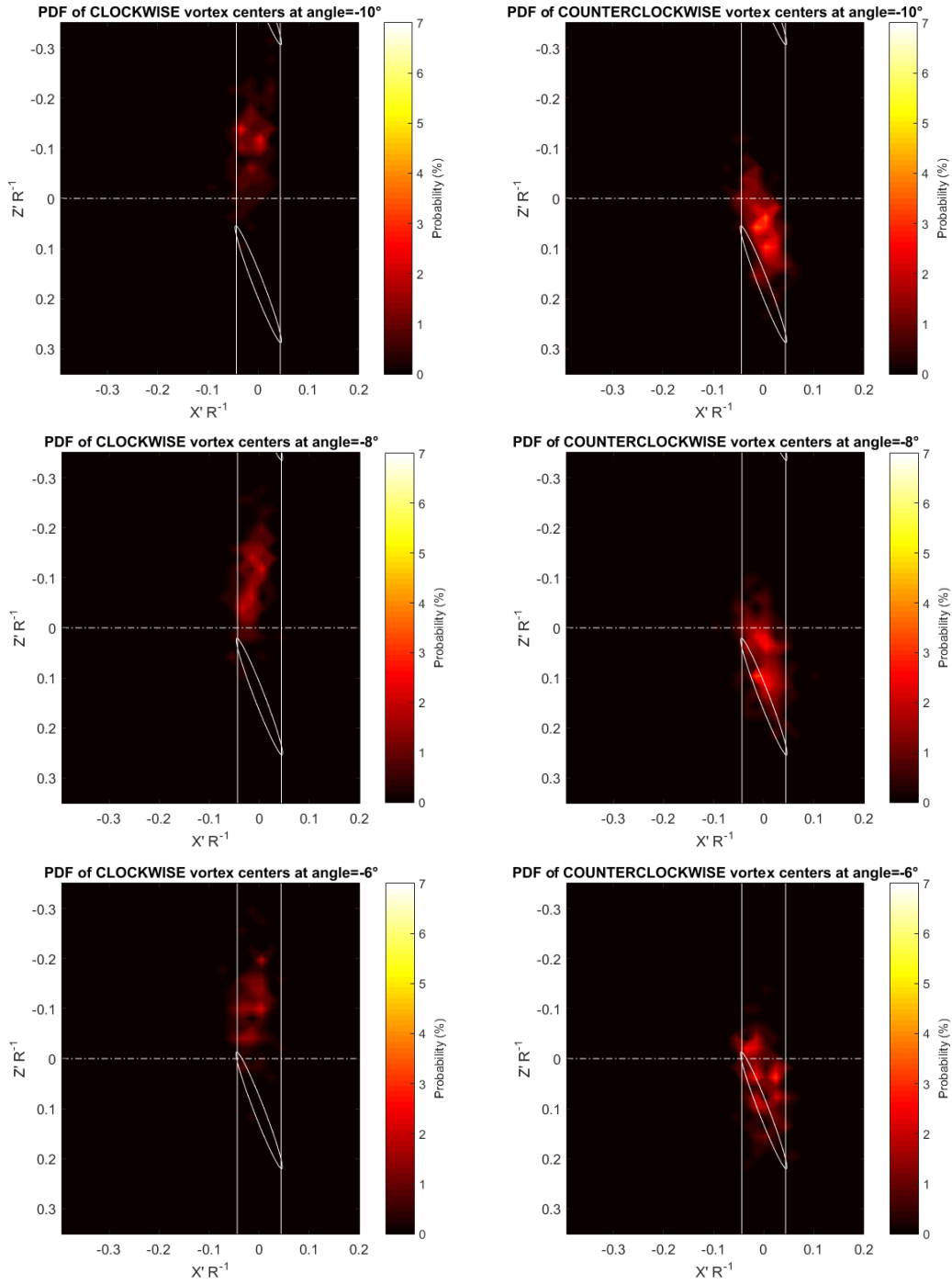


Figure 83: All phase averaged probability density functions (left column) and mean Q -criterion (right column).

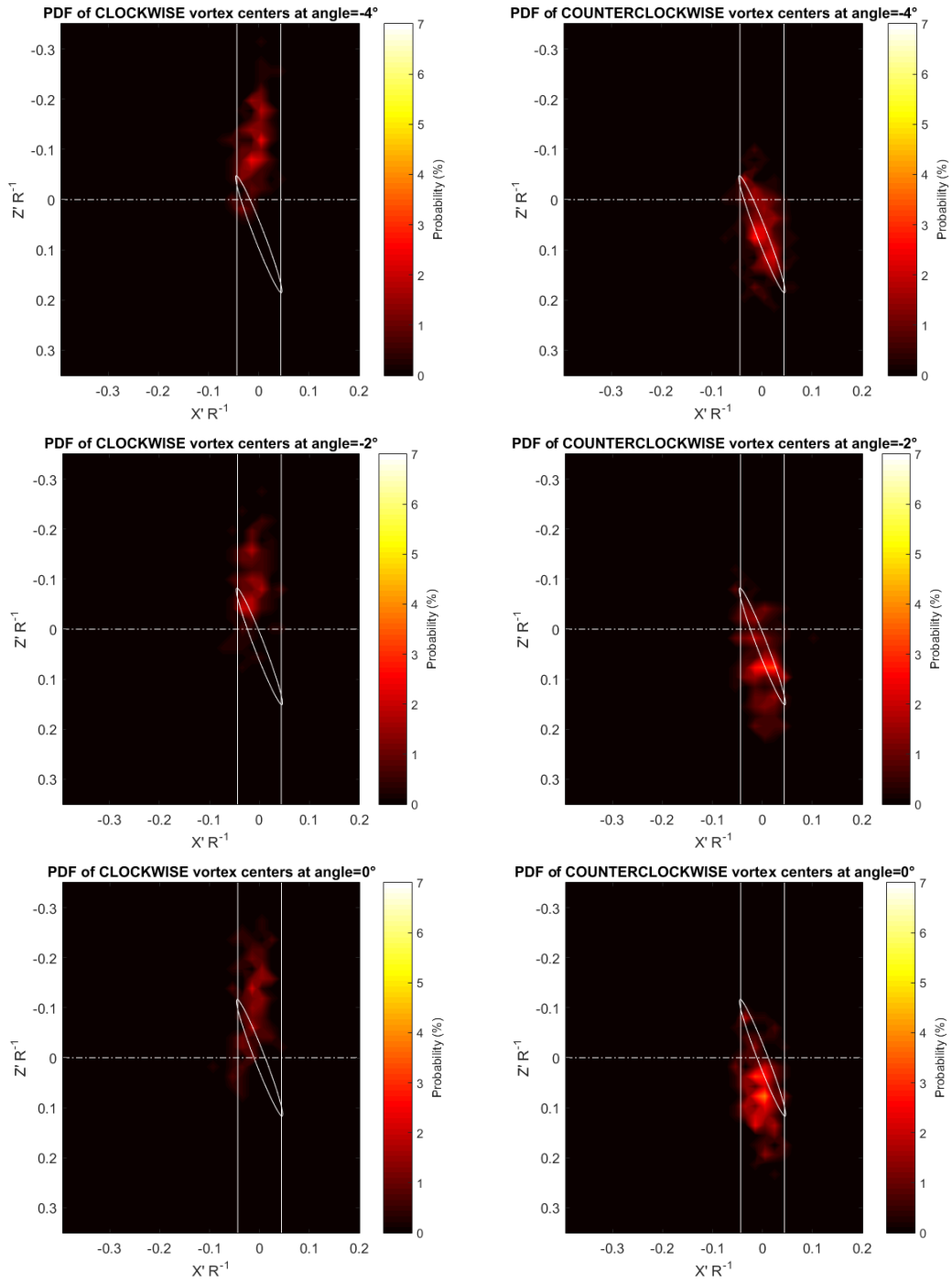
Sweep of Clockwise and Counterclockwise Vortices



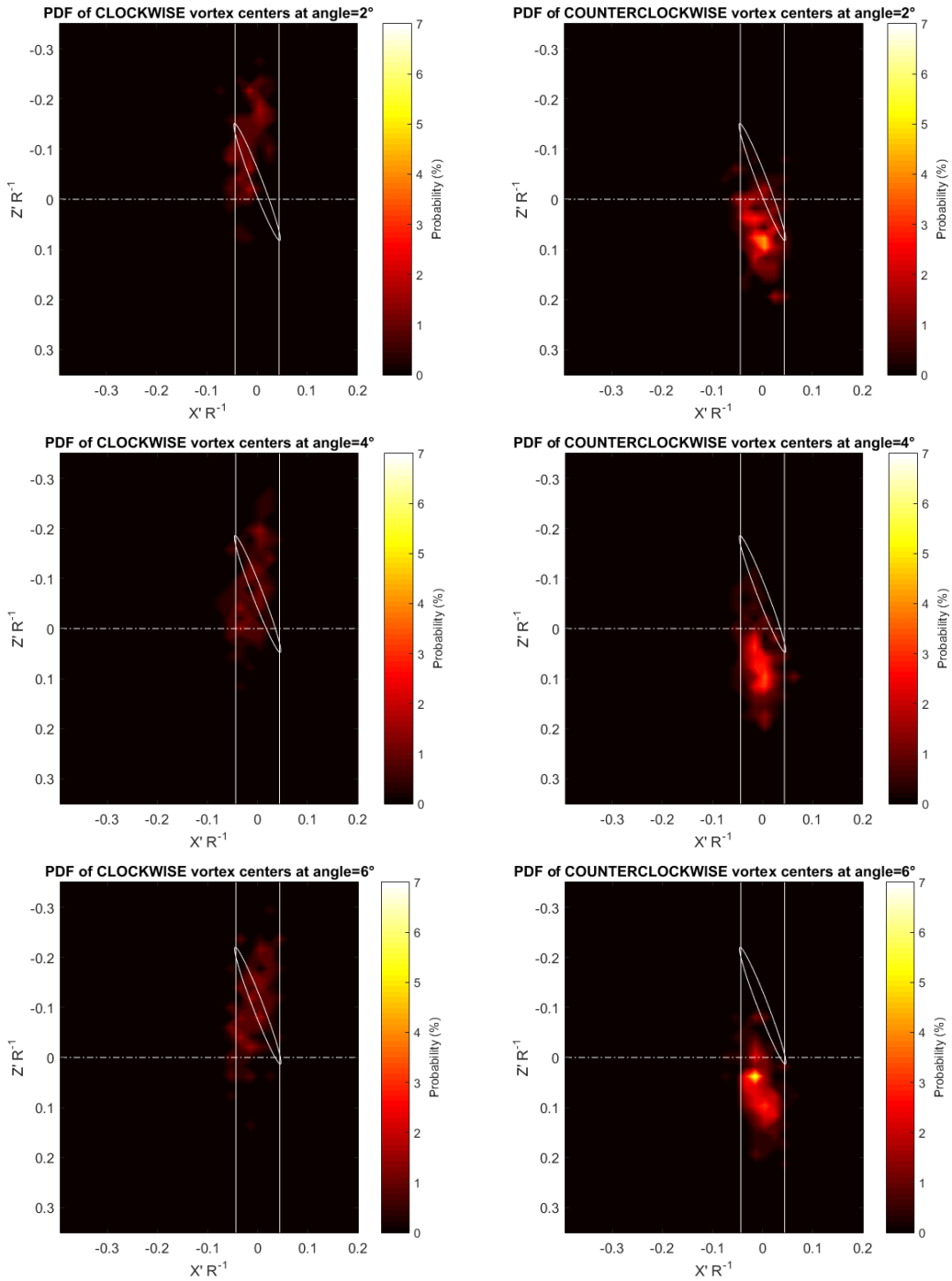
Note: Figure is continued on next page.



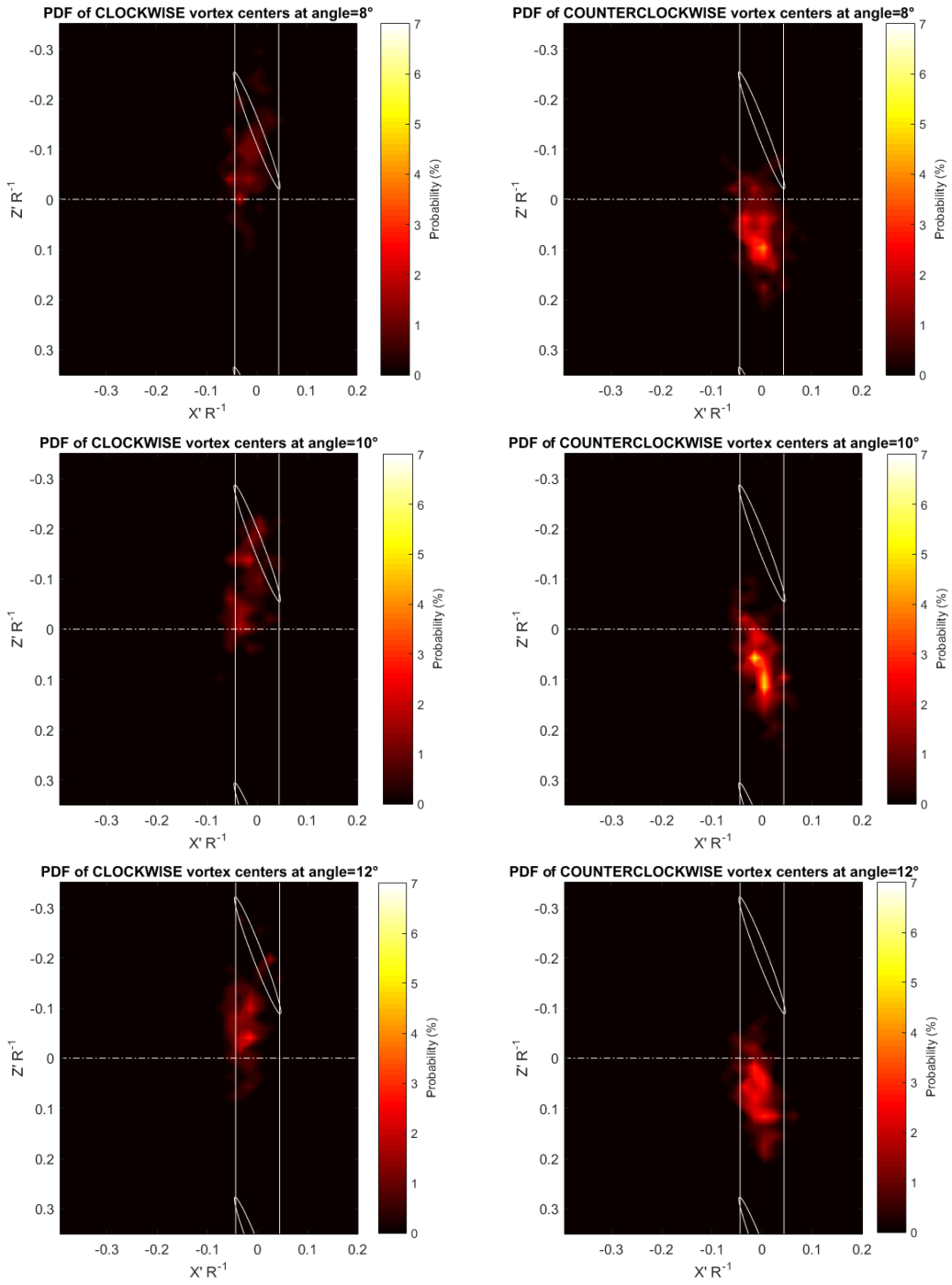
Note: Figure is continued on next page.



Note: Figure is continued on next page.



Note: Figure is continued on next page.



Note: Figure is continued on next page.

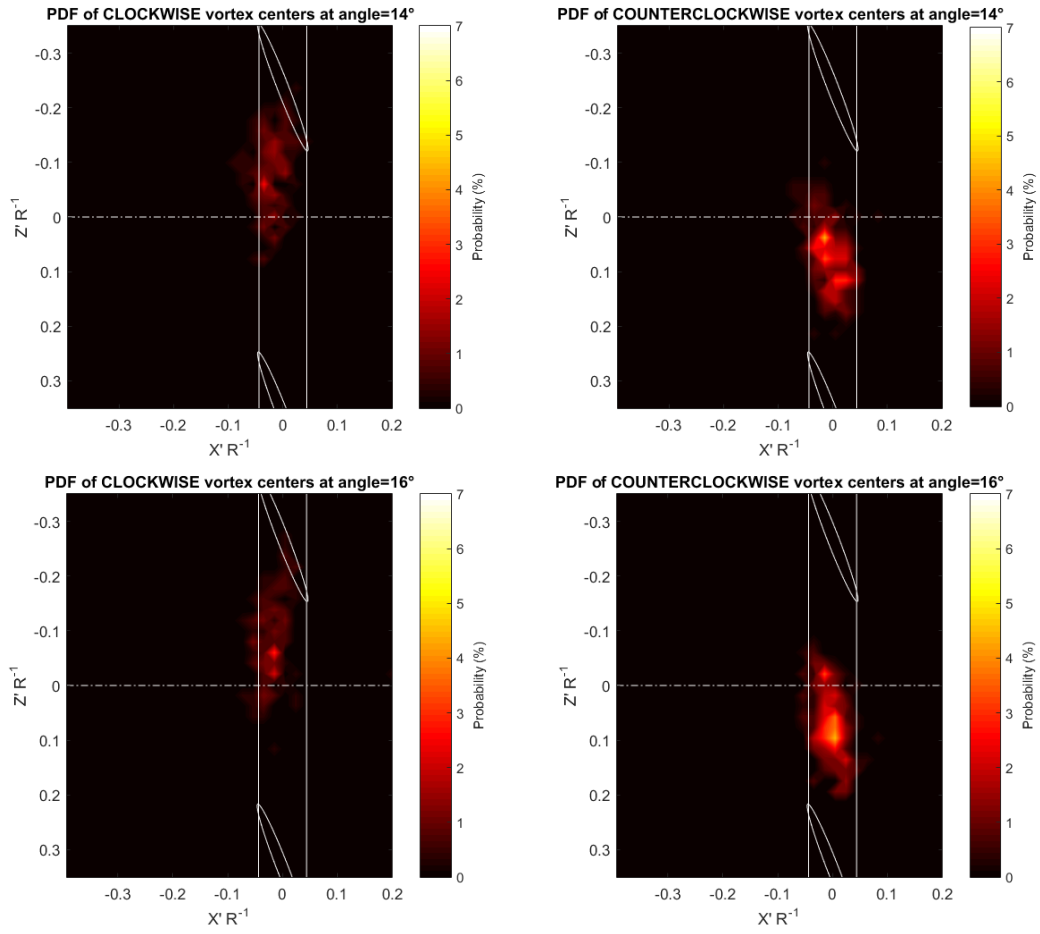


Figure 84: All phase averaged probability density functions for the clockwise (left column) and counter-clockwise (right column) vortex center locations.